Personalization of Computer Models for the Assessment of Atrial Fibrillation Vulnerability

Zur Erlangung des akademischen Grades einer

DOKTORIN DER INGENIEURWISSENSCHAFTEN (Dr.-Ing.)

von der KIT-Fakultät für

Elektrotechnik und Informationstechnik

des Karlsruher Instituts für Technologie (KIT)

genehmigte

DISSERTATION

von

Lourdes Patricia Martínez Díaz, M.Sc.

geb. in Mexiko Stadt

Tag der mündlichen Prüfung:	19. Juli 2024
Referent:	Priv.-Doz. Dr.-Ing. Axel Loewe
Korreferent:	Prof. Dr. María Guillem
Korreferent:	Prof. Dr. rer. nat. Olaf Dössel

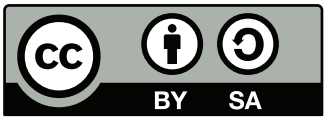

Abstract

Atrial fibrillation is the most prevalent cardiac arrhythmia in the adult population associated with an elevated risk of cardiovascular events and sudden cardiac death. In 2020, more than 50 million people worldwide were estimated to have atrial fibrillation, and its prevalence is expected to double by 2060. Despite significant progress in diagnosing and treating atrial fibrillation, current therapies often fail to prevent adverse outcomes due to their one-size-fits-all approach, ignoring patient variability. Patient-specific atrial computer models, also known as atrial digital twins, have emerged to improve our understanding of the pathophysiology of atrial fibrillation and to address the growing public health burden posed by atrial fibrillation today. The vision of atrial digital twins is to serve as a tool supporting the evaluation of different treatment strategies and selecting the most appropriate one to address the specific needs of each patient.

Personalization refers to the process of incorporating patient data, such as anatomical, functional, and substrate-related, into model parameters that reflect specific physical properties of the cardiac cells, tissue, or heart of the individual. Currently, there is no consensus on the methodology for constructing a digital twin to inform atrial fibrillation treatment. Some studies have developed methodologies using only non-invasive pre-procedural data, while others have employed invasive procedural data or a combination of both. The overall effect of the selected input data on the behavior of the patient-specific model is currently unknown.

In this thesis, arrhythmia vulnerability and tachycardia cycle length were quantified to assess the impact of different input data on the behavior of the patient-specific model. Arrhythmia vulnerability was defined as the ratio of the number of inducing points divided by the number of stimulation points on the atrial surface. Tachycardia cycle length was measured at the stimulation location and defined as the average time between peaks of the $\mathrm{d}V/\mathrm{d}t$ of induced reentries. In particular, the effect of three types of clinical data was evaluated: 1) anatomical personalization by comparing monoatrial versus biatrial models, 2) functional personalization by comparing models with personalized refractory period versus non-personalized models, and 3) functional and substrate personalization by comparing pre-procedural versus procedural data. Finally, a larger cohort of 22 patient-specific biatrial computer models was developed to train a machine learning classifier model for predicting arrhythmia vulnerability and evaluating the importance of personalized features on the prediction.

The results of the first project showed that incorporating the right atrium increased the mean vulnerability of the left atrium and revealed new induction points per patient model, which did not induce reentry in the monoatrial model. The right atrium had a substrate state-dependent effect on arrhythmia dynamics.

In the second project, the non-personalized scenario with homogeneous effective refractory period distribution was the least vulnerable to arrhythmia, while the regional personalized scenario was the most vulnerable. Heterogeneities in the form of regions promote unidirectional blocks, thereby increasing vulnerability, while the homogeneous scenario makes it less likely to induce reentry even with a shorter effective refractory period. Incorporating the effective refractory period as a continuous distribution slightly decreased vulnerability compared to the state-of-the-art heterogeneous non-personalized scenario. Increased dispersion of the effective refractory period in personalized scenarios has a greater effect on reentry dynamics than on the absolute value of vulnerability. Tachycardia cycle length of the personalized vs the non-personalized scenarios was significantly slower.

In the third project, total activation times and patterns were markedly different between invasive and non-invasive modalities. Arrhythmia vulnerability was more influenced by the extent of fibrosis than by the activation patterns. Finally, the machine learning classifier achieved a moderate accuracy for the prediction of arrhythmia vulnerability. Fibrosis density measured at 10 mm from the stimulation points and global conduction velocity were the features showing the highest impact on point inducibility prediction.

The results presented in this thesis provide evidence that the selection of input data affects the behavior of the patient-specific computer model. The right atrium plays an important role in the maintenance and induction of arrhythmia, thus the use of biatrial models seems advisable. Personalization of the effective refractory period has a greater effect on reentry dynamics than on the absolute value of vulnerability. Substrate-related personalization was the feature with the highest influence on vulnerability, therefore, further detection methods are needed to ensure its correct representation. The machine learning classifier may offer a fast alternative reducing the need of expensive computations of virtual pacing protocols, thus aiding the transition to clinical applications. The use of patient-specific models with highly detailed anatomy, function, and substrate may improve the development of tools for therapy planning for atrial fibrillation.

Zusammenfassung

Vorhofflimmern ist die verbreitetste Herzrhythmusstörung unter Erwachsenen und geht mit einem erhöhten Risiko kardiovaskulärer Krankheiten und plötzlichem Herztod einher. Im Jahr 2020 hatten schätzungsweise mehr als 50 Millionen Personen weltweit Vorhofflimmern und es wird erwartet, dass sich seine Prävalenz bis 2060 verdoppeln wird. Trotz beachtlicher Fortschritte bezüglich Diagnose und Behandlung von Vorhofflimmern bleiben therapeutische Ansätze unzureichend, was mit dem One-Size-Fits-All-Ansatz erklärt werden kann, welcher die Variabilität von Patient*innen nicht berücksichtigt. In dem Zusammenhang sind patient*innenspezifische Computermodelle des Vorhofs, auch Digitale Zwillinge genannt, nützlich, um das Verständnis der Pathophysiologie des Vorhofflimmerns zu verbessern und um sich der dadurch immer größer werdenden Belastung der Gesundheitssysteme zu widmen. Das Ziel atrialer Digitaler Zwillinge ist es, unterschiedliche Behandlungsstrategien zu evaluieren und die für die Patient*innen passendste zu bestimmen.

Personalisierung bedeutet, Patient*innendaten, beispielsweise anatomische, funktionelle und substratspezifische, in Modellparameter zu integrieren, um die physikalischen Eigenschaften der Herzzellen, des Herzgewebes oder des gesamten Herzens der Patient*innen widerzuspiegeln. Aktuell herrscht bezüglich der Methodik, Digitale Zwillinge zu konstruieren, um die Behandlung von Vorhofflimmern zu unterstützen, kein Konsens. Es existieren Studien, in denen ausschließlich nichtinvasive, vorprozedurale Daten genutzt werden, wohingegen andere invasive, prozedurale Daten oder eine Kombination beider nutzen. Der Gesamteffekt der Wahl der Input-Daten auf das Verhalten patient*innenspezifischer Modelle ist aktuell noch nicht bekannt.

In dieser Arbeit wurden die Anfälligkeit für Herzrhythmusstöungen und die Zykluslänge von Tachykardien quantifiziert, um ebendieses zu untersuchen. Die Anfälligkeit wurde als Verhältnis zwischen der Anzahl induzierender und stimulierender Punkte auf der Vorhofoberläche definiert. Die Zykluslänge einer Tachykardie wurde an der Stimulationsstelle gemessen und als durchschnittliche Zeitraum zwischen den $\mathrm{d}V/\mathrm{d}t$-Peaks des induzierten Reentries definiert. Im Speziellen wurde der Effekt drei unterschiedlicher klinischer Datentypen untersucht: (i) anatomische Personalisierung durch einen Vergleich monoatrialer und biatrialer Modelle, (ii) funktionelle Personalisierung durch einen Vergleich von Modellen mit personalisierter Refraktärzeit und unpersonalisierten Modellen sowie (iii) funktionelle und substratbezogene Personalisierung durch einen Vergleich vorprozedualer und prozedualer Daten. Schließlich wurde eine größere Kohorte von 22 patient*innenspezifischen biatrialen Computermodellen entwickelt, um ein maschinelles Lernklassifizierungsmodell

zur Vorhersage der Anfälligkeit für Arrhythmien zu trainieren und die Bedeutung personalisierter Merkmale für die Vorhersage zu bewerten.

Die Ergebnisse dieser Arbeit zeigen, dass die Wahl der Input-Daten das Verhalten der patient*innenspezifischen Computermodelle beeinflusst. Der rechte Vorhof spielt eine wichtige Rolle bei der Induzierung und Aufrechterhaltung von Arrhythmien, weshalb der Gebrauch biatrialer Modelle empfehlenswert erscheint. Die Personalisierung der effektiven Refraktärzeit hat einen größeren Einfluss auf die Reentry-Dynamik als auf den Gesamtwert der Anfälligkeit. Die substratspezifische Personalisierung hatte den größten Einfluss auf die Anfälligkeit, weshalb weitere Methoden gebraucht werden, um seine korrekte Repräsentierung zu gewährleisten. Der maschinelle Lernklassifikator kann eine schnelle Alternative darstellen, die den Bedarf an teuren Berechnungen von virtuellen Schrittmacherprotokollen reduziert und so den Übergang zu klinischen Anwendungen erleichtert. Der Gebrauch patient*innenspezifischer Modelle mit hochaufgelöster Anatomie, Funktion und Substrat kann die Entwicklung von Therapieplanungsmethoden für Vorhofflimmern verbessern.

Resumen

La fibrilación auricular es la arritmia cardíaca mas prevalente en la población adulta, asociada a un elevado riesgo de eventos cardiovasculares y muerte súbita cardiaca. Se estima que en 2020 más de 50 millones de personas en todo el mundo padecían fibrilación auricular, y se prevé que la prevalencia de esta enfermedad se duplique para el año 2060. A pesar de los notables avances en el diagnóstico y el tratamiento de la fibrilación auricular, los enfoques terapéuticos actuales siguen siendo insuficientes para prevenir los resultados adversos debido a que cuentan con un enfoque estandarizado que ignora la variabilidad de los pacientes. Los modelos computacionales personalizados del corazón, también conocidos como gemelos digitales cardiacos, han surgido para mejorar nuestra comprensión de la fisiopatología de la fibrilación auricular y abordar la creciente carga para la salud pública que supone esta enfermedad. La visión de los gemelos digitales es servir como herramienta para ayudar a evaluar diferentes estrategias de tratamiento de la enfermedad y seleccionar la más adecuada que aborde las necesidades específicas de cada paciente.

La personalización es el proceso de incorporación de los datos clínicos del paciente, ya sean anatómicos, funcionales, o relacionados con el sustrato cardíaco, mediante parámetros en el modelo que reflejen propiedades físicas de las células cardiacas, el tejido o el corazón del paciente. Actualmente no existe un consenso en cuanto a la metodología a seguir para construir un gemelo digital que informe sobre el tratamiento de la fibrilación auricular. Estudios previos han realizado gemelos digitales utilizando exclusivamente datos clínicos no invasivos obtenidos previos al procedimiento, mientras que otros han empleado datos clínicos invasivos obtenidos al momento del procedimiento o una combinación de ambos tipos de datos clínicos. Actualmente se desconoce el efecto global que los datos de entrada seleccionados tienen sobre el comportamiento del modelo personalizado del paciente.

En esta tesis, se calculó la vulnerabilidad arrítmica y la duración del ciclo de taquicardia con el fin de evaluar el impacto de los distintos datos de entrada en el comportamiento del modelo específico del paciente. La vulnerabilidad arrítmica se definió como la relación entre el número de puntos inductores dividido entre el número total de puntos de estimulación en la superficie auricular. La duración del ciclo de taquicardia se cuantificó midiendo el tiempo entre picos de $\mathrm{d}V/\mathrm{d}t$ de la reentrada inducida. En particular, se evaluó el efecto de tres tipos de datos clínicos: 1) la personalización anatómica comparando modelos monoatriales frente a biatriales, 2) personalización funcional comparando modelos con periodo refractario personalizado frente a modelos no personalizados, y 3) personalización funcional y del sustrato comparando datos previos al procedimiento frente a datos obtenidos durante el

procedimiento. Por último, se creó una cohorte de 22 modelos biatriales específicos de pacientes para entrenar un modelo de aprendizaje automático para predicir la vulnerabilidad arrítmica y para evaluar la importancia de los parámetros personalizados en la predicción de la inducibilidad.

Los resultados mostraron que la incorporación de la aurícula derecha aumentó la vulnerabilidad media de la aurícula izquierda. Al incorporar la aurícula derecha se detectaron nuevos puntos de inducción por modelo de paciente que no inducían reentrada en el modelo monoauricular. La aurícula derecha tuvo un efecto sobre la dinámica de la arritmia que depende del nivel de remodelado. El escenario no personalizado con distribución homogénea del periodo refractario efectivo fue el menos vulnerable a arritmia, mientras que el escenario regional personalizado fue el más vulnerable. Las heterogeneidades en forma de regiones favorecen los bloqueos unidireccionales, aumentando así la vulnerabilidad, mientras que el escenario homogéneo hace menos probable la inducción de reentrada incluso con un periodo refractario efectivo más corto. La incorporación del periodo refractario efectivo como distribución continua disminuyó ligeramente la vulnerabilidad en comparación con el escenario heterogéneo no personalizado de última generación. El aumento de la dispersión del periodo refractario efectivo en los escenarios personalizados tiene un mayor efecto sobre la dinámica de la reentrada que sobre el valor absoluto de la vulnerabilidad. La duración del ciclo de taquicardia de los escenarios personalizados frente a los no personalizados fue significativamente más lenta. Los tiempos y patrones de activación total fueron notablemente diferentes entre las modalidades invasiva y no invasiva. La vulnerabilidad arrítmica estuvo más influida por la extensión de la fibrosis que por los patrones de activación. Por último, el clasificador de aprendizaje automático alcanzó una precisión moderada para la predicción de la vulnerabilidad arrítmica. La densidad de fibrosis medida a 10 mm de distancia de los puntos de estimulación y la velocidad de conducción global fueron las características que tuvieron el mayor impacto en la predicción de la inducibilidad.

Los resultados presentados en esta tesis aportan pruebas de que la selección de los datos de entrada afecta al comportamiento del modelo computacional específico del paciente. La aurícula derecha tiene un papel importante en el mantenimiento e inducción de arritmias, lo que sugiere el uso de modelos biatriales. La personalización del periodo refractario efectivo tiene un mayor efecto sobre la dinámica de las arritmias que sobre el valor absoluto de la vulnerabilidad. La personalización relacionada con el sustrato fue la característica con mayor influencia en la vulnerabilidad. Debido a las diferencias que existen en los métodos actuales para la detection de fibrosis, es aconsejable el estudio de métodos de detección más robustos para garantizar su correcta representación en los modelos computacionales. El clasificador de aprendizaje automático puede ser una alternativa rápida para reducir la necesidad de cálculos costosos de los protocolos de estimulación virtuales, ayudando así a la transición de los modelos computacionales a las aplicaciones clínicas. El uso de modelos específicos de paciente con anatomía, función y sustrato altamente detallados puede mejorar el desarrollo de herramientas para la planificación de la terapia de la fibrilación auricular.

"We are not going in circles, we are going upwards. The path is a spiral; we have already climbed many steps."

– Hermann Hesse, Siddhartha

Acknowledgments

This work was made possible through the support and contributions of many individuals. First of all, I express my sincere gratitude to Prof. Olaf Dössel for providing me with the opportunity to pursue my PhD studies at the IBT, enabling me to fulfill my dream of conducting research in Germany. His passionate lectures on electromagnetism and his active participation in conferences have been truly inspiring. I also extend my thanks to PD Dr.-Ing. Axel Loewe for his guidance and dedicated support over these years. His impeccable management skills made all the manuscripts of this work possible, and taught me to pursue efficiency and organized research. Additionally, I am grateful to Prof. Maria Guillem for welcoming me into her laboratory and for the warm treatment I received while at the ITACA institute in Valencia. I am thankful to Prof. Ursula Ravens for our fruitful scientific discussions regarding the right atrium and her invaluable support every time we meet. I am thankful to Prof. Blanca Rodríguez for her support during the writing of our manuscript and for her inspirational talks during our meetings. I would also like to express my gratitude to Prof. Francesca Spadea for her caring attitude and for our meaningful conversations about women in science and studying abroad.

I am also thankful to my colleagues at IBT: Carmen, for being by my side from the very beginning and for spreading her joy; Cristian, for our scientific and long life-related discussions, Joshi, for being my tandem buddy offering me hugs whenever I needed them, and for his assistance with German bureaucracy; Tomas, for our engaging discussions about open science and specially for being a great officemate; Jorge for his extraordinary support through all these years; Claudia, for her positive energy and inspiring spirit; Laura, for her clinical expertise and German lessons; Debbie, for her kindness; Eki, for her motivation to keep learning German; and Marie, for always being ready to assist with IT matters. Special thanks to Moritz, Silvia, Steph, Domenico, and Ciro for proofreading my thesis. Thanks also to Joni, Matthias, Lorena, Miriam, Alex, for the time we spend playing tennis and having fun. I also want to express my gratitude to all the students whose hard work contributed to this thesis: Christian, Nikola, Jule, and Annika. Special thanks go to Pascal for helping me at the end of the PhD journey and for being patient with my German. I also would like to thank Ramona for motivating me to speak German, helping me with the Ausländerbehörde and for taking care of my plants when I was at home.

Additionally, I would like to thank my colleagues in the PersonalizeAF consortium. I was fortunate to share my journey with 14 exceptional individuals, and I was extremely happy every time we met. Special thanks to Albert for his brilliant assistance with the ERP

project and our discussions about the future, Marilu for cheering me up and being there whenever I needed it, Narimane for her joyful and easy-going attitude, and Tere for her energy and dedication. Special thanks to Arantxa for being an excellent project manager of the PersonalizeAF consortium. To all the partners in the hospitals in Karlsruhe, Valencia, and Barcelona: Dr. Armin Luik, Annika Haas, Dr. Joaquin Osca, Dr. Maite Izquierdo, Pedro Pimenta, Dr. Lluis Mont, Dr. Till Althoff, Eric, and Jana. I would also like to thank the collaborators at ADAS3D company for their support and warm welcoming: Rosa, Barbara, Ana, Lluis, Gelsy, and Francia. It was an honor to work with you all.

I am also thankful to my family and friends who have supported me. To my dear friends in Mexico—Patty, Soco, Danny, Erika, and Pam—for their genuine care and support from afar. To Luisa, for making me feel truly understood and accompanied. To Inma, for reminding me to dream big. To Ana, for our time in Barcelona, our video calls, and for giving me hope when I needed it the most. To Alina, for every time we met in Mexico, reminding me how special our connection is, and for her love and constant support. I am deeply grateful with my parents and little brother, for filling up my batteries whenever I was home and for believing in me all this time. To Remy, Ivy, Bambi, and Tamy, for their unconditional love. Special thanks to my mom for reminding me about the important things in life and for sending me good morning vibes to start my days. Finally, to my dearest Dominik, for his loving care during stressful times and specially, for making me feel at home in Germany.

Contents

Abbreviations

AF	atrial fibrillation
AFl	atrial flutter
AP	action potential
APD	action potential duration
AV	atrioventricular
AVN	atrioventricular node
BB	Bachmann's bundle
BEM	boundary element method
CA	catheter ablation
CCS	cardiac conduction system
CS	coronary sinus
CT	crista terminalis
CTI	cavotricuspid isthmus
CV	conduction velocity
EAM	electro-anatomical map
EAMS	electro-anatomical mapping system
ECG	electrocardiogram
ECGI	electrocardiographic imaging
EP	electrophysiological
ERP	effective refractory period
FEM	finite element method
IAC	interatrial connection
IIR	image intensity ratio
IP	inducing points
IVC	inferior vena cava
LA	left atrium
LAA	left atrial appendage
LAPW	left atrial posterior wall
LAT	local activation time
LGE	late gadolinium enhancement
LLR	left lateral ridge
LV	left ventricle
LVA	low voltage area

ML	machine learning
MR	magnetic resonance
MRI	magnetic resonance imaging
MV	mitral valve
PCL	pacing cycle length
PEERP	pacing at the end of the effective refractory period
PM	pectinate muscles
PV	pulmonary vein
PVI	pulmonary vein isolation
RA	right atrium
RAA	right atrial appendage
RAPW	right atrial posterior wall
RCT	randomized controlled trial
RF	random forest
RV	right ventricle
SAN	sinoatrial node
SP	stimulating points
SSM	statistical shape model
SVC	superior vena cava
TCL	tachycardia cycle length
TP	transmembrane potential
TV	tricuspid valve
UQ	uncertainty quantification
VR	virtual reality
VTK	Visualization Toolkit

Chapter 1

Introduction

1.1 Motivation

Atrial fibrillation (AF) is a highly prevalent cardiac arrhythmia characterized by irregular and rapid electrical activity within the atria [1]. In 1876, the German clinician Carl W. Nothnagel was among the first to describe pulse irregularity, referred to as *delirium cordis* [2]. In 1909, the British cardiologist Thomas Lewis described the relationship between this pulse irregularity and AF, referring to this rhythm disorder as "an extremely common condition" [3]. Since then, many clinicians and researchers have sought to define the complex interplay of pathological mechanisms involved in AF. The intricate nature of AF mechanisms spanning multiple time and space scales, from molecular interactions to whole-heart dynamics, requires the development of advanced tools to improve our understanding of AF [4]. Nearly 150 years later, advanced tools such as patient-specific computer models, known as *cardiac digital twins*, have emerged to address the growing public health burden posed by AF today by enhancing our comprehension of AF pathophysiology, improving early diagnosis, predicting disease trajectory, and tailoring treatment selection [5, 6].

In the year 2020, it was estimated that over 50 million people worldwide suffered from AF [7], and its prevalence is projected to double by the year 2060 [8]. AF is associated with a two-fold higher risk of mortality, with women exhibiting a higher risk of death compared to men [9, 10]. AF has been correlated to an elevated risk of stroke, dementia, chronic renal disease, peripheral artery disease, heart failure, myocardial infarction, and sudden cardiac death [1, 7]. AF often remains asymptomatic in its initial stages, and its diagnosis typically occurs in a late state when symptoms emerge and lead to hemodynamic instability and subsequent health complications [11]. Given all these adverse outcomes associated with AF, early detection and implementation of effective management strategies is crucial for addressing this growing global health concern.

Despite notable advancements in the diagnosis and treatment of AF, current therapeutic approaches are insufficient in preventing these negative outcomes [12]. The failure of current therapeutic approaches for the management of AF may be attributed to the one-size-fits-all approach, which disregards patient variability [13]. In this context, precision

medicine aims to deliver personalized treatments tailored to the patient's unique needs [14]. With the advent of precision medicine, patient-specific computer models of the atria, are enhancing our understanding of intricate interactions during AF and have already been used to identify ablation targets [15, 16], tailor ablation strategies [17], and predict recurrence in AF patients [18, 19]. Indeed, these advancements in patient-specific computer models of the atria offer promising prospects for improving patient outcomes through personalized medicine [20].

Currently, there is no consensus regarding the methodology for constructing digital twins to inform AF treatment. Particularly, the effect of the selected input data on the model behavior is unknown. Some studies have developed methodologies utilizing only pre-procedural data, e.g. including anatomy and substrate derived from late gadolinium enhancement magnetic resonance imaging (LGE-MRI) [15, 19, 21]. In this context, *substrate* refers to an area of atrial tissue with pathological characteristics leading to the initiation and/or maintenance of AF. The primary advantage of building a patient-specific model using pre-procedural data is the ability to generate the model prior the arrival of the patient in the electrophysiology lab, enabling computationally expensive simulations to be conducted beforehand. However, a key limitation is the lack of personalization of the electrophysiology of the patient-specific model, relying instead on population-based data to parameterize the model. Furthermore, discrepancy exists between the spatial distribution of fibrosis informed by LGE-MRI and low voltage areas (LVA), potentially influencing the behaviour of the patient-specific model. Determining which data is crucial for constructing a patient-specific atrial computer model and its impact on the model behaviour remains uncertain. The next chapter introduces the concepts of cardiac digital twins and personalization.

1.2 Cardiac Digital Twins

A *cardiac digital twin*, or patient-specific cardiac model, is a virtual representation of the physical heart of a patient which integrates clinical data and uses mathematical equations to describe the relationship between function and anatomy in the heart [14, 22]. The vision of the cardiac digital twin encompasses the synergy of four components: personalization, mechanistic modeling, statistical modeling, and clinical applications (Figure 1.1) [13, 23]. Creating a digital twin is known as *twinning*. During the twinning process, personalized clinical data derived from the patient, and non-personalized data derived from clinical trials, rule-based observations or experimental data, are incorporated into the model. The integration of non-personalized data, also referred to as population-based data, enables the estimation of model parameters that are unavailable due to limited access to patient-specific clinical data [24].

Personalized and non-personalized data play essential roles in the twinning process. For instance, Figure 1.3 depicts an example of the creation of a patient-specific model using both personalized and non-personalized data. The personalized atrial anatomy derived from MRI is used together with non-personalized rule-based anatomical definitions to account for

regional heterogeneity in the atria. Substrate spatial distribution is obtained from LGE-MRI and the local activation times (LAT) are derived from electro-anatomical map (EAM).

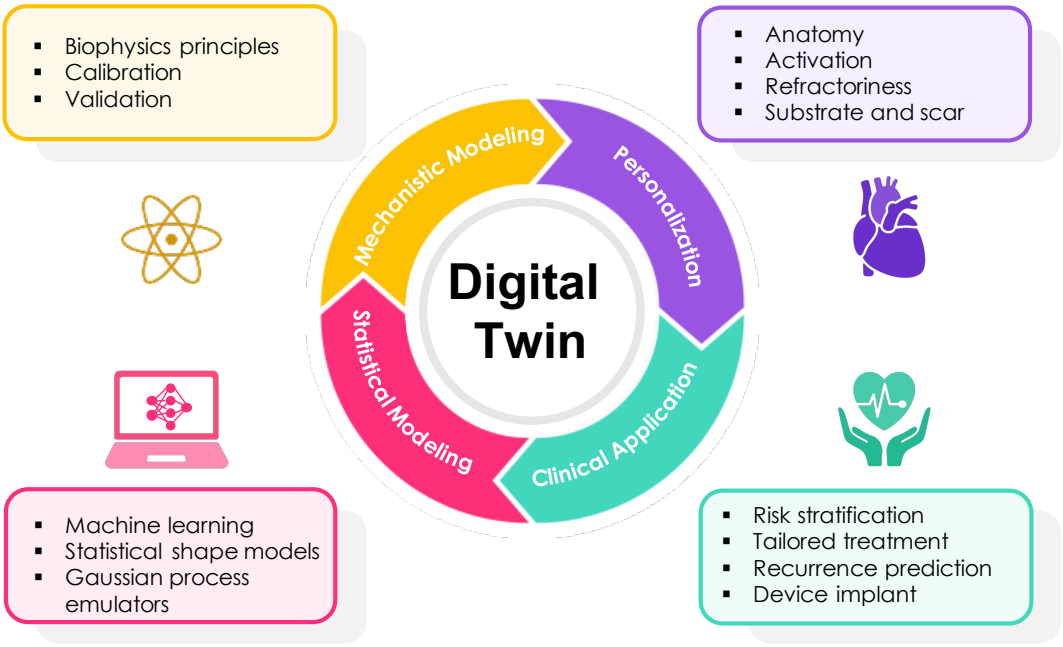

Figure 1.1: The vision of the cardiac digital twin for cardiac electrophysiology applications. The main four components of cardiac digital twins include personalization, clinical application, statistical and mechanistic modeling. Inspired by [13, 23].

Personalization refers to the process of translating patient data into model parameters that reflect specific physical properties of the cardiac cells, tissue, or organ of the individual, for example, cellular action potential duration, myocyte arrangement, tissue conductivity, tissue stiffness, myocardium wall thickness, and gross cardiac anatomy [25]. Personalization can be further classified into two main streams: anatomical and functional (Figure 1.2). Anatomical personalization refers to generating a geometrical representation of the patient's heart anatomy derived from imaging data modalities such as MRI or computed tomography (CT) scanners. Functional personalization involves integrating physiological and pathophysiological data into the model about the cardiac electrical activation, dispersion of refractoriness, mechanical contraction, substrate distribution, etc. Examples of data used for the personalization of cardiac function include conduction velocity (CV) maps, LAT, effective refractory period (ERP) measurements, pressure-volume loops, among others [17, 26, 27]. Personalization of the arrhythmogenic substrate is an important part of the functional personalization process and involves incorporating information about the spatial distribution and characteristics of fibrosis and scar tissue. Techniques such as LGE-MRI and the detection of LVA (voltage$<$0.5 mV) are commonly used to derive information about the state of the substrate [17, 28].

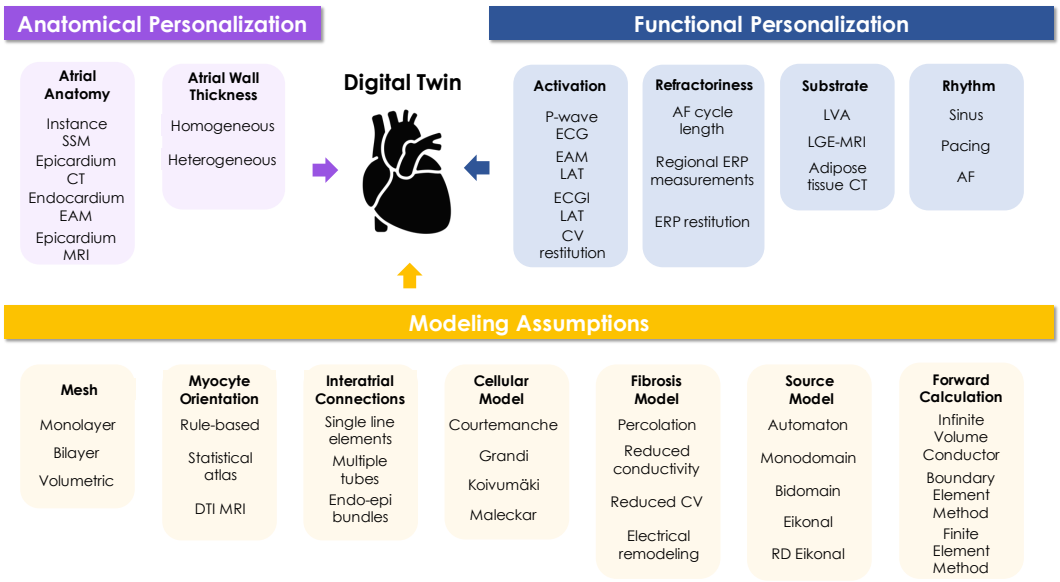

Figure 1.2: Anatomical and functional personalization of digital twins in cardiac electrophysiology and modeling assumptions. Overview of methods and modalities used to infer anatomical and functional information for cardiac digital twins, highlighting the wide range of modeling assumptions that can influence model behavior. AF: atrial fibrillation, CT: computed tomography, CV: conduction velocity, DTI: diffusion tensor imaging, EAM: electro-anatomical map, ERP: effective refractory period, LVA: low voltage area, LGE: late gadolinium enhancement, MRI: magnetic resonance imaging, RD: reaction-diffusion, SSM: statistical shape model.

The generation and implementation of cardiac digital twins in clinical practice pose significant challenges [12]. Figure 1.4 summarizes current challenges encountered towards the implementation of digital-twin-based therapies in cardiac electrophysiology. Data availability is one of the principal challenges that modellers face during the twinning process. Patient-specific data can be derived from clinical measurements or be directly measured, for instance, during tissue biopsies [25]. Data ranging from cellular to organ scale is required to parameterize patient-specific computer models for cardiac electrophysiology applications [13]. Model calibration involves the adjustment of model parameters in order to optimize the agreement between observed data and simulation output [29]. Some studies have suggested employing Gaussian process emulators to address the computationally demanding calibration step, elucidating the influence of specific parameters on the model output [30, 31]. This approach enables focusing on key model parameters, thereby reducing computational costs by calibrating only the necessary parameters.

Clinically available electrocardiogram (ECG) recordings have already been used to personalize global CV of patient-specific cardiac digital twins [33, 34]. However, ECG data provide limited information regarding activation and repolarization patterns within the heart. For instance, to personalize local CV changes of a patient-specific model, cardiac tissue conductivity values are required in three directions orthogonal to the cardiac fibers (longitudinal, transversal, and normal) [35]. However, measuring tissue conductivity is already technically challenging *in vivo* as it requires measurements with small electrode spacing (500 μm) and

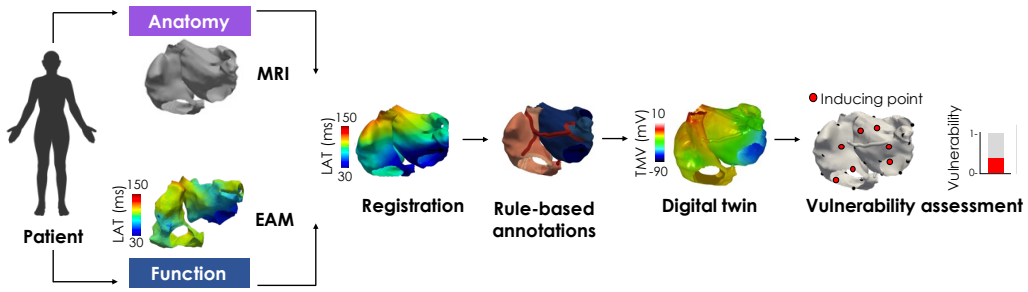

Figure 1.3: Creation of a patient-specific atrial model (digital twin) for the evaluation of the selected input data used for personalization on arrhythmia vulnerability. The personalization process involves two main components: anatomy and function. Personalized and non-personalized data are incorporated into the model. Vulnerability assessment quantifies the ratio between inducing (red) and non-inducing (black) points [32]. EAM: electro-anatomical map, LAT: local activation time, MRI: magnetic resonance imaging, TMV: transmembrane voltage.

the solution of an inverse method, which is generally ill-posed [36]. An alternative method for inferring patient-specific CV involves obtaining clinically recorded LAT maps, whereby the intra and extracellular tissue conductivities can be iteratively parameterized to match activation sequences, resulting in the desired CV [17, 37].

The scarcity of electrophysiological data available before the procedure limits functional personalization of cardiac digital twins. As a consequence, some studies opt for generalization assumptions instead, particularly in terms of CV, and generate patient-specific models based on population-based electrophysiological data [14, 15, 21, 38]. The personalization of other electrophysiological parameters such as the ERP has scarcely been studied [27]. An alternative for the personalization of cardiac electrophysiology is the use of non-invasive electrocardiographic imaging ECGI data [39, 40], although main concerns arise regarding ECGI limited spatial accuracy [41]. Currently, there is no consensus within the modeling community regarding whether electrophysiological personalization should be performed and to what extent it influences the behaviour of the patient-specific model.

Another challenge concerns the acquisition of patient-specific clinical data, such as the spatial distribution and characteristics of fibrosis and atrial wall thickness, from current imaging modalities. Atrial fibrosis characterized by LGE-MRI has the limitation that atrial wall thickness is often thinner (1-4 mm) [42] than the spatial resolution of clinically available MRI systems (voxel size: 1.25 mm $\times$ 1.25 mm $\times$ 2.5 mm) [43]. Therefore, assessing patterns of fibrosis distribution based on LGE-MRI data remains questionable. In addition, the identification of low voltage areas (LVA) using endocardial catheters during sinus rhythm has also been used to inform fibrosis distribution of patient-specific models [17]. The main limitation of this technique is the standardization of a cutoff value of 0.5 mV which might differ for each individual patient or even among different atrial regions [28]. Another limitation is that endocardial electrograms used for the assessment of LVA do not provide information about fibrosis on the epicardium. Furthermore, the acquisition patient-specific atrial myocyte fiber orientation is currently unavailable due to thin atrial wall thickness and limited spatial resolution of MRI [44, 45]. In fact, the majority of current patient-

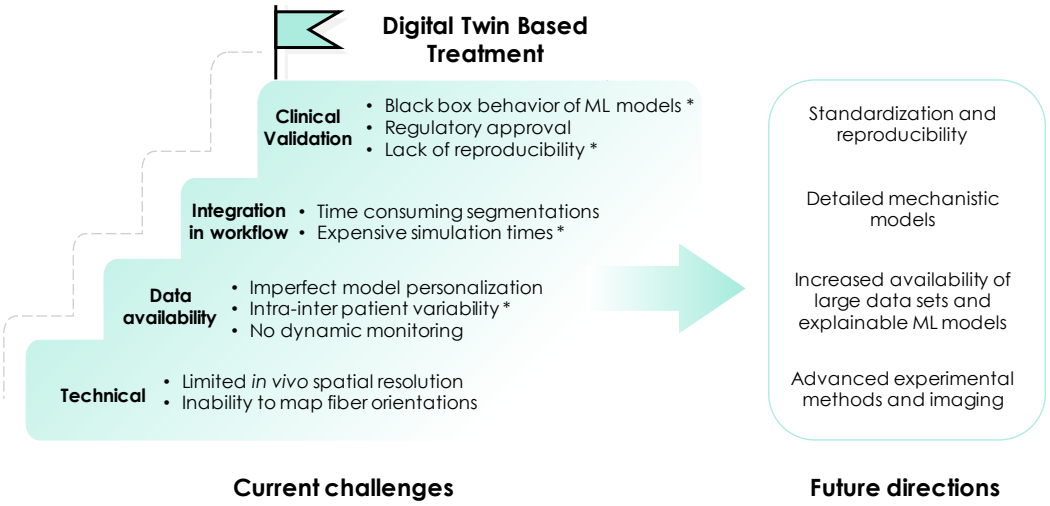

Figure 1.4: Current challenges and future directions in the implementation of digital-twin based treatments. This thesis seeks to contribute to tackling the challenges denoted with *. Inspired by [12, 13].

specific models do not personalize fiber orientations; instead, fiber orientations are modelled using rule-based definitions or extracted from statistical atlases and mapped using atrial and ventricular coordinate systems [46–49].

Two main gaps exist for the integration of cardiac digital-twin based technologies into routine clinical practice. Firstly, the transition between basic science to clinical validation, and secondly, the transition between clinical validation to clinical implementation [13]. Future technological advances will likely facilitate the acquisition of clinical data required for personalizing patient-specific computer models, thereby aiding in bridging the first gap. For example, the development of advanced experimental methodologies to mimic the response of physiological systems in vitro, as human induced pluripotent stem cells [50] or the advent of high resolution MRI, will further aid in the generation of more accurate and comprehensive cardiac digital twins [12]. Randomized controlled trials (RCT) are also essential to prove the validity of such digital twin based tools and to aid in their clinical implementation [13]. Finally, efforts should be directed towards integrating digital twin technologies into clinical workflows. This integration should prioritize the development of faster, more accurate and reproducible patient-specific models to enhance their efficacy and reliability in clinical practice [12]. In the following section, an overview of patient-specific computer models in the field of AF is presented.

1.3 State of the Art

This section presents an overview of patient-specific atrial computer models developed in recent years for informing AF treatment. The section is divided into three decades from 2000s, 2010s and 2020s, highlighting key advancements in modeling approaches. The main contributions are summarized in Figure 1.5.

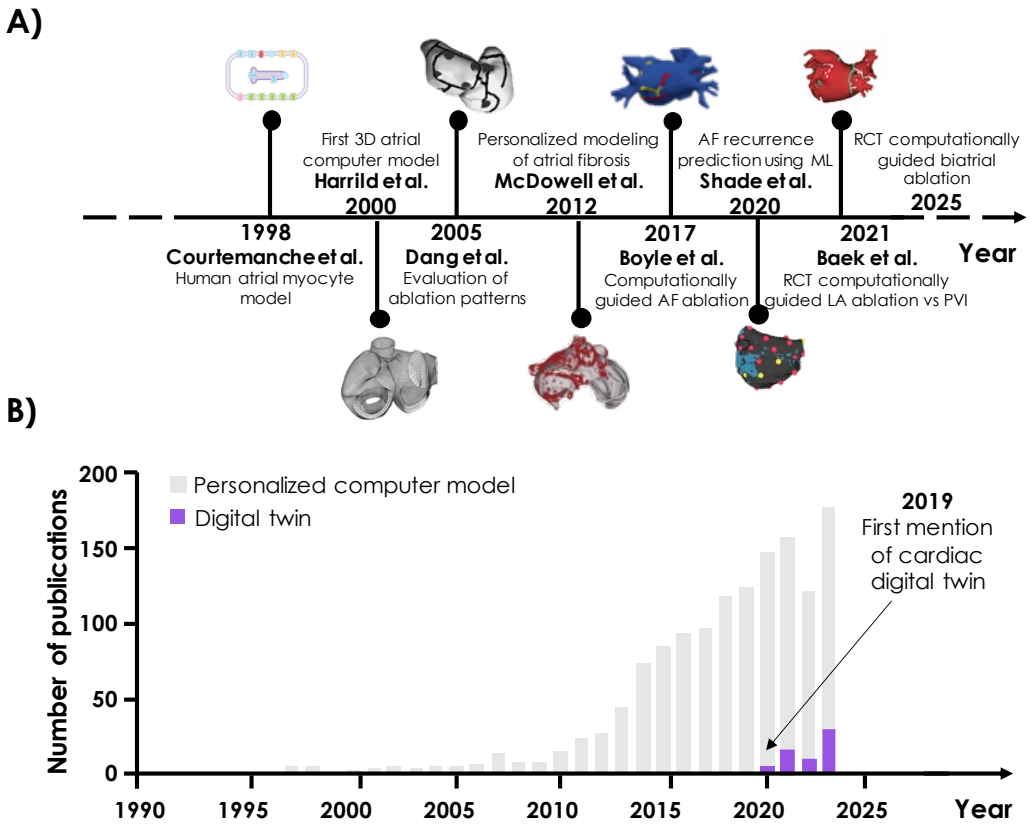

Figure 1.5: Timeline showing scientific breakthroughs leading to the development and implementation of patient-specific computer models of the atria in the treatment of atrial fibrillation. A) From human atrial myocyte models [51], to the use of biophysical models with personalized substrate together with machine learning to predict atrial fibrillation recurrence [19] and up to the first randomized controlled trials with computationally guided ablation [20, 52]. B) Number of publications on digital twins as in [13]. AF: atrial fibrillation, ML: machine learning, RCT: randomized controlled trial. Figures were taken with permission from the publishers.

1.3.1 Earlier Atrial Computer Models: 2000s

The formulation of the first mathematical models of the human atrial myocyte by Courtemanche *et al*. [51] and Nygren *et al.* [53] in 1998, paved the way for developing the first computational models of the atria [54]. Atrial myocyte models have enabled the study of AF mechanisms [54–56], ionic channel mutations [57], the effects of drugs on cellular dynamics [58], the simulation of cellular processes such as inflammation and ischemia [59], and to conduct pre-clinical pharmacological studies [24].

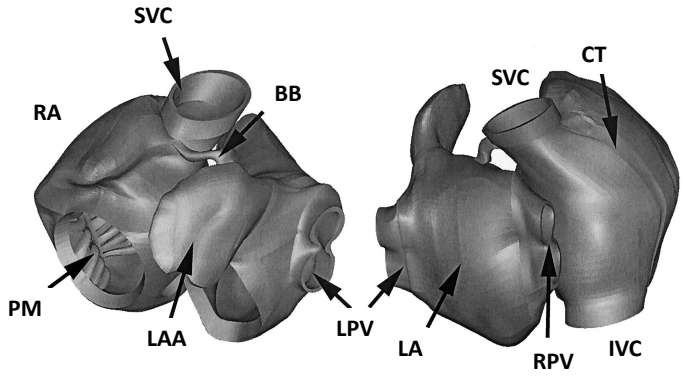

Figure 1.6: First 3D biophysical model of the human atria with main anatomical structures [60]. Left atrium: LA, LA: right atrium, CT:crista terminalis, PM: pectinate muscles, BB: Bachmann's bundle, SVC: superior vena cava, IVC: inferior vena cava, LPV: left pulmonary veins, RPV: right pulmonary veins. Reproduced from [60] with permission from the publisher.

The first 3D biophysical model of the human atria (Figure 1.6) was developed in 2000 by Harrild *et al.* [60]. The 3D model incorporated the main anatomical structures such as the left atrium (LA), the right atrium (RA), the crista terminalis (CT), pectinate muscles (PM), the fossa ovalis, and the Bachmann's bundle (BB). The electrical propagation in the atria was simulated using the monodomain model and the finite volume method. Conductivities were assigned to simulate realistic local conduction velocities in the bulk tissue. In 2001, Vigmond *et al.* described atrial anatomical features that promote reentry in a reconstructed representation of a canine biatrial model [61]. In 2005, Deng *et al.* studied surgical and ablation lesions using a simplified single-layer biophysical model of the human atria derived from MRI slices [62]. Lesions were modeled by setting the conductivity tensor to zero. In their investigation, they were able to document the mechanisms of ablation lines stopping fibrillation and incomplete lesion formation promoting atrial flutter. In 2006, Seemann *et al.* developed an anatomically detailed human biatrial model based on the visible female dataset incorporating heterogeneous regional electrophysiology and the sinoatrial node (SAN) [63]. Computer models at that time were also used to elucidate mechanisms of AF, such as the the role of triggers in the pulmonary veins in the generation of dynamic spatial dispersion of repolarization in the atria [64].

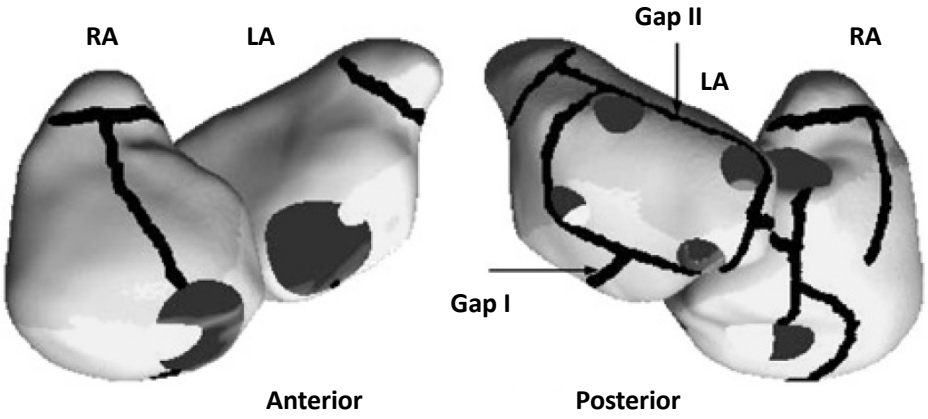

Figure 1.7: Study of ablation lesions in a biatrial model [62]. Ablation lesions are depicted in black. Gap stands for incomplete ablation lesions. LA: left atrium, RA: right atrium, SVC: superior vena cava. Reproduced from [62] with permission from the publisher.

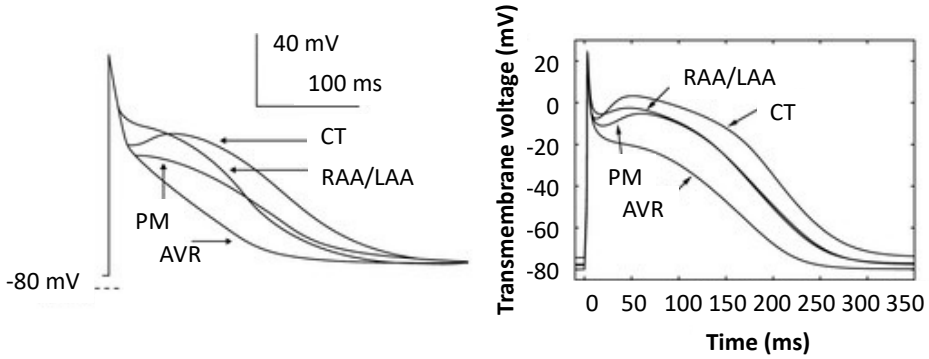

Maximum ionic channel conductances (nS/pF)

	PM	CT	AVR	RAA/LAA
g_{to}	0.1652	0.2115	0.1652	0.1123
g_{CaL}	0.1238	0.2067	0.0829	0.1312
g_{Kr}	0.0294	0.0294	0.0449	0.0294

Figure 1.8: Regional electrophysiological heterogeneity in the atria as described in [63]. Top: Action potential characteristics. Bottom: Maximum ionic channel conductances for the Courtemanche *et al.* model [51] expressed in nS/pF. CT: crista terminalis, PM: pectinate muscles, AVR: atrioventricular rings, RAA/LAA: right and left atrial appendages. Reproduced from [63] with permission from the publisher.

1.3.2 Modern Atrial Computer Models: 2010s

The increased availability of cardiac imaging modalities such as MRI and CT in the last decade has facilitated the reconstruction of anatomically detailed patient-specific atrial models on a regular basis. Over the last decade, more advanced models have been used to investigate mechanisms underlying AF, including endo-epi dissociation [65], the role of the autonomic nervous system in trigger activity [66], and the impact of fibrosis spatial distribution on arrhythmia drivers [21, 39, 67]. Equally significant at the end of that decade was the publication of the first studies guiding ablation based on patient-specific computer simulations, demonstrating their potential as clinical decision-support tools [15, 68].

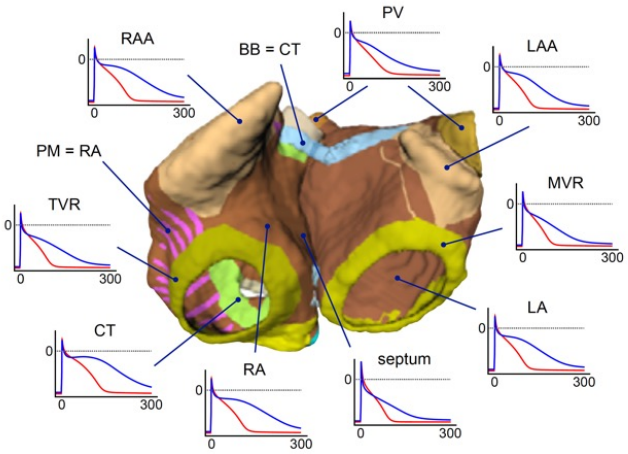

Applied factors on maximum conductance

Region	g_{CaL}	g_{to}	g_{Kr}	g_{Ks}	g_{K1}	g_{Kur}
RA / PM	1.00	1.00	1.00	1.00	1.00	1.00
CT	**1.67**	1.00	1.00	1.00	1.00	1.00
BB	**1.67**	1.00	1.00	1.00	1.00	1.00
TVR	**0.67**	**1.53**	**1.53**	1.00	1.00	1.00
MVR	**0.67**	**1.53**	**2.44**	1.00	1.00	1.00
RAA	**1.06**	**0.68**	1.00	1.00	1.00	1.00
LAA	**1.06**	**0.68**	**1.60**	1.00	1.00	1.00
LA	1.00	1.00	**1.60**	1.00	1.00	1.00
PV	**0.75**	**0.75**	**2.40**	**1.87**	**0.67**	1.00
*	**0.45**	**0.35**	1.00	**2.00**	**2.00**	**0.50**

Figure 1.9: Patient-specific modeling of atrial anatomy and electrophysiology with fiber orientation and anatomical annotations as described in [69]. Top: Volumetric biatrial model with regional distribution of physiological action potentials shown in blue and with AF-induced remodeling in red. Bottom: Factors applied relative to the original Courtemanche *et al.* [51] to model heterogeneities in atrial electrophysiology of the human atria. Highlighted factors differ from normal myocardium. RA: right atrium, BB: Bachmann's bundle, CT: crista terminalis, TVR: tricuspid valve ring, MVR: mitral valve ring, RAA: right atrial appendage, LAA: left atrial appendage, PV: pulmonary vein.* Denotes applied factors in AF-induced remodeling as described in [70]. Reproduced from [69] under CC BY-NC-ND 3.0 license.

A paradigm shift in atrial modeling was the emergence of the first bilayer models. These bilayer models enabled faster calculations of atrial electrophysiology by incorporating atrial wall thickness and transmural diffusion through linear elements between layers, eliminating the need of tetrahedrons as in commonly used volumetric meshes [65, 71]. Model personalization also advanced in this decade through the utilization of both invasive and non-invasive clinical data to fine-tune electrophysiology parameters [27, 33, 37, 72]. Moreover, multiple studies presented methodologies for defining atrial electrophysiological heterogeneities (Figure 1.9) [73], for inferring fiber orientations based on anatomical rules [35, 74], and based on the solution of Laplace problems [33, 75].

Another milestone of the decade was the creation of the Comprehensive in Vitro Proarrhythmia Assay (CIPA) initiative, a collaboration involving industry, the academic community, and regulatory bodies in the United States, Europe, Canada, and Japan for the assessment of the proarrhythmic effect of new drugs entering the market [76], which is relevant for the design of new pharmacological treatments for AF [12]. The concept of *in silico* clinical trials emerged in this decade, paving the way to the design of trials utilizing "individualized computer simulations for the development or regulatory evaluation of a medicinal product, medical device, or medical interventions" [77]. Finally, during this decade machine learning (ML) models together with atrial modeling and simulation were used to assess fibrotic substrate characteristics on reentrant driver perpetuation [21] and to predict localization of atrial ectopic foci [78].

1.3.3 Current Atrial Computer Models: 2020s

The beginning of this decade was marked by the COVID-19 pandemic. Throughout the three years of the pandemic, ML models demonstrated their usefulness as clinical decision-support tools for predicting the progression of the coronavirus disease, thereby assisting in patient prioritization and optimizing the utilization of in-hospital resources [79]. Applications of ML models together with atrial computational modeling include the prediction of arrhythmia recurrence after pulmonary vein isolation (PVI) [19], the evaluation of AF ablation techniques [80], the identification of substrate characteristics of post-ablation lesions promoting reentry anchoring [81], and the discrimination of driver locations based on ECG data [82]. The use of explainable methods holds potential to address the black box behaviour of ML models [80, 81]. Regarding model personalization, physics-informed neural networks have also been used for inferring fiber orientations and atrial activation from LAT maps [83, 84].

Recently, two major trends have been distinguished in the field of cardiac modeling: the first involves the creation of patient-specific models (digital twins) by incorporating information from an individual patient, while the other trend involves generating synthetic models (digital chimeras) derived from observations of the studied population [23]. The development of publicly available methodologies and data has promoted the creation of populations of both digital twins and chimeras. These methodologies include statistical shape models [85, 86], human atrial and ventricular fiber atlas [87, 88], pipelines for model generation [17, 34, 46, 89], and model personalization [84, 90–92]. In terms of data avail-

ability, significant efforts have been directed towards sharing resources including simulated data [93–95], and simulation-ready meshes [30, 96, 97].

In 2021, the first prospective RCT was published involving 170 patients comparing additional computationally guided ablation with PVI alone [20]. The results of this study suggest that the computationally guided ablation group had reduced recurrence to AF. Two additional RCTs using atrial modeling and simulation are currently recruiting patients and are estimated to be completed by 2025. The ReCETT-AF study, aims to define patient-specific AF mechanisms in a cohort of 115 patients [98]. The second one is a follow-up study based on the work presented by [15] called OPTIMA, which aims to compare PVI with PVI plus computationally guided ablation [52] in a cohort of 200 AF patients. For the interested reader, the following Table 1.1 compiles recent reviews related to the field of patient-specific computational modeling of atrial electrophysiology.

Table 1.1: State of the art reviews in the field of computational modeling of atrial electrophysiology.

Author	Year	Title	Reference
Johnson *et al.*	2017	Enabling Precision Cardiology Through Multiscale Biology and Systems Medicine	[99]
Gray *et al.*	2018	Patient-Specific Cardiovascular Computational Modeling: Diversity of Personalization and Challenges	[25]
Vagos *et al.*	2018	Computational Modeling of Electrophysiology and Pharmacotherapy of Atrial Fibrillation: Recent Advances and Future Challenges	[58]
Grandi *et al.*	2019	Computational modeling: what does it tell us about atrial fibrillation therapy?	[100]
Niederer *et al.*	2019	Computational Models in Cardiology	[24]
Corral-Acero *et al.*	2020	The 'Digital Twin' to enable the vision of precision cardiology.	[23]
Gilbert *et al.*	2020	Artificial Intelligence in Cardiac Imaging With Statistical Atlases of Cardiac Anatomy	[101]
Nguyen *et al.*	2020	An Introductory Overview of Image-Based Computational Modeling in Personalized Cardiovascular Medicine	[102]
Heijman *et al.*	2021	Computational Models of Atrial Fibrillation: Achievements, Challenges, and Perspectives for Improving Clinical Care.	[12]
Kwon *et al.*	2021	Computational Modeling of Atrial Fibrillation	[103]
Pagani *et al.*	2021	Data Integration for the Numerical Simulation of Cardiac Electrophysiology	[104]
Trayanova *et al.*	2021	Machine Learning in Arrhythmia and Electrophysiology	[105]
Wu *et al.*	2021	Current progress of computational modeling for guiding clinical atrial fibrillation ablation	[106]
Loewe *et al.*	2022	Cardiac Digital Twin Modeling	[107]
Bai *et al.*	2022	How Synergy Between Mechanistic and Statistical Models is Impacting Research in Atrial Fibrillation	[108]
Coveney *et al.*	2022	Atrial Conduction Velocity Mapping: Clinical Tools, Algorithms and Approaches for Understanding the Arrhythmogenic Substrate	[31]
Rodero *et al.*	2023	A Systematic Review of Cardiac *in silico* Clinical Trials	[109]
Trayanova *et al.*	2023	Computational Modeling of Cardiac Electrophysiology and Arrhythmogenesis	[110]
Cluitmans *et al.*	2024	Digital Twins for Cardiac Electrophysiology: State of the Art and Future Challenges	[13]
Laubenbacher *et al.*	2024	Digital Twins in Medicine	[111]
Jaffery *et al.*	2024	A Review of Personalised Cardiac Computational Modelling Using Electroanatomical Mapping Data	[112]

1.4 Definition of Arrhythmia Vulnerability

The term *vulnerability* is frequently used in the context of cardiac arrhythmias, but its precise definition is not consistent among studies [32, 91, 113–116]. The Cambridge dictionary defines vulnerability as "the quality of being easily hurt, influenced, or attacked" [117]. In the field of cardiac electrophysiology, *arrhythmia vulnerability* refers to the susceptibility to develop an abnormal rhythm, and if AF is induced, then it can be termed as *AF vulnerability*. AF is marked by rapid and unsynchronized activation, usually diagnosed through a surface electrocardiogram (ECG) characterized by the absence of distinct repeating P waves, irregular atrial activations, an arrhythmia cycle length $<$200 ms and irregular RR intervals [118]. In general, studies quantifying arrhythmia vulnerability involve a pacing protocol delivered at specific locations in the atria aiming to induce an arrhythmia.

Multiple concepts have been associated with AF vulnerability, including: atrial vulnerability [115], AF inducibility [21, 119, 120], arrhythmogenic propensity [15] and AF risk [121]. Table 1.2 provides an overview of various definitions found in the literature regarding AF vulnerability and related concepts. In this thesis, arrhythmia vulnerability is defined as the ratio between the number of inducing points divided by the total number of stimulation points (Equation 1.1). Figure 1.10 illustrates an example of the definition of arrhythmia vulnerability.

$$\text{Vulnerability} = \frac{\text{Number of inducing points}}{\text{Number of stimulating points}} \tag{1.1}$$

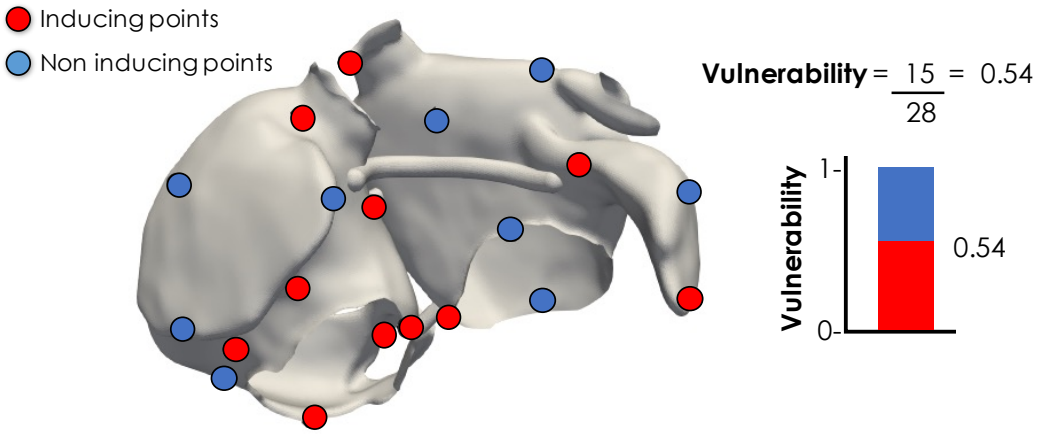

Figure 1.10: Example of the definition of arrhythmia vulnerability in a biatrial model. Arrhythmia vulnerability is defined as the ratio between the number of inducing points (red) divided by the total number of stimulation points on the atrial surface based on the pacing protocol as described in [32].

Table 1.2: Review of the definition of atrial fibrillation vulnerability and associated concepts across *in vivo*, *in silico*, animal and human models.

Concept	Metric	Methodology	Model
AF vulnerability	Percentage of sites at which AF was induced lasting >1 s	Single premature stimuli pacing protocol at 8 sites in both atria	canine *in vivo* [113]
	Presence of AF or RAF defined as two or more successive activations in a 2 h ECG trace lasting >60 s	Single premature stimulation during SR and at 600, 500, and 400 ms in the lateral or anterior free wall of the right atrium	ovine *in vivo* [115]
	Binary induction of AF lasting more than 5 cycles	Single premature stimulation or incremental pacing from 600-300 ms at the RAA or distal CS	human *in vivo* [122]
	Presence of APD alternans defined as $\pm$ 5% variation of mean APD	Rapid pacing protocol with 74 beats at PCL ranging from 500-300 ms, with 50 ms intervals	human *in vivo* [114]
	Number of subjects with at least one AF episode lasting >10 min	Rapid pacing with 1200 bpm lasting 10 s at 1 site in the LA and 1 in the RA, tested 10 times site	porcine *in vivo* [116]
	Binary induction of AF lasting >30 s	Three pacing protocols delivered at the LA posterior wall	human *in vivo* [91]
	Percentage of points inducing reentry lasting >1 s	Single premature stimuli pacing protocol at different sites separated by 1 cm in both atria	human *in silico* [32]
AF inducibility	Percentage of sites inducing AF lasting >1 s	Single premature stimuli at the epicardial right and left midatrial walls at total 24 sites	leporine *in vivo* [119]
	Number of models in which AF was induced and lasting >2.5 s	Rapid pacing protocol with 14 stimuli with PCL ranging from 300-150 ms in 25 ms at 30 sites in both atria	human *in silico* [21]
	Proportion of cases inducing reentry lasting >2 s	Single premature stimuli pacing protocol from each of the four pulmonary veins with 5 stimuli at 160 ms with 8 coupling intervals ranging from 200-500 ms	human *in silico* [120]
Arrhythmogenic propensity	Number of reentrant drivers per patient lasting >5 s	Rapid pacing protocol with 12 stimuli with PCL ranging from 300-150 ms at 40 sites in both atria	human *in silico* [15]
AF risk	Clinical variables from electronic health records	Development of a multivariate AF risk model to predict the probability of developing AF within 5 years	human *in vivo* [121]

AF: atrial fibrillation, APD_{90}*: action potential duration at 90% of depolarization, bpm: beats per minute, LA: left atrium, PCL: pacing cycle length, RA: right atrium, RAF: rapid atrial firing, SR: sinus rhythm*

Arrhythmia vulnerability was assessed by the pacing at the end of the effective refractory period (PEERP) protocol [32]. Stimulation points were obtained by merging mesh points with an absolute tolerance of 2 cm, therefore, the number of stimulation points is dependent on the atrial size [123]. The PEERP pacing protocol delivers at each stimulation point a first stimulus, namely S1, with a fixed pacing cycle length (PCL), followed by an extra stimulus S2 at the end of the ERP. The coupling interval is modified until the S2 stimulus induces an atrial activation. Arrhythmia induction detection is a two step process. First, atrial activation is defined if the transmembrane voltage is $>$-50 mV in at least one node located inside a ring with a radius of 4-6 mm surrounding the stimulation point. Second, a point is considered to be inducing arrhythmia if an atrial activation is detected 50 ms after the initial detection and if the arrhythmia is maintained for at least 1 s. The protocol in each stimulation point is stopped either when the maximum number of stimuli was applied, usually set to 4, or when an arrhythmia was detected.

1.5 Aim of the Thesis

The aim of this thesis is to evaluate the effect of incorporating different types of clinical data for the personalization of patient-specific atrial models on arrhythmia vulnerability. The investigation presented in this thesis was guided by the main research question shown in Figure 1.11. In particular, the effect of three types of clinical data was evaluated: personalization of the atrial anatomy, personalization of the effective refractory period, and personalization of local activation times and substrate.

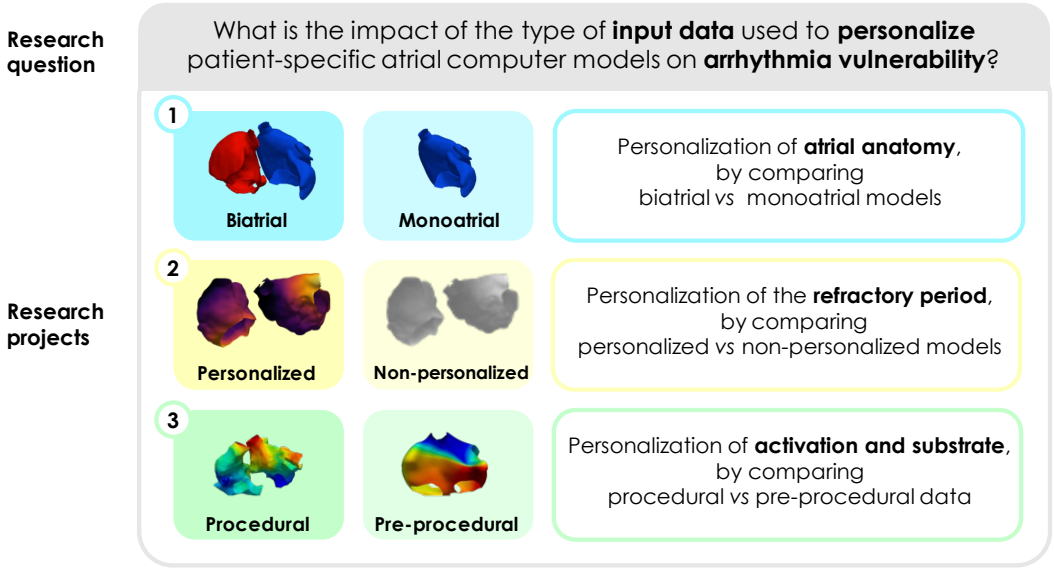

Figure 1.11: Overview of the thesis structure. Main research question and thesis projects.

To answer the main research question, the following key research questions are addressed:

1. Which role does the RA play in the development of AF *in silico*?
2. What is the impact of the RA in the development of arrhythmia under different substrate remodeling states?
3. To what extent does incorporating personalized ERP measurements influence arrhythmia vulnerability of the patient-specific model?
4. How does arrhythmia vulnerability change when both the ERP and substrate are personalized?
5. What is the effect of the interplay between the personalization of activation and substrate on arrhythmia vulnerability?
6. Can ML models be used to predict arrhythmia vulnerability *in silico*?

Additionally, within the scope of this thesis, the following tools were developed:

- A method to generate synthetic distributions of fibrosis
- A pipeline to personalize ERP based on clinical measurements
- A standard nomenclature definition to consistently divide the atria into 15 segments
- A virtual reality tool to visualize electrophysiology simulations
- A publicly available cohort of 7 simulation ready meshes with personalized ERP
- A publicly available cohort of 8 simulation ready meshes with and without the incorporation of the RA
- A cohort of 22 biatrial simulation ready meshes with fibrosis informed by LGE-MRI

1.6 Structure of the Thesis

This thesis is organized into ten chapters as described below:

Chapter 1 outlines the motivation of the thesis, introduces the concepts of cardiac digital twins and personalization, reviews the state of the art in atrial computer models, provides an overview of the definition of arrhythmia vulnerability, and defines the aims of the thesis.

Part I introduces the medical and mathematical fundamentals relevant to this work.

- **Chapter 2** offers a detailed overview of the embryology and anatomy of the left and right atrium, followed by a description of atrial electrophysiology. The chapter concludes by presenting key concepts related to atrial fibrillation diagnosis and treatment.

- **Chapter 3** covers the mathematical concepts related to cardiac computational modeling, spanning from cellular and tissue electrophysiology to forward cardiac electrocardiography. The chapter also presents a description of the methods used to tune CV based on clinical data. Finally, the chapter introduces key concepts related to machine learning and model explainability.

Part II presents the effects of different input data used for the personalization of atrial digital models and the effect on arrhythmia vulnerability.

- **Chapter 4** evaluates the effect of incorporating the right atrium by comparing left atrial models in monoatrial and biatrial configurations.

- **Chapter 5** describes the effect of including personalized ERP measurements into patient-specific atrial models and compares different personalization approaches.

- **Chapter 6** presents the comparison between simulation of P-waves using invasive and non-invasive local activation times.

- **Chapter 7** presents a random forest ML classifier used for the prediction of arrhythmia vulnerability, with evaluation of feature importance.

Part III presents the clinical tools developed within the scope of the collaborative work performed for the PersonalizeAF project.

- **Chapter 8** presents the 15-segment nomenclature definition to consistently divide atrial geometries.

- **Chapter 9** provides a description of the virtual reality tool utilized to visualize simulations and identify ablation targets.

Part IV offers the final remarks of this work.

- **Chapter 10** summarizes the principal findings, conclusions, and main implications of the thesis, providing insights into future research directions.

PART I

FUNDAMENTALS

Chapter 2

Medical Fundamentals

This chapter provides an overview of the essential principles of cardiac anatomy, physiology and pathophysiology, to put in context the work presented in the following chapters. The chapter covers key aspects of cardiac anatomy, the electrical conduction system, and concludes with an overview of cardiac electrophysiology with emphasis placed on the atria.

2.1 Introduction

The heart is a muscular organ in the middle mediastinum responsible for pumping blood throughout the body and comprises four chambers: the upper chambers are the right atrium (RA) and left atrium (LA), while the lower chambers are the right ventricle (RV) and the left ventricle (LV). The interatrial septum separates the right and left atria, while the interventricular septum separates the right and left ventricles (Figure 2.1).

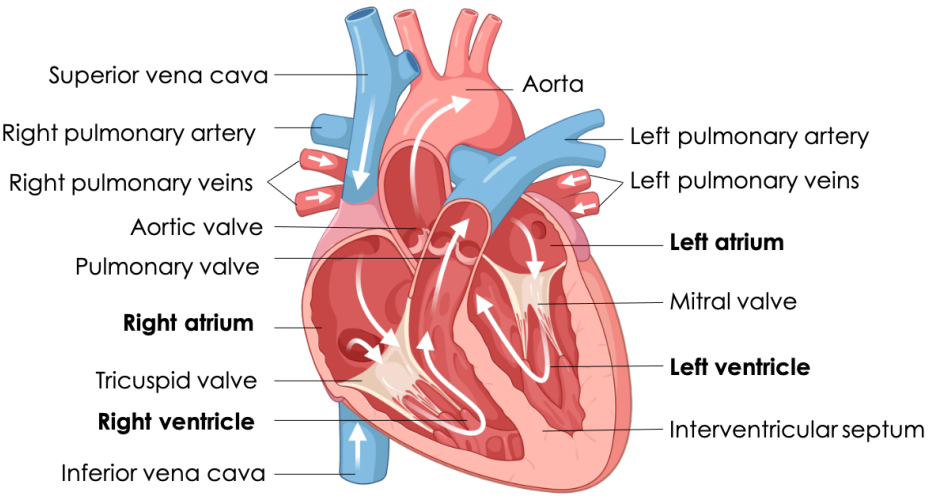

Figure 2.1: Cardiac anatomy and the main vessels. Blood flow direction is indicated with white arrows. Generated with Biorender under academic license.

Deoxygenated blood from the systemic circulation reaches the RA through the superior vena cava (SVC), the inferior vena cava (IVC), and deoxygenated blood from the heart itself through the coronary sinus (CS). Subsequently, the RA sends the blood to the RV passing through the tricuspid valve (TV). The right ventricle (RV) ejects blood to the lungs via the pulmonary artery through the pulmonary valve. The blood is oxygenated in the lungs and returns to the LA through the pulmonary vein (PVs). The blood passes through the mitral valve (MV) reaching the LV which will finally eject the blood into the aorta after passing through the aortic valve.

2.2 Atrial Embryology

Understanding the process of heart formation is essential for comprehending the rationale behind the description of the atrial anatomy and the concept of atrial regionalization. The heart begins its formation during the third week of gestation and is derived from the mesodermal tissue layer [124]. By day 18, cellular aggregation results in the formation of bilaterally paired heart tubes. These tubes fuse at the midline of the ventral embryonic surface, forming a primitive cardiac tube by day 23 (Figure 2.2).

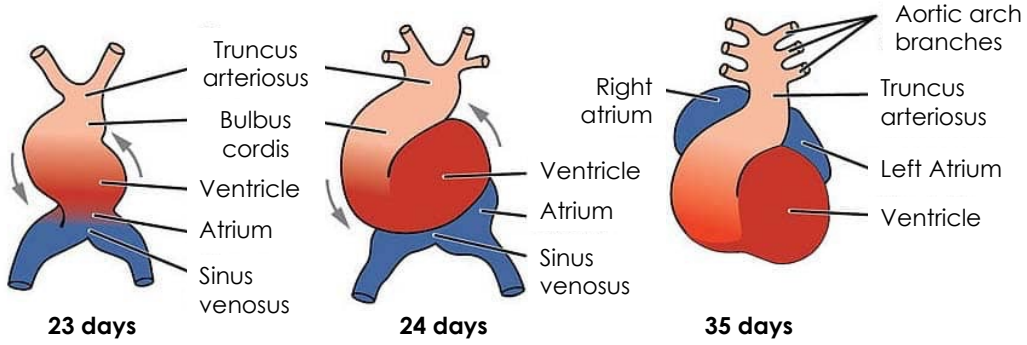

Figure 2.2: Cardiogenesis timeline showing primitive structures of the embryonic heart. Adapted from [125] with CC BY 3.0 license.

The formation of the primitive heart involves the development of five dilations: the truncus arteriosus, the bulbus cordis, the primitive ventricle, the primitive atrium, and the sinus venosus [126], as shown in Figure 2.2. These dilations correspond to structures in the mature heart. The truncus arteriosus serves as the foundation for forming the ascending aorta and pulmonary trunk. The sinus venosus and the primitive atrium become the right and left atria, while the primitive ventricle becomes the LV, and the bulbus cordis becomes the trabeculated part of the RV [124]. During the fourth week of gestation, the sinus venosus collects deoxygenated blood from the right and left sinus horns and directs blood flow into the primitive atrium [127]. As the blood flow moves mainly towards the right side of the heart, the left sinus horn shrinks and later becomes the CS.

The right sinus horn enters into the RA wall through the sinoatrial orifice. Around this orifice, the right and left venous valves develop alongside a ridge known as the septum spurium, as shown in Figure 2.3. The left venous valve merges with the septum spurium, forming the atrial septum. Additionally, the lower section of the right venous valve gives rise to the valves of the IVC and the CS [127]. The crista terminalis (CT) delineates the boundary between the trabeculated region of the RA and the smooth-walled region, referred to as the sinus venarum, originated from the right sinus venosus horn. On the left side, a single pulmonary vein forms as a projection from the posterior wall of the LA. Afterwards, the pulmonary vein and its branches are merged into the LA, forming the smooth area of the LA. In the embryo, the foramen ovale allows blood flow between the right and left atria by the opening of the fossa ovalis valve. Due to changes in the right-left atrial pressure, this communication closes two years after birth [128]. However, a patent foramen ovale is observed in up to 35 % of the adult population [129].

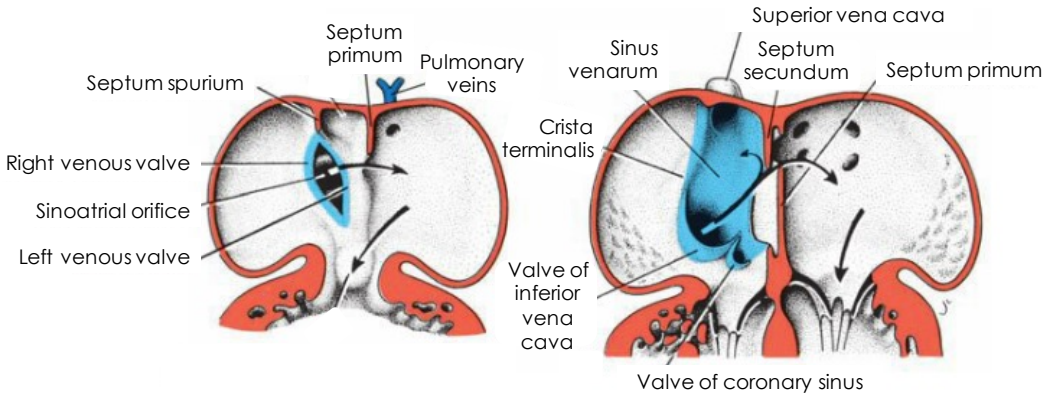

Figure 2.3: Formation of the main atrial structures. Left: coronal view of the atria at the fifth week of gestation. The septum spurium merges with the left venous valve to form the interatrial septum. Right: formation of the smooth wall of the right atrium (sinus venarum) and the crista terminalis. Adapted from [127] with permission from the publisher.

2.3 Atrial Anatomy

To describe the atrial anatomy accurately, it is essential to understand the heart's position within the thoracic cavity in the standard anatomical position. The anatomical position of the body and the cardiac axis are shown in Figure 2.4. The heart is typically located in the mediastinum, with about one-third located to the right of the longitudinal body axis. The cardiac axis is oriented from the right shoulder towards the left hypochondrium (upper left abdominal region) and extends from the cardiac base to the apex, perpendicular to the atrioventricular valve plane [130]. A frontal chest radiography (Figure 2.5) shows the

location of the atria within the thoracic cavity. The heart is positioned in the body with its axis at an oblique angle. The RV is found most anteriorly, while the LV is positioned posteriorly. The atrial chambers are positioned to the right of their corresponding ventricles, with the RA located in front of the LA [130, 131].

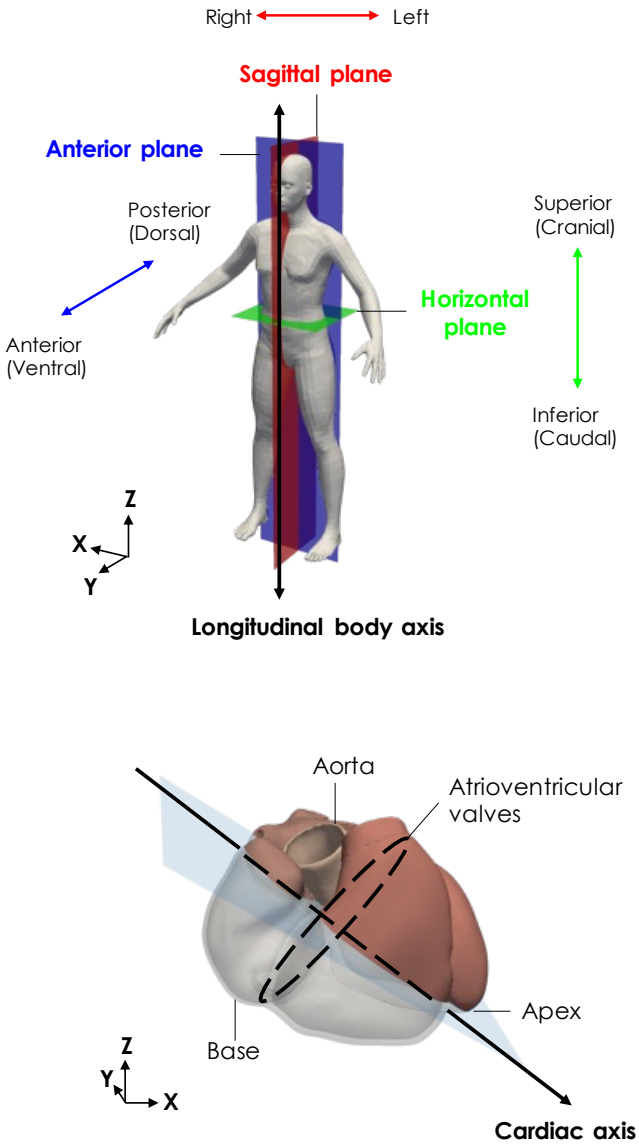

Figure 2.4: Anatomical position of the human body and heart. Top: The anterior plane (blue) divides the body into anterior and posterior. The horizontal plane (green) divides the body into cranial and caudal portions, while the sagittal plane (red) divides the body into right and left sides. Bottom: Orientation of the cardiac axis. The heart model was obtained from [132] under CC BY 4.0 license.

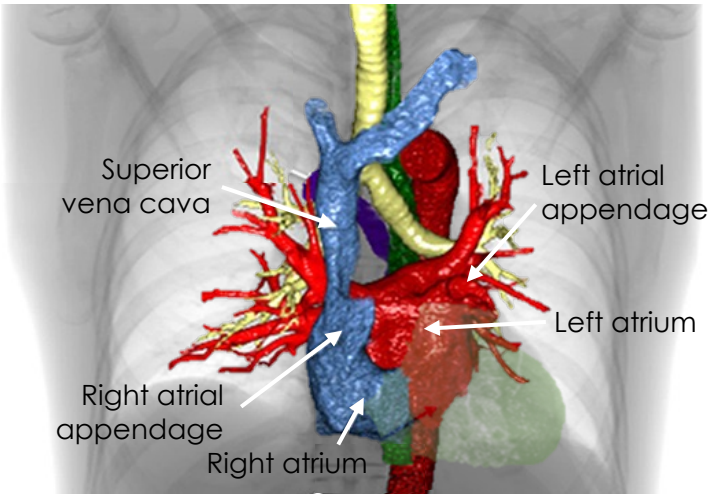

Figure 2.5: Location of the atria within the thoracic cavity. Frontal chest radiography showing structures segmented from computed tomography imaging. The ventricles appear attenuated in green. Adapted from [131] with permission from the publisher.

2.3.1 Right Atrium

The RA has an ellipsoid shape and is located dorsally and cranially to the RV and anteriorly to the LA [129]. Normal values for the RA measured at the end of the systolic phase range from 3.4-5.3 cm in the long axis and 2.6-4.4 cm in the short axis [128]. The RA comprises four components: the venous component, the vestibule, the appendage, and the right aspect of the interatrial septum [133]. The venous component is derived from the embryological sinus venarum and corresponds to the region that receives deoxygenated blood from the SVC, IVC, and the CS. The vestibule is composed of smooth atrial muscle and corresponds to the region surrounding the TV (Figure 2.6). The RAA normally has a triangular shape and originates from the embryological primitive atrium. The apex of the RAA lies anterior to the aortic arch and exhibits a wider neck than the LAA.

The interatrial septum is a complex structure composed of various anatomical features derived from multiple embryological origins. The true atrial septum is located on the floor of the fossa ovalis and the infero-anterior rim, as depicted in Figure 2.7. The fossa ovalis is a round concavity composed of thin fibrous tissue located in the infero-posterior part of the interatrial septum. The fossa ovalis has a size of 14.1 ± 3.6 mm in the anteroposterior diameter and 12.1 ± 3.6 mm in the craniocaudal diameter [128]. The floor of the fossa ovalis derives from the septum primum [128], while the septal border is mainly derived from the septum secundum [133]. During electrophysiological studies, the true atrial septum is crucial for safe transseptal puncture access to the LA.

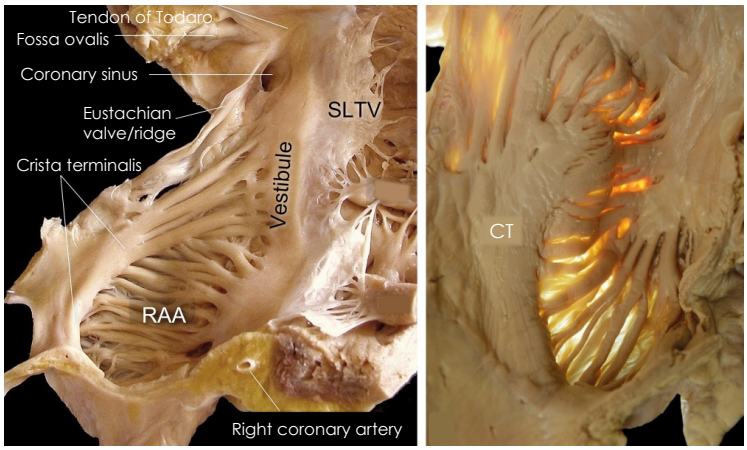

Figure 2.6: Endocardial view of the lateral wall of the right atrium. Left: Main anatomical features of the right atrium. Right: Transillumination showing pectinate muscle arrangement. CT: crista terminalis, RAA: right atrial appendage, SLTV: septal leaflet of the tricuspid valve. Modified from [133] with permission of the publisher.

The crista terminalis (CT) is a muscular band between the RAA and the venous component running vertically along the SVC and IVC. The CT has an average length of 51 ± 9 mm and 5.5 mm thickness [128]. The CT holds electrophysiological significance in typical atrial flutter, as it can promote conduction block in the transversal direction while enhancing fast propagation in the longitudinal direction [129]. The CT ramifies to form the pectinate muscles (PM). Various anatomical variations are observed for the PM which can extend perpendicularly or obliquely from the CT. The sagittal bundle, or tenia sagittalis, represents the largest PM, dividing the RAA into anteromedial and posterolateral regions.

The cavotricuspid isthmus (CTI), also known as the RA isthmus, is a quadrilateral-shaped region within the RA vestibule delimited anteriorly by the septal leaflet of the tricuspid valve and posteriorly by the Eustachian valve. The Eustachian valve is an embryological remnant from the right venous valve and sinus septum around the IVC orifice. The CTI is divided in three regions: paraseptal, central and inferolateral isthmus (Figure 2.8). The Eustachian ridge is an extension of the Eustachian valve with a length of 25.5 ± 4.1 mm and thickness of 3.6 ± 1.9 mm [128]. The paraseptal isthmus corresponds to the line defined between the end of the Eustachian ridge, the CS orifice, and the tricuspid anulus. The central isthmus is the line in the mid of the Eustachian ridge and the septal leaflet of the TV. The inferolateral isthmus is the line at the right end of the Eustachian ridge and the right end of the septal leaflet of the TV [128]. The paraseptal, central, and inferolateral isthmus have mean lengths of 18.5 ± 4.0 mm, 24.0 ± 4.2 mm, and 29.3 ± 4.9 mm, respectively [128]. The CTI region holds clinical significance for isthmus-dependent flutter, as reentrant circuits can travel counter-clockwise around the TV ring. Thus, the CTI can be a target for ablation [128]. Nevertheless, as the right phrenic nerve passes near the inferolateral isthmus, ablating that region might potentially result in its damage. In addition, paraseptal isthmus ablation may lead to complete AV block [129].

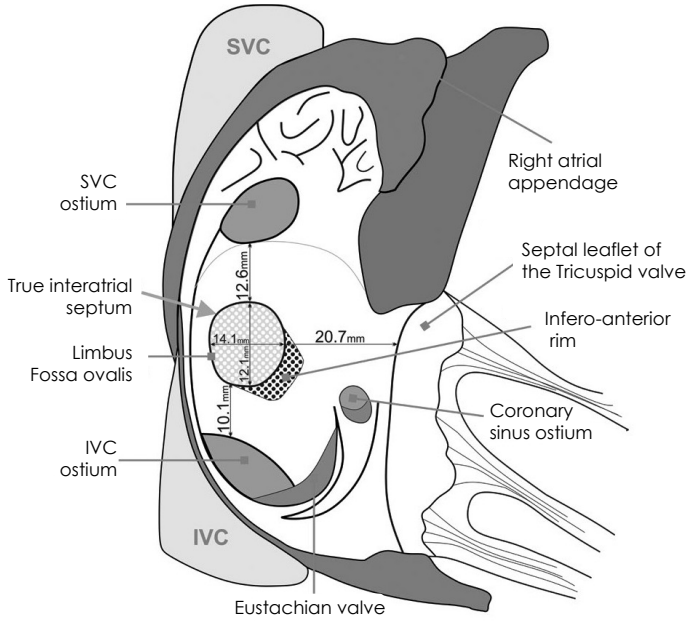

Figure 2.7: Diagram of the interatrial septum viewed from the right atrium. SVC: superior vena cava, IVC: inferior vena cava. Adapted from [128] under CC BY 4.0 license.

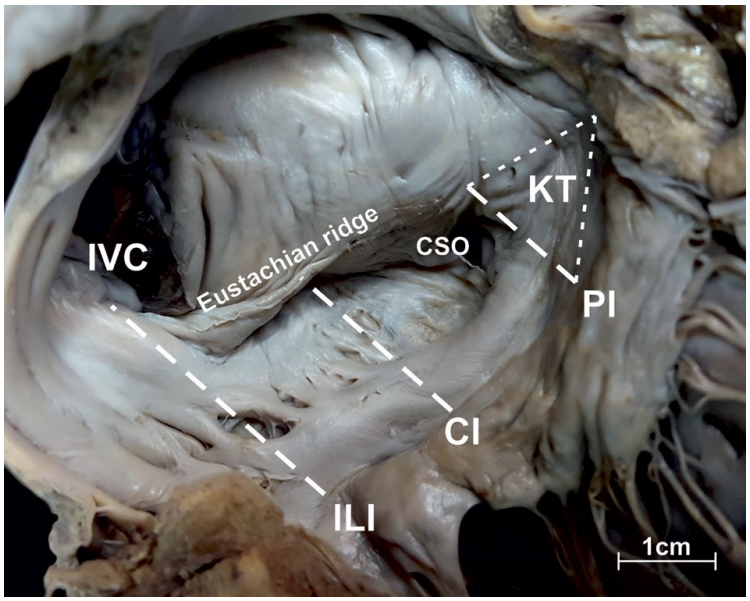

Figure 2.8: The cavotricuspid isthmus and the Koch's triangle. CI: central isthmus, CSO: coronary sinus ostium, IVC: inferior vena cava, ILI: inferolateral isthmus, KT: Koch's triangle, PI: paraseptal isthmus. Obtained from [128] under CC BY 4.0.

The Koch's triangle, located in the RA vestibule, is an anatomical reference to locate the AV node [128]. The base corresponds to the paraseptal line of the CTI, while the apex marks the location where the bundle of His penetrates the septum. The anterior border extends from the apex to the base, touching the TV ring, whereas the posterior border is situated between the apex and the left end of the Eustachian ridge (Figure 2.8). The average measurements for the dimensions of Koch's triangle are 18.5±4.0 mm for the base, 18.0±3.8 mm for the anterior edge, and 20.3±4.3 mm for the posterior edge. Additionally, the average height of the triangle from the apex to the base is 16.0±3.7 mm [128].

The CS drains blood into the RA and its ostium is located at the base of the Koch's triangle. The CS ostium has a diameter of 9-15 mm and is usually covered by the Thebesian valve in up to 85 % of the individuals [128]. The Thebesian valve is derived from the inferior portion of the right sinus valve. The CS is used as a common entrance to the LA and LV epicardium during cardiac catheterizations [128]. The inferior vena cava (IVC) has an orifice of 24±6 mm [129], while the superior vena cava (SVC) has a diameter of 20.1±3.2 mm [128]. The SVC is typically free from anatomical obstacles, making it the preferred access point to the heart during cardiac electrophysiology studies [128]. A summary of the main anatomical structures of the RA is presented in Table 2.1.

Table 2.1: Main anatomical structures of the right atrium, size, origin and their clinical relevance [128, 129].

	Size	Origin	Clinical relevance
CS	9.0-15.0 mm (D)	Left sinus horn	Common access for left ventricle catheterization
CT	51.0±9.0 mm (L) 5.5 mm (T)	Boundary between the primitive atrium and sinus venarum	Transverse conduction block in typical atrial flutter
CTI	18.5±4.0 mm (PS) 24.0±4.2 mm (C) 29.3±4.9 mm (IL)	Embryonic folding of the heart	Reentrant circuits can travel counter-clockwise around the TV ring
Eustachian valve	5.0 mm (D)	Right venous valve and sinus septum	Covering of the IVC towards CS can avoid cannulation
Eustachian ridge	25.5±4.1 mm (L) 3.6±1.9 mm (T)	Folding of the right sinus venosus	Can promote conduction block line during typical flutter
Fossa ovalis	14.1±3.6 mm 12.1±3.6 mm	Foramen ovale	Patent foramen ovale present up to 35 % of the population
IVC	20.1±3.2 mm (D)	posterior cardinal veins, subcardinal veins, and supracardinal veins	Covering of the IVC towards CS can avoid cannulation
Koch's triangle	18.5±4.0 mm (B) 18.0±3.8 mm (A) 20.3±4.3 mm (P)	Various	AV node found at the apex
RAA	ND	Primitive atrium	Prominent trabeculations promote reentry and thrombus formation
SVC	20.1±3.2 mm (D)	Common cardinal veins	Preferred access to the heart

A: anterior border, B: base, C: central isthmus, CS: coronary sinus, CT: crista terminalis, CTI: cavotricuspid isthmus, D: diameter, IL: inferolateral isthmus, IVC: inferior vena cava, L: length, ND: not determined, P: posterior border, PS: paraseptal isthmus, RA: right atrium, T: thickness, TV: tricuspid valve

2.3.2 Left Atrium

The left atrium (LA) is situated centrally within the chest, intersecting the mid-longitudinal body axis, and positioned posteriorly and to the right of the LV (Figure 2.5). The LA has a mean anteroposterior diameter of 38.4±4.9 mm and increases up to 74.0 mm in patients with AF [134]. The LA has four components: the venous component, the vestibule, the appendage, and the left aspect of the interatrial septum [134]. The venous component corresponds to the area where the pulmonary vein (PVs) drain oxygenated blood from the lungs. Typically, four PVs, each with distinct ostia on both sides, are present in 70 % of adults. Nonetheless, anatomical variations are also observed, as depicted in Figure 2.9.

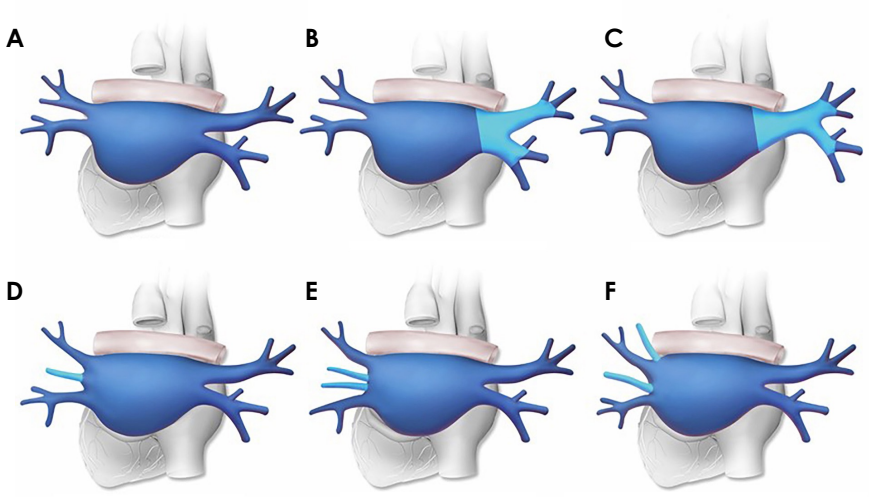

Figure 2.9: Anatomical variants of the pulmonary veins. A: typical, B: short common left trunk, C: long common trunk, D: right middle pulmonary vein, E: two right middle pulmonary veins, F: right middle and right upper pulmonary veins. Adapted from [135] with permission of the publisher.

The PV orifices have an ovoidal shape and a diameter between 13.0-15.0 mm, with the superior veins having larger diameters [134]. The myocardial sleeves of the PVs have been acknowledged to initiate focal triggering activity [136]. Their distinctive anatomical characteristics lead to heterogeneous and anisotropic conduction around the PV antra, facilitating fibrillatory activity. The venoatrial junction is a complex structure marking the transition from the PVs to the LA, typically exhibiting a gradual transition from smooth muscle cells from the veins and myocardial cells from the LA chamber. Myocardial sleeves extend approximately 2.0-3.0 cm from the PVs to the LA [118]. Wall thickness of the LA in the PV antra varies from 2.0 to 8.0 mm, for the posterior wall and the ridge separating the left superior PV from the LAA, respectively [118]. The posterior wall of the LA shares the same embryological origin as the PVs, leading to suggestions that the posterior wall exhibits similar vulnerability to AF [118].

The left atrial appendage (LAA) is a lateral protrusion in the LA derived from the left side of the primitive LA (Figure 2.10). The LAA typically exhibits a narrow neck and a tubular shape in the lobar region with a length ranging from 16.0-51.0 mm [134]. The LAA endocardium is highly trabecular due to the presence of thin pectinate muscles with an average thickness of 1.0 mm (Figure 2.11). The orifice of the LAA is oval-shaped, with diameters of 17.4±4.0 mm (long axis) and 10.9±4.2 mm (short axis) [134]. The shape of the LAA varies greatly between individuals. In 2010, Wang *et al.* proposed four classes to distinguish between different LAA morphologies, as shown in Figure 2.10 [137]. The left LAA holds clinical significance, as it has been shown to contribute to thrombus formation and subsequent stroke [138, 139]. There are discrepancies regarding the most prevalent LAA morphology in the adult population. Autopsy studies have revealed that the cauliflower shape was the most common (41 %), followed by chicken wing (37 %), cactus (12 %), and windsock (10 %) [134]. However, an in-vivo study involving 932 patients showed that chicken wing was present in 48% of the individuals, followed by cactus in 30 %, windsock in 19 %, and cauliflower 3 % of the cases [140]. Particularly, the chicken wing, large double lobes, and cone-shaped morphologies present significant challenges during the implantation of LAA occlusion devices [139].

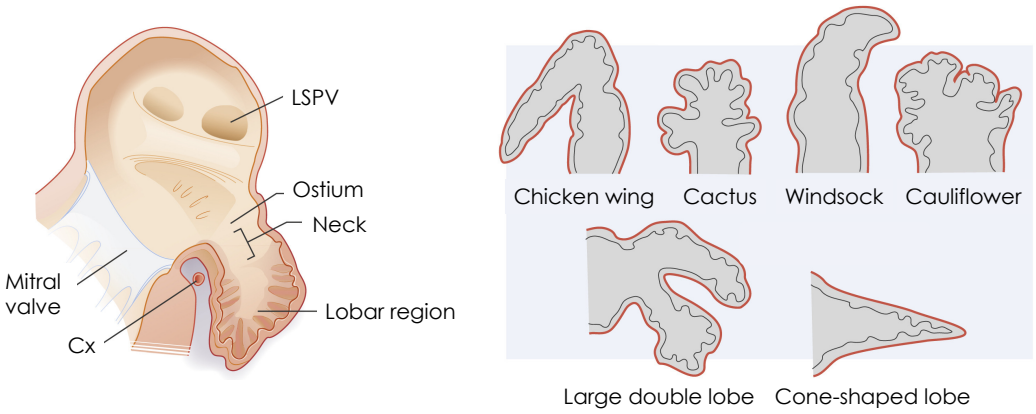

Figure 2.10: Anatomy of the left atrial appendage (LAA). Left: a cross-sectional view of the LAA and its relation to other anatomical structures. Right: classification of various LAA morphologies based on the categories proposed by Wang et al. [137]. Cx: circumflex artery, LSPV: left superior pulmonary vein. Adapted from [139] with permission from the publisher.

The left lateral ridge (LLR), also referred to as the Coumadin ridge, separates the orifices between the LAA and the left PV. The LLR formed by the invagination of the atrial wall, occurring during the formation of the left-sided cardinal veins [141]. The LLR is present in 59.5 % of adults, has a mean length of 22.4±5.1 mm and a diameter of 5 mm[142, 143]. The LLR extends up to lateral aspect of the Bachmann's bundle (BB), enclosing the vein or ligament of Marshall within its fold. The average distance between the left superior PV and the LAA is 3.8±1.1 mm, whereas the average distance between the left inferior PV and

the LAA is 5.8±2.0 mm [143]. The LLR bears clinical significance due to its heterogeneous composition, which promotes anatomical reentries and ectopic activity [133, 143]. The mitral isthmus is located between the left inferior PV and the mitral valve ring in the posteroinferior region of the lateral wall (Figure 2.11). The mitral isthmus has a length of 28.8±7.0 mm and can reach up to 51 mm in some individuals [133, 134]. The thickness of the mitral isthmus varies across its different sections, ranging from 1.9±1.0 mm to 3.0±1.5 mm, which can present challenges during ablation procedures for perimitral flutter [133, 134]. The primary anatomical structures of the LA are summarized in Table 2.2.

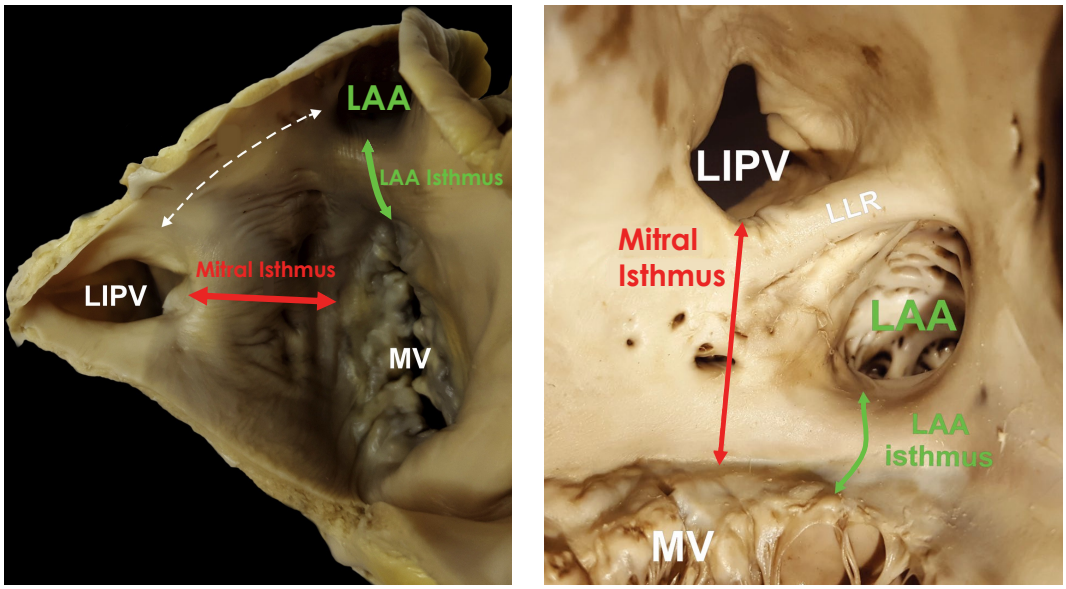

Figure 2.11: Location of the left lateral ridge and mitral isthmus from an endocardial view from cadaveric specimens. Left: posteroinferor region of the lateral wall of the left atrium showing the location of the mitral isthmus line (red), the left atrial appendage isthmus line (green) and the distance between the left inferior pulmonary vein ostium and the left atrial appendage (3). Right: location of the lateral ridge and its relationship to other anatomical structures. LAA: left atrial appendage, LLR: left lateral ridge, LIPV: left inferior pulmonary vein, MV: mitral valve. Adapted from [133, 144] with permission from the publisher.

2.3.3 Atrial Muscle Architecture

The left atrium (LA) wall is comprised of multiple layers of myocardial bundles, resulting in greater thickness compared to the right atrium (RA) [133]. Anatomical dissections have revealed predominantly circular bundles around the openings of the PVs, the atrioventricular valves, and the LAA [118]. The Bachmann's bundle (BB), also known as antero-superior interatrial bundle, is the major interatrial muscle connection, consisting of parallel atrial myocardial strands. The BB originates anteriorly to the right side of the SVC orifice, passes across the interatrial groove, and runs along the anterior wall of the LA reaching

the LAA, where it splits into two branches. The upper branch extends along the left lateral ridge and the lower branch extends into the LA vestibule merging into the muscles of the lateral and inferoposterior LA wall [118]. In addition, two bundles originate from the septum: the septoatrial bundle and the septopulmonary bundle, as shown in Figure 2.12. The septoatrial bundle mostly covers the LA body, the LAA, and the vestibule. In contrast, the septopulmonary bundle largely encircles the pulmonary veins in the posterior wall.

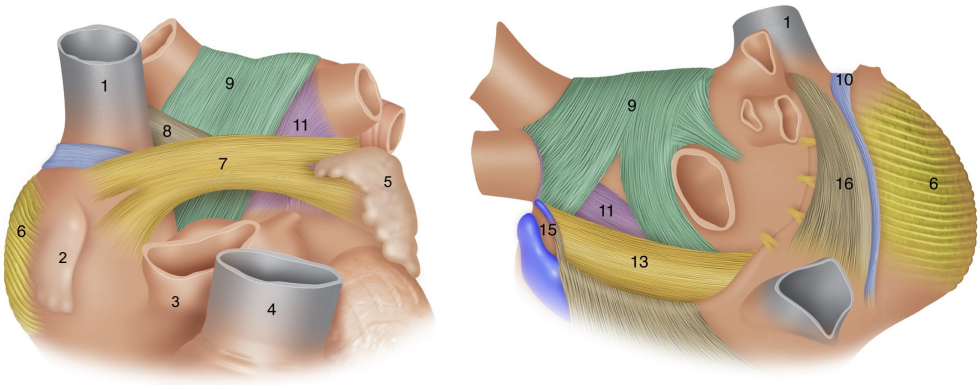

Figure 2.12: Atrial muscle architecture. Left: main atrial muscular bundles from an anterior view. Right: main atrial muscular bundles from a posterior view. 1. Superior vena cava, 2. Right atrial appendage, 3. Ascending aorta, 4. Pulmonary artery, 5. Left atrial appendage, 6. Pectinate muscles, 7. Antero-superior interatrial bundle, 8. Posterior-superior interatrial bundle, 9. Septopulmonary bundle, 10. Precaval bundle, 11. Septoatrial bundle, 13. Circumferential band, 14. Coronary sinus and musculature, 15. Marshall vein and bundle, 16. Intercaval bundle, 17. Postero-inferior interatrial bundle, 18. Terminal bundle. Obtained from [118] under CC NC-ND license.

Table 2.2: Main anatomical structures of the left atrium, size, origin and their clinical relevance [134].

	Size	Origin	Clinical relevance
PV	13.0-15.0 mm (D) 2.0-3.0 cm (L) 2.0-8.0 mm (T)	Single embryonic pulmonary vein outgrowing from the posterior wall of LA	Triggering ectopic activity in AF
LAA	16.0-51.0 mm (D) 10.9$\pm$4.2 mm (D) 2.0-8.0 mm (T)	Primitive atrium	Prominent trabeculations promote reentry and thrombus formation
Mitral isthmus	28.8$\pm$7.0 mm(L) 1.9-3.0 mm (T)	Boundary between the primitive atrium and mitral valve	Macro-reentrant activity in perimitral atrial flutter
Lateral ridge	22.4$\pm$5.1 mm (L) 5.0 mm(D)	Embryonic folding of the heart during the formation of the left-sided cardinal veins	Triggering ectopic activity in AF

AF: atrial fibrillation, D: diameter, L: length, LA: left atrium, LAA: left atrial appendage, T: thickness

2.3.4 Cardiac Conduction System

The cardiac conduction system (CCS) is responsible for initiating and transmitting electrical pulses in the heart, allowing for a rhythmic and coordinated muscular contraction. This coordinated contraction is necessary to effectively pump blood throughout the body. The sinoatrial node (SAN) is the natural pacemaker of the heart. The SAN consists of highly specialized electrical cells located sub-endocardially at the junction of the SVC and the RAA, and extending down to the inferolateral aspect of the CT, as shown in Figure 2.13 [145]. The SAN has multiple exit pathways that spread towards the interatrial septum and the sulcus terminalis [128].

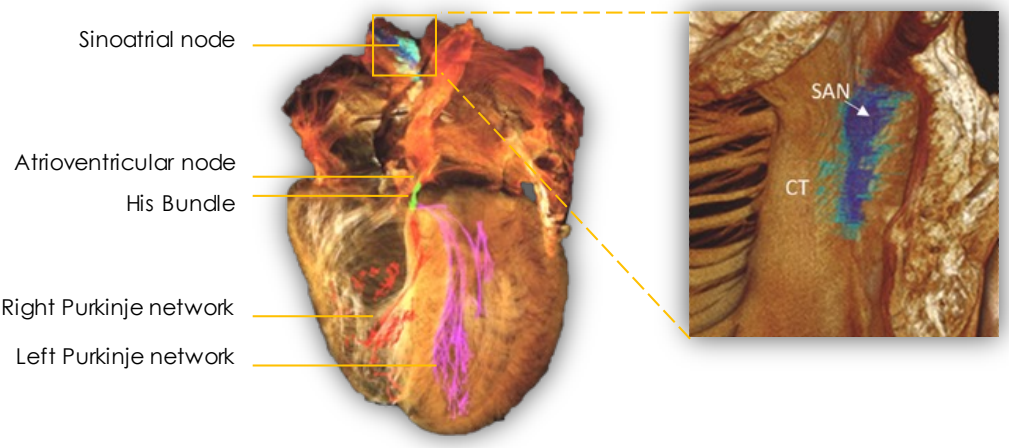

Figure 2.13: Components of the cardiac conduction system determined by micro-computed tomography. SAN: sinoatrial node, CT: crista terminalis. Modified from [145] under CC-BY license.

SAN cells undergo spontaneous depolarization and generate electrical impulses that travel across the atrial myocardium. The depolarization wave reaches the LA primarly through the Bachmann bundle (BB), extending across the interatrial sulcus close to the SVC and the LAA [146]. The depolarization wave travels through the atrial myocardium and reaches the atrioventricular node (AVN), which is located in the proximity of the triangle of Koch. In a healthy heart, the AVN is the only electrical conduction pathway between the atria and ventricles. The conduction is intentionally slowed down when arriving at the AVN to allow the atria to empty and the ventricles to fill with blood. In the ventricles, the CCS consists of the bundle of His, the right and left bundle network, and the Purkinje fibers. Purkinje fibers establish connections with the ventricular working myocardium, facilitating coordinated ventricular contraction.

2.4 Atrial Electrophysiology

Cardiac myocytes have ion channels embedded in their cellular membrane that regulate the flow of ions between the intracellular and extracellular space (Figure 2.14a). The action potential (AP) describes the changes in transmembrane voltage over time of a cardiac myocyte. Figure 2.14b shows a schematic representation of the atrial AP and the major ionic currents. In the resting state, atrial cells typically have a transmembrane voltage around -80 mV [147]. During the phase 0, rapid depolarization occurs once the cell reaches the threshold of -50 mV due to the inward sodium current (I_{Na}) activation, resulting in an upstroke potential up to +30 mV. The time of the maximum change during phase 0, also referred to as dV/dt_{max}, is typically used as an estimate of the cellular activation time [148].

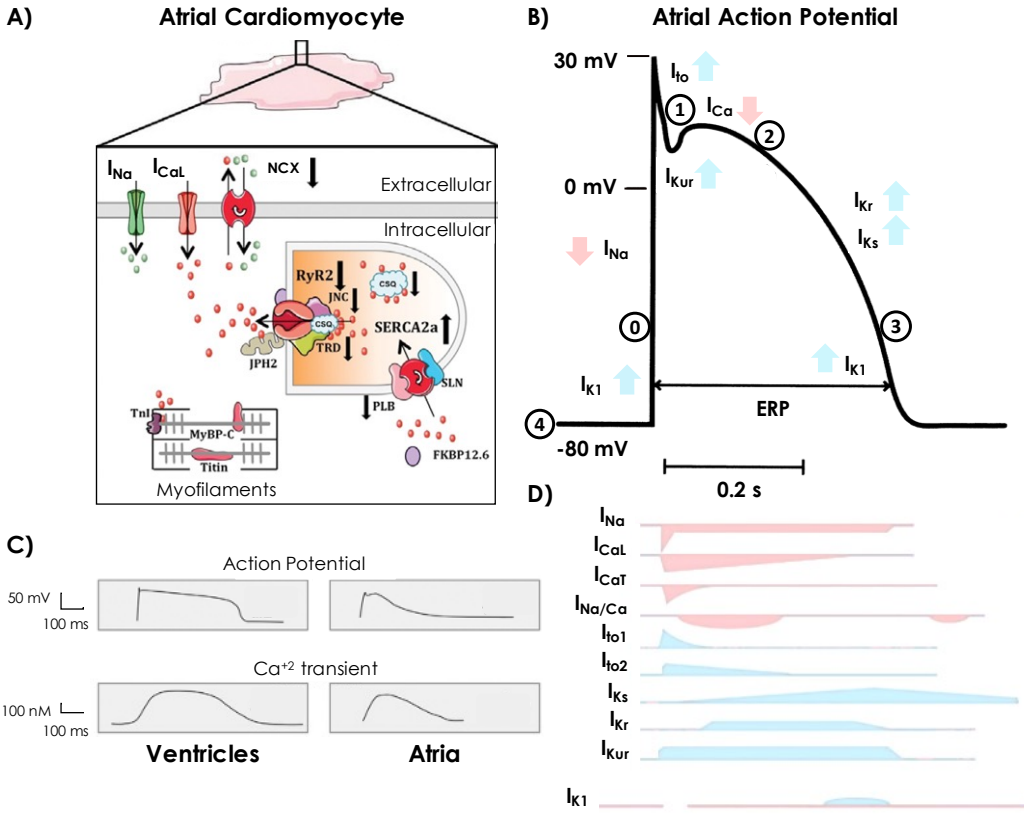

Figure 2.14: Atrial cardiomyocyte and its action potential. A) Diagram of an atrial myocyte depicting the membrane, sarcoplastic reticulum (SR) and myofilaments. B) Action potential (AP) with phases indicated by numbers. Inward currents are shown in pink while outward currents in blue. C) Differences between ventricular and atrial myocytes. D) Major ionic currents related to the AP. Calcium: Ca^{+2}, CSQ: calsequestrin, ERP: effective refractory period, Na^{+}: sodium, SERCA2a: SR calcium (Ca^{+2})-ATPase2a, PLB: SERCA2a-inhibitor phospholamban, RyR2: Ryanodine receptor, JPH2: Junctophilin-2, FKPB12.6: FK506-binding protein 12.6. NCX: sodium (Na^{+}) Ca^{+2}, SLN: sarcolipin, MyBP-C: Myosin bindig protein C. Adapted from [147, 149, 150] with permission from the publishers.

The regulation of the intracellular calcium concentration is principally carried out by ion channels, ATPases (pumps), exchangers, and calcium-binding proteins. Voltage-gated L-type calcium channels are activated after phase 0, allowing small calcium intake. Intracellular calcium ions bind and activate the ryanodine receptor 2 (RYR2), causing the release of more calcium from the sarcoplasmic reticulum (SR). Released calcium ions bind to troponin C, which allows cross-bridge cycling between actin and myosin filaments, leading to muscular contraction. The relaxation phase begins when calcium release is stopped and calcium ions are pumped back into the SR via the sarcoplasmic/endoplasmic reticulum calcium ATPase 2A (SERCA2A) or via the sodium calcium exchanger 1 (NCX1) [151].

Repolarization comprises phases 1-3 of the AP and involves the return of the cell to its resting state, mainly driven by outward potassium currents. In phase 1, known as rapid repolarization, the I_{Na} is inactivated and the short-lasting transient outward potassium current (I_{to}) limits the AP amplitude. A plateau is present during phase 2 mainly caused by inward calcium currents. Three major potassium currents also contribute to the plateau phase: the rapidly activating I_{Kr} current, the slowly activating I_{Ks}, and the ultra-rapidly delayed rectifier I_{Kur} current, the latter being mainly expressed in the atria. Phase 3 exhibits a sharp decline due to the complete activation of I_{Ks} and the inactivation of L-type Ca^{+2} current (I_{CaL}).

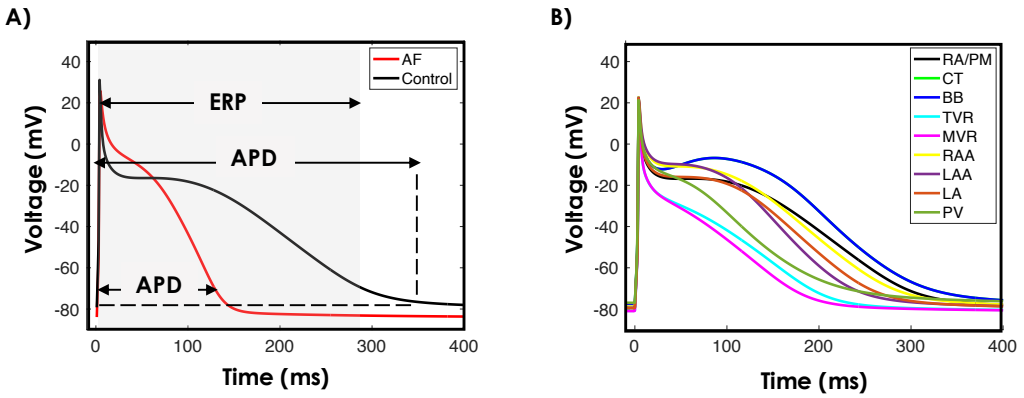

Figure 2.15: Changes in human atrial action potential duration (APD). A) Relationship between the APD and the effective refractory period (ERP) in normal cardiomyocytes (black) and with atrial fibrillation (AF)-induced remodeling (red). B) Regional heterogeneity of the action potentials in the atria as in [33].

Refractoriness is an electrophysiological property that characterizes the response of cardiac tissue to premature stimulation. At the cellular level, the effective refractory period (ERP) spans from the initial depolarization until excitability is fully restored during phase 3. The action potential duration at 90 % of repolarization (APD_{90}) serves as an approximation for quantifying the ERP. Human atrial APD_{90} at 1 Hz varies from 150 to 500 ms [152]. The absolute refractory period refers to the time during which no activation can be initiated regardless of the stimulus intensity. This period of absolute refractoriness is followed by the relative refractory period. However, due to the recovery of sodium channels at the end of

phase 3, APs with slow upstrokes can be elicited. The duration of the AP is determined by three factors: 1) the availability of sodium channels, 2) the equilibrium between depolarizing and repolarizing currents at the cellular level, and 3) the degree of electrical coupling between neighboring myocytes at the tissue level [153].The ERP can be measured experimentally and is defined as the longest coupling interval that fails to generate a capture in the tissue [147].

Atrial cardiomyocytes exhibit unique AP characteristics compared to ventricular cardiomyocytes. The background inward-rectifier potassium current (I_{K1}) is smaller in the atria, leading to a less negative resting potential and a more gradual repolarization phase than in the ventricles (Figure 2.14c). Atrial cardiomyocytes possess two potassium currents: I_{Kur} and the acetylcholine-regulated potassium current (I_{KACh}). Cell to cell proteins called connexins facilitate coupling between cardiomyocytes. While conexin-43 is mainly present in the ventricles, atrial cardiomyocytes express also connexin-40, alterations of which have been associated with AF. Additionally, significant differences exist in the calcium handling proteins present in the atria and ventricles. The sarcoplasmic reticulum calcium-ATPase2a protein (SERCA2a) levels are two-fold higher in the atria than in the ventricles, while SERCA2a-inhibitor phospholamban (PLB) is less abundant. As a consequence, the atria show decreased contraction and relaxation durations, as well as shorter duration of calcium transients. These distinctive characteristics may potentially influence responses to atrial arrhythmias [150].

2.5 Atrial Fibrillation

Atrial fibrillation (AF) is the most common supraventricular tachyarrhythmia and is associated with increased morbidity and mortality rates [1, 7]. Over 50 million people worldwide suffer from AF and its prevalence is projected to double by the year 2060 [8]. AF often remains asymptomatic in its initial stages, and its diagnosis typically occurs when symptoms emerge and lead to haemodynamic instability and subsequent health complications [11]. According to the latest guidelines of AF [1], the diagnosis of AF requires documentation of AF episodes lasting at least 30 s on a surface electrocardiogram (ECG). The following criteria is used to diagnose AF: absence of distinct repeating P-waves, irregular atrial activations, arrhythmia cycle length $<$200 ms and irregular RR intervals (Figure 2.16).

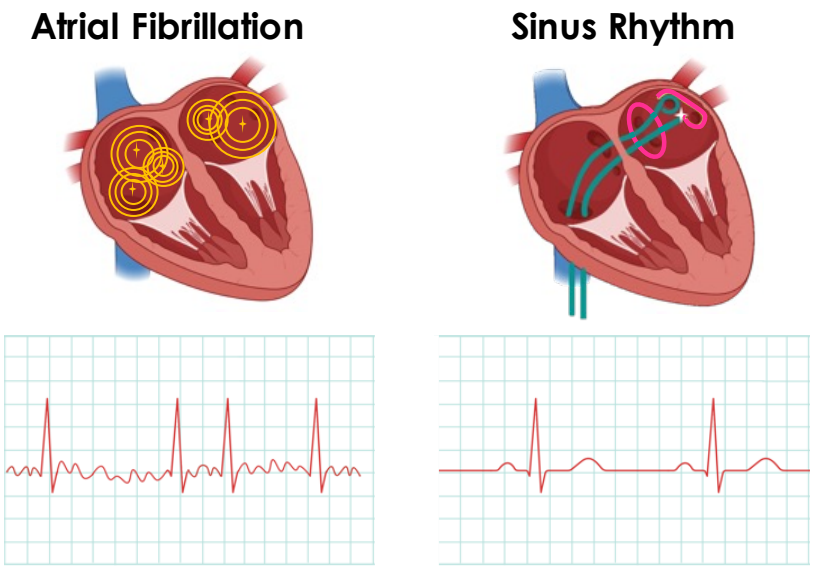

Figure 2.16: Criteria for the diagnosis of atrial fibrillation on the body surface electrocardiogram (ECG) [118]. Representative ECG trace with atrial fibrillation (left) and sinus rhythm (right). The goal of atrial fibrillation catheter ablation (right) is to restore sinus rhythm. Created with Biorender under academic license.

2.5.1 Classification

The classification of AF can be based on the duration of AF episodes [1, 118] or on the progression of the disease [7]. Clinical patterns of AF based on episode duration include: *paroxysmal AF*, lasting longer than 30 s and terminating spontaneously or with intervention within 7 days; *persistent AF*, lasting longer than 7 days but less than 1 year; *long-standing persistent AF*, lasting for at least 1 year where rhythm control management is pursued; and *permanent AF*, characterized by a joint decision between the clinician and the patient not to

restore sinus rhythm through treatment. In addition, due to the progressive nature of AF, new guidelines from the American Heart Association (AHA) propose a classification based on different stages of the disease rather than episode duration [7]. Table 2.3 shows a comparison of the classification between both guidelines.

Table 2.3: Atrial fibrillation classification and stages proposed by current clinical guidelines. A) Classification based on episode duration as described in the 2024 EHRA expert consensus statement on catheter and surgical ablation of atrial fibrillation [118]. B) Stages based on disease progression and treatment as described in the 2023 AHA guidelines for the diagnosis and management of atrial fibrillation [7]. AF: atrial fibrillation, AHA: American Heart Association, EHRA: European Heart Rhythm Association.

A) Classification based on episode duration [118]

Classification	Episode duration	Termination	Considerations
Early paroxysmal	$>$ 30 s	$<$ 1 day	Termination is spontaneous or due to medical intervention
Paroxysmal	$>$ 30 s	$<$ 7 days	Termination is spontaneous or due to medical intervention
Early persistent	$>$ 7 days	$<$ 3 months	Termination is spontaneous or due to medical intervention
Persistent	$>$ 7 days	$<$ 12 months	Termination is spontaneous or due to medical intervention
Long-standing persistent	$>$ 12 months	-	Rhythm control is pursued
Permanent	-	-	Therapeutic attitude between clinician and patient to not pursue sinus rhythm

B) Stages based on disease progression [7]

Stage number	Stage name	Considerations
1	At risk for AF	Presence of risk factors associated with AF
2	Pre-AF	Evidence of structural and electrical findings predisposing to AF
3A	Paroxysmal AF	Intermittent AF $<$ 7 days
3B	Persistent AF	Continuous and sustained AF episode $>$ 7 days
3C	Long-standing persistent AF	Continuous and sustained AF episode $>$ 12 months
3D	Successful AF ablation	Freedom from AF after intervention
4	Permanent AF	No attempt to restore sinus rhythm

2.5.2 Pathophysiology

The pathophysiology of AF is driven by a complex interplay of mechanisms that promote its initiation, maintenance and progression [100]. These mechanisms are originated from alterations in atrial electrophysiological, structural, mechanical, neurohumoral and metabolic properties [154]. A common conceptual framework explaining the existence of AF is shown in Figure 2.17. *Remodeling* is the hallmark of AF pathogenesis and refers to persistent changes in the structure and function of the atria [155]. In particular, electrical remodeling refers to changes in the ion channel properties of atrial cardiomyocytes, while structural remodeling refers to the presence of fibrosis and atrial dilation [156]. This conceptual framework also postulates that both a trigger and a vulnerable substrate are necessary for reentry formation.

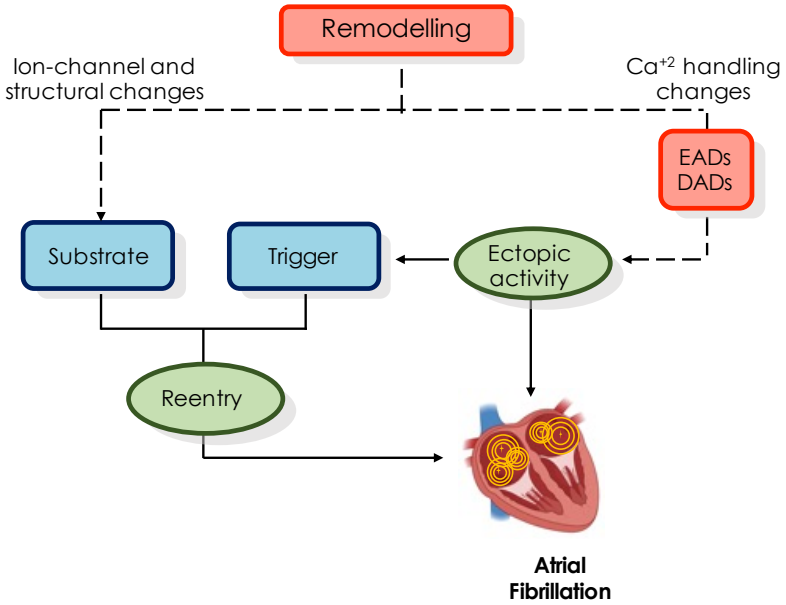

Figure 2.17: Conceptual framework representing the role of remodeling in atrial fibrillation. Modified from [157] with permission from the publisher. Created using Biorender under academic license. Ca^{+2}: calcium ions, EAD: early afterdepolarizations, DAD: delayed afterdepolarization.

Reentry is defined as a "repetitive excitation of tissue by recirculating wavefronts" [47]. *Ectopic activity* is an abnormality in impulse formation in the atria related to the spontaneous release of calcium ions from the sarcoplasmic reticulum via leaky ryanodine receptors [118]. The presence of early afterdepolarizations (EAD) due to loss-of-function mutations in outward potassium channels and gain-of-function mutations in inward calcium channels, has been associated to ectopic activity [118]. Furthermore, both ectopic activity and reentry can maintain AF [155]. Abnormal calcium release also increases the presence of delayed

afterdepolarization (DAD), predisposing the pulmonary vein to ectopic activity. Figure 2.18 illustrates the concepts of EAD and DAD in the cardiac tissue causing ectopic activity.

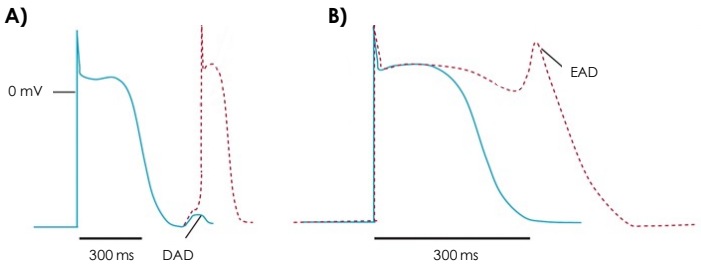

Figure 2.18: Basic mechanisms related to ectopic activity in the atria. A) delayed after depolarizations (DAD) are caused by spontaneous diastolic Ca^{2+} release which promotes the exchange of Na^{+} into the cell provoking ectopic beats (red). B) early after depolarizations (EAD) occur when the action potential is prolonged due to K^{+} inhibition, allowing Ca^{2+} currents to repolarize the cell. Adapted from [157] with permission from the publisher.

The sleeves of the pulmonary veins (PV) are the most frequent form of AF triggers [136]. Non-PV triggers have also been identified in the crista terminalis (CT), the interatrial septum, the left atrial (LA) posterior wall, the left atrial appendage (LAA), the ligament of Marshall, the superior vena cava (SVC), and the coronary sinus (CS); yet their precise role in initiating AF remains uncertain [118]. The *vulnerable substrate* refers to the presence of electrical heterogeneity and conduction abnormalities caused by electrical and structural remodeling (e.g., presence of fibrosis, adipose tissue infiltration, changes in the extracellular matrix, inflammation, atrial dilatation, etc.) [1, 118].

2.5.3 Mechanisms

The mechanisms of AF can be classified into classical and novel mechanistic concepts [158]. While most of the classical mechanisms were proposed more than 100 years ago, the most recent ones have been described in the past 20 years [158]. Classical mechanisms of AF consist of a single ectopic foci, single circuit reentry and multiple wavelet reentry. Novel mechanisms include stable rotors, unstable fibrosis linked rotors and endo-epi dissociation [158]. Figure 2.19 illustrates classical and novel mechanisms of AF.

In 1913, Mines proposed a circuit model (Figure 2.20A) to explain the concept of *anatomical reentry*, where a wavefront propagates around a fixed anatomical obstacle [159]. He suggested that a wave would continue to propagate around the circuit if there was an excitable gap between the wavelength, which is the product of conduction velocity and refractory period, and the length of the circuit. This model helped to elucidate the relationship between the refractory phase and the speed of propagation in cardiac tissue. In 1921, the British cardiologist Sir Thomas Lewis was among the first to propose that *single reentry circuits*, also referred to as *circus movement*, might be the main mechanism of AF [160].

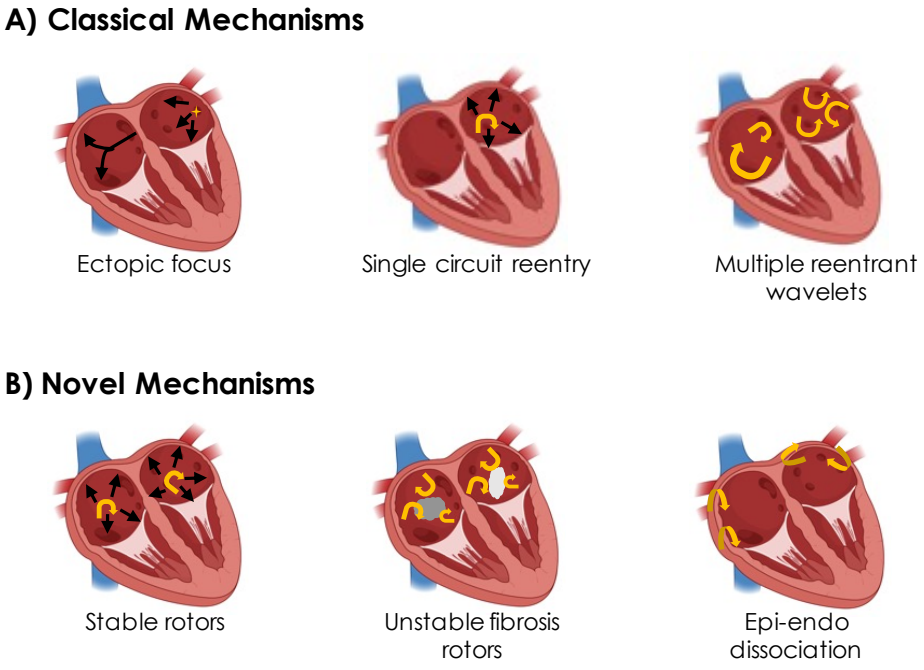

Figure 2.19: Classical and novel mechanisms of atrial fibrillation. A: classical mechanisms include a single ectopic foci, single circuit reentry and multiple wavelet reentry. B: novel mechansisms include stable rotors, unstable fibrosis linked rotors and endo-epi dissociation. Inspired by [158]. Created using Biorender under academic license.

This concept was later challenged and refuted using dog hearts in tachycardia inducing experiments following aconitine injection in the left or right atrium appendages [161]. They argued that fibrillation occurred from triggered activity coming from a singular location, in this case the injection, and that cooling of the region immediately stopped fibrillation.

In 1959, Moe and Abildskov proposed the hypothesis that AF is maintained by *multiple wavelets* or multiple reentrant circuits [162]. To test this hypotheses, Moe *et al.* developed the first computer model simulating disorganized turbulent activity similar to AF, proposing that at least 26 wavelets are required to maintain fibrillation [163]. The experimental work in a canine model from Allesie *et al.* favoured the multiple wavelet hypothesis and suggested that fibrillation was maintained as long as there were a critical minimal number of 4-6 fibrillation waves [164]. In 1973, Allesie *et al.* demonstrated in a rabbit model of the LA that no anatomical obstacle is needed for the ocurrence of reentry, proposing the concept of *functional reentry* [165]. In 1977, they introduced the *leading circle reentry* theory, suggesting that unidirectional block, due to centripetal activation rendering the center refractory, causes the wavefront to propagate along a circular trajectory (Figure 2.20B) [166]. Their findings also demonstrated that even within a limited region of atrial muscle without any anatomical obstacle, the wavefront can be self-sustained in a circular fashion.

Most of the concepts described so far come from the notion that electrophysiology of the thin-walled atria could be studied assuming a 2D surface. Using simultaneous recordings in

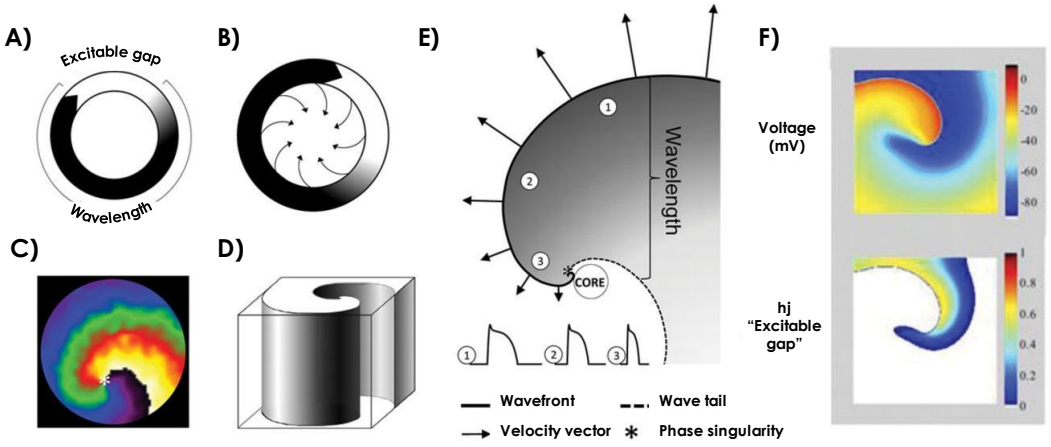

Figure 2.20: Reentrant circuit mechanisms. A) Anatomical reentry based on the ring model of [159] where the propagating wave (black) is separated by an excitable gap (white) around an anatomical obstacle. The wavelength, shown in black, is the product of the conduction velocity (CV) and the effective refractory period (ERP). B) Leading circle reentry around a functional obstacle. Centripetal forces point towards a refractory center. C) Spiral wave in 2D showing the tip with a white asterisk (*). D) Scroll wave in 3D. E) Electrotonic changes in a spiral wave. Changes in action potential duration are shown with numbers 1-3, and decreased conduction velocity is indicated by the length of the arrows. Wavelength decreases near the rotor tip. A phase singularity occurs when the tip of the wavefront meets the tail. F) Simulated reentry. The top image in 2D shows the transmembrane voltage, while the bottom image shows the excitable gap calculated by the product of the fast (h) and slow (j) sodium current inactivation variables. The tissue is unexcitable (white) when h $\times$ j = 0, meaning no I_{Na} is available. Reproduced from [167] with permission from the publisher.

the epicardial and endocardial surfaces of the canine RA under sinus rhythm and tachycardia, Schuessler *et al.* showed that there are locations where the epicardium and endocardium have different patterns of activation, and that these differences are increased in regions where thickness was >0.5 mm [168]. This separation between endocardial and epicardial propagation is referred to as *endo-epi dissociation* [169].

There is an ongoing discussion over the mechanisms that initiate and maintain AF [170]. The main debate is whether the AF disorganization is produced by external factors (sources) or if the disorganization itself supports AF [171]. While some researchers support the idea that AF is sustained by random multiple wavelets [172], others claim that AF is maintained by spatially localized drivers known as rotors [167]. A *rotor*, or spiral wave, is a type of functional reentry where the curvature of the wavefront causes the wavelength to be shorter at the center (Figure 2.20 C-F) [169]. A *phase singularity* refers to the organizing center (tip) of the propagating wave [173]. The concept of the presence of rotors comes from evidence derived from animal experiments and clinical studies showing hierarchical organization during AF [174]. The main difference between the leading circle reentry theory and the rotors theory is that in the leading circle reentry theory, the center of the circuit is continuously activated, leading to local refractoriness. In contrast, in the rotors theory, rotor waves can meander around the atria as there is no truly refractory tissue. [156].

Understanding the mechanisms underlying AF can enhance treatment efficacy [158]. The work of Moe *et al.* and Allesie *et al.* put strong emphasis on the atrial size and lead to the development of the Cox-Maze surgical procedure which aims to divide the atria to reduce the probability of reentrant circuits [175]. However, with the advent of minimally invasive strategies, the Cox-Maze procedure is seldom performed, primarily for patients undergoing cardiac surgery [176]. In addition, the notion that AF may stem from individual or localized rotors suggests that these locations might be targeted during catheter ablation [177]. In the subsequent section, therapeutic approaches for AF, particularly catheter ablation, are described.

2.5.4 Treatment

Before AF manifests, optimal management includes treating risk factors and implementing lifestyle changes that reduce the likelihood of AF development [7]. Common symptoms associated with AF include palpitations, shortness of breath, dizziness, weariness, and syncope [118]. Once AF is diagnosed, treatment should focus on avoiding stroke, maintaining sinus rhythm and minimizing AF burden [7, 118]. Two main therapeutic strategies have emerged for AF: *rate control* focuses on managing ventricular rate, and *rhythm control* aims to restore and maintain sinus rhythm.

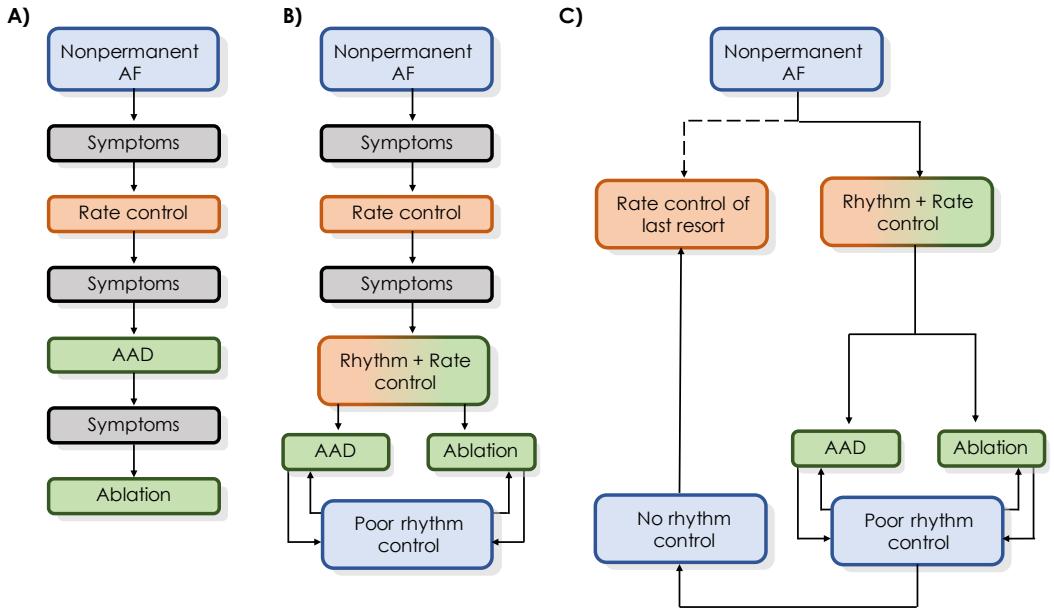

Figure 2.21: Evolution of atrial fibrillation treatment management. A) Past strategy focused on escalation based on symptoms from initial rate control to rhythm control. B) Current strategy as a combination of rhythm and rate control for symptomatic patients. C) Future strategy with focus on rhythm control. AF: atrial fibrillation, AAD: antiarrhythmic drugs. From [178] under CC license.

Rhythm control strategies include antiarrhythmic drugs, such as amiodarone, sotalol, flecainide and propafenone; cardioversion, and catheter ablation. Rate control strategies include beta blockers, calcium antagonists, and AV nodal ablation [178]. Rate control is a necessary component of AF therapy and is often sufficient to alleviate AF-related symptoms [1]. However, there is a growing evidence supporting early rhythm control strategies [178], with a paradigm shift towards rhythm control over rate control as shown in the following Figure 2.21. In addition, rhythm control may lead to reduced symptoms and increased quality of life [1, 7].

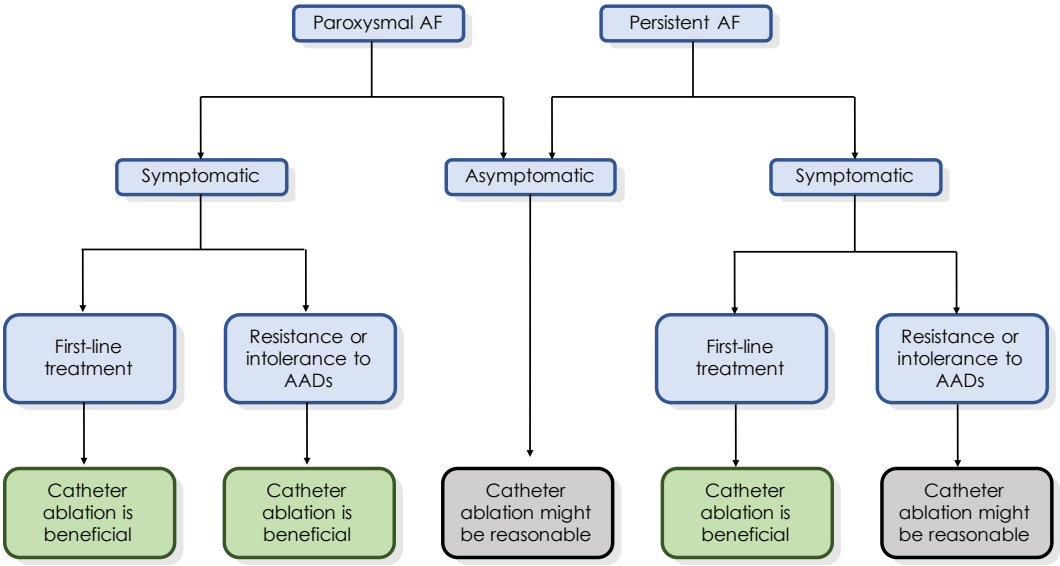

Figure 2.22: Current recommendations on catheter ablation for patients with paroysmal and persistent AF based on the occurrence of symptoms. AADs: antiarrhythmic drugs. Adapted from [118] with permission from the publisher.

Catheter ablation is a well-established minimally invasive rhythm control strategy [179]. Moreover, catheter ablation has shown to be more effective in maintaining sinus rhythm and improving symptoms than anti-arrhythmic drugs [1, 7, 180]. More recently, it was suggested that catheter ablation is beneficial as a first-line treatment for symptomatic patients [118]. Figure 2.22 illustrates recent recommendations on catheter ablation in patients with paroxysmal or persistent AF, based on the occurrence of symptoms. Ultimately, the decision between rate control and rhythm control is complex and often depends on the patient's preferences, clinical presentation, and associated comorbidities [7, 181].

The isolation of the pulmonary veins (PVI) is the cornerstone of catheter ablation and is required in every AF ablation procedure [118]. The main goal of PVI is to electrically disconnect the PVs from the LA (Figure 2.23A). Although PVI is a useful rhythm control strategy that has been shown to reduce AF burden, PVI still has significant recurrence rates at 12 months (25–50 %), with different rates for paroxysmal and persistent forms of AF [182]. Adjunctive ablation strategies beyond PVI include: linear lesions, ablation of focal triggers,

ablation of rotors, vein of Marshall ethanol infusion, ablation of low voltage (<0.5 mV) areas in sinus rhythm, isolation of the left posterior wall, and the ablation of regions of enhancement with late gadolinium enhancement MRI. The following Table 2.4 provides a summary of the recommendations for AF ablation strategies. Additionally, the ablation of multiple targets beyond PVI, including biatrial ablation, remains controversial and has not yet demonstrated additional benefits over PVI alone [1, 7]. The current PVI approach, often considered as a one-size-fits-all strategy, may overlook the unique characteristics of individual patients, potentially contributing to high recurrence rates.

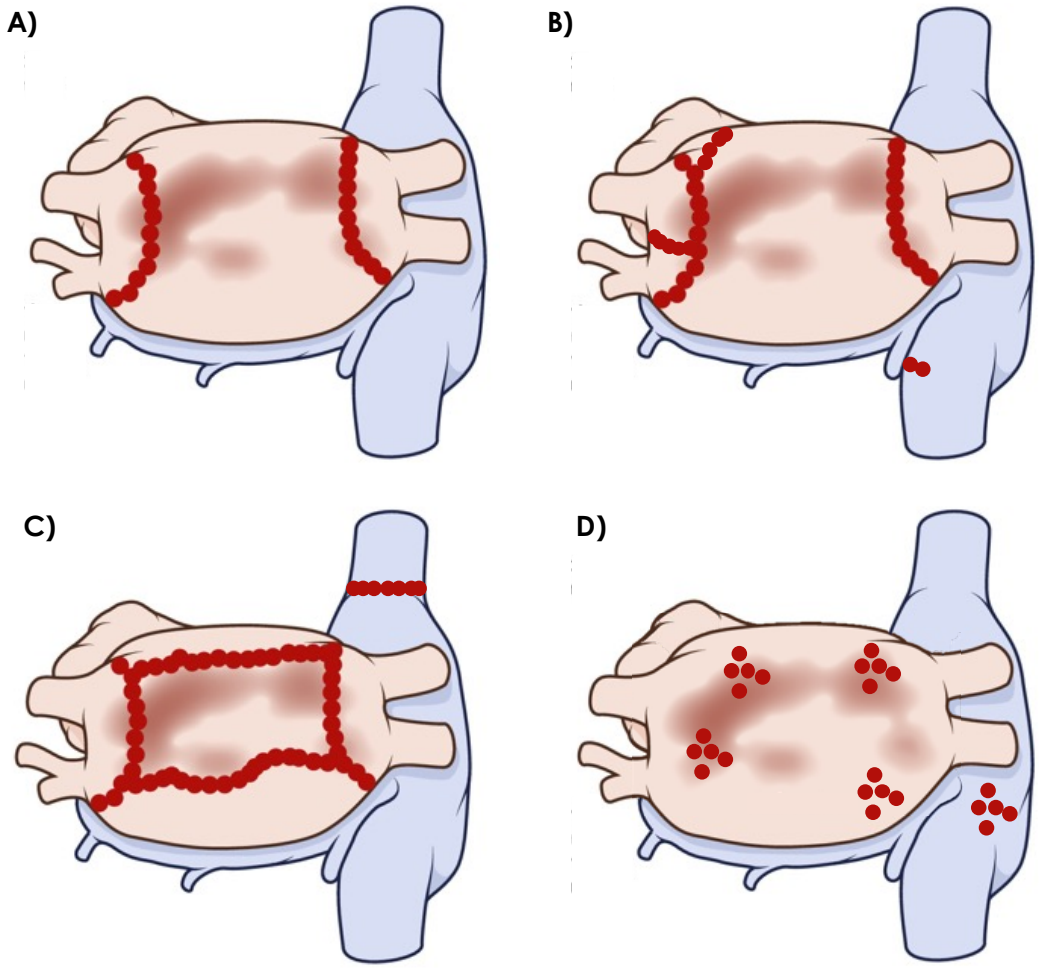

Figure 2.23: Current ablation strategies for atrial fibrillation management. Posterior view of the atria, the substrate is indicated in darker color in the posterior wall of the left atrium. A) PVI. B) PVI + ablation of the cavo tricuspid isthmus and lines connecting the left PV to the mitral valve. C) posterior wall isolation + superior vena cava isolation. D) ablation of complex fractionated electrograms or substrate ablation with low voltage amplitude (<0.5 mV). PVI: pulmonary vein isolation. Adapted from [183] with permission from the publisher.

Table 2.4: Recommendations for atrial fibrillation catheter ablation [118]. A) Pulmonary vein isolation recommendations. B) Recommendations for adjunctive ablation targets beyond pulmonary vein isolation. AF: atrial fibrillation, PVI: pulmonary vein isolation.

A) Pulmonary vein isolation

Recommendation	Category of advice
Electrical isolation of the PVs is required during all AF ablation procedures	Advice to do
Achievement of electrical isolation requires, at a minimum, assessment and demonstration of entrance block into the PVs	Advice to do
A waiting period (e.g. 20 min) following initial PVI may be reasonable to monitor for PV reconnection	Uncertainty
Administration of adenosine 20 min following initial PVI, with reablation if PV reconnection occurs, may be reasonable to improve PVI durability	Uncertainty
Pace capture–guided approach following PVI using RF energy may be reasonable to improve PVI durability	Uncertainty

B) Adjuctive ablation targets beyond pulmonary vein isolation

Recommendation	Category of advice
If linear ablation lesions are deployed, mapping and pacing maneuvers are required to document conduction block	Advice to do
If a reproducible focal trigger that initiates AF is identified outside the PV ostia at the time of an AF ablation procedure, ablation of the focal trigger is beneficial	Advice to do
Vein of Marshal ethanol infusion is reasonable to facilitate achieving block in the lateral mitral isthmus in patients with mitral annular flutter	May be appropriate
Ablation of areas of abnormal myocardial tissue identified with voltage mapping during sinus rhythm may be reasonable during persistent AF ablation	Uncertainty
Vein of Marshal ethanol infusion may be reasonable during persistent AF ablation	Uncertainty
Mapping and ablation of non-PV triggers may be reasonable during persistent AF ablation	Uncertainty
Isolation of the left atrial posterior wall may be reasonable during repeat ablation of persistent AF	Uncertainty
Ablation of MRI-detected atrial delayed enhancement areas is not beneficial during persistent AF ablation	Advice not to do

2.6 Atrial Fibrosis

Atrial fibrosis is one of the major factors leading to the development of AF [184]. In this section, a review of the reported values of biatrial fibrosis informed by different imaging techniques is presented.

2.6.1 Left Atrial Fibrosis

Fibrotic burden, defined as the percentage of the fibrotic tissue of the total atrial wall, has been extensively described mainly using LGE-MRI in the LA (Table 2.5). Different authors reported the mean burden of fibrosis in the LA in patients with AF to range between 8.4 and 24.4% defined as IIR > 1.2 by LGE-MRI [43, 185–187]. The DECAAF II study showed that most patients with paroxysmal AF were classified in UTAH stages 2 and 3, i.e., mean LA fibrosis burden between 10 and 30% [188]. According to Benito *et al.*, the posterior wall and the floor are the regions more affected by fibrosis in the LA. This is in line with the findings reported by Higuchi *et al.*, where the highest probability of enhancement was observed in the posterior wall close to the left inferior pulmonary vein antrum [189]. However, Nairn *et al.* showed that the location of the LA fibrotic substrate differs depending on the selected modality, suggesting that the anterior wall might also be prone to fibrosis, especially if the fibrotic substrate is assessed using LVA with a voltage threshold< 0.5 mV [187].

Table 2.5: Biatrial fibrotic burden in patients with atrial fibrillation defined by late gadolinium enhancement-magnetic resonance imaging.

LA fibrosis (%)	n	RA fibrosis (%)	n	AF History	Reference
8.5 ± 8.7	113	-	-	PAF and PeAF	[186]
21.2 ± 11.6	87	-	-	PAF	[189]
24.6 ± 11.9	73	-	-	PeAF	[189]
17.0 ± NR	36	-	-	PeAF	[187]
24.4 ± 16.1	110	28.60 ± 19.48	110	PAF and PeAF	[190]
8.6 ± 6.1	35	10.1 ± 8.6	33	PAF	[191]
16.7 ± 11.1	344	5.3 ± 6.4	134	PAF and PeAF	[192]
22.8 ± 6.1	20	19.7 ± 5.7*	20	PeAF	[21]
8.1 ± 17	55	4.0 ± 6.4%	55	ParoxAF	[193]
10.5 ± 12	45	4.4 ± 7.4	45	PeAF	[193]

LA: left atrium, n: number of patients, PAF: paroxysmal atrial fibrillation, PeAF: persistent atrial fibrillation, RA: right atrium

2.6.2 Right Atrial Fibrosis

The mean burden for the RA using LGE-MRI described in the literature varied between 4.0 to 28.6% [21, 190, 192, 193]. Akoum *et al.* showed in a group of 134 patients that the RA fibrotic burden was 5.3% ± 6.4%, with the septal region showing the highest enhancement together with the free wall towards the vena cava in more advanced stages [192]. Similar results were found in a more recent study with 55 paroxysmal AF patients by Gunturiz-Beltran *et al.* , where the RA fibrotic burden was 4.0 ± 6.4%, showing the largest fibrotic presence in the IVC junction [193]. In another study, the mean fibrotic burden of the RA was 28.60% ± 19.48% in a cohort of 110 patients with AF [190].

2.6.3 Biatrial Fibrosis Ratio

In terms of the ratio between left and right fibrosis, there is still controversy about the comparison of the right vs. left fibrotic burden. In a cohort of 20 patients, Zahid *et al.* reported a mean biatrial fibrotic burden of 19.7%, which was comparable to the measured mean LA burden of 22.8% [21]. Hopman *et al.* observed a strong correlation ($r = 0.88$, $P < 0.001$) between the right and left amount of fibrosis assessed using LGE-MRI [190], which is in line with a post-mortem analysis where the extent of fibrosis between RA and LA locations did not differ [194]. Interestingly, these results are contrary to the histological observations from the CATCHME study [195], where RA samples showed more extracellular matrix (ECM) and endomysial fibrosis when compared to LA samples. In the case of the CATCHME study, the samples were taken from the RAA and LAA samples, which are in most cases excluded during LGE-MRI fibrosis assessment. Additionally, the difference between RA and LA could be explained due to differences in the stage or progression of the disease (paroxysmal vs. persistent AF) or the presence of other diseases affecting primarily the RA, such as pulmonary hypertension or congenital diseases such as atrial septal defects [191]. Finally, it could also be due to the intrinsic limitations of the current LGE-MRI technique, such as lack of threshold validation and low image resolution affecting atrial wall delineation, incorporating uncertainty to biatrial segmentations.

Chapter 3

Mathematical Fundamentals

In this chapter, the mathematical foundations of multiscale cardiac computational modeling are introduced, ranging from the simulation of single cell cardiac electrophysiology to the forward calculation of P-waves on the body surface. The chapter concludes with an overview of machine learning and explainability methods.

3.1 Cellular Cardiac Electrophysiology

In 1952, Hodgkin and Huxley formulated the first mathematical model to describe the electrical changes in the cellular membrane of the squid axon [196]. The cellular membrane was modeled as an equivalent electrical circuit (Figure 3.1) comprising a set of of resistors, representing ion channels with their respective ionic currents I_x, and one capacitor representing the membrane capacitance C_m. The movement of ions across the membrane generates a potential difference V_m.

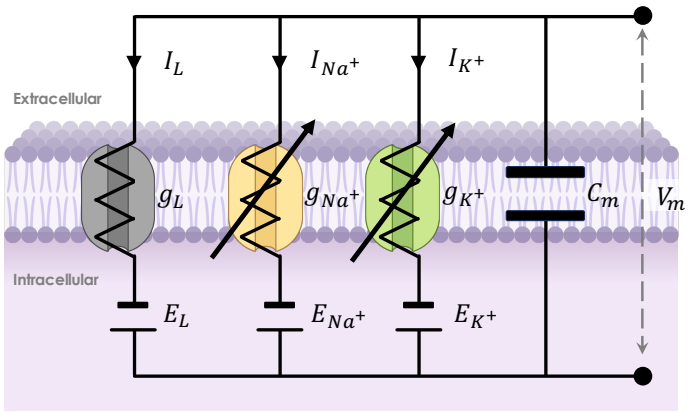

Figure 3.1: Hodking and Huxley equivalent electrical circuit for the definition of cellular gating kinetics [196]. x denotes an arbitrary ion, I_x denotes ionic currents, E_x are the Nerst potentials, g_x is the conductance of the channel, C_m is the capacitance of the membrane per unit area and V_m is the potential difference across the membrane. Created with Biorender under academic license.

The current I_{x} of a channel is defined as:

$$I_{\mathrm{x}} = g_{\mathrm{x}} \left(V_{\mathrm{m}} - E_x \right) \tag{3.1}$$

where, x denotes an arbitrary ion, E_{x} corresponds to the Nerst potential and g_{x} is the conductance of the channel of that particular ion. The Nerst potential is given by:

$$E_{\mathrm{x}} = \frac{RT}{z_{\mathrm{x}} F} \ln \left(\frac{[\mathrm{x}]_{\mathrm{e}}}{[\mathrm{x}]_{\mathrm{i}}} \right) \tag{3.2}$$

where E_{x} is the Nernst potential (in volts), R is the gas constant (8.314 J/(mol K)), T is the absolute temperature (in Kelvin), z_{x} is the charge number of the ion x, F is the Faraday constant (96485 C/mol), $[\mathrm{x}]_{\mathrm{e}}$ is the extracellular concentration of the ion, and $[\mathrm{x}]_{\mathrm{i}}$ is the intracellular concentration of the ion. In the Hodgkin and Huxley model, there are three ionic currents, I_{Na} for the sodium ions, I_{K} for the potassium ions and I_{L} for the leakage current from unspecified ions. As the conductances are arranged in parallel, it is possible to represent I_{ion} as the sum of the ionic currents:

$$I_{\mathrm{ion}} = I_{\mathrm{Na}} + I_{\mathrm{K}} + I_{\mathrm{L}} \tag{3.3}$$

If I_{ion} is placed in parallel to the capacitor, then the current flow through the membrane I_{m} can be defined as a partial differential equation as a function of time and voltage:

$$I_{\mathrm{m}} = C_{\mathrm{m}} \frac{\partial V_{\mathrm{m}}}{\partial t} + I_{\mathrm{ion}} \tag{3.4}$$

If the changes of the transmembrane potential are represented as a function of time, the action potential of a single cell can be calculated by solving:

$$\frac{dV_{\mathrm{m}}}{dt} = -\frac{I_{\mathrm{ion}} + I_{\mathrm{stim}}}{C_{\mathrm{m}}} \tag{3.5}$$

where I_{stim} represents an external stimulation current required for the cell to reach its threshold potential. The Hodgkin and Huxley model does not have an analytical solution, therefore numerical methods are required to find an approximate solution.

3.1.1 The Courtemanche Cellular Model

The Courtemanche *et al.* mathematical model represents the action potential of human atrial cardiomyocytes [51]. The model is based on the the guinea pig ventricular model of Luo and Rudy [197] with most of the currents adapted from human experimental data [54]. The Courtemanche *et al.* model incorporates multiple ion currents and pumps, and the sarcoplasmic reticulum (SR) is divided into two compartments to account for intracellular calcium uptake, in the network sarcoplasmic reticulum (NSR) and release in the junctional sarcoplasmic reticulum (JSR). Figure 3.2 illustrates the Courtemanche *et al.* atrial cellular model with ionic currents, pumps and exchangers. The action potential of the Courtemanche *et al.* model exhibits a pronounced spike and dome [54]. Multiple ion currents in the

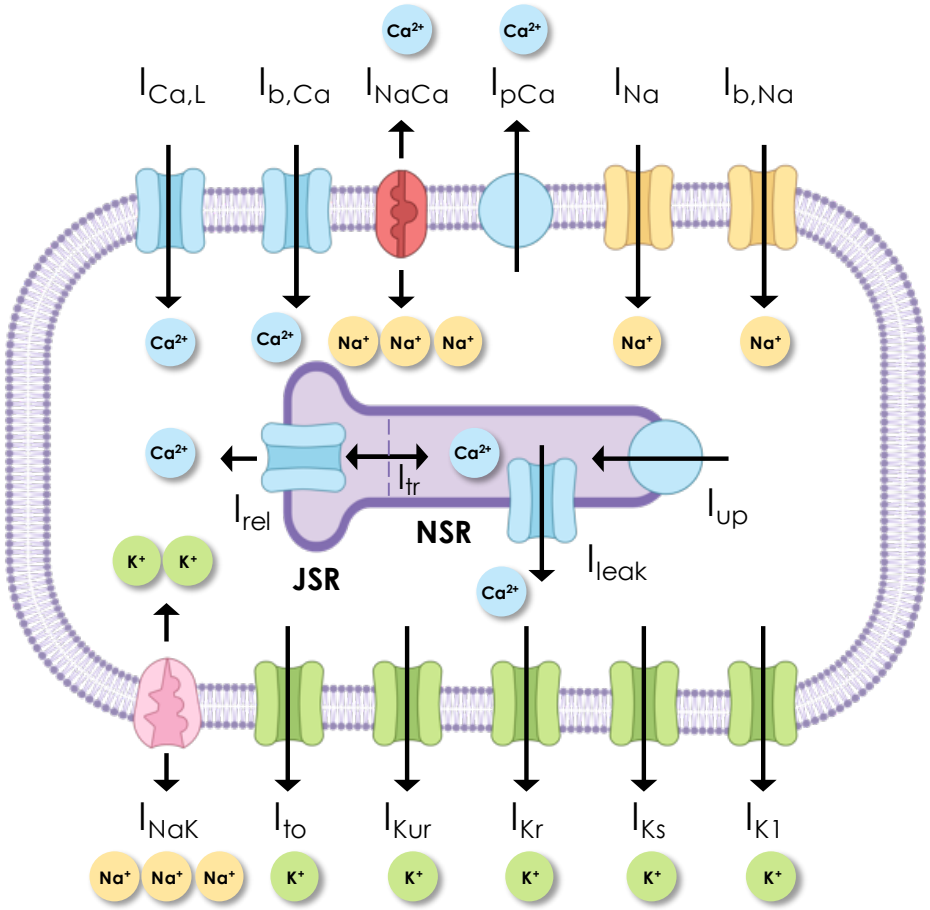

Figure 3.2: Schematic representation of the Courtemanche *et al.* model with currents (arrows), pumps, and exchangers. Arrows show the direction of the current flow. JSR: junctional sarcoplasmic reticulum, NSR: network sarcoplasmic reticulum. Inspired by [51]. Created with Biorender under academic license.

Courtemanche *et al.* model are responsible for its characteristic action potential morphology. However, as shown in Figure 3.3, the action potential duration of the Courtemanche *et al.* model is mainly defined by reduction in the maximum conductances of the L-type Ca^{2+} current I_{CaL}, and the inward rectifier K^+ current I_{K1}.

3.2 Modeling of Tissue Electrophysiology

Models of cardiac tissue electrophysiology are based on the reaction-diffusion processes, where the reaction process is associated with the cellular action potential, and the diffusion process reflects the flow of current between cells [198]. At the macroscopic scale, cardiac tissue is often described as a *functional syncytium*. A functional syncytium refers to a group of cells that are interconnected and function as a single unit, allowing coordinated electrical activity. Cardiac myocytes are electrically coupled via gap junctions, enabling the propagation of depolarisation and repolarisation waves [198]. In contrast to discrete electrophysiology models, which explicitly represent individual cardiac cells [199], continuous models conceptualize cardiac tissue as a functional syncytium.

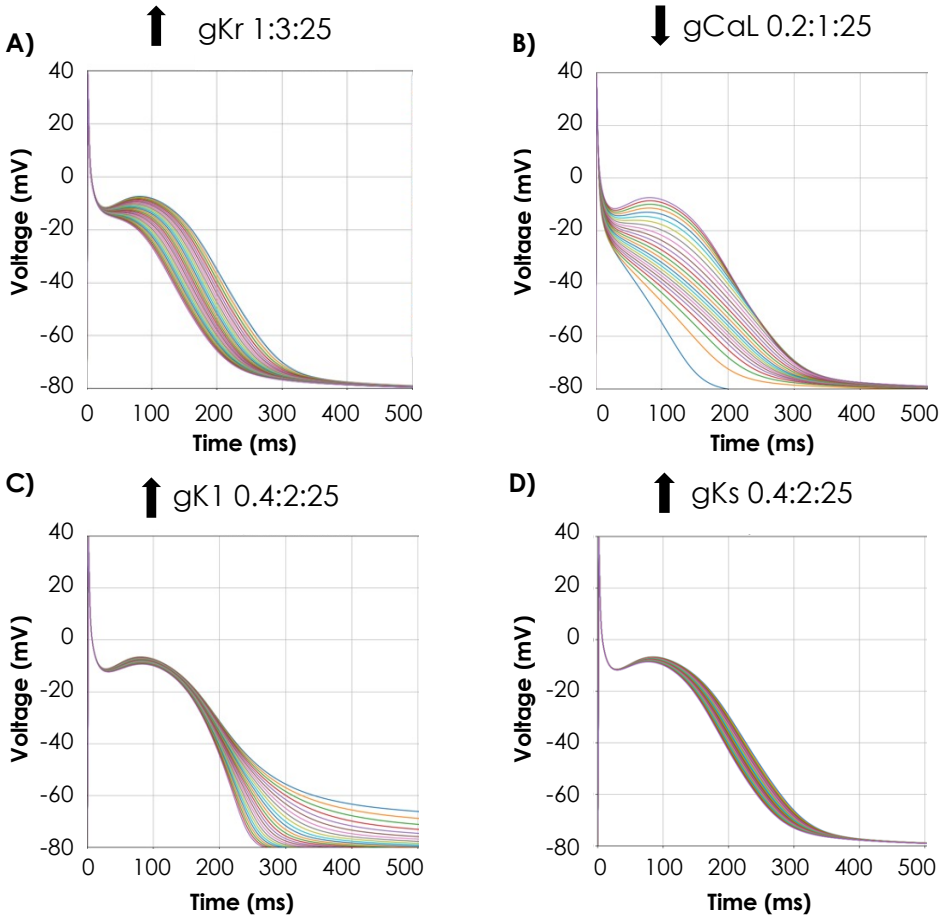

Figure 3.3: Changes of different ionic conductances of the Courtemanche *et al.* model and their impact on action potential duration. The numbers next to the conductance represent the minimum and maximum multiplying factors and the number of samples. The arrows indicate either increase (up) or decrease (down) of the scaling factors.

3.2.1 Bidomain Model

The bidomain model represents cardiac tissue as a syncytium composed of intracellular and extracellular domains, separated by the cell membrane. The mathematical derivation of the bidomain model is based on the principles of current flow, electrical potential distribution, and the conservation of charge and current [198]. In the bidomain model, each domain is described based on a generalized version of Ohm's law, which relates the current density $\mathbf{J}$ to the electric field $\mathbf{E}$, through the conductivity tensor $\mathbf{G}$, where cardiac sources are represented by impressed currents $\mathbf{J}^{imp}$ [200]. The total current density $\mathbf{J}$ is given by:

$$\mathbf{J} = \mathbf{G}\,\mathbf{E} + \mathbf{J}^{imp}. \tag{3.6}$$

The electrical field $\mathbf{E}$ can be expressed as a potential gradient:

$$\mathbf{E} = -\nabla\phi, \tag{3.7}$$

where ϕ denotes the potential. Substituting $\mathbf{E}$ in equation 3.6 we obtain:

$$\mathbf{J} = -\mathbf{G}\,\nabla\phi + \mathbf{J}^{imp}. \tag{3.8}$$

Therefore, for each domain we have:

$$\mathbf{J}_\mathrm{i} = -\mathbf{G}_\mathrm{i}\,\nabla\phi_\mathrm{i} + \mathbf{J}_\mathrm{i}^{imp}, \tag{3.9}$$

$$\mathbf{J}_\mathrm{e} = -\mathbf{G}_\mathrm{e}\,\nabla\phi_\mathrm{e} + \mathbf{J}_\mathrm{e}^{imp}, \tag{3.10}$$

where $\mathbf{J}_\mathrm{i}$ and $\mathbf{J}_\mathrm{e}$ are the intracellular and extracellular current densities ($\mathrm{A\,m^{-2}}$), $\mathbf{G}_\mathrm{i}$ and $\mathbf{G}_\mathrm{e}$ the intracellular and extracellular conductivity tensors ($\mathrm{S\,m^{-1}}$), $\mathbf{J}_\mathrm{i}^{imp}$ and + $\mathbf{J}_\mathrm{e}^{imp}$ are the intracellular and extracellular impressed current densities, and ϕ_e and ϕ_i are the electrical potential ($\mathrm{V\,m^{-1}}$) in the intracellular and extracellular spaces, respectively [200]. The conductivity tensors are determined by the anisotropy of the cardiac tissue and the tissue conductivity [198]. Expressing the divergence of the current densities $\mathbf{J}_\mathrm{i}$ and $\mathbf{J}_\mathrm{e}$ in terms of transmembrane current per unit volume I_m ($\mathrm{A\,m^{-3}}$) we obtain:

$$\nabla\cdot\mathbf{J}_\mathrm{i} = -I_\mathrm{m}, \tag{3.11}$$

$$\nabla\cdot\mathbf{J}_\mathrm{e} = I_\mathrm{m}. \tag{3.12}$$

By considering current and charge conservation laws, and assuming that only sources associated with the membrane exist in the intra- and extracellular domains, we can express divergence equations as:

$$\nabla\cdot(\mathbf{J}_\mathrm{i} + \mathbf{J}_\mathrm{e}) = 0, \tag{3.13}$$

$$-\nabla \mathbf{J}_{\mathrm{i}} = \nabla \mathbf{J}_{\mathrm{e}} = I_{\mathrm{m}}, \tag{3.14}$$

In addition, the transmembrane current I_{m} can be expressed in terms of the ionic current I_{ion}, resulting from the flow through all ion channels:

$$I_{\mathrm{m}} = \beta_{\mathrm{m}} \left(C_{\mathrm{m}} \frac{\partial V_{\mathrm{m}}}{\partial t} + I_{\mathrm{ion}} \right). \tag{3.15}$$

Here, β_{m} is the membrane surface-to-volume ratio of a cardiac cell (m^{-1}), C_{m} is the membrane capacitance ($\mathrm{F\,m}^{-2}$) and V_{m} is the transmembrane voltage (V), given by:

$$V_{\mathrm{m}} = \phi_{\mathrm{i}} - \phi_{\mathrm{e}}. \tag{3.16}$$

Combining equation 3.16 with equations 3.14 and 3.15 and casting the equations with V_{m} and ϕ_{e} as the independent variables we obtain:

$$\nabla \cdot \mathbf{G}_{\mathrm{i}} \left(\nabla V_{\mathrm{m}} + \nabla \phi_{\mathrm{e}} \right) = \beta_{\mathrm{m}} I_{\mathrm{m}}, \tag{3.17}$$

$$\nabla \cdot \left((\mathbf{G}_{\mathrm{i}} + \mathbf{G}_{\mathrm{e}}) \nabla \phi_{\mathrm{e}} \right) = -\nabla \cdot \mathbf{G}_{\mathrm{i}} \nabla V_{\mathrm{m}}. \tag{3.18}$$

The Bidomain model can be expressed as two partial differential equations. Equation 3.17 is a parabolic equation that describes the reaction-diffusion equation in terms of the transmembrane voltage, while equation 3.18 is an elliptic equation. If we assume that there is no current flowing from the extracellular space to the adjacent spaces, a Neuman boundary condition can be imposed on the boundary Γ:

$$\Gamma : \mathbf{n} \cdot (\mathbf{G_i} \nabla \phi_{\mathbf{i}}) = \mathbf{n} \cdot (\mathbf{G_i} \nabla (V_m + \phi_e)) = 0, \tag{3.19}$$

$$\Gamma : \mathbf{n} \cdot (\mathbf{G_e} \nabla \phi_{\mathbf{e}}) = 0, \tag{3.20}$$

where $\mathbf{n}$ is the outward normal to the boundary Γ. Table 3.1 provides common ranges used for the parametrization of the bidomain tissue model.

3.2.2 Monodomain Model

The bidomain model can be simplified by assuming that the intracellular conductivity tensor $\mathbf{G}_{\mathrm{i}}$ is proportional to the extracellular conductivity tensor $\mathbf{G}_{\mathrm{e}}$, meaning that the anisotropy ratios in both spaces are the same:

$$\mathbf{G}_{\mathrm{e}} = \lambda \mathbf{G}_{\mathrm{i}}, \tag{3.21}$$

where λ is the scalar ratio between intra- and extracellular conductivities σ_{i} and σ_{e}. The monodomain conductivity tensor $\mathbf{G}$ is half of the harmonic mean between intracellular and extracellular conductivities [37].

$$\mathbf{G} = \mathbf{G}_{\mathrm{i}} \mathbf{G}_{\mathrm{e}} (\mathbf{G}_{\mathrm{i}} + \mathbf{G}_{\mathrm{e}})^{-1}. \tag{3.22}$$

Parameter	Range	Units	Reference
$\mathbf{G}_{\text{il}}$	0.17 – 0.45	(S m^{-1})	[201]
$\mathbf{G}_{\text{el}}$	0.12 – 0.62	(S m^{-1})	[201]
$\mathbf{G}_{\text{it}}$	0.019 – 0.06	(S m^{-1})	[201]
$\mathbf{G}_{\text{et}}$	0.08 – 1.74	(S m^{-1})	[201]
β	2400 – 8900	(cm^{-1})	[202]
β	1000 – 5000	(cm^{-1})	[203]
C_{m}	1 – 10	($\mu\text{F cm}^{-2}$)	[198]

Table 3.1: Parameter ranges for the bidomain tissue model obtained from experimental data presented in Clayton *et al.* [198]. For further reference details, the reader is referred to the original publication [198]. $\mathbf{G}_{\text{il}}$: intracellular longitudinal conductivity, $\mathbf{G}_{\text{el}}$: extracellular longitudinal conductivity, $\mathbf{G}_{\text{it}}$: intracellular transversal conductivity, $\mathbf{G}_{\text{et}}$: extracellular transversal conductivity, β: surface-to-volume ratio, C_{m}: cellular membrane capacitance.

If we define the monodomain conductivity tensor $\mathbf{G}$ in terms of the intracellular conductivity, we obtain:

$$\mathbf{G} = \frac{\lambda}{1+\lambda}\mathbf{G}_{\text{i}}. \tag{3.23}$$

Substituting equation 3.23 into equation 3.17 yields:

$$\nabla \cdot \frac{\lambda}{1+\lambda}\,\mathbf{G}_{\text{i}} \nabla V_{\text{m}} = \beta_{\text{m}} I_{\text{m}}, \tag{3.24}$$

$$\nabla \cdot (\mathbf{G}\nabla V_{\text{m}}) = \beta_{\text{m}} I_{\text{m}}, \tag{3.25}$$

where equation 3.25 is the monodomain equation. If we define a no-flux boundary condition, the monodomain equation can be written as:

$$\Gamma : \mathbf{n} \cdot (\mathbf{G}\nabla V_{\text{m}}) = 0, \tag{3.26}$$

$$\nabla \cdot (\mathbf{G}\nabla V_{\text{m}}) = \beta \left(C_{\text{m}} \frac{\partial V_{\text{m}}}{\partial t} + I_{\text{ion}} \right), \tag{3.27}$$

$$\frac{\partial V_{\text{m}}}{\partial t} = \nabla \cdot \mathbf{D}\nabla V_{\text{m}} - \frac{I_{\text{ion}}}{C_{\text{m}}}, \tag{3.28}$$

where $\mathbf{D}$ ($\text{m}^2\,\text{s}^{-1}$) is the diffusion tensor. The monodomain equation, consisting of a single partial differential equation (PDE), is computationally less expensive than the bidomain solution. Numerous studies have compared bidomain and monodomain models of cardiac electrophysiology, revealing similarities in action potential patterns and spiral wave trajectories [204, 205]. The monodomain assumption of equal anisotropy generally holds, except in scenarios where extracellular fields are imposed, as in defibrillation studies, where the bidomain model is recommended [206].

3.3 Forward Problem of Electrocardiography

The forward problem of electrocardiography consists on the calculation of the electrical fields on the body surface coming from sources in the heart. A *cardiac source* refers to the electrical activation of cardiac cells. To compute the forward problem, the electrical activity of the heart can be modeled as a distribution of current dipole with the body having properties of a volume conductor. The equations governing the electrical potential in the torso are named after the Scottish mathematician James Clerk Maxwell. The solutions to these equations are approximated using the boundary element method (BEM) for an electrically isotropic medium or using the finite element method (FEM) when anisotropic features are required. Each electrocardiography recording consists of the projection of the current dipole into the measuring axis, also referred to as *lead*. A *volume conductor* consists of a 3D conducting medium. A *current dipole* is a pair of electrically opposed charges q with equal magnitude, separated by a distance d. A dipole generates an electrical field, which allows currents to flow through the conducting medium. Therefore, the electrical activity in the heart can be measured on the body surface as the potential difference generated by the electrical field.

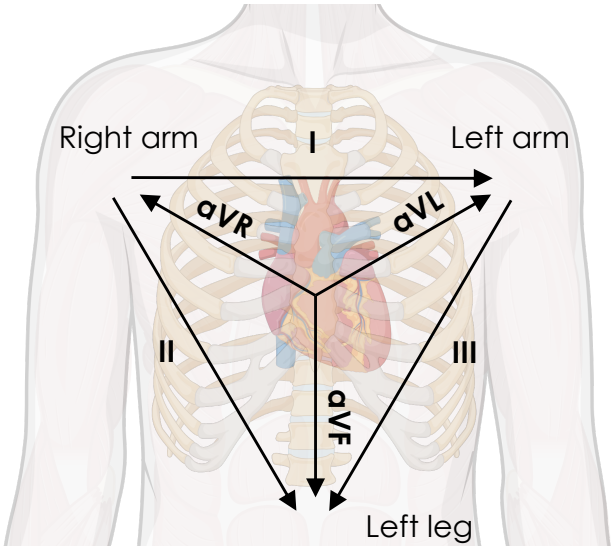

Figure 3.4: Einthoven Triangle. Bipolar leads are calculated as the potential difference measured between two points on the body surface. Created with Biorender under academic license.

Three bipolar leads (I, II, and III) and three augmented leads (aVR, aVL, and aVF) can be calculated as follows, where LA stands for left arm, RA for right arm, and LL for left leg:

$$
\begin{aligned}
\mathrm{I} &= \phi_{\mathrm{LA}} - \phi_{\mathrm{RA}} \\
\mathrm{II} &= \phi_{\mathrm{LL}} - \phi_{\mathrm{RA}} \\
\mathrm{III} &= \phi_{\mathrm{LL}} - \phi_{\mathrm{LA}} \\
\mathrm{aVR} &= \phi_{\mathrm{RA}} - \frac{\phi_{\mathrm{LA}} + \phi_{\mathrm{LL}}}{2} \\
\mathrm{aVL} &= \phi_{\mathrm{LA}} - \frac{\phi_{\mathrm{RA}} + \phi_{\mathrm{LL}}}{2} \\
\mathrm{aVF} &= \phi_{\mathrm{LL}} - \frac{\phi_{\mathrm{LA}} + \phi_{\mathrm{RA}}}{2}
\end{aligned}
$$

Augustus D. Waller was a British physiologist and is considered to be the father of electrocardiography. He was the first to demonstrate the possibility to non-invasively measuring the electrical activity of the heart in intact animals and in humans, and he became the first to coin the term *electrocardiogram* (ECG). He was renowned for his experiments with his bulldog Jimmie standing in buckets of saline, serving as electrodes, and the use of a Lipmann capillary electrometer, where the pulsation of a mercury column help record the ECG [207]. In 1887 he published the first human ECG. Years later in 1912, a Dutch physiologist who attended Waller's demonstrations, Willem Einthoven improved the recording method of Waller with the invention of the string galvanometer. The name of the 5 deflections in the ECG, namely P, Q, R, S and T, were identified by Einthoven (Figure 3.5). The P-wave corresponds to the depolarization of the atria, while the PR interval accounts for the atrioventricular (AV) delay from the AV node. The QRS complex depicts the electrical ventricular depolarization. Finally, the T wave corresponds to the ventricular repolarisation.

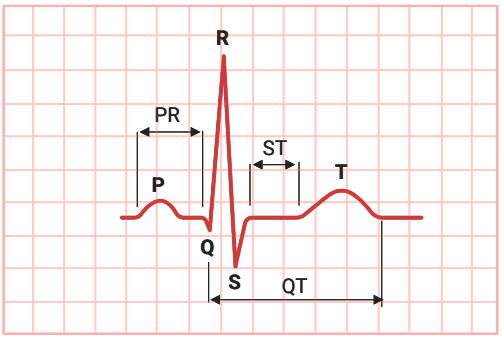

Figure 3.5: A representative electrocardiographic trace showing the five deflection waves observed during sinus rhythm. P, Q, R, S, and T waves; three segments and three intervals: PR, QT and ST. Segment corresponds to the isopotential line, while intervals include the beginning of the wave deflection. Created with Biorender under academic license.

3.4 Conduction Velocity

Conduction velocity (CV) is an important electrophysiological property that corresponds to the time needed by the electrical depolarization wave to spread throughout the cardiac tissue [148]. Changes in CV are related to alterations in the cardiac muscle; therefore, when creating patient-specific computer models, it is important to tune CV to more accurately represent electrical propagation. Currently, it is not possible to directly measure CV, so its value must be subrogated from other clinical measurements such as the P-wave duration from the body surface electrocardiogram (ECG) or local activation times (LAT) maps obtained from either non-invasive electrocardiographic imaging (ECGI) or from invasive electrograms (EGM) from electro-anatomical mapping system (EAMS). In the following part, a brief summary describes how CV can be tuned using P-wave duration and LAT data, as detailed in [33, 37].

3.4.1 Personalization of Global Conduction Velocity Using P-wave Duration

The relationship between conduction velocity $\mathbf{V}$ and the conductivity σ in the monodomain equation is given by:

$$\sigma = a\,\mathbf{V}^2 + b\,\mathbf{V} + c. \tag{3.29}$$

Assuming that the quadratic term dominates, equation 3.29 can be simplified as:

$$\begin{aligned} \sigma &\approx \mathbf{V}^2 \\ \sqrt{\sigma} &\approx \mathbf{V} \end{aligned} \tag{3.30}$$

Global conduction velocity in the atria can be defined as the ratio between atrial size $\mathbf{S}$ and the total atrial depolarization time t_{D}:

$$\mathbf{V} = \frac{S}{t_{\mathrm{D}}} \tag{3.31}$$

In addition, t_{D} can be inferred from the duration of the P-wave (t_{real}) in the body surface ECG or from the latest activation time in the ECGI or EGM activation map. Considering the above, the latest simulated atrial activation time (t_{sim}) is defined as:

$$t_{\mathrm{sim}} \approx t_{\mathrm{real}} \tag{3.32}$$

The simulated monodomain conductivity σ_{sim} of the patient-specific model can be iteratively tuned until the simulated atrial depolarization time t_{sim}, reaches approximately the same value as the real depolarization time. Meaning that equation 3.29 can be written as:

$$\frac{\sigma_{\mathrm{real}}}{\sigma_{\mathrm{sim}}} = \frac{\mathbf{V}_{\mathrm{real}}^2 + b\,\mathbf{V}_{\mathrm{real}} + c}{\mathbf{V}_{\mathrm{sim}}^2 + b\,\mathbf{V}_{\mathrm{sim}} + c} \tag{3.33}$$

Simplifying equation 3.33:

$$\frac{\sigma_{\text{real}}}{\sigma_{\text{sim}}} \approx \frac{\mathbf{V}_{\text{real}}^2}{\mathbf{V}_{\text{sim}}^2} \tag{3.34}$$

Substituting conduction velocity as in equation 3.31 we get:

$$\frac{\sigma_{\text{real}}}{\sigma_{\text{sim}}} \approx \frac{\left(\frac{\mathbf{S}}{t_{\text{real}}}\right)^2}{\left(\frac{\mathbf{S}}{t_{\text{sim}}}\right)^2} \tag{3.35}$$

Solving for σ_{real}, we obtain:

$$\sigma_{\text{real}} \approx \sigma_{\text{sim}} \left(\frac{t_{\text{sim}}}{t_{\text{P}}}\right)^2 \tag{3.36}$$

As the real conductivity σ_{real} is unknown, the conductivities σ_{init} are initialized with an initial value and then further tuned to achieve the desired total activation from the P-wave duration:

$$\sigma_{\text{sim}} \approx \sigma_{\text{init}} \left(\frac{t_{\text{sim}}}{t_{\text{P}}}\right)^2 \tag{3.37}$$

Using the electrophysiology simulator openCARP, the initial conductivities σ_{init} can be obtained given an input CV. The conductivities are obtained by calculating the electrical propagation using a linear core conductor model, as described in [37]. In the terminal, using the *tuneCV* function and given the following simulation parameters, the intracellular and extracellular monodomain conductivities can be obtained:

```
$ tuneCV --velocity 0.7 --resolution 400 --model Courtemanche
--dt 20 --tol 0.001 --lumping True --sourceModel monodomain
--surf True --converge True --log tuneCV.log --np 2
```

3.4.2 Personalization of Local Conduction Velocity Using Local Activation Times

The method described earlier can be used to globally tune the CV based on a single measurement of either the P-wave duration or the latest activation from local activation time (LAT) maps. However, it may be desired to not only account for global activation but also to tune the conductivities so that the pattern of propagation is also personalized. This can be achieved by adapting the method described before and defining isochrones of activation in the LAT map. The approach described in this section iteratively adjusts the conductivity of each element to reduce the root mean squared error (RMSE) between the simulated LAT and the clinical LAT as described in [49].

Firstly, to disregard artifacts, the activation LAT sequence is verified by leveraging a priori knowledge about the expanding wavefront. The set P of points x in the LAT map are

divided into **N** activation bands Γ_i starting at the earliest activation point (EAP) up to the latest activation point (LAP), with a temporal resolution $dt = 5$ ms:

$$\Gamma_i = \{x \in P \mid \mathrm{LAT}(x_{\mathrm{EAP}}) + dt \cdot i < \mathrm{LAT}(x) \leq \mathrm{LAT}(x_{\mathrm{EAP}}) + dt \cdot (i+1)\} \tag{3.38}$$

Where x_{EAP} is defined as the 2.5th percentile of the LAT distribution and the x_{LAP} as the 97.5th percentile. All points x with an LAT value higher that the x_{LAP} are given the time of the LAP, and the points having an earliest activation will have the time of the x_{EAP}. If points are at >1 mm away from the current band, then they are set as wrong annotation and not used in the iterative tuning process. These points will receive the mean conductivity value of the band boundary.

Finally, the LAT map is divided into **M** activation bands γ_i from the EAP to the LAP with steps of 30 ms. The conductivities of the elements in each active band γ are tuned to minimize the RMSE between the simulated and the clinical LAT. Adapting equation 3.37 we can obtain:

$$\sigma_{\mathrm{sim}} \approx \sigma_{\mathrm{init}} \left(\frac{\mathrm{LAT}_{\mathrm{sim}}}{\mathrm{LAT}_{\mathrm{clin}}} \right)^2 \tag{3.39}$$

3.5 Machine Learning

Machine learning (ML) is a branch of artificial intelligence focused on the creation of algorithms and statistical models that allow computers to learn from data and make predictions or judgments [105].

3.5.1 Random Forest

Random forests (RF) are supervised ML algorithms used for regression or classification tasks. RF models perform a classification task when the target variable is categorical, while regression is performed if the target variable has a continuous value. A tree with M leaves divides the feature space into M numbers, where the leaves are restricted to $1 \leq m \leq M$. The prediction function of a tree is defined as:

$$f(x) = \sum_{m=1}^{M} c_m I(x, R_m). \tag{3.40}$$

Where R_{m} is a region in the feature space corresponding to leaf m, c_m is a constant for region m which corresponds to the ratio of the response variables of samples in the region R_{m}, and I is the indicator function (with $I = 1$ if $x \in R_m$). The prediction of a forest is the average of the predictions of all trees:

$$F(x) = \frac{1}{J} \sum_{j=1}^{J} f_j(x) \tag{3.41}$$

3.5.2 Model Explainability

In many ML applications, it is not only desired to have a model with good predictive performance, *accuracy*, but also can be desired to understand why the model makes certain predictions, *interpretability*. A correct interpretation of the output of a model can increase user trust, and enhance the understanding of the phenomena or process being modelled [208]. The concept of interpreting the importance of input features on the output of the model is known as *explainability*. In other words, consists of understanding the black box of the model and having a white box, as shown in Figure 3.6:

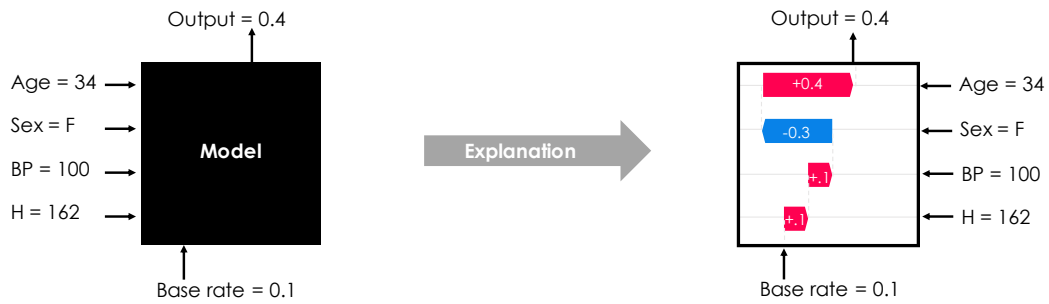

Figure 3.6: Example demonstrating the concept of explainability. The contribution of each input features on the model outcome is shown on the right. Inspired from [209].

RF algorithms are formed by many decision trees and each tree is trained using randomly selected features during the decision process. This implies that a tree can have multiple branches of thousands of nodes, therefore an analysis or the definition of an explanatory model is not always possible [208]. Feature importance analysis can help determine which of the input features had a higher contribution to the decision outcome. Two methods for defining feature importance are *permutation*, by permuting each value of each feature and checking model performance, or *impurity* computing, where the amount of variance or entropy/Gini coefficient is used when each feature is removed. The Gini coefficient represents the likelihood of misidentifying a randomly selected element within a dataset, whereas entropy quantifies the level of uncertainty or randomness present in the dataset. SHAP (SHapley Additive exPlanations) is an approach used to explain the output of ML models. SHAP is derived from game theory which links the input model features to the concept of players in a game and the model function to the rules of the game [208]. The SHAP algorithm assigns an importance value to each feature for a specific prediction.

PART II

EFFECTS OF PERSONALIZATION OF ATRIAL COMPUTER MODELS ON ARRHYTHMIA VULNERABILITY

Chapter 4

Personalization of Atrial Anatomy

Impact of the Incorporation of the Right Atrium on Arrhythmia Vulnerability

For many years, atrial fibrillation (AF) has been regarded as an arrhythmia primarily affecting the left atrium (LA). In the development of patient-specific computer models, it remains unclear whether LA-only models are adequate for informing AF treatment. Specifically, the impact of incorporating the right atrium (RA) on arrhythmia vulnerability needs further investigation. This chapter addresses this concern by comparing monoatrial and biatrial models on their impact on arrhythmia vulnerability, while also debating the adequacy of monoatrial models for the assessment of inducibility. The main objective is to quantify the impact of incorporating the RA in the development of AF *in silico*.

The content of this chapter is taken and adapted from a paper that has been published open access under Creative Commons CC-BY license in Heart Rhythm [210]. Most passages have been quoted verbatim from the publication.

4.1 Introduction

The role of the RA in AF has long been overlooked. Multiple studies have examined clinical conditions associated with AF, such as atrial enlargement, fibrosis extent, electrical remodeling, and wall thickening, but have been mainly concentrated on the LA [184, 211–213]. AF research predominantly focuses on the LA due to two key paradigms: Firstly, the well-established view that AF onset is primarily triggered by activity originating in the pulmonary veins (PVs) of the LA [214]. Secondly, comorbidities linked to AF, such as hypertension, valvular disease, and heart failure, primarily impact the left side of the heart, contributing to increased mortality and reduced quality of life. Thus AF research continues to focus mostly on the LA, and as a consequence, the role of RA in AF is barely understood.

With the advent of personalized medicine, patient-specific computer models of the atria are enhancing our understanding of intricate interactions during AF and have already been used to identify ablation targets, tailor ablation strategies, and predict recurrence in AF patients [215–218]. Nevertheless, those methodologies did not specifically focus on the role of the RA, with some excluding RA tissue and others neglecting the assessment of AF induction or maintenance from RA sources. Computer models of the atria can aid in assessing how the RA influences arrhythmia vulnerability and also in studying the role of RA drivers in the induction of AF, both aspects difficult to assess clinically and experimentally. This work assesses the "Creative Concept" of incorporating the RA in computational arrhythmia studies based on 1398 virtual pacing sequences in 8 biatrial and 8 monoatrial patient-specific models under 3 different substrate conditions, resulting in a total of 48 distinct model configurations.

4.2 Methods

A general overview of the study methodology is provided in Figure 4.1.

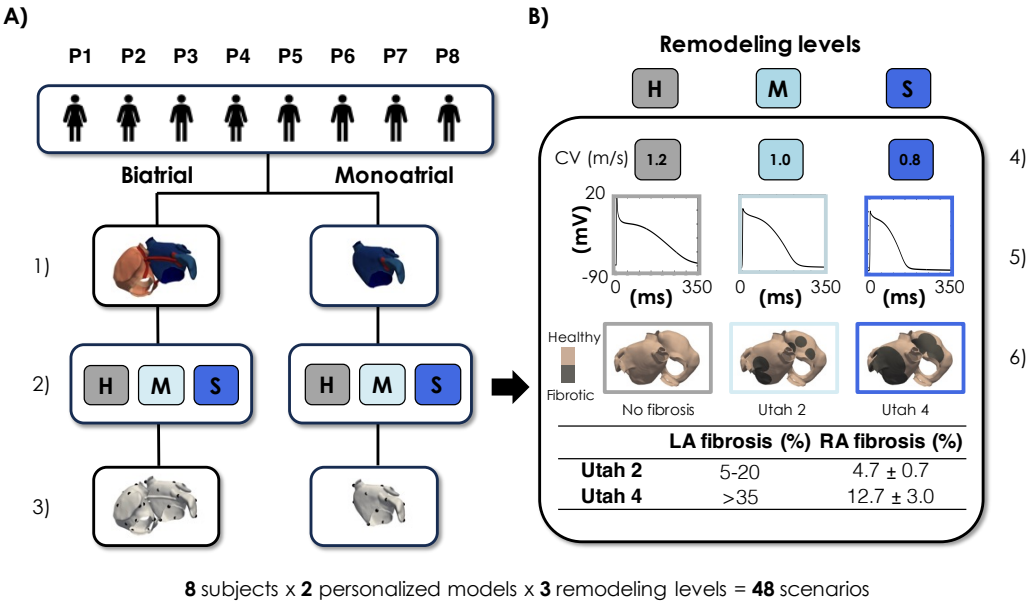

Figure 4.1: Study methodology. A) virtual cohort generation considering biatrial and monoatrial configurations (1) with 3 remodeling levels (2) to assess arrhythmia vulnerability (3). B) fibrotic substrate modeling approach considering changes in conduction velocity (CV) (4), electrical remodeling (5), and fibrosis extent(6) (H: healthy, M: mild, S: severe).

4.2.1 Patient-specific Anatomical Modeling

Imaging data from 8 subjects (P1-P8) were obtained as described in [33] and used to generate the biatrial personalized anatomical models. Subjects provided written informed consent and the study protocol was reviewed and approved by the ethical committee of Guy's Hospital, London, UK, and University Hospital Heidelberg, Heidelberg, Germany. The research reported in this article adhered to the Helsinki Declaration guidelines. The cohort characteristics are described in Table 4.1. Patient-specific bilayer models were generated following the methodology described by Azzolin *et al.* [49]. For each subject, we created two models: a *monoatrial* with only the LA, and a *biatrial* with both the RA and LA.

Table 4.1: Clinical characteristics of subjects for the generation of biatrial models. F: Female, M: Male, HR: Heart rate, PWd: P-wave duration, RA: right atrium, LA: left atrium, Ctl: control; LQT: long-QT syndrome, AF: atrial fibrillation.

	P1	**P2**	**P3**	**P4**	**P5**	**S6**	**P7**	**P8**
Sex	F	F	M	M	M	M	M	M
Diagnosis	Ctl	LQT2	Ctl	LQT1	Ctl	Ctl	AF	Ctl
HR (1/min)	81	76	69	62	70	53	62	86
PWd (ms)	95	95	107	91	103	97	176	99
RA blood volume (ml)	98	52	117	88	132	99	155	72
LA blood volume (ml)	55	27	63	79	81	87	136	53
RA myocardium (mm^3)	26	12	27	38	52	21	38	36
LA myocardium (mm^3)	19	10	25	32	26	19	34	29

4.2.2 Modeling of Inter-atrial Connections

Using rule-based definitions [74], 4 interatrial connections (IAC) were added automatically to the biatrial models: 1) middle posterior bridge, 2) upper posterior bridge, 3) Bachmann bundle (BB) bridge, and 4) coronary sinus (CS) bridge. IAC were defined by creating geodesic paths on the epicardium surfaces of the RA and LA and constructing tubular structures along these paths [49, 74]. Further details on IAC modeling can be found in Figure 4.2. In the RA septum, the start point (A) of the geodesic path AB was determined as the nearest point to the centroid of the superior vena cava (SVC) ring, while the termination point (B) was the closest point to the centroid of the inferior vena cava (IVC) ring. The points at 40 % and 60 % along the geodesic path were designated as the starting points for the upper

posterior bridge (C) and the middle posterior bridge (D), respectively. We found the nearest point in the LA septum for the upper posterior bridge (E) and the middle posterior bridge (F). Tubular structures with a radius of 1.65 mm were created using the geodesic paths as an axis to finally connect the septum. For the CS bridge, an auxiliary point corresponding to the centroid of the CS ostium moved 10% towards the centroid of the tricuspid valve ring was defined. Point G is the nearest point in the RA epicardium closer to this auxiliary point. Point H is the closest point to point G on the LA surface. Finally, a tube of 1.65 mm was created along the path from point G to point H.

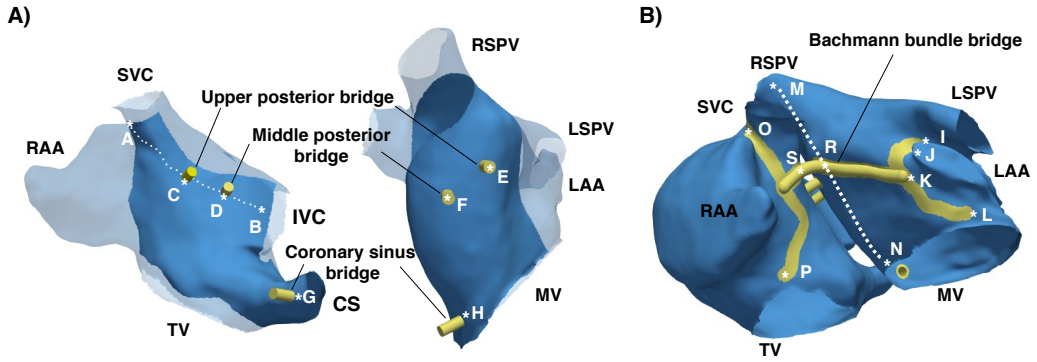

Figure 4.2: Modeling of inter-atrial connections (IAC). Four inter-atrial connections: 1) middle posterior bridge, 2) upper posterior bridge, 3) Bachmann bundle (BB), and 4) coronary sinus (CS) bridge. IAC were defined by establishing geodesic paths in the right atrium and left atrium epicardium surfaces and generating tubular structures along these paths [49, 74]. IVC: inferior vena cava, LAA: left atrial appendage, LSPV: left superior pulmonary vein, MV: mitral valve, RAA: right atrial appendage, RSPV: right superior pulmonary vein, SVC: superior vena cava, TV: tricuspid valve.

The BB is composed of three different sections: the left bundle path, the intermediate bundle bridge, and the right bundle path. For the left bundle path, 4 auxiliary points (I-L) on the LA epicardium surface surrounding the LAA to the MV were placed and connected with a geodesic line with a width of 2.3 mm around the path. For the right bundle path, two points on the RA epicardium in the SVC and TV (O, P) were placed and connected with a geodesic line with a width of 2.3 mm around the path. To generate the intermediate BB bridge, two points (M, N) in the LA surface served as a reference to generate a path used to find the midpoint R. Point S was the nearest point to point R in the RA epicardium and then connected with a geodesic path. A tube of 2.13 mm is generated following the geodesic path.

4.2.3 Electrophysiological Modeling

Cellular electrophysiology of atrial myocytes was modeled using the mathematical model of Courtemanche *et al.* (CRN) [219]. To compute electrical propagation in the human atria we solved the monodomain equation using the electrophysiology simulator openCARP [220,

221]. A carputils bundle containing the openCARP experiment, along with all associated parameters, is publicly available [222].

A) Multiplying factors to maximum ionic conductances

	H	M	S	TGF-ß1
gK1	1.00	1.50	2.00	1.00
gKs	1.00	1.50	2.00	2.00
gKr	1.00	1.30	1.60	1.00
gCaL	1.00	0.73	0.45	0.23
gKur	1.00	0.75	0.50	0.50
gto	1.00	0.68	0.35	0.35
maxIpCa	1.00	1.25	1.50	1.50
maxINaCa	1.00	1.30	1.60	1.60
gNa	1.00	1.00	1.00	0.60

B) Action potential trace for each remodeling state

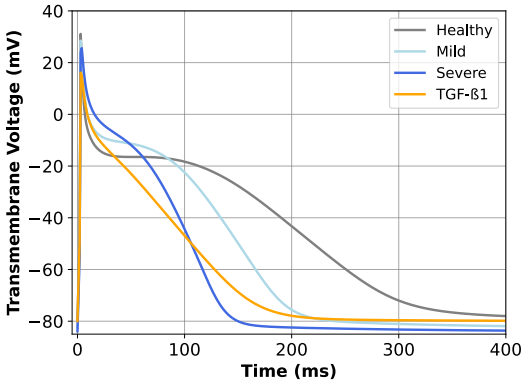

C) Action potential features for each remodeling state

	H	M	S	TGF-ß1
APD_{90} (ms)	278.20	185.29	130.10	153.05
dV/dt max (mV/ms)	77.86	81.14	78.87	65.56
Vr (mV)	-79.17	-82.40	-83.90	-79.97

Table 4.2: Atrial electrophysiology modeling. Multiplying factors applied to ionic conductances of the Courtemanche *et al.* model [219] to represent healthy (H), mild (M), and severe (S) states [223] (A). Respective action potentials (B) and features (C). APD_{90}: action potential duration at 90% repolarization, dV/dtmax: upstroke velocity, TGF-β1: transforming growth factor-β1 remodeling, V_r: resting membrane potential.

We defined 3 different levels of AF-induced remodeling, namely: healthy (H), mild (M), and severe (S) by reducing the conductance of a set of ionic channels in the CRN model as described in [223] with 0 %, 50 % and 100 % changes for H, M and S, respectively. The

maximum scaling of the ionic conductances affects the action potential in line with the changes observed in human atrial myocytes in patients suffering from persistent AF [54]. The scaling factors applied to the ionic conductances and their corresponding action potential features are detailed in Table 4.2. A mean conduction velocity (CV) of 1.0 m/s was reported in patients with persistent AF [224]. To consider the 3 remodeling states, we introduced a 20% variation in CV. The models were parameterized to yield a CV along the myocyte preferential direction of 1.2, 1.0, and 0.8 m/s for each remodeling level, respectively. Intra- and extracellular conductivities were scaled $\times 3$ for the BB and $\times 2$ for the CT and PM with respect to normal myocardium. Regional ionic heterogeneity and anisotropy ratios are detailed in Table 4.3 [33, 225].

Table 4.3: Relative values of ionic conductances of the Courtemanche *et al.* model [219] to represent regional anatomical heterogeneity and anisotropy factors [33]. BB: Bachmann bundle, CT: crista terminalis, LA: left atrium, LAA: left atrial appendage, MVR: mitral valve ring, PM: pectinate muscles, PV: pulmonary veins, RA: right atrium, RAA: right atrial appendage, TVR: tricuspid valve ring.

	gK1	gKs	gKr	gCaL	gKur	gto	gNa	Anisotropy
RA	1.00	1.00	1.00	1.00	1.00	1.00	1.00	3.75
PM	1.00	1.00	1.00	1.00	1.00	1.00	1.00	10.52
CT	1.00	1.00	1.00	1.67	1.00	1.00	1.00	6.56
BB	1.00	1.00	1.00	1.67	1.00	1.00	1.00	9.00
TVR	1.00	1.00	1.53	0.67	1.00	1.00	1.00	3.75
MVR	1.00	1.00	2.44	0.67	1.00	1.00	1.00	3.75
RAA	1.00	1.00	1.00	1.06	1.00	0.68	1.00	3.75
LAA	1.00	1.00	1.60	1.06	1.00	0.68	1.00	3.75
LA	1.00	1.00	1.60	1.00	1.00	1.00	1.00	3.75
PV	0.67	1.87	2.40	0.75	1.00	0.75	1.00	3.75

4.2.4 Fibrotic Substrate Modeling

The fibrotic substrate was modeled based on Nagel *et al.* [226], as illustrated in Figure 4.3. Fibrosis extent corresponded to Utah 2 $(5-20\,\%)$ and Utah 4 $(>35\,\%)$ stages for the M and S states, while the H state was modeled without fibrosis. The proportion of RA and LA fibrosis extent was based on the percentages reported by Akoum *et al.* [192]. To consider the multifactorial nature of fibrosis, we modeled fibrotic regions with 30% of the elements as non-conductive, with $\sigma = 10^{-7}$ S/m to account for electrical myocyte decoupling, and the rest affected by TGF-β1-induced electrical remodeling in response to cellular inflammation [227, 228].

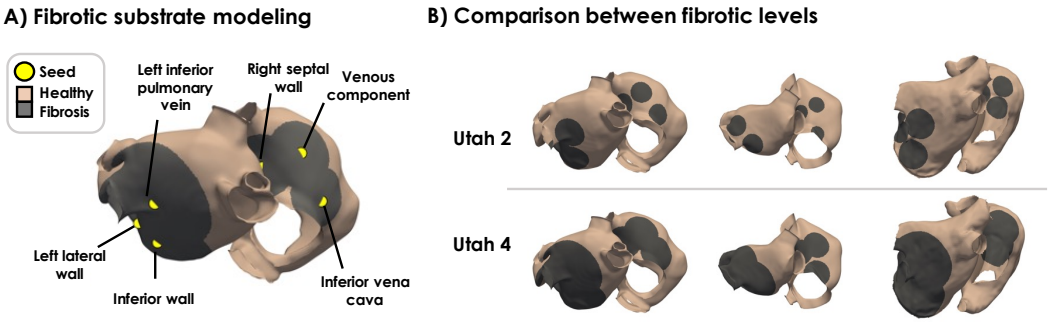

Figure 4.3: Fibrotic substrate modeling. A) A total of 6 seeds were placed in each biatrial geometry to generate fibrosis distributions corresponding to the clinical Utah stages [192]. B) Fibrosis distributions in 4 subjects in state M (top, Utah 2) and S (bottom, Utah 4).

4.2.5 Arrhythmia Vulnerability

Arrhythmia vulnerability was assessed by an S1-S2 pacing protocol [229] with 2 cm inter-point distance on the atrial surface. Stimulation points and earliest activation sites on the LA remained consistent between monoatrial and biatrial configurations. A point was classified as inducing if reentry was maintained for at least 1 s. The vulnerability ratio was defined as the number of inducing points divided by the number of stimulation points. The mean tachycardia cycle length (TCL) of the induced reentries was assessed at the stimulation site as depicted in Figure 4.4.

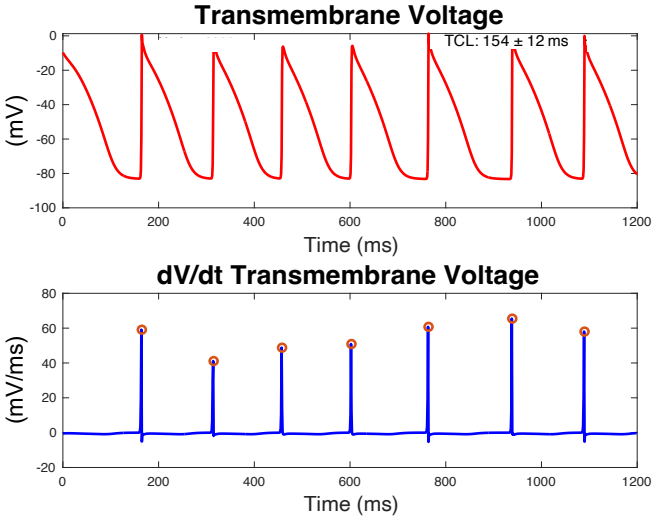

Figure 4.4: Quantification of mean tachycardia cycle length based on transmembrane voltage series. The derivative of the voltage with respect to time (dV/dt) is quantified.

Subsequently, we calculated the derivative of the voltage with respect to time (dV/dt), established a threshold of 5 mV/ms to identify activations, and calculated the mean time between activations and its standard deviation.

4.2.6 Statistical Analysis

Data are reported as mean $\pm$ SD. To evaluate statistical significance between the sample means, we conducted a two-sampled t-test. A p-value < 0.05 was considered statistically significant.

4.3 Results

The 8 biatrial anatomical models and the number of stimulation points in each chamber are shown in Figure 4.5. The amount of fibrosis for each subject in each stage is shown in Table 4.4.

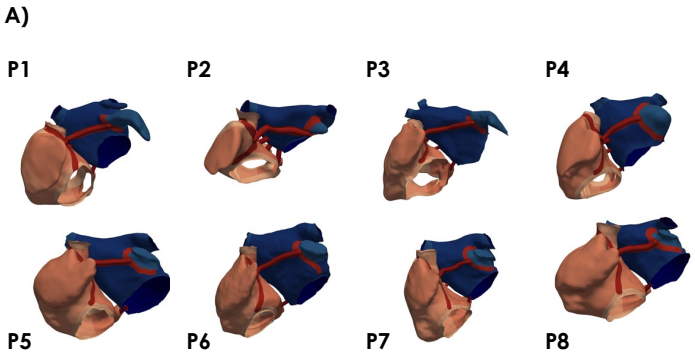

B)

Subject	LA	RA	Total
P1	14	17	31
P2	7	10	17
P3	18	24	42
P4	18	19	37
P5	24	29	53
P6	23	21	44
P7	29	32	61
P8	15	18	33

Figure 4.5: Personalized models (A) and the total number of stimulation points (B) used to assess arrhythmia vulnerability.

Table 4.4: Fibrosis percentage for each remodeling level. Fibrosis corresponds to Utah 2 $(5-20\%)$ and Utah 4 ($> 35\%$) stages for M and S states, respectively. RA: right atrium, LA: left atrium.

	P1		P2		P3		P4		P5		P6		P7		P8	
Utah stage	2	4	2	4	2	4	2	4	2	4	2	4	2	4	2	4
LA (%)	10.9	36.4	12.1	42.3	12.7	35.4	12.7	38.3	13.0	34.8	11.7	40.3	13.1	41.9	11.4	41.7
RA(%)	5.4	12.8	5.3	13.3	5.3	13.4	5.9	14.1	5.36	11.7	5.3	13.4	5.4	13.1	5.4	11.9

4.3.1 Vulnerability of the Left Atrium in Monoatrial and Biatrial Configurations

We ran 444 monoatrial simulations, from a total of 148 stimulation points $\times$ 3 remodeling states in the 8 LA models, and 954 biatrial simulations, from a total of 318 stimulation points $\times$ 3 remodeling states in the 8 biatrial models to assess arrhythmia vulnerability. The number of inducing points and the vulnerability ratio V_{LA} for each subject in each configuration are shown in Figure 4.6. A total of 79 reentry episodes were induced in the monoatrial configuration, of which 32 episodes were in the M state and 47 in the S state. No reentries were induced in the H state. In the biatrial configuration, a total of 281 reentry episodes were induced, of which 130 were induced by pacing from the LA. In the H state, only one reentry was induced by pacing from the LA anterior wall in proximity to the mitral valve in P6. The monoatrial vulnerability ratio V_{LA} among all subjects in the M and S states was 0.19 ± 0.13 and 0.31 ± 0.14, respectively. The biatrial vulnerability ratio V_{LA} between the M and S states showed minimal changes (0.41 ± 0.22 vs. 0.40 ± 0.15). Incorporating the RA increased in the mean V_{LA} vulnerability by 115.8 % in the M state and 29.0 % in the S state, as illustrated in Figure 4.7a. In the monoatrial configuration, there was a 20.0% increase in the mean TCL between states M and S (186.94 ± 13.3 vs. 224.32 ± 27.6 ms, $p < 0.001$). While in the biatrial configuration, the mean TCL of LA-induced reentries showed a 5.6% increase between the M and S states (197.24 ± 18.3 vs. 208.24 ± 34.8 ms, $p = 0.026$). Including the RA led to changes in the mean TCL of the LA-induced reentries by 5.5% ($p = 0.006$) in the M scenario and a decrease of 7.2% ($p = 0.010$) in the scenario S, as illustrated in Figure 4.7b.

Increased remodeling from M to S in the monoatrial configuration revealed 4.3 ± 2.9 new inducing points in the LA per patient, as shown in Figure 4.8a. The points became inducing when going from M to S due to rotational activity near the fibrotic regions. Deceleration of the wavefront and a shortened action potential in S enabled propagation within the fibrotic region. In contrast, in M, the faster wavefront encountered refractory tissue and failed to activate the surrounding tissue. To assess the role of the RA on LA inducibility in more detail, we evaluated changes in LA inducibility by comparing points within the LA initiating reentry with and without the RA, as shown in Figure 4.8b. The inclusion of the RA resulted in an elevated LA inducibility, uncovering 5.5 ± 3.0 inducing points in the LA biatrial scenarios that did not induce in the monoatrial configuration, as shown in Figure 4.9. IAC contributed to the increased reentry inducibility, as shown in Figure 4.10.

A) Monoatrial

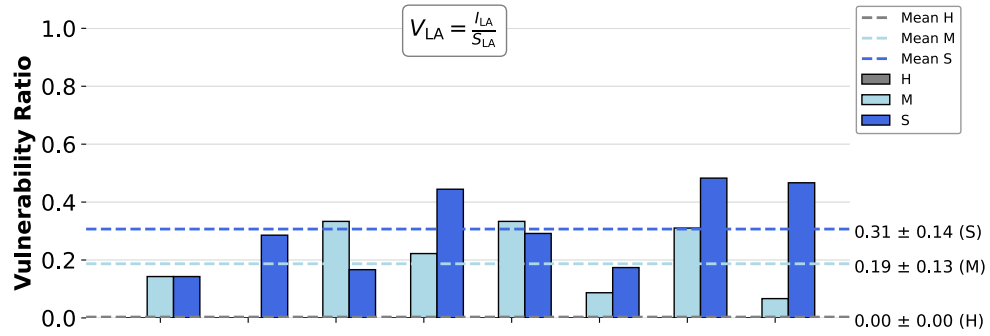

	P1	P2	P3	P4	P5	P6	P7	P8	
	LA	LA	LA	LA	LA	LA	LA	LA	**Total**
SP	14	7	18	18	24	23	29	15	**148**
I_H	0	0	0	0	0	0	0	0	**0**
I_M	2	0	6	4	8	2	9	1	**32**
I_S	2	2	3	8	7	4	14	7	**47**

B) Biatrial

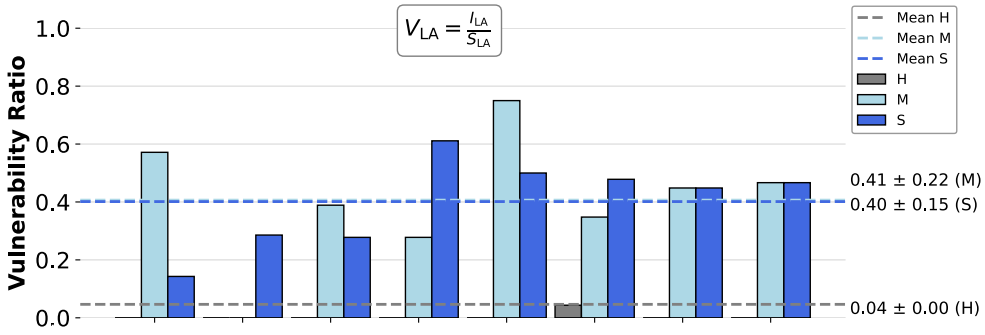

	P1		P2		P3		P4		P5		P6		P7		P8		
	LA	RA	LA	RA	LA	RA	LA	RA	LA	RA	LA	RA	LA	RA	LA	RA	**Total**
SP	14	17	7	10	18	24	18	19	24	29	23	21	29	32	15	18	**318**
I_H	0	0	0	0	0	0	0	0	0	0	1	0	0	0	0	0	**1**
I_M	8	4	0	0	7	9	5	0	18	12	8	10	13	12	7	5	**118**
I_S	2	16	2	4	5	9	11	11	12	20	11	13	13	19	7	7	**162**

Figure 4.6: Vulnerability of the left atrium (LA) in monoatrial (A) and biatrial (B) configurations. Dashed lines represent mean vulnerability ratios for each remodeling level (I_{LA}: inducing points in the LA, *SP*: stimulation points, H: healthy, M: mild, S: severe, I_H, I_M, I_S: inducing points in each remodeling level).

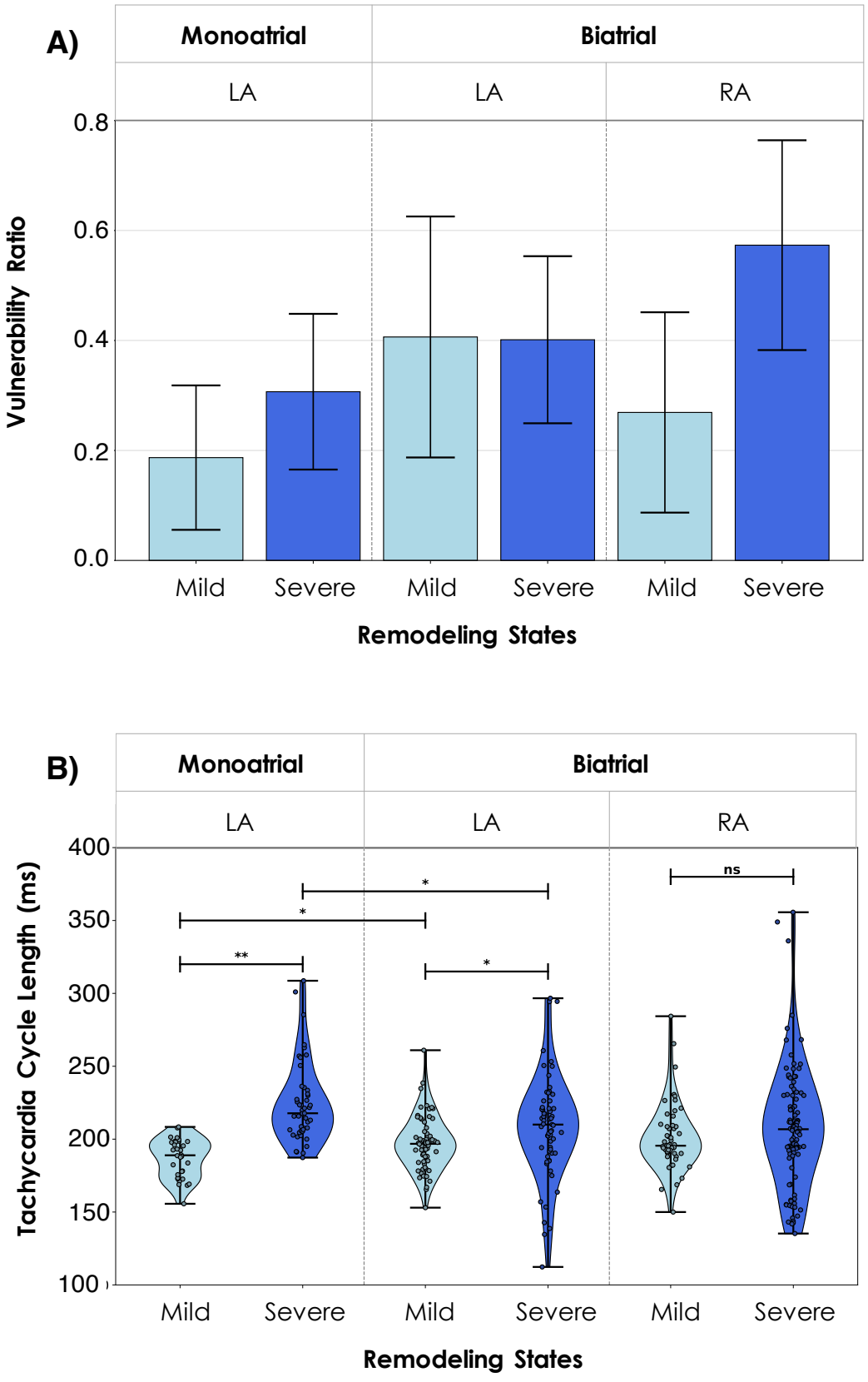

Figure 4.7: Impact of the right atrium (RA) on arrhythmia vulnerability ratio (A) and tachycardia cycle length (TCL) (B). Bars depict vulnerability ratios, calculated as the number of induced points to the total points in each chamber across all 8 subject models. Violin plots show the probability density of TCL measurements, with scatter points representing each reentry measurement. * p-value <0.05, ** p-value <0.001 (ns: not statistically significant).

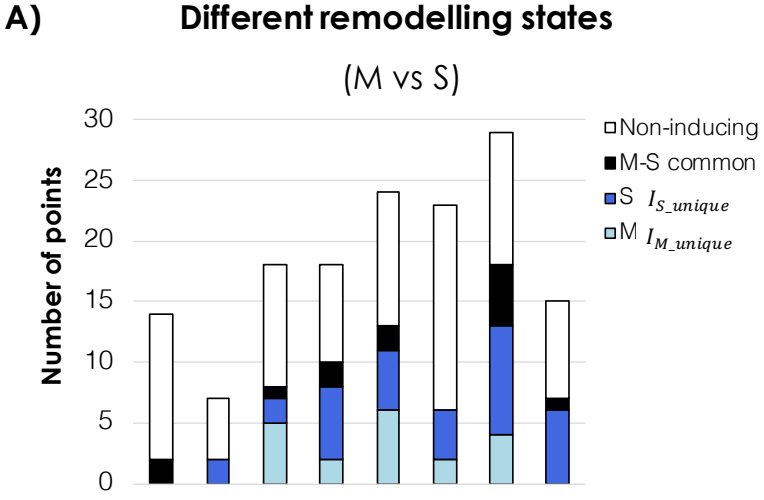

	P1	P2	P3	P4	P5	P6	P7	P8	Mean ± SD
I_{M_total}	2	0	6	4	8	2	9	1	**4.0 ± 3.3**
I_{S_total}	2	2	3	8	7	4	14	7	**5.9 ± 4.1**
I_{M_unique}	0	0	5	2	6	2	4	0	**2.4 ± 2.4**
I_{S_unique}	0	2	2	6	5	4	9	6	**4.3 ± 1.9**
I_{common}	2	0	1	2	2	0	5	1	**1.6 ± 1.6**
N_{common}	12	5	10	8	11	17	11	8	**10.3 ± 3.5**

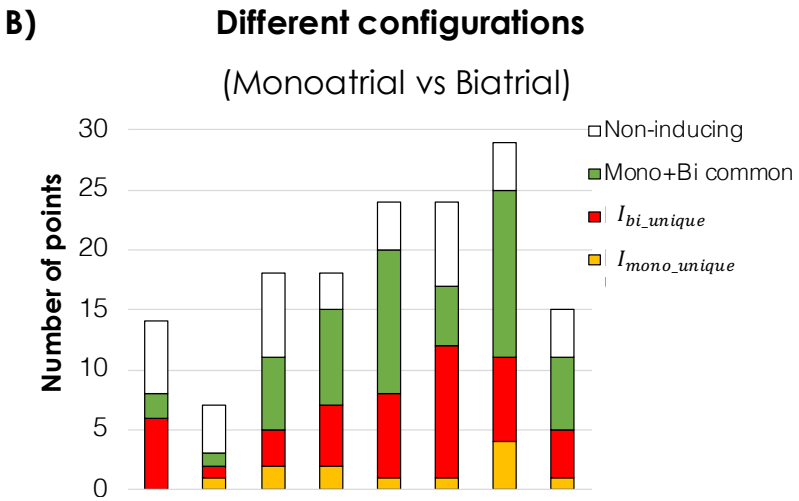

	P1	P2	P3	P4	P5	P6	P7	P8	Mean ± SD
I_{mono_total}	2	2	8	10	13	6	18	7	**8.3 ± 5.4**
I_{bi_total}	8	2	9	13	19	16	21	10	**12.3 ± 6.3**
I_{mono_unique}	0	1	2	2	1	1	4	1	**1.5 ± 1.2**
I_{bi_unique}	6	1	3	5	7	11	7	4	**5.5 ± 3.0**
I_{common}	2	1	6	8	12	5	14	6	**6.8 ± 4.5**
N_{common}	6	4	7	3	4	7	4	4	**4.9 ± 1.6**

Figure 4.8: Proportion of inducing (I) and non-inducing (N) points in the left atrium. The proportion is higher with increased remodeling in the monoatrial configuration (A) and with the incorporation of the right atrium in biatrial configuration (B). Unique refers to points that exclusively induce in a specific setup. (M: mild, S: severe).

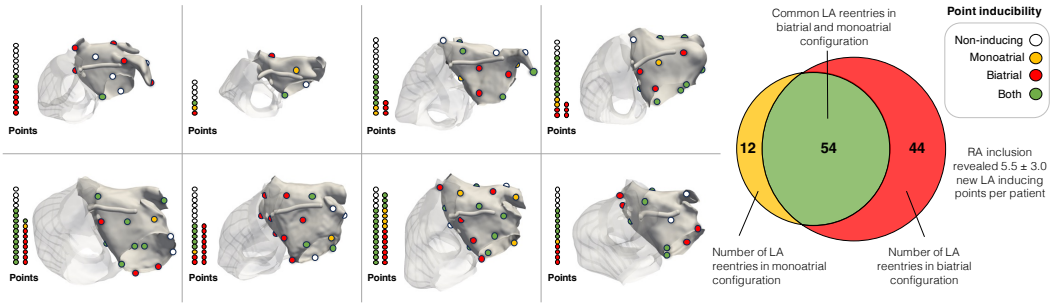

Figure 4.9: Increased left atrium (LA) inducibility due to right atrium (RA) incorporation. Meshes display LA stimulation points inducing reentry in monoatrial (yellow), biatrial (red), both (green) configurations, or non-inducing (white). Columns represent the inducibility type at each stimulation point. The Venn diagram (right) depicts monoatrial and biatrial reentry distribution among all subjects.

4.3.2 Vulnerability of the Right Atrium

A total of 151 out of 281 biatrial reentry episodes were induced by pacing from the RA. The vulnerability ratio of the RA (V_{RA}) showed 111.1% increase between states M and S in V_{RA} (0.27 ± 0.18 vs. 0.57 ± 0.19), as depicted in Figure 4.7a. The mean TCL of the RA-induced reentries for the M and S state was 201.33 ± 23.0 ms and 207.87 ± 41.6 ms ($p = 0.295$), as shown in Figure 4.7b.

4.4 Discussion

This study assessed 48 arrhythmia vulnerability scenarios in 8 patient-specific anatomical models considering monoatrial and biatrial configurations and 3 remodeling states (H, M, and S). The main focus was to assess the role of the RA in arrhythmia vulnerability.

4.4.1 Impact of the Right Atrium

The notion that the RA could play a role in AF is not a novel concept, as indicated by Nitta *et al.* [230]. However, the existing literature often neglects this potential role and provides limited evidence regarding the extent to which the RA contributes to the initiation and maintenance of AF. The term *right atrium* is scarcely mentioned in the latest guidelines for AF treatment [231, 232]. This highlights a lack of comprehensive studies investigating the role of the RA in the context of AF prevention and treatment.

Among all investigated configurations, the RA was the chamber with the highest vulnerability in the S state. A possible explanation could be the larger RA size and the increased electrophysiological heterogeneity due to the presence of the PM, CT, and TV. Despite the lower fibrotic extent in the RA compared to the LA, the RA was more vulnerable to developing reentry upon stimulation than the LA.

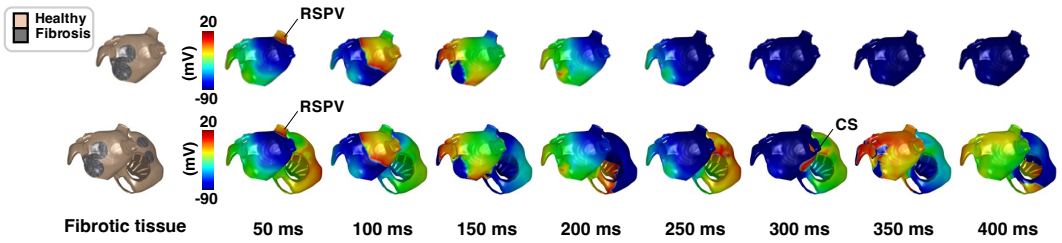

Figure 4.10: Reentry induction in biatrial configuration aided by inter-atrial connections (IAC) involving the posterior wall of the left atrium (LA). The stimulation point at the right superior pulmonary vein (RSPV) of the LA, initiates the reentrant pathway through the IAC, via the coronary sinus (CS) and middle posterior bridge, unsupported by the monoatrial setup.

We identified additional inducing points in the LA biatrial configuration which did not induce reentry in the LA-only model, as shown in Figure 4.10. IAC can promote reentrant circuits and facilitate arrhythmia maintenance as shown by Roney *et al.* [233]. Furthermore, for reentry to occur, an excitable gap is crucial, requiring the wavelength to be shorter than the reentrant circuit length. As a result, incorporating the RA increases the likelihood of new reentrant circuits influenced not only by larger size but also by changes in the wavelength affected by regional differences in CV and effective refractory period [33].

Previous computational model studies have established that the dynamics of reentrant drivers are influenced by the extent and distribution of the fibrotic substrate, in the RA [234] and LA [235]. Moreover, investigations by Boyle *et al.* [215] and Zahid *et al.* [234] have identified reentrant drivers in the RA through the utilization of biatrial models. We also observed simultaneous interactions of multiple reentries (functional and anatomical) in the biatrial simulations, such as rotational activity around the atrioventricular valves, unidirectional blocks in the BB region, reentrant pathways aided by IAC, and rotors associated with the fibrotic substrate. We propose that the increased inducibility in the LA biatrial model, i.e. additional reentrant drivers, resulted from the interplay between fibrosis characteristics and novel circuit paths, as shown in Figure 4.11.

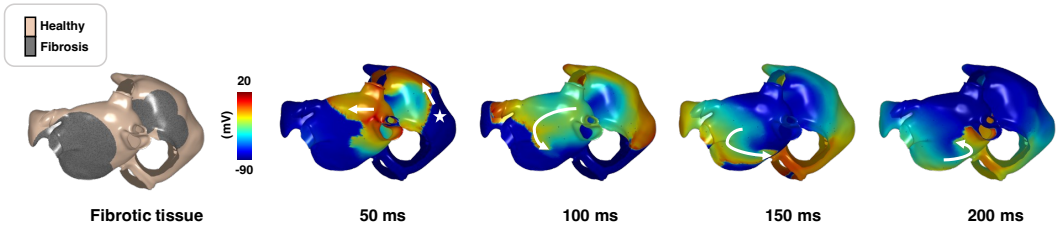

Figure 4.11: Example of reentry induction from stimulation point in the right atrium (RA) in S state. The inducing point (star) is located in the RA near the inferior vena cava. The reentry is anchored at the inferior wall of the left atrium and the wave propagation slows down at the border of the fibrotic region.

Incorporating the RA had an impact on LA vulnerability and TCL distribution. Without the RA, the vulnerability of the LA was markedly higher in the S than in the M state. Incorporating the RA notably diminished this difference in LA vulnerability. Adding the RA led to 5.5 % slower LA reentries in the M state but 7.2 % faster LA reentries in the S state, indicating a state-dependent influence of the RA on reentry dynamics in the LA. The similar TCL between the LA and RA in the biatrial configuration suggests changes are influenced by additional reentrant activity promoted by the RA substrate. These findings have important implications for computer-based tools informing ablation therapy as the arrhythmia vulnerability ratio is expected to change with RA inclusion. This is especially relevant as successful virtual ablation therapies for AF are based on non-inducibility criteria. Therefore, performing biatrial simulations appears advisable.

4.4.2 Arrhythmia Vulnerability in Different Remodeling States

The majority of subject models exhibited higher vulnerability in the S state. Yet for some, the vulnerability ratio was higher in the M state. To understand this behavior, we analyzed activation patterns of reentries induced only in the M state. In the M state, the fibrotic substrate impeded wavefront propagation, causing unidirectional blocks and anchoring reentries. Conversely, in the S state, increased fibrosis led to a slower wavefront progression, facilitating tissue recovery and promoting regular activation. For the other cases where the S state had a higher vulnerability, the faster wavefront in M encountered refractory tissue and failed to activate the surrounding tissue. While in S, wavefront deceleration and a shortened action potential enabled propagation within the fibrotic region. The overall outcome was a combination of both effects.

4.4.3 Limitations

To our knowledge, this study represents the first dedicated examination of the role of the RA in arrhythmia vulnerability in patient-specific computer models, however the limited sample size may impact the generalization of our findings. Different IAC configurations including varying number, locations, and widths, might affect reentrant pathways. All virtual patient models had a similar fibrosis pattern. CV variation was constrained to 20 %. Sustained reentry episodes were simulated for 1 s only. We did not assess changes in structural remodeling concerning endo-epi dissociation, a phenomenon observed in AF patients also in the RA [236]. The absence of electrogram recordings from the study participants prevents the assessment of clinical AF maintenance mechanisms for the simulated reentries.

4.5 Conclusions

LA reentry vulnerability in a biatrial model is higher than in a monoatrial model. Incorporating the RA in patient-specific computational models unmasked potential inducing points in the LA. The RA had a substrate-dependent effect on reentry dynamics and affected the TCL of the LA-induced reentries. As virtual ablation strategies for AF rely on non-inducibility criteria, performing biatrial simulations is advisable. Our study highlights the importance of the RA for the maintenance and induction of arrhythmia in patient-specific computational models.

Chapter 5

Personalization of the Effective Refractory Period

Impact of Effective Refractory Period Personalization on Arrhythmia Vulnerability in Patient-Specific Atrial Computer Models

Although the effective refractory period (ERP) is one of the main electrophysiological properties governing atrial tachycardia maintenance, ERP personalization is rarely performed when creating patient-specific computer models of the atria to inform clinical decision-making. State-of-the-art models usually do not consider physiological ERP gradients but assume a homogeneous ERP distribution. This assumption might have an influence on the ability to induce reentries in the model. In this chapter, the effect of the incorporation of personalized measurements of the ERP under four different scenarios is presented. The main goal was to assess the influence of the personalization of the ERP on arrhythmia vulnerability of atrial computer models.

The content of this chapter is taken and adapted from a paper that has been published open access under Creative Commons CC-BY license in Europace [237]. Most passages have been quoted verbatim from the publication.

5.1 Introduction

Refractoriness is an electrophysiological property that characterizes the response of cardiac tissue to premature stimulation. Shortened cardiac refractoriness promotes sustained reentrant activity [238] and can be assessed during electrophysiological studies following the extra stimulus S1S2 pacing technique, where a train of S1 stimuli is given at a certain cycle length followed by a premature S2 stimulus [239]. The effective refractory period (ERP) can then be defined as the longest S1S2 interval that fails to generate a capture in the tissue. Refractory period can only be determined at one region at a time (between stimulus and measurement locations); thus, multiple measurements are necessary for estimations of spatial distribution [238].

Although ERP is often linked to the action potential duration (APD), this relationship is inconsistent, particularly in the presence of structural abnormalities [240, 241]. ERP can be influenced by the stimulus type and the local structural environment, such as electrotonic loading. This makes ERP especially relevant in cases of fibrosis, as fibrosis can affect ERP without significantly altering APD.

Clinical and pre-clinical investigations have demonstrated heterogeneous refractoriness properties across different atrial regions, which also vary from patient to patient [242–244]. During atrial fibrillation (AF), high stimulation frequencies induce electrical remodeling, resulting in shortened APD and ERP [245]. However, contrary to the belief that prolonged exposure to AF always shortens ERP, patients with persistent AF may exhibit longer ERP due to the presence of atrial dilatation [241]. So, the overall contribution of refractoriness to increased reentrant inducibility remains unclear.

A common theory explaining the existence of AF postulates that both a trigger and a vulnerable substrate are necessary for the initiation and maintenance of AF [246]. Ectopic activity from the sleeves of the pulmonary veins (PV) is the most frequent form of AF triggers [136]. Non-PV triggers have been identified in the crista terminalis (CT), the interatrial septum, the left atrium (LA) posterior wall, the left atrial appendage (LAA), the ligament of Marshall, the superior vena cava (SVC), and the coronary sinus; yet their precise role in initiating AF remains uncertain [247]. The vulnerable substrate refers to changes in electrical and structural remodeling (e.g., shortening of the APD, presence of fibrosis, atrial dilatation, adipose tissue infiltration, inflammation, etc.) [1]. The presence of electrical heterogeneity, such as regional variations in conduction velocity (CV), APD, and ERP, can favour unidirectional block in response to ectopy/stimulation, which can then initiate reentry [118]. However, it is still challenging to characterize the vulnerable substrate in a clinical or experimental setting. Understanding the interplay between electrophysiological and structural factors, and how their regional distribution (heterogeneity) influences arrhythmia maintenance remains a complex task in cardiac electrophysiology research.

In this sense, patient-specific atrial computational models provide a robust framework for studying, under controlled conditions, the integrated effect of substrate features unique to each patient and their impact on arrhythmia vulnerability [15, 17, 120]. The creation of

patient-specific computer models of the atria typically involves anatomical personalization using image data obtained from magnetic resonance imaging (MRI), computed tomography scans or electroanatomic mapping systems (EAMS). Electrophysiological personalization is rarely performed since patient electrophysiological data is usually not available beforehand [248]. Some studies have conducted personalization of atrial electrophysiology, by fitting model parameters to patient clinical data [17, 27, 248–250]. Their findings suggest that personalized electrophysiological parameter values vary among patients and differ from standardised literature parameter values. Nevertheless, the effect of incorporating patient-specific clinical ERP measurements on arrhythmia vulnerability has not yet been assessed. In this work, we investigate the role of incorporating personalized ERP values from various clinical measurements on the *in silico* assessment of arrhythmia vulnerability.

5.2 Methods

5.2.1 Electrophysiological Study

Six patients with a history of AF and prior pulmonary vein isolation (PVI) and one patient with atrial flutter (AFl) underwent an electrophysiological study at Städtisches Klinikum Karlsruhe, Germany. Patients gave written informed consent, and the ethics committee approved the study protocol. Electroanatomic maps during sinus rhythm were generated using the Rhythmia 3D mapping system (Boston Scientific, USA). For patients with prior PVI, LA mapping was conducted, whereas for the patient with AFl, the right atrium (RA) was mapped. ERP measurements were obtained from multiple locations in the atria (5.7 ± 1.4 measurements) following an S1S2 protocol with seven S1 stimuli at a basic cycle length of 500 ms and an S2 stimulus with intervals between 300 and 200 ms, decreasing by 10 ms until loss of capture. Pacing stimuli for clinical ERP identification had an amplitude of 5 V with a duration of 1 ms in a bipolar configuration, using either the Intellamap Orion™ 8.5 F catheter or the Intellanav Stablepoint™ 7F catheter (Boston Scientific, USA). Stimulus capture was verified for each location, and the amplitude was incrementally increased at locations where no capture was achieved initially. ERP measurements were taken in different anatomical regions such as the anterior wall, posterior or lateral wall, appendage and at least one PV in the case of LA geometries. A representative endocardial trace of the stimulation protocol is shown in Figure 5.1A. ERP was defined as the longest S1S2 interval without capture. To characterize the patient-specific fibrotic substrate, low voltage areas (< 0.5 mV) were identified from bipolar voltage maps.

5.2.2 Patient-Specific Anatomical Modeling

The atrial anatomy derived from the EAMS was utilized to generate personalized simulation-ready bilayer meshes. The seven bilayer meshes were created using AugmentA [49]

including rule-based anatomical annotations and fiber orientations. For the LA models, the LAA, mitral valve (MV), PV, and left Bachmann's bundle (BB), were automatically annotated; for the RA model, the tricuspid valve (TV), right atrial appendage (RAA), SVC, inferior vena cava (IVC), pectinate muscles (PM), right BB, and CT. An open-source Python-based algorithm was used to subdivide the meshes into anatomical regions: anterior wall, septal wall, posterior wall, lateral wall, inferior wall, appendage, for the RA and LA accordingly [251].

5.2.3 Atrial Electrophysiology Modeling

Electrical propagation in the atria was modelled using the monodomain equation and simulated with openCARP [221]. Anisotropy in different parts of the atria were modelled as described in Krueger M. *et al* [248]. CV was doubled in the CT and tripled in the PM and in the BB [252]. As both ERP and CV influence reentry maintenance [249], our aim was to identify the CV at which vulnerability was highest. We tuned the longitudinal monodomain conductivity to achieve a mean CV of 0.3, 0.5, and 0.7 m/s in the bulk myocardium, for each patient-specific model. A CV of 0.3 m/s, as shown in Figure 5.2, exhibited the highest number of inducible points and was therefore selected for further vulnerability assessments. To reach a limit cycle, single-cell models were paced 100 times with a basic cycle length of 500 ms. Single-chamber models were paced four times from the earliest activation site identified from local activation maps, also with a basic cycle length of 500 ms.

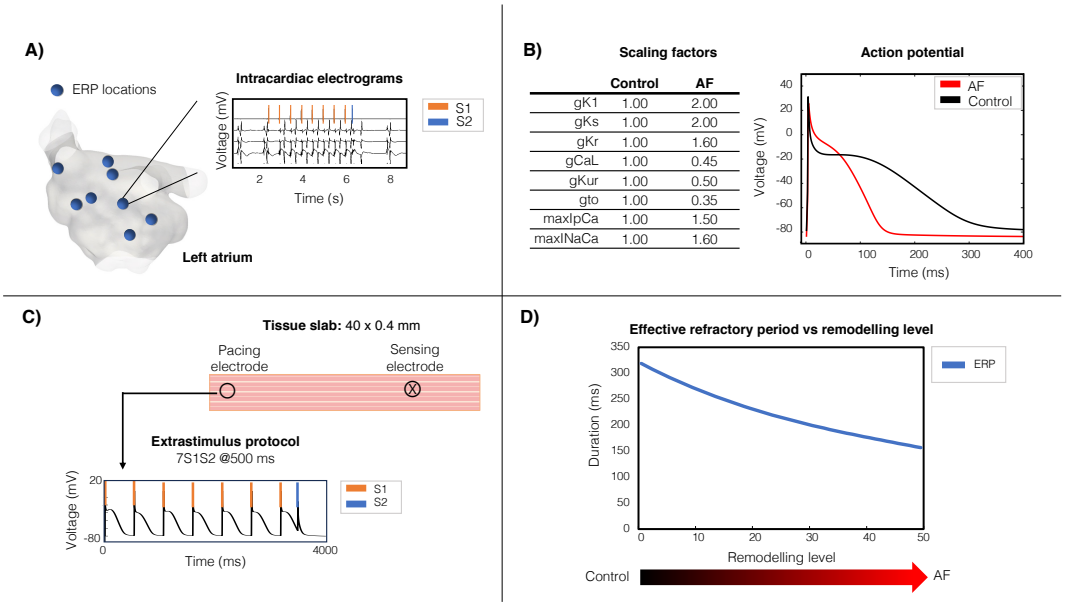

Figure 5.1: Modeling of patient-specific effective refractory period. A) ERP was measured in multiple locations in the atria with an S1S2 protocol. B) Scaling of the maximum ion channel conductances of the Courtemanche *et al.* cellular model from healthy to AF. C) *In silico* pacing protocol in tissue cable. D) ERP with respect to remodeling level. AF: atrial fibrillation; ERP: effective refractory period

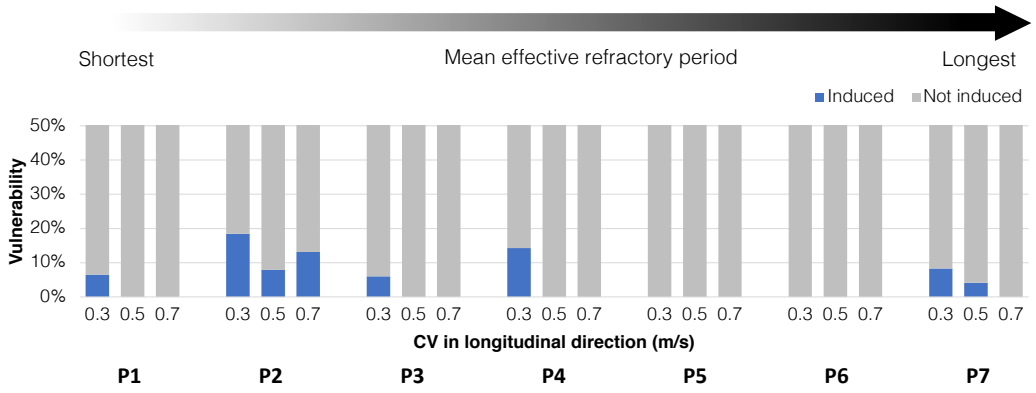

Figure 5.2: Comparison of arrhythmia vulnerability with non-personalized heterogeneous effective refractory period distribution (scenario B). A CV of 0.3 m/s revealed a higher number of inducing points in the control scenario. P1–P7 indicate individual patients. CV: conduction velocity, ERP: effective refractory period.

5.2.4 Patient-Specific ERP Modeling

To reproduce patient-specific clinical ERP *in silico*, the maximum conductances of key ionic channels affecting action potential morphology of the established Courtemanche M. *et al.* cellular model [51] were modified from control conditions to a setup that reflects changes in the action potential observed in patients with persistent AF [252]. We modified the maximum conductances of the inward rectifier K^+ current (g_{K1}), the ultrarapid (g_{Kur}), the rapid (g_{Kr}), the slow delayed-rectifier (g_s), and the transient outward (g_{to}) K^+ currents; the L-type Ca^{2+} current (g_{CaL}), the sarcoplasmic Ca^{2+} pump current (I_{pCa}), and the Ca^{2+}/Na^+ exchanger ($\max I_{NaCa}$). The ion channel conductances were linearly scaled to generate a set of 50 different cellular models with gradually increasing remodeling levels. We generated an *in silico* tissue cable for each cellular model with a length of 40 mm and a resolution of 0.4 mm and performed a virtual S1S2 pacing protocol to obtain the ERP (Figure 5.1C-D). The scaling factors for each combination and the corresponding ERP can be found in Table 5.1. Pacing stimuli for *in silico* ERP identification had a current density of $30\,\mu A/cm^2$ with a duration of 3 ms and an S2 coupling interval ranging from 350 ms up to loss of capture in steps of 1 ms.

5.2.5 Generation of ERP Scenarios

To assess the role of ERP personalization, we generated four scenarios: homogeneous (A), heterogeneous (B), regional (C), and continuous (D) ERP distribution. The first two configurations were non-personalized based on literature data, the latter two were personalized based on patient measurements. In scenario A, the same cellular model corresponding to AF-induced remodeling [252] was applied to the whole atrium. In scenario B, anatomical structures had individual cellular model variants with specific ERP assigned based on literature data [248]. For scenario C, all nodes in anatomical regions were assigned distinct cellular

Table 5.1: Scaling factors applied to the maximum ionic conductances for each combination resulting in the corresponding effective refractory period (ERP) (ms).

GK1	GKs	GKr	GCaL	factorGKur	Gto	maxIpCa	maxINaCa	ERP
1.0000	1.0000	1.0000	1.0000	1.0000	1.0000	1.0000	1.0000	320
1.0204	1.0204	1.0122	0.9888	0.9898	0.9867	1.0102	1.0122	310
1.0408	1.0408	1.0245	0.9776	0.9796	0.9735	1.0204	1.0245	310
1.0612	1.0612	1.0367	0.9663	0.9694	0.9602	1.0306	1.0367	300
1.0816	1.0816	1.0490	0.9551	0.9592	0.9469	1.0408	1.0490	300
1.1020	1.1020	1.0612	0.9439	0.9490	0.9337	1.0510	1.0612	290
1.1224	1.1224	1.0735	0.9327	0.9388	0.9204	1.0612	1.0735	290
1.1429	1.1429	1.0857	0.9214	0.9286	0.9071	1.0714	1.0857	280
1.1633	1.1633	1.0980	0.9102	0.9184	0.8939	1.0816	1.0980	280
1.1837	1.1837	1.1102	0.8990	0.9082	0.8806	1.0918	1.1102	270
1.2041	1.2041	1.1224	0.8878	0.8980	0.8673	1.1020	1.1224	270
1.2245	1.2245	1.1347	0.8765	0.8878	0.8541	1.1122	1.1347	260
1.2449	1.2449	1.1469	0.8653	0.8776	0.8408	1.1224	1.1469	260
1.2653	1.2653	1.1592	0.8541	0.8673	0.8276	1.1327	1.1592	250
1.2857	1.2857	1.1714	0.8429	0.8571	0.8143	1.1429	1.1714	250
1.3061	1.3061	1.1837	0.8316	0.8469	0.8010	1.1531	1.1837	250
1.3265	1.3265	1.1959	0.8204	0.8367	0.7878	1.1633	1.1959	240
1.3469	1.3469	1.2082	0.8092	0.8265	0.7745	1.1735	1.2082	240
1.3673	1.3673	1.2204	0.7980	0.8163	0.7612	1.1837	1.2204	240
1.3878	1.3878	1.2327	0.7867	0.8061	0.7480	1.1939	1.2327	230
1.4082	1.4082	1.2449	0.7755	0.7959	0.7347	1.2041	1.2449	230
1.4286	1.4286	1.2571	0.7643	0.7857	0.7214	1.2143	1.2571	230
1.4490	1.4490	1.2694	0.7531	0.7755	0.7082	1.2245	1.2694	220
1.4694	1.4694	1.2816	0.7418	0.7653	0.6949	1.2347	1.2816	220
1.4898	1.4898	1.2939	0.7306	0.7551	0.6816	1.2449	1.2939	220
1.5102	1.5102	1.3061	0.7194	0.7449	0.6684	1.2551	1.3061	210
1.5306	1.5306	1.3184	0.7082	0.7347	0.6551	1.2653	1.3184	210
1.5510	1.5510	1.3306	0.6969	0.7245	0.6418	1.2755	1.3306	210
1.5714	1.5714	1.3429	0.6857	0.7143	0.6286	1.2857	1.3429	210
1.5918	1.5918	1.3551	0.6745	0.7041	0.6153	1.2959	1.3551	200
1.6122	1.6122	1.3673	0.6633	0.6939	0.6020	1.3061	1.3673	200
1.6327	1.6327	1.3796	0.6520	0.6837	0.5888	1.3163	1.3796	200
1.6531	1.6531	1.3918	0.6408	0.6735	0.5755	1.3265	1.3918	190
1.6735	1.6735	1.4041	0.6296	0.6633	0.5622	1.3367	1.4041	190
1.6939	1.6939	1.4163	0.6184	0.6531	0.5490	1.3469	1.4163	190
1.7143	1.7143	1.4286	0.6071	0.6429	0.5357	1.3571	1.4286	190
1.7347	1.7347	1.4408	0.5959	0.6327	0.5224	1.3673	1.4408	180
1.7551	1.7551	1.4531	0.5847	0.6224	0.5092	1.3776	1.4531	180
1.7755	1.7755	1.4653	0.5735	0.6122	0.4959	1.3878	1.4653	180
1.7959	1.7959	1.4776	0.5622	0.6020	0.4827	1.3980	1.4776	180
1.8163	1.8163	1.4898	0.5510	0.5918	0.4694	1.4082	1.4898	180
1.8367	1.8367	1.5020	0.5398	0.5816	0.4561	1.4184	1.5020	170
1.8571	1.8571	1.5143	0.5286	0.5714	0.4429	1.4286	1.5143	170
1.8776	1.8776	1.5265	0.5173	0.5612	0.4296	1.4388	1.5265	170
1.8980	1.8980	1.5388	0.5061	0.5510	0.4163	1.4490	1.5388	170
1.9184	1.9184	1.5510	0.4949	0.5408	0.4031	1.4592	1.5510	160
1.9388	1.9388	1.5633	0.4837	0.5306	0.3898	1.4694	1.5633	160
1.9592	1.9592	1.5755	0.4724	0.5204	0.3765	1.4796	1.5755	160
1.9796	1.9796	1.5878	0.4612	0.5102	0.3633	1.4898	1.5878	160
2.0000	2.0000	1.6000	0.4500	0.5000	0.3500	1.5000	1.6000	160

models with the ERP value matching the spatially closest available clinical measurement. In case of multiple measurements present in the same region, the average ERP value was considered for the whole region. In scenario D, the measured ERPs were assigned to the corresponding catheter tip positions and then continuously mapped to the whole surface by Laplacian interpolation [253]. The measuring points were defined as boundary conditions, so that the ERP values never exceeded the measured ERP range. The ion channel conductances for each individual mesh node were then adjusted accordingly to match the interpolated ERP. For each modified ionic channel conductance in the Courtemanche M. *et al.* model [51], an adjustment file was generated, consisting of a list with the corresponding scaling factor for the ERP value at each node in the mesh. Adjustment files were generated in openCARP using the adjustment function as described in Boyle P. [254]. The four personalization scenarios are shown in Figure 5.3.

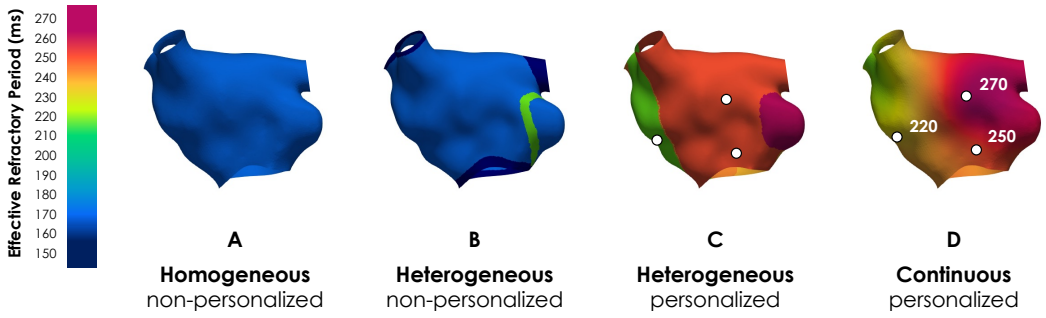

Figure 5.3: Scenarios for the evaluation of ERP personalization. Homogeneous (A) with non-personalized ERP based on literature data [252], heterogeneous (B) with different non-personalized ERP based on anatomical structures [248], regional (C) with personalized ERP divided into anatomical regions, and continuous (D) with personalized ERP from interpolated measurements. Circles denote catheter tip locations where the pacing stimulus was delivered. ERP: effective refractory period.

5.2.6 Patient-Specific Substrate Modeling

Substrate was incorporated into the meshes based on the identification of low voltage areas (LVA). To distinguish between ablation lesions from PVI and native fibrosis, we defined ablation lesion regions as having voltage $< 0.1\,\mathrm{mV}$ and native fibrosis regions as having a voltage between 0.1 and 0.5 mV [118]. To model native fibrosis, we accounted for two different cellular mechanisms: replacement fibrosis and inflammation. For regions defined as native fibrosis, 30% of the elements were randomly selected and set to non-conductive with $\sigma = 10^{-7}\,\mathrm{S/m}$ to represent replacement fibrosis, while the remaining 70% were set to be electrically remodelled in response to cellular inflammation [17, 39]. Several ionic conductances were rescaled to represent the effects of electrical remodeling ($g_{\mathrm{CaL}} \times 22.5\%$, $g_{\mathrm{Na}} \times 60\%$, factor$g_{\mathrm{Kur}} \times 50\%$, $g_{\mathrm{to}} \times 35\%$, $g_{\mathrm{Ks}} \times 200\%$, max$I_{\mathrm{pCa}} \times 150\%$, max$I_{\mathrm{NaCa}} \times 160\%$).

To model ablation lesions, all elements were set to be non-conductive [255]. To assess the influence of ablation lesions and native fibrosis on arrhythmia vulnerability, we created four additional scenarios, namely A2, D2, A3 and D3. The first two scenarios, A2 and D2, included ablation lesions and native fibrosis. Scenario A2 had the same ERP as scenario A (homogeneous), and scenario D2 corresponding to same ERP personalization as scenario D (continuous). Lastly, to model a stage before PVI, we generated scenarios A3 and D3 including only native fibrosis regions, and ablation lesions were modeled as healthy.

5.2.7 Vulnerability Assessment

Arrhythmia vulnerability was assessed by virtual S1S2 pacing at different locations in the atria separated by an average distance of 2 cm [32]. The vulnerability ratio was defined as the number of inducing points divided by the number of stimulation points. Stimulation points locations remained consistent among scenarios. Transmembrane voltage traces were recorded for 1 s for each reentry at the inducing stimulus location. We determined the tachycardia cycle length (TCL) of the reentries by calculating the average between peaks of $\mathrm{d}V/\mathrm{d}t$.

5.2.8 Sensitivity Analysis

To study the influence of uncertainty in ERP measurements, we conducted a sensitivity analysis by including perturbation in ERP measurements in the ranges of ±2, ±5, ±10, ±20 and ±50 ms, randomly drawn from a uniform distribution. We generated 10 perturbation sets for each perturbation range, resulting in a total of 40 new perturbed ERP sets; a separate random value was drawn for each measured ERP. Finally, we generated new interpolated maps using the perturbed ERP sets. Due to the high computational cost of the vulnerability assessment (15±2.4 min per stimulation point, utilizing 4 nodes × 40 CPU cores with Intel Xeon Gold 6230 2.1GHz), the sensitivity analysis was limited the assessment to patient P3 model, which showed the highest vulnerability in the LA model cohort.

5.2.9 Statistical Analysis

The data are presented as mean±SD. We used a two-sample t-test to determine statistical significance between the sample means. P-values <0.05 were considered significant.

5.2.10 Data Availability

The data underlying this article including bilayer models, adjustment files and source code to reproduce the simulated reentries are accessible under open licences at [256].

5.3 Results

Patient characteristics are outlined in Table 5.2. The overall mean clinically measured ERP was 254.0 ± 32.7 ms. The dispersion of the ERP measurements is shown in the boxplot in Figure 5.2A. The ERP distribution maps for each patient is illustrated in Figure 5.2B. Bipolar voltage maps for each patient are shown in Figure 5.5A. LVA accounted for 42.8 ± 16.4 % of the atrial surface. The amount of fibrosis, ablation lesions, and healthy tissue for each patient are shown in Figure 5.5B.

Table 5.2: Clinical characteristics of patient cohort

Patient	Sex	Chamber	Age (years)	Volume (ml)	Area (cm^2)	LVA (%)	ERP (ms)	ERP (#)	Dx
P1	F	LA	67	270.1	267.4	45.49	222.0±11.0	5	PAF
P2	M	RA	63	221.4	200.7	25.78	222.5±14.9	8	AFl
P3	F	LA	72	175.9	179.8	46.04	232.0±16.4	7	PAF
P4	M	LA	76	175.6	187.4	74.02	236.3±21.3	5	PeAF
P5	M	LA	61	86.9	120.0	47.36	284.0±20.7	5	PeAF
P6	F	LA	63	95.2	121.2	28.85	286.0±13.4	4	PAF
P7	M	LA	65	106.8	136.9	32.35	295.0±20.8	6	PAF

Dx: diagnosis, ERP: effective refractory period, LA: left atrium, LVA: low voltage area, PAF: paroxysmal atrial fibrillation, PeAF: persistent atrial fibrillation, RA: right atrium, #: number of measurements.

The ERP of *in silico* tissue cables varied from 320 ms in the healthy state to 157 ms in the AF remodeling state. Non-personalized scenarios had a shorter ERP and reduced dispersion with an ERP of 158.9 ± 5.3 ms, while personalized scenarios had an ERP of 254.0 ± 32.7 ms. From a total of 214 stimulation points (30.6 ± 8.9 stimulation points per patient), 61 simulated reentries were induced across the four scenarios without fibrotic substrate, with individual counts of 7, 18, 20, and 16 reentries for scenarios A, B, C, and D, respectively. Vulnerability values are shown in Figure 5.6. The vulnerability for scenario A was $3.4 \pm 4.0\%$, $7.7 \pm 3.4\%$ for scenario B, $9.0 \pm 5.1\%$ for scenario C and $7.0 \pm 3.6\%$ for scenario D. The mean TCL was 167.07 ± 12.58 ms for scenario A, 158.42 ± 27.52 ms for scenario B, 265.17 ± 39.87 ms for scenario C and 285.88 ± 77.31 ms for scenario D, as shown in Figure 5.7.

We assessed the impact of incorporating fibrotic substrate informed by LVA into the models along with ERP personalization on arrhythmia vulnerability. Given that most patients had undergone previous PVI, we compared vulnerability with and without ablation lesions defined by regions where bipolar amplitude was < 0.1 mV. To avoid additional confounding factors, we compared scenario A (homogeneous non-personalized) and scenario D (continuous with personalized ERP) without fibrosis with their respective counterparts with fibrosis and ablation lesions A2 and D2 (Figure 5.8). Incorporating fibrosis and ablation

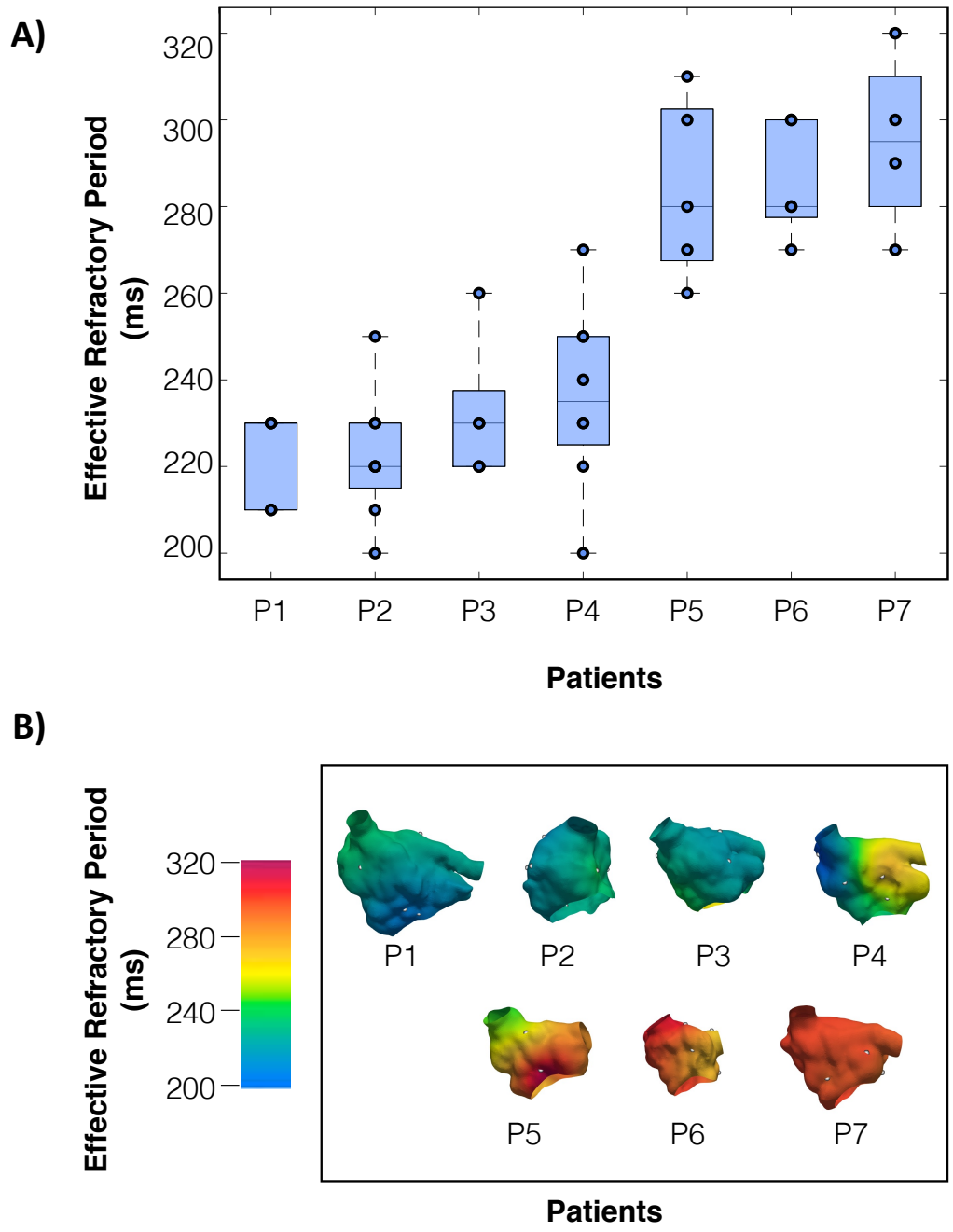

Figure 5.4: Distribution of clinically measured effective refractory period. 1) Boxplots show the dispersion of ERP measurements for each patient, where the points represent each individual measurement. 2) ERP distribution map generated from interpolated clinical measurements from an anterior view. P1-P7 indicate individual patients. ERP: effective refractory period.

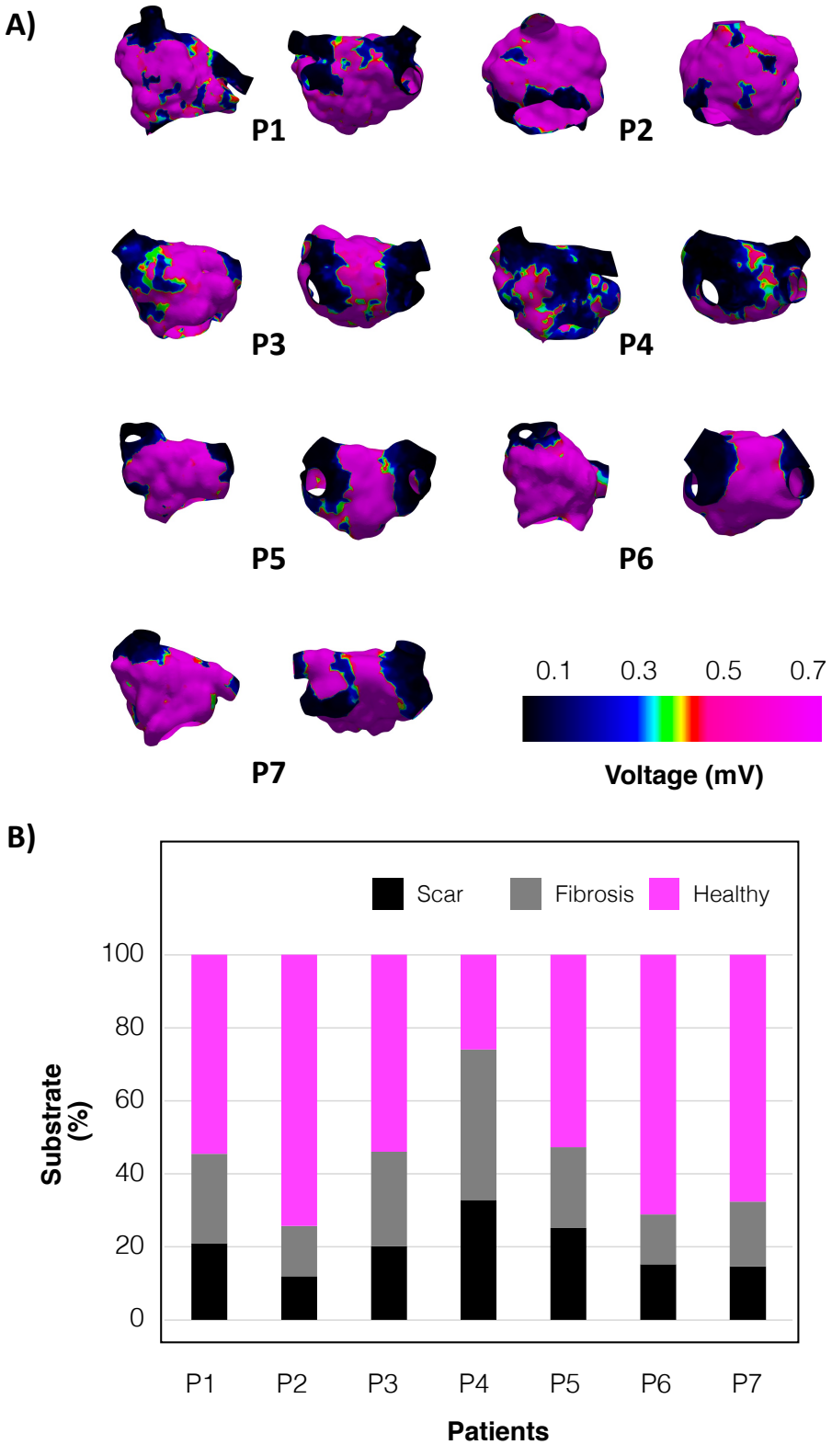

Figure 5.5: Distribution of substrate based on the identification of low voltage areas. A) Bipolar voltage maps from an anterior and posterior views. B) Percentage of substrate defined as ablation lesions ($\leq$ 0.1 mV), fibrotic regions (0.1-0.5 mV), and healthy tissue ($\geq$ 0.5 mV).

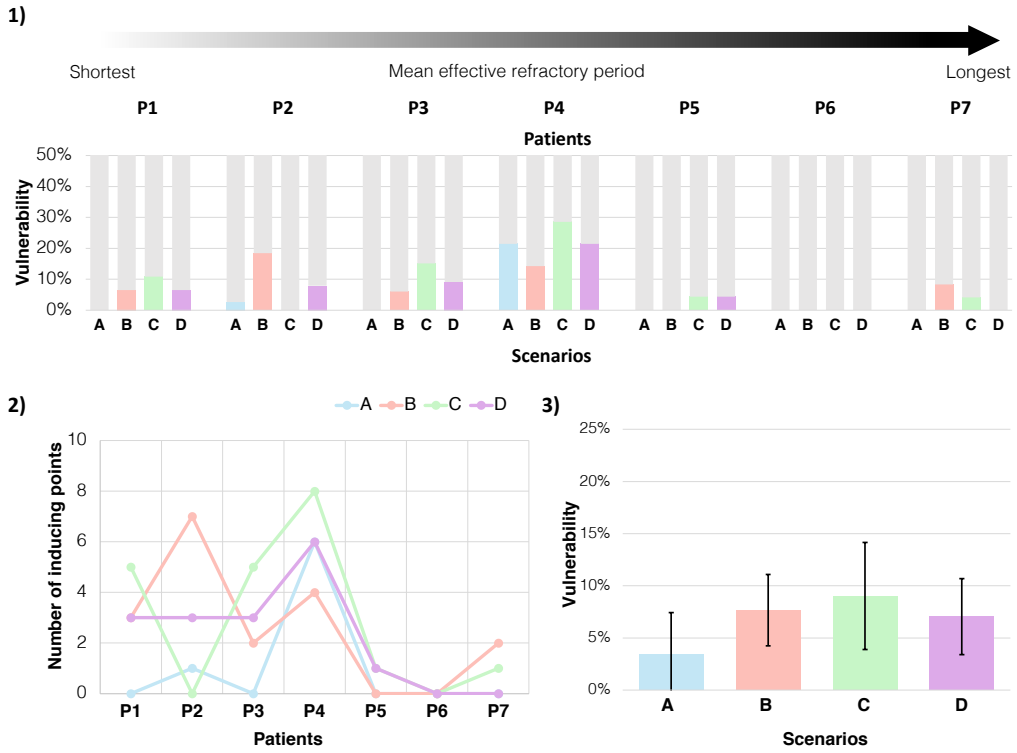

Figure 5.6: Comparison of arrhythmia vulnerability and number of inducing points among four scenarios. 1) Vulnerability for each patient in four personalization scenarios without fibrotic substrate 2) Number of inducing points for each patient. 3) Mean vulnerability, bars indicate standard deviation. P1-P7 indicate individual patients. Scenarios are defined as A: homogeneous, B: heterogeneous, C: regional, and D: continuous ERP distribution. ERP: effective refractory period.

lesions resulted in a vulnerability of $11.3 \pm 7.28\%$ and $3.93 \pm 3.33\%$ for A2 and D2, respectively. Incorporating only fibrosis without ablation lesions resulted in a vulnerability of $47.54 \pm 31.96\%$ and $39.4 \pm 30.31\%$ for A3 and D3, respectively. Area reduction due to PVI decreased vulnerability by 36.2% when comparing A3 vs A2 ($47.5 \pm 32.0\%$ vs $11.3 \pm 7.3\%$), and by 35.5% when comparing D3 vs D2 ($39.4 \pm 30.3\%$ vs $3.9 \pm 3.3\%$) (Figure 5.8). The magnitude of the difference between A3 and D3 varied among patients, with some experiencing small differences in vulnerability, e.g., P2 and P4, while others showing a bigger difference, e.g., P1 and P7. On average, the homogeneously reduced ERP in A3 in the presence of native fibrosis without ablation lesions resulted in higher vulnerability compared to D3.

Incorporating perturbations to the measured ERP in the sensitivity analysis slightly impacted the vulnerability of the model from 9.1% to $5.8 \pm 2.7\%$, $6.1 \pm 3.5\%$, $6.9 \pm 3.7\%$, and $5.2 \pm 3.5\%$, observed for perturbations in the range of ± 2, ± 5, ± 10 and ± 20 ms, respectively (Figure 5.9). Only when the perturbations were in the range of ± 50 ms, a higher standard deviation was observed ($9.7 \pm 10.0\%$).

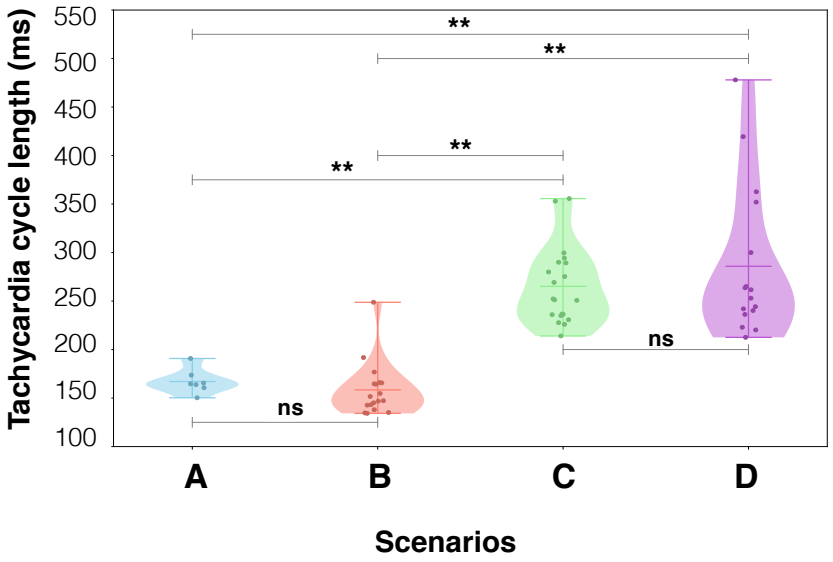

Figure 5.7: Tachycardia cycle length of induced reentries. Each individual point represents one reentry Conduction velocity in the bulk myocardium was set to 0.3 m/s in the longitudinal direction. **: p<0.05; ns: not statistically significant. Scenarios are defined as A: homogeneous, B: heterogeneous, C: regional, and D: continuous ERP distribution. ERP: effective refractory period.

5.4 Discussion

In this study, we assessed arrhythmia vulnerability in a cohort of seven patient-specific atrial models, each with information on the distribution of ERP and low voltage substrate. We compared vulnerability across four ERP personalization scenarios: non-personalized homogeneous (A), non-personalized heterogeneous (B), personalized regional (C), and personalized continuous (D) distribution of ERP without substrate. Secondly, we investigated the impact on vulnerability of the interaction between native fibrosis and ablation lesions with ERP. Thirdly, we conducted a sensitivity analysis to evaluate the effects of uncertainty in ERP measurements on arrhythmia vulnerability. The four main highlights of our study are: 1) differences in arrhythmia vulnerability between personalized and non-personalized scenarios should be acknowledged, particularly for patients with low ERP, 2) an increased dispersion of the ERP in personalized scenarios had a greater effect on reentry dynamics than on mean vulnerability values, 3) the incorporation of personalized ERP had a greater impact on inducibility than had a homogeneously reduced ERP, however, this effect reversed when native fibrosis was included, with a higher inducibility for the homogeneously reduced ERP scenario, and 4) ERP measurement uncertainty up to 20ms slightly influences arrhythmia vulnerability.

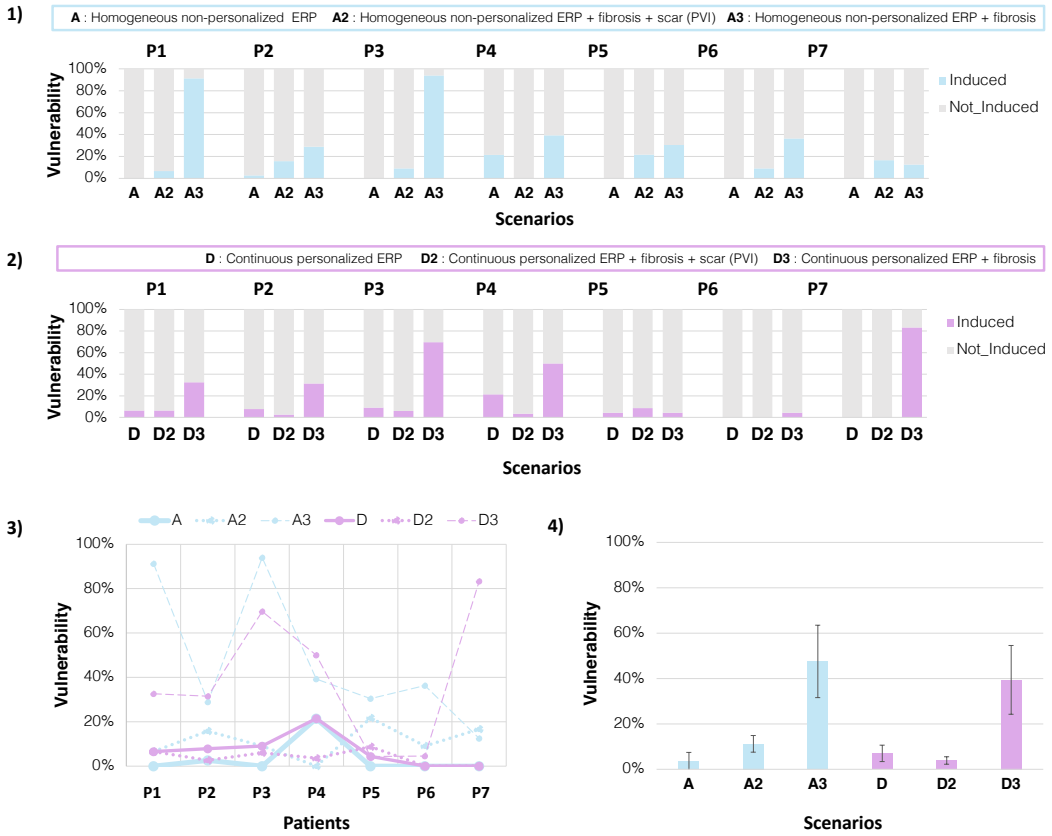

Figure 5.8: Comparison of fibrotic substrate modeling and effective refractory period personalization between scenario A (homogeneous non-personalized ERP) and scenario D (continuous with personalized ERP). 1) Vulnerability for scenario A and two LVA substrate modeling scenarios: A2 with ablation lesions (<0.1 mV) and native fibrosis (<0.5 mV), and A3 as a state before PVI with only native fibrosis (>0.1 mV). 2) Vulnerability for scenario D and two LVA substrate modeling scenarios: D2 with personalized continuous ERP + with ablation lesions (<0.1 mV) and native fibrosis (<0.5 mV) and D3 as a state before PVI with personalized continuous ERP and only native fibrosis (>0.1 mV). 3) Comparison of six scenarios for each patient. 4) Mean vulnerability per scenario. Vertical lines denote standard deviation. P1-P7 indicate individual patients. ERP: effective refractory period, LVA: low voltage area.

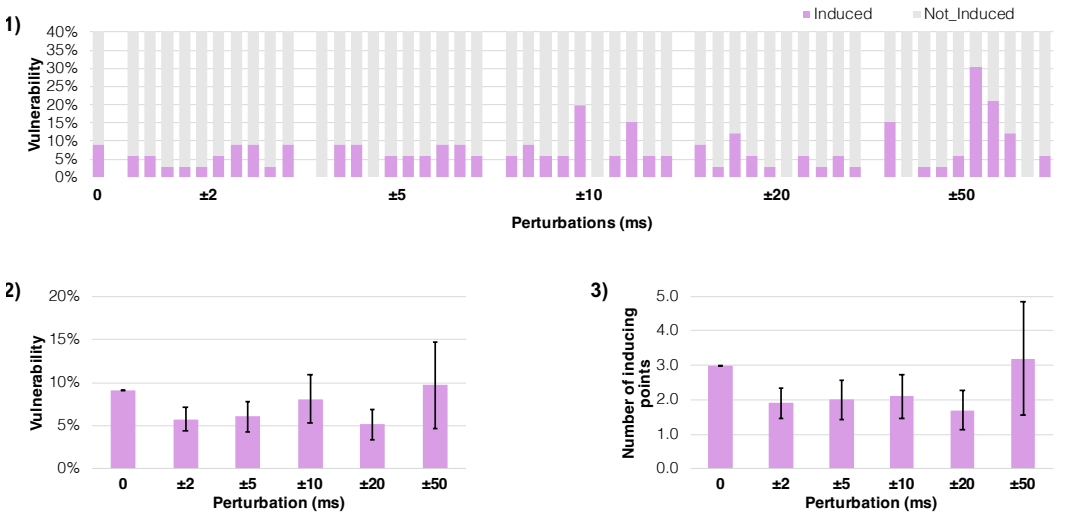

Figure 5.9: Sensitivity analysis for arrhythmia vulnerability of patient P3 comparing scenario D (personalized with continuous ERP) and perturbed ERP measurements. 1) Vulnerability for each perturbation range. 2) Mean vulnerability. 3) Mean number of inducing points for each perturbation range. Bars indicate standard deviation. Perturbations of ±2, ±5, ±10, ±20, and ±50 ms, were randomly drawn, 10 times for each perturbation range, from a uniform distribution. The perturbations were incorporated to each measured ERP value and new interpolated continuous maps were generated from the perturbed ERP measurements. ERP: effective refractory period.

5.4.1 Effect of ERP Personalization on Arrhythmia Vulnerability and Dynamics

Personalized and non-personalized scenarios were different in the mean and dispersion of the ERP. Among all scenarios, the homogeneous non-personalized scenario A had the lowest vulnerability, while the regional personalized scenario C had the highest vulnerability. Heterogeneities in the form of regions in scenario C promote unidirectional blocks, thereby increasing vulnerability, while the homogeneous scenario A makes it less likely to induce reentry even with a shorter ERP [257]. Differences in vulnerability between personalized and non-personalized scenarios were greater in patients with lower ERP (< 240 ms), corresponding to P1-P4, with a total of 56 inducing points. In contrast, the remaining three patients (P5-P7) were almost non-inducible, with only five inducing points in total. During cursory follow-up, two out of seven patients (P1 and P3) recurred with AF after four and eight months, respectively. Decreased inducibility in P5-P7 could be attributed to the reduced effective atrial size [258]. Thus, differences in vulnerability between personalized and non-personalized scenarios cannot be neglected, particularly for patients with low ERP.

The effect of ERP personalization becomes more evident when analysing reentry dynamics. There were no significant differences in the TCL of the non-personalized scenarios A and B (167.1±12.6 ms vs. 158.4±27.5 ms, $p = 0.43$), nor were there significant differences between the personalized scenarios C and D (265.2±39.9 ms vs. 285.9±77.3 ms, $p = 0.31$).

However, personalized scenarios had significantly slower TCL compared to non-personalized scenarios ($p < 0.001$). This finding suggests that the increased dispersion of the ERP in the personalized scenarios has a greater effect on reentry dynamics than on the absolute value of vulnerability.

5.4.2 Increased ERP Dispersion is Associated with Higher Arrhythmia Vulnerability

Previous clinical and simulation studies have analyzed the effect of ERP and APD dispersion on arrhythmia vulnerability in patients with persistent and paroxysmal AF [114, 122, 241, 259]. Dispersion can be defined both spatially and temporally. Spatial dispersion refers to the difference between the maximum and minimum values of ERP measurements [122], while temporal dispersion refers to variation exceeding 5% from the baseline value [114]. In the study of Narayan *et al.*, pacing-induced AF from either the PVs or high RA was always preceded by an increased temporal APD dispersion [114]. In a cohort of 47 patients with paroxysmal AF, ERP was measured in 5 sites in both atria and a higher ERP dispersion was found to be the only clinical predictor of AF inducibility [122]. An interesting finding of this study was that in patients with induced AF, ERP dispersion was similar in those with self-sustained and self-terminated AF. In another cohort of 22 patient-specific biatrial models without personalized ERP, where the substrate was modeled based on LGE-MRI by applying changes in anisotropy, conduction, and remodeled electrophysiology, the 13 models in which AF was induced had significantly larger APD gradients [21]. In our results, scenarios with higher ERP dispersion in patients with a lower ERP mean had higher inducibility.

Previous studies have demonstrated that introducing a ±10% homogeneous variation to the baseline APD increases uncertainty in both the quantity and preferred locations of reentrant drivers [38, 260]. Consequently, it is expected that higher variations would also impact reentry inducibility. In our results, the clinical ERP ranged from 222 ms to 295 ms, indicating a variation of 32.9%. When compared to literature-based ERP values (157 ms), the variation between the literature-based value and the maximum observed clinical ERP reaches 87.9%. We conclude that increased inducibility depends on both reduced mean ERP and increased dispersion.

In this study, electrophysiological and substrate information was obtained through single-chamber electroanatomical mapping. A previous study from our group [210] showed that arrhythmia vulnerability is higher in biatrial models than LA-only models. This increased vulnerability is due to exacerbated electrophysiological and substrate heterogeneity in the RA and the presence of interatrial connections [261]. ERP measurements can typically only be obtained during the mapping procedure, which shortens the time frame available to build the personalized model and run the simulation to a few minutes. This warrants faster simulation approaches [262], reduced-order models or surrogate measurements of ERP distribution if no data from previous procedures can be utilized.

5.4.3 Interaction Between ERP and Substrate Heterogeneities

In current clinical practice, it remains challenging to identify patients for whom PVI will be sufficient to prevent AF recurrence without additional extra-PVI ablation. Six out of seven patients in our cohort had undergone prior PVI, indicating that PVI was ineffective in preventing AF recurrence. It is likely that substrate progression and gaps in PVI promoted AF recurrence [81, 263]. Regional heterogeneities in ERP dispersion are believed to be capable of sustaining AF on vulnerable substrates. Several atrial *in silico* studies have shown that fibrosis regions can anchor or block reentrant drivers [46, 234, 264]. Our results showed that the presence of fibrosis and ablation lesions had a higher impact on vulnerability than ERP. However, the combination of fibrotic substrate and ERP had different effects on vulnerability. Scenarios in which both native fibrosis and ablation lesions were considered had lower vulnerability compared to those having native fibrosis only. A possible explanation is the reduced effective atrial size due to PVI lesions [258]. We tried to simulate a state prior to PVI in scenarios A3 and D3, although it is likely that native fibrosis based on the identification of regions with voltage >0.1 and <0.5 mV might not accurately represent the pre-ablation state. On average, the lower mean ERP in A3 in the presence of native fibrosis without ablation lesions resulted in higher vulnerability compared to a dispersed ERP distribution as in D3. As substrate areas have a significant impact on model inducibility, further studies should focus on providing a more detailed description of their spatial distribution for informing patient-specific models.

5.4.4 Incorporating Uncertainty to ERP measurements

Measured ERP values depend on the time resolution of the S2 coupling interval, with higher resolution leading to more accurate values. To determine whether the addition of ERP perturbations would affect vulnerability, we conducted a sensitivity analysis by running 50 additional vulnerability assessments. Our results suggest that variations in the range of 2-20 ms did not markedly change the number of inducing points, and vulnerability remained similar, indicating that further reductions ($<$10 ms) in the S2 coupling interval would not impact model inducibility. Only when the perturbations were in the range of 50 ms, a higher standard deviation was observed. However, these differences in vulnerability might become more pronounced when functional substrate is incorporated. As mentioned before, reentry dynamics are affected when ERP is personalized, rather than inducibility; therefore, future studies should assess the impact of ERP uncertainty together with substrate information on reentry dynamics.

5.5 Limitations

The small sample size can limit the generalization of our findings. No biatrial electrophysiological mapping data were available; therefore, single-chamber patient-specific models were generated, which did not allow for the assessment of ERP dispersion effects between the LA and RA on arrhythmia vulnerability. In the optimisation process to adapt the cellular electrophysiology model to measured ERP, we reduced the dimensionality of the parameter set space by constraining the range of variation for each parameter in a linear fashion from normal healthy to changes due to persistent AF. We did not personalize CV distribution. The rate-dependent nature of ERP was not evaluated in our study as clinically measurements of the ERP were only obtained at 500 ms S1 cycle length.

5.6 Conclusions

Incorporation of patient-specific ERP values affects the assessment of AF vulnerability. Differences in arrhythmia vulnerability between personalized and non-personalized scenarios should be acknowledged, particularly for patients with low ERP. An increased dispersion of the ERP in personalized scenarios had a greater effect on reentry dynamics than on mean vulnerability values. The incorporation of personalized ERP had a greater impact on inducibility than had a homogeneously reduced ERP, with this effect reversing once fibrosis was included. ERP measurement uncertainty up to 20 ms slightly influences arrhythmia vulnerability. Functional personalization of atrial *in silico* models appears essential and warrants confirmation in larger cohorts.

Chapter 6

Personalization of Activation Times

Personalized Modeling of Atrial Activation and P-waves: a Comparison Between Invasive and Non-invasive Cardiac Mapping

This chapter compares the use of invasive and non-invasive patient-specific activation data for the generation of P-waves and for the assessment of arrhythmia vulnerability *in silico*. Firstly, local activation times from non-invasive electrocardiographic imaging (ECGI) and from minimally invasive electro-anatomical mapping system (EAMS) were used to perform a forward calculation to generate simulated P-waves and compared with measured P-waves from two patients. Secondly, activation and substrate data obtained from 8 patients measured invasively and non-invasively were used to generate patient-specific computer atrial models and to evaluate the effect of the selected clinical data on arrhythmia vulnerability.

6.1 Introduction

Personalized atrial models including anatomical and functional features have been used as mechanistic tools to understand the dynamics of atrial fibrillation (AF) and to predict therapy success [17]. One of the principal features of interest in the process of functional twinning is the incorporation of conduction velocity (CV) information into the personalized model. CV is an electrophysiological (EP) property that describes the direction-dependent

(anisotropic) and spatially heterogeneous speed with which the electrical depolarization wave spreads in the cardiac tissue [31]. Changes in CV can be associated with the location of the underlying arrhythmogenic substrate [266]. When creating a patient-specific digital model for therapy planning, it is therefore important to match this parameter to represent the electrical propagation accurately. Mean CV can be estimated from P-wave duration from the body surface electrocardiogram (ECG) [33]. Regional CV can be calculated from local activation time (LAT) maps obtained from non-invasive electrocardiographic imaging (ECGI) [267] or from invasive intracardiac electrograms (IEGM) [31, 268] from electro-anatomical mapping system (EAMS). LAT maps from EAMS have usually higher resolution and provide a more accurate representation of the electrical propagation as the catheter is placed closer to the cardiac source [269]. On the other hand, ECGI has the advantage of reconstructing atrial activation from torso recordings, eliminating the risk of an invasive procedure.

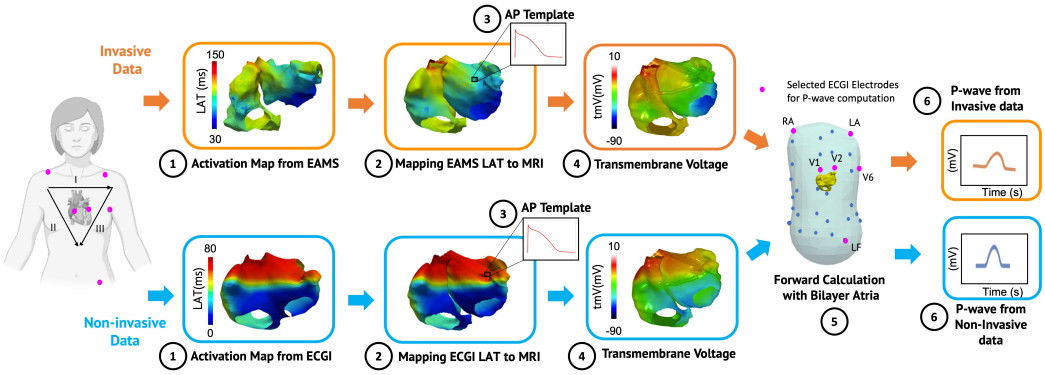

Figure 6.1: Study pipeline. Local activation times (LAT) data were mapped to the magnetic resonance imaging (MRI) geometry and interpolated. A precomputed atrial action potential (AP) was placed in every node of the bilayer model and shifted in time according to the LAT. Extracellular potentials were recovered at selected electrode positions on the torso surface to obtain virtual P-waves.

Several research groups have described processes to create personalized atrial models, these include the use of only pre-procedural information such as magnetic resonance imaging (MRI) and computed tomography scans (CT) [15, 19], or the use of procedural data together with non-invasive imaging techniques [16–18]. However, it remains unclear whether using non-invasive pre-procedural data is sufficient when creating personalized atrial models for therapy planning or if further activation data is required from invasive recordings [38]. Our method generated synthetic P-waves using LAT maps from invasive and non-invasive data. We studied the influence of the selected input data modality on the morphology of the computed P-waves and we finally compared them with the P-waves measured on the surface of the torso.

6.2 Methods

Data from the invasive Carto® 3 EAMS (Biosense Webster), from the non-invasive ECGI system Acorys® (Corify Care), and biatrial geometries from a 3-Tesla CMR scanner (Siemens Healthcare) segmented using ADAS® software (Galgo Medical) were obtained from two patients at Hospital Clínic, Barcelona undergoing catheter ablation of AF (Patient A: female, 61 years with persistent AF and patient B: male 58 years with paroxysmal AF). Both patients are part of the NOISE-AF study (NCT04496336), provided written informed consent and the protocol was approved by the hospital ethics committee. Invasive and non-invasive LAT maps before ablation were obtained during sinus rhythm for patient A and during coronary sinus pacing for patient B. A summary of the study pipeline is presented in Figure 6.1.

6.2.1 Electrocardiographic Imaging Data

The electrical activation of the atria was reconstructed by solving the inverse electrocardiography problem from body surface potential recordings. The torso surface was reconstructed from a 360° video of the patient's chest while wearing the 64-electrode vest. The biatrial geometries from ECGI consisted of a shell of the MRI segmentation having both atria fused. The ECGI shell was already aligned to the original MRI geometry, so no additional co-registration step was needed. To compare the measured P-waves to our computed P-waves, 6 electrodes from ECGI resembling standard ECG locations were used to obtain 9-lead reference traces (I, II, III, aVR, aVL, aVF, V1, V2 and V6).

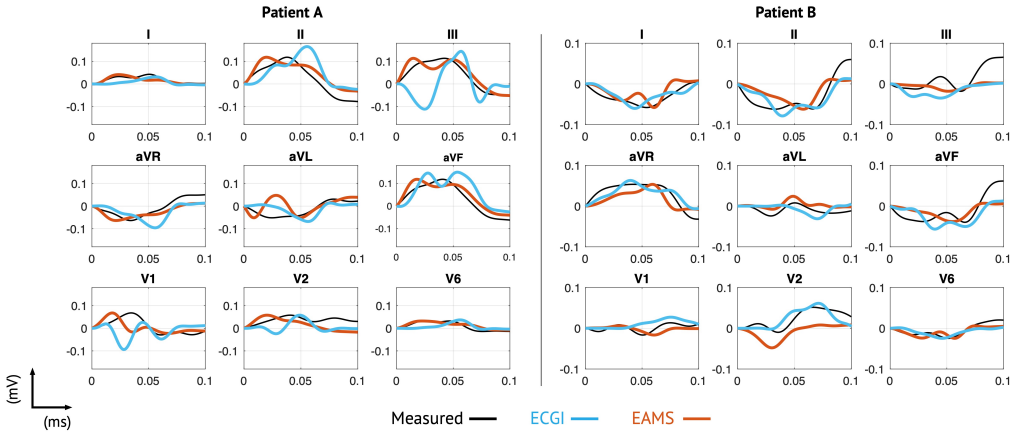

Figure 6.2: Comparison between computed and measured P-waves. Patient A data was obtained during sinus rhythm while Patient B data was obtained during coronary sinus pacing. Measured P-waves are shown in black, the P-waves computed based on EAMS LAT maps are colored in orange, and the P-waves from ECGI LAT data are colored in blue. The signals were aligned and amplified to match the amplitude of the measured P-wave for each lead.

6.2.2 Electroanatomical Mapping Data

Endocardial biatrial geometries and LAT maps were generated from the CARTO® 3 cases using IEGM recordings. The activation sequence was verified to disregard LAT artifacts by leveraging a priori knowledge about the expanding wavefront [49]. We divided the set P of points x in the LAT map into N activation bands Γ_i starting at the earliest activation point (EAP) up to the latest activation point (LAP), with a temporal resolution $dt = 5$ ms:

$$\Gamma_i = \{x \in P \mid \mathrm{LAT(EAP)} + dt \cdot i < \mathrm{LAT}(x) \leq \mathrm{LAT(EAP)} + dt \cdot (i+1)\} \tag{6.1}$$

To disregard outliers, EAP was defined as the center of mass of the region below the 2.5th percentile of the LAT distribution and LAP of those above the 97.5th percentile. The biggest connected island within the 2.5th percentile of the LAT was used to initialize the first reliable region X_0. The domain of each band Γ_i contains M_i islands of points x to be classified as reliable or artifact annotations. Islands are classified as reliable and added to the region C if a maximum distance between the centroid of the current reliable region X_i and the centroid of the island $X_{i,j}$ is fulfilled:

$$\|C(X_i) - C(X_{i,j})\| \leq 1 + i, \mathrm{mm} \tag{6.2}$$

X_i is then initialized with X_{i-1} and a new centroid is calculated in the next iteration. The final LAT map consisted only of reliable regions and was then mapped to the MRI geometry. For image co-registration, the veins and valves were manually clipped using Paraview v5.9.1 (Kitware). Then the centroids of the valve and vein rings were extracted and used as landmarks to perform rigid alignment of the EAMS geometry to the biatrial MRI. The iterative closest point algorithm was used to further co-register the clipped biatrial endocardial geometry to the MRI geometry with Scalismo® [270].

6.2.3 P-wave Forward Computation

Each LAT map was transferred to the MRI geometry using nearest neighbor projection and Laplacian interpolation was performed to fill the gaps in the data distribution. A bilayer model was generated for each patient from the MRI data [49]. LAT maps from ECGI and EAMS on the MRI surface were used to shift a pre-computed atrial action potential template in time for each of the nodes in the bilayer model, respectively. For the forward calculation of virtual P-waves, extracellular potentials on the body surface were recovered using openCARP [221] from the same 6 previously selected electrode locations. The atria were assumed to be immersed in an infinite volume conductor [271]. Simulated P-waves were low-pass filtered with a cutoff frequency of 40 Hz and then individually amplified to match the maximum amplitude of their corresponding measured P-wave per lead. The two sets of virtual P-waves were aligned to the corresponding measured P-wave using cross-correlation and the root-mean-square error (RMSE) was calculated for the whole set.

6.2.4 Personalization Using Invasive and Non-Invasive Data

Non-invasive local activation time (LAT) maps were obtained from electrocardiographic imaging (electrocardiographic imaging) (Acorys v1, Corify, Valencia, Spain) from another eighth patients undergoing AF catheter ablation together with invasive LAT maps from electro-anatomical map (EAM) (Carto v3, Biosense Webster, California, USA). All patients underwent LGE-MRI before the ablation procedure and the geometries were segmented using ADAS 3D software v2.12.0 (Adas3D Medical SL, Barcelona, Spain). The left atrium (LA) mesh from EAM and the extracted LA mesh from ECGI were rigidly aligned to the patient LA-MRI to enable the mapping of the LAT data (Figure 6.3). Image intensity ratio (IIR>1.32) from LGE-MRI and bipolar low voltage areas (LVA<0.5 mV) from EAM were used to define fibrotic substrate in which 30% of the elements were modeled as non-conductive and the rest as TGF-β1 induced electrically remodeled [46, 227]. Monodomain conductivities were adjusted to match LAT from EAM or ECGI [49]. The Courtemanche *et al.* cellular model was adjusted to represent AF-induced electrical remodeling [51]. Arrhythmia vulnerability was assessed by identifying the number of inducing points with S1S2 pacing protocol from various locations using openCARP [32].

6.3 Results

6.3.1 Simulated P-waves

Virtual P-waves obtained from ECGI and EAMS LAT maps were compared to the measured P-waves as shown in Figure 6.2. For the computed P-waves based on the LAT maps derived from both modalities - ECGI and EAMS, the morphology matches the simulated P-waves qualitatively. However, quantitative differences exist. The RMSE was measured for each lead for the whole atrial activation time defined by the P-wave duration on the surface ECG and then averaged among all leads. Values are presented as mean and standard deviation across all 9 leads. In general, the polarity of virtual signals in lead II coincides with the expected direction of the P-wave, meaning that lead II is positive during sinus rhythm and negative during pacing from the coronary sinus. P-waves computed based on ECGI LAT maps show a reduced P-wave duration as seen in the non-invasive LAT map. P-waves computed based on EAMS LAT maps have a similar duration to the measured P-wave on the body surface.

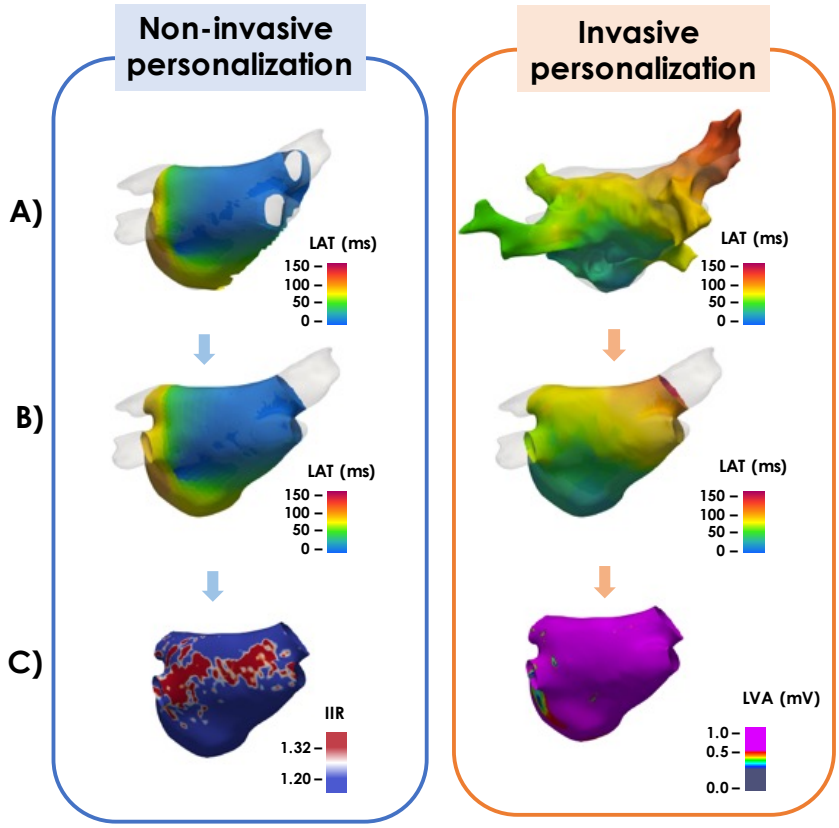

Figure 6.3: Methodology for the mapping and registration of invasive and non-invasive local activation times and substrate data. The left atrium mesh from EAM and the extracted LA mesh from ECGI were rigidly aligned to the patient LA-MRI to enable the mapping of the LAT data. A) Rigid registration, B) LAT mapping into MRI, and C) Substrate annotation. IIR: image intensity ratio, LAT: LAT.

Table 6.1: Root-mean-square error (RMSE) and correlation between measured P-wave and simulated P-wave. Values are presented as mean and standard deviation across all 9 leads.

Patient	LAT data	RMSE (mV)	Correlation
A	ECGI	0.26 ± 0.11	0.69 ± 0.34
	EAMS	0.38 ± 0.31	0.71 ± 0.26
B	ECGI	0.21 ± 0.09	0.71 ± 0.18
	EAMS	0.14 ± 0.05	0.72 ± 0.18

6.3.2 Arrhythmia Vulnerability

The total activation times and patterns were markedly different between modalities with a mean difference of 54.2 ms, ECGI being faster than EAM on average. There was a higher extent of substrate identified by LVA compared to IIR (18.2±23.5% vs. 4.0±8.0%) (Table 7.1). Overall, arrhythmia vulnerability was related to the extent of fibrosis.

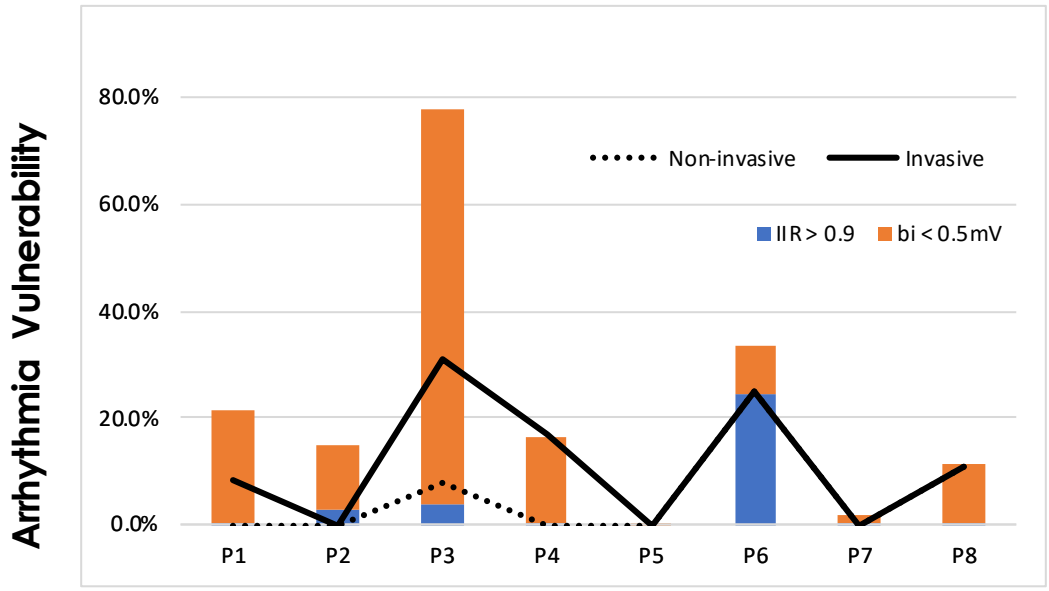

Figure 6.4: Results of vulnerability assessment using invasive and non-invasive local activation times and substrate data. Arrhythmia vulnerability shown in dotted (invasive) and straight (non-invasive) lines. Arrhythmia vulnerability was lower when using only non-invasive data and was related to the extent of fibrosis. IIR: image intensity ratio, bi: bipolar voltage.

Table 6.2: Vulnerability results and substrate data informed by invasive and non-invasive modalities.

Patient	Surface (cm^2)	Substrate		Vulnerability	
		IIR >1.32	bi <0.5mV	Non-invasive	Invasive
P1	14.3	0.1%	21.2%	0.0%	8.3%
P2	11.7	2.6%	12.4%	0.0%	0.0%
P3	15.3	3.9%	73.7%	7.7%	23.1%
P4	8.1	0.2%	16.2%	0.0%	16.7%
P5	10.6	0.0%	0.2%	0.0%	0.0%
P6	8.6	24.3%	9.3%	25.0%	0.0%
P7	10.0	0.3%	1.7%	0.0%	0.0%
P8	9.8	0.2%	11.2%	11.1%	0.0%

IIR: image intensity ratio, bi: bipolar voltage

6.4 Discussion

This work comprises simulations performed to compare the differences in computing P-waves derived from invasive EAMS and non-invasive ECGI LAT maps, and simulations to assess differences in arrhythmia vulnerability when creating atrial *in silico* models using non-invasive data vs. invasive data. For both patients (A and B), ECGI LAT maps had a total activation time shorter than the total duration of the surface P-wave, therefore the P-wave

duration of synthetic signals was also shortened. This can be explained because the slew rate of P-waves is usually slower than the one of the IEGM. In addition, noisy recordings and baseline fluctuations can also affect the ECGI LAT activation threshold. Another cause that may explain the reduction of the ECGI P-wave duration is the loss of information in the septum, which causes the right atrium and left atrium to be activated almost simultaneously.

We assigned the same activation in the endocardial and epicardial layers, this means that the activation was modeled as transmurally homogeneous [272]. Future work could examine the influence of incorporating transmural conduction delay or fibrosis information to personalize our bilayer model. In addition, the impact of the chosen clinical data on the arrhythmia vulnerability of the model can be further tested by using established pacing protocols [32].

6.5 Conclusions

In this study, we computed P-waves from clinically measured invasive and non-invasive LAT maps and showed that the selection of input data affects the activation pattern of the patient-specific model and that the differences between ECGI and EAMS LAT maps are also reflected in the computed P-wave on the body surface. In a cohort of 8 patients, arrhythmia vulnerability was lower when using only non-invasive data and was related to the extent of fibrosis.

Chapter 7

Prediction of Arrhythmia Vulnerability in Larger Cohorts

Insights from Explainable Machine Learning on Biatrial Arrhythmia Vulnerability Assessment

In this chapter, a study is presented that involves the use of modeling and simulation together with a machine learning random forest model in a cohort of 22 patient-specific biatrial models. In particular, three questions guided the research presented in this chapter: What causes some patient-specific models to be more vulnerable to arrhythmia than others? Can arrhythmia vulnerability be predicted using machine learning models, reducing the need for expensive computations of virtual pacing protocols? Which features have the greatest influence on the assessment of arrhythmia vulnerability? This study is among the first to use explainable machine learning to define feature importance in the assessment of arrhythmia vulnerability in a biatrial cohort.

The content of this chapter is taken and adapted from a paper that has been accepted for publication in Computing in Cardiology under open access under Creative Commons CC-BY license [273]. Most passages have been quoted verbatim from the publication.

7.1 Introduction

Atrial fibrillation (AF) is a highly prevalent and complex arrhythmia resulting from the interplay of structural and electrophysiological characteristics, which vary across patients [28]. Generally, a trigger and a vulnerable substrate are the main determinants responsible for initiating and maintaining AF [156]. Ectopic trigger activity originating in the sleeves of the pulmonary veins (PV) has long been recognized to initiate arrhythmia in the atria. Regarding vulnerable substrate, fibrosis, dilation, and remodeling have been associated with an

increased AF propensity [212]. Due to the complex nature of AF, the specific arrhythmia vulnerability for individual patients remains unclear. Personalized atrial computer models can serve as a valuable research tool for unraveling the intricate mechanisms of AF in an individualized manner. *In silico* assessment of arrhythmia vulnerability can assist in quantifying the ease of inducibility of an atrial model based on patient-specific characteristics. Multiple studies have assessed vulnerability in atrial patient-specific models [15, 17, 19, 21, 81, 210]. However, evaluation of arrhythmia vulnerability is computationally expensive and restricts application to centers with access to high-performance computing. In this work, we used patient-specific biatrial modeling and simulation to train a machine learning (ML) model for predicting point-wise inducibility. SHAP explainability was utilized to understand the interaction between patient-specific model features and their effect on the prediction of arrhythmia vulnerability.

7.2 Methods

A general overview of the study methodology is provided in Figure 7.1.

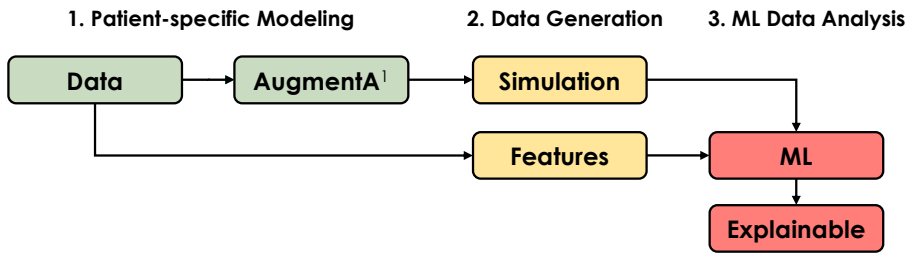

Figure 7.1: Study pipeline. Three main steps comprised the study methodology. ML: machine learning.

7.2.1 Patient-specific Modeling

We generated 22 patient-specific biatrial models (Figure 7.2) from late gadolinium enhancement magnetic resonance imaging (LGE-MRI) data from Hospital Clinic (Barcelona, Spain), and University Heart Center (Freiburg-Bad Krozingen, Germany). Patients provided written informed consent and the ethical committee of both institutions approved the study. Biatrial anatomies were segmented from the MRI blood pool using ADAS 3D software v2.12.0 (Adas3D Medical SL, Barcelona, Spain). Substrate regions were identified using image intensity ratio (IIR>1.2) [185]. Biatrial bilayer models with anatomical annotations, interatrial connections (IAC), and myocyte preferential orientation were generated using AugmentA [49].

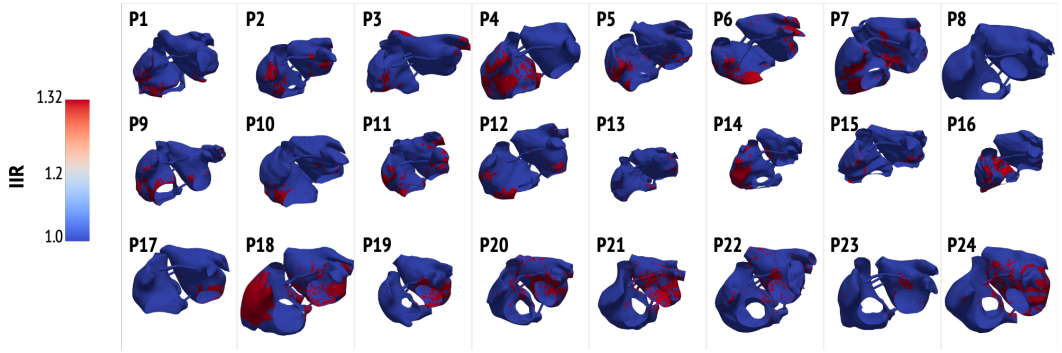

Figure 7.2: Cohort of patient-specific biatrial models. Regions of high intensity are shown in red. IIR:image intensity ratio.

7.2.2 Atrial Electrophysiology Modeling

Cellular electrophysiology of human atrial myocytes was modelled using the Courtemanche M. *et al.* mathematical model [51]. Ionic channel conductances were modified to represent persistent AF [225]. Electrical propagation heterogeneity in the atria was modelled based on anisotropy ratios defined previously [33]. To model substrate in regions of high LGE intensity (IIR>1.2), 70 % of the elements were set to have electrical remodeling, while the rest of the elements had electrical decoupling with $\sigma = 10^{-7}$ S/m [228]. Electrical propagation in the atria was simulated by solving the monodomain equation using openCARP [221]. We ran simulations under three CV (conduction velocity) scenarios. Monodomain tissue conductivities were tuned to achieve a CV in the longitudinal direction of 0.7, 0.5, and 0.3 m/s in the bulk atrial myocardium.

Arrhythmia vulnerability was evaluated with a virtual S1S2 inducing protocol from a set of stimulation points evenly distributed on the biatrial surface with a 2 cm interpoint distance, with 51±15 stimulation points per biatrial model. Vulnerability was defined as the ratio between the number of inducing points to the total number of stimulation points. Binary point inducibility was defined as reentrant activity maintained for at least 1 s [32].

7.2.3 Calculation of Features

We selected features associated with arrhythmia propensity: anatomical factors such as atrial volume, surface, sphericity, and point location; fibrosis characteristics including burden, density and entropy, and the electrophysiological factor CV. Features were quantified globally, and fibrotic features were further assessed locally. Global features are shown in Table 7.1. Sphericity ψ describes the similarity of an object to a sphere and is defined as the ratio of the nominal surface area of a sphere S_n, having the same volume V as the object, to the actual surface area of the object S:

$$\Psi = \frac{S_n}{S} = \frac{\sqrt[3]{36\pi V^2}}{S}. \tag{7.1}$$

Table 7.1: Clinical global features of patient cohort

Feature	LA	RA
Volume (cm^3)	108.2 ± 49.5	100.2 ± 39.7
Sphericity (%)	82.9 ± 5.1	79.4 ± 5.3
Surface (cm^2)	129.0 ± 34.0	128.7 ± 30.7
Fibrosis burden (%)	10.7 ± 8.0	8.4 ± 7.5
Fibrosis density (%)	6.7 ± 5.7	6.1 ± 6.0
Fibrosis entropy (%)	5.2 ± 3.8	3.3 ± 2.3

LA: left atrium, RA: right atrium. Values are shown as mean $\pm$ SD.

PVs and appendages were excluded in ψ calculation. Fibrosis burden **B** was obtained from the normalized IIR derived from LGE-MRI. According to Zahid *et al.* [21], border zones with high fibrosis density **D** and entropy **E** promote reentrant activity. To calculate fibrosis features in each node, we identified subsets within a radius of 1 mm, i.e. maximum edge length. We quantified **D** as the ratio between the number of fibrotic nodes $\mathbf{N}_\mathrm{f}$, divided by the total number of nodes **N** in the subset, and assigned that value to the centre node. In addition, local **E** for each node i in the subset was calculated based on Shannon entropy:

$$\mathbf{E} = \sum_{i=1}^{\mathrm{N}} \frac{-p_i \cdot ln\,(p_i)}{\mathbf{N}}, \tag{7.2}$$

where p_i is the fraction of nodes in the subset with a node type (fibrotic or non-fibrotic) different to the node in the centre. An example of the calculation of local fibrotic features is shown in Figure 7.3.

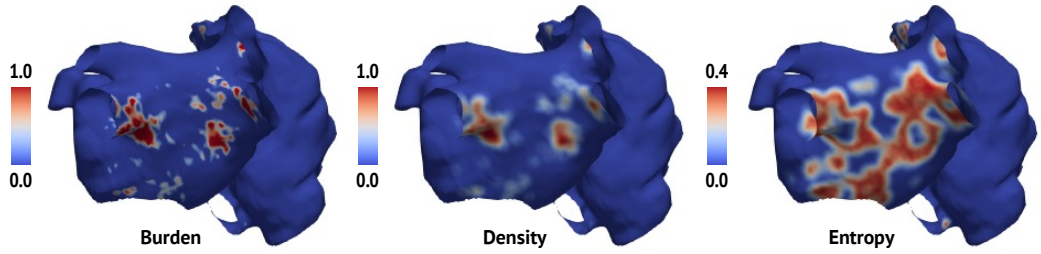

Figure 7.3: Biatrial fibrotic features for patient 1. Density and entropy were calculated for each node with a defined subset of radius equal to cell edge length (1 mm).

We established five six reference regions (Figure 7.4) around each stimulation point: three circles (conjunction) and three concentric rings (disjunction). The regions had radii of 5, 10, and 20 mm, representing near, mid, and far proximity. We calculated the mean E and B for each reference region.

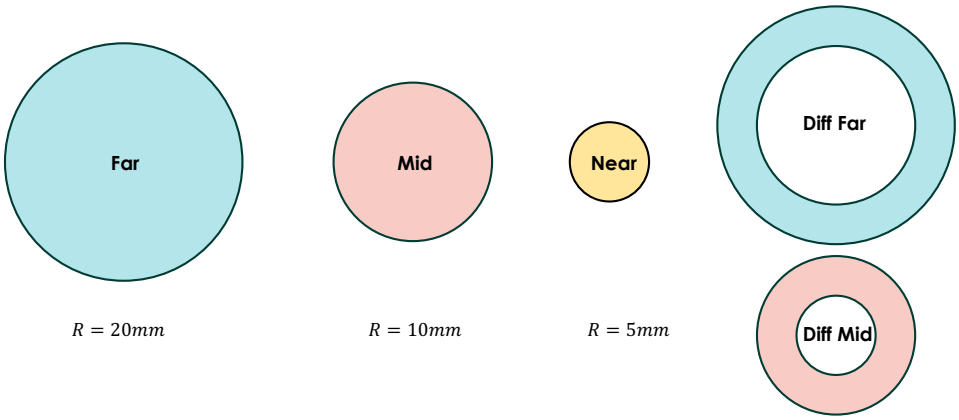

Figure 7.4: Regions for the calculation of fibrotic features. Radii ranging from 20,10 and 5 mm, namely far, mid and near proximity.

Finally, we included four positional features: the atrial chamber and three Laplace-Dirichlet rule-based coordinates (φ_{ab}, φ_{v}, and φ_{r}) for each stimulation point. The Laplace equation was solved in openCARP as contained in AugmentA [49] with Dirichlet boundary conditions to find a solution φ. The value and domain of the boundary conditions for the three Laplace equations are shown in the Figure 7.5.

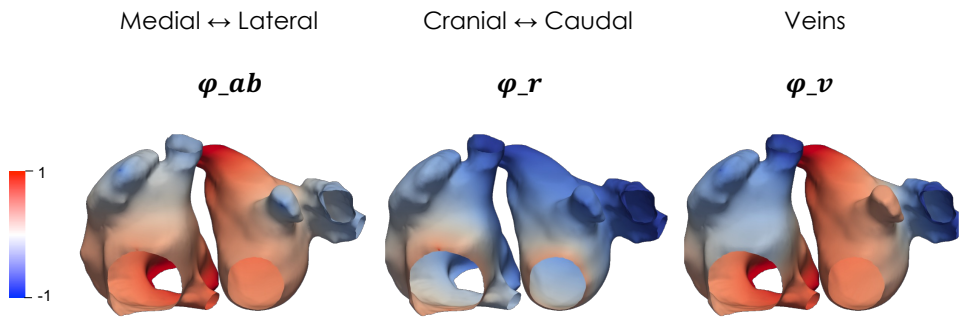

Figure 7.5: Calculation of positional features using Laplace–Dirichlet rule-based method coordinates. Position can help identify inducing points in the proximity of certain anatomical structures such as the appendages (φ_{ab}), atrio-ventricular valve rings (φ_{r}), and pulmonary veins (φ_{v}).

7.2.4 Explainable Machine Learning

A random forest classifier (RF) was trained to identify stimulating points inducing reentry based on feature characteristics. The performance of different RF instances was evaluated using the area under the receiver operating characteristic curve (AUC ROC) metric and ten-fold cross-validation. The optimal hyperparameter setting was used to train the final RF classifier with an 80:20 training and test split. Data were split on a patient basis rather than

individual points to avoid overfitting. To improve the performance of the RF algorithm, we evaluated sample normalization, modification of RF parameters, class weights and extraction of different feature subsets. For explainability, SHAP (SHapley Additive exPlanations) were selected to assess the impact of each feature on the prediction of inducibility as proposed before [274].

7.3 Results

A total of 1438 reentries were induced from 7131 stimulating points across the 22 biatrial models. The pacing protocol duration was 765±256.2 min per biatrial model, with each stimulation point lasting 15±2.4 min, utilizing 4 nodes×40 CPU cores (Intel Xeon Gold 6230 2.1GHz). The RF ML model was exposed to 5704 stimulating points with 27 features and required 0.6 s for training and 0.01 s for validation with 1427 stimulating points (Intel Core i5 3.1GHz). The RF classifier achieved an AUC of 0.75±0.03 (Figure 7.6). AUC with feature selection (top 5 features of SHAP from Figure 7.7) was 0.69±0.05, with balanced classes 0.72±0.05 and with sample normalization 0.66±0.05.

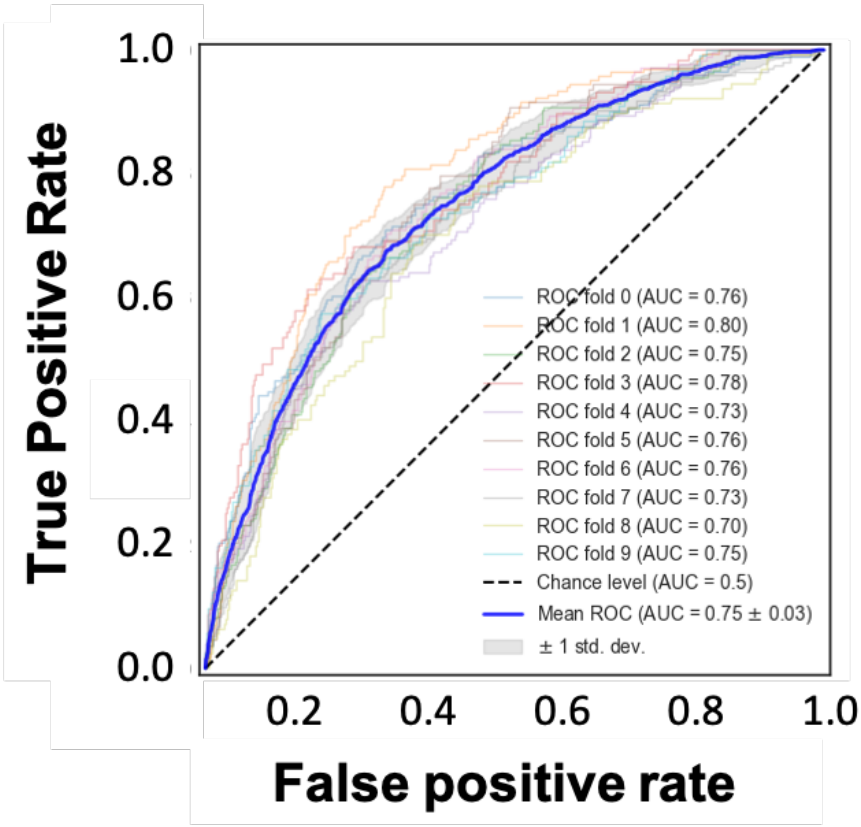

Figure 7.6: Receiver operating characteristic (ROC) of the random forest algorithm with ten-fold cross validation. AUC: area under the curve.

SHAP identified the features showing the highest impact on the prediction of point inducibility (Figure 7.7). Among global features, CV had the greatest impact on inducibility prediction, whereas fibrosis density in the mid-proximity regions (10 mm) was the most influential local feature.

7.4 Discussion

This study assessed arrhythmia vulnerability in 22 biatrial models with personalized anatomy and substrate informed by LGE-MRI. We trained and evaluated an ML RF classifier to predict point-wise inducibility with both global and local features. Modeling and simulation combined with ML algorithms can enhance mechanistic understanding of AF and provide digital solutions compatible with clinical timeframes. Previous studies demonstrated this potential by exploring the role of LA native fibrosis and post-ablation lesions on arrhythmia inducibility using explainable ML [274]. Our work is one of the first studies to assess feature impact on inducibility prediction in a biatrial cohort.

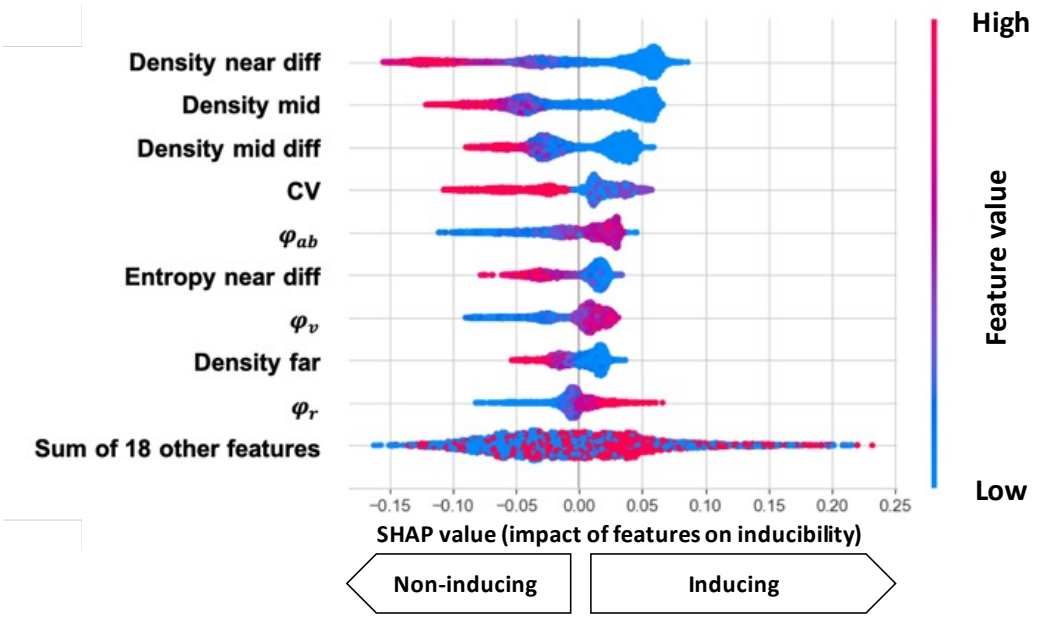

Figure 7.7: Beeswarm explainability plot of SHAP values showing the impact of each feature on point inducibility predictions. Points in the plot represent the features for every stimulation point and the color represents their associated SHAP values. Points at the right of the midline are indicative of a predictive impact towards induction, whereas those on the left suggest a predictive impact towards non-induction. CV: conduction velocity, conj: conjunction, disj: disjunction near, mid and far: 5, 10, and 20 mm.

Fibrosis density at near and mid proximities had the highest impact on model inducibility prediction. Specifically, low fibrosis density in the surrounding 10 mm was associated with an increased inducibility. The study by Zahid *et al.* proposed that regions with higher fibrosis density aid reentrant activity [21]. Our results indicate that for inducibility, the areas surrounding the stimulation point should have a low fibrosis burden to facilitate impulse propagation. Among global features, CV had the highest impact on inducibility prediction. Previous studies have shown the impact of global CV on model vulnerability, however CV was not included as feature in their ML model [274]. A decrease in global CV increases vulnerability of biatrial models [275]. High CV was associated with reduced inducibility. In terms of positional features, φ_{ab} had the greatest influence on the model prediction. Stimulation points located closer to the interatrial septum (low φ_{ab}) were associated with increased inducibility, while those closer to the appendage and lateral walls were associated with non-inducibility. Interatrial connections may facilitate the formation of reentrant circuits between the LA and RA. Sphericity, LA volume, and RA volume showed minimal impact on the prediction of inducibility.

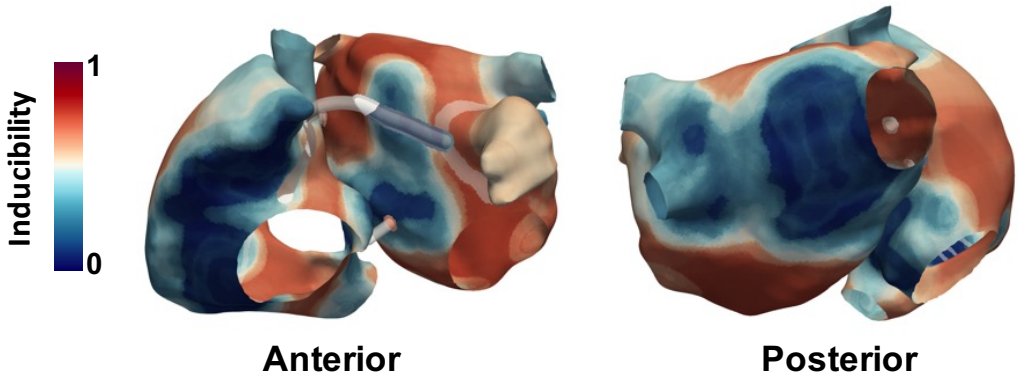

Figure 7.8: Analysis of model inducibility prediction Color represents inducibility, where red denotes non-inducing and blue indicating inducing regions. Ground-truth inducibility from electrophysiological model. Mesh courtesy of Pascal Maierhofer.

Our results demonstrate moderate prediction accuracy, as evidenced by AUC-ROC. The ML classifier had a good performance in detecting true non-inducible points, as depicted in Figure 7.8. Our results showcase the complexity of point inducibility, suggesting that induction depends on the interplay of global and local factors, some of which might extend beyond the 20 mm proximity. We did not include other features associated with AF propensity, such as wall thickness, fat infiltration, and endo-epi dissociation. We did not incorporate personalized electrophysiology information. We utilized LGE-MRI data to get information on the substrate; however the discrepancy in the spatial distribution between low voltage areas and LGE-MRI is likely to influence vulnerability [17, 28]. To increase accuracy, expanding the sample size an incorporating further features could help to develop a computationally efficient and sufficiently accurate model.

7.5 Conclusions

Our work is one of the first studies to assess feature impact on arrhythmia vulnerability in a biatrial cohort. Fibrosis density measured at 10 mm from the stimulation points and global CV were the features showing the highest impact on point inducibility prediction. Our study suggests that ML models offer a promising tool for predicting arrhythmia vulnerability *in silico*, potentially reducing the need for expensive computations in virtual pacing protocols and bridging the gap for clinical application of patient-specific models with compatible clinical timings.

PART III

CLINICAL TOOLS

Chapter 8

Biatrial Regionalization: 15-Segment Model

For the study of atrial fibrillation (AF), it can be useful to quantify regional differences of functional and substrate-related features in the atria and link these differences to therapy response or disease prognosis. Multiple studies have already performed quantitative regional analyses in the atria, each defining their own boundaries between regions for their respective aims [186, 187, 276–288]. However, each unique regional definition was not intended to be shared among institutions, making comparisons among studies unfeasible. Additionally, the complex anatomy of the atria hinders the creation of a standardized definition of regions, unlike the ventricles where a segment definition has already been proposed more than 20 years ago [289].

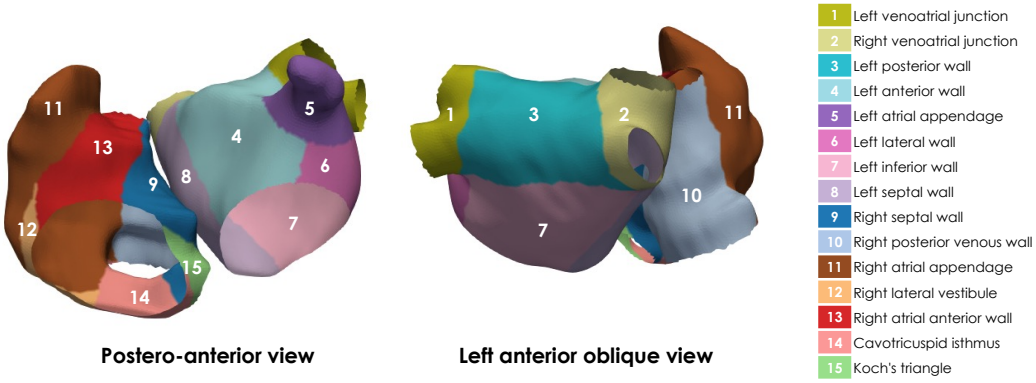

Figure 8.1: The 15-segment biatrial model definition proposed by the PersonalizeAF consortium. Division generated with [251], mesh courtesy of Christian Götz.

In this section, a summary of the 15-segment biatrial model definition from the PersonalizeAF consortium is presented (Table 8.1). The main goal of the proposed nomenclature is to provide standardized segment definitions, allowing for consistent and reproducible biatrial regionalizations. The manuscript containing a full description of the segments and reference points has been submitted for publication and is currently under review. The KIT algorithm to perform biatrial regionalization was developed by Christian Götz during his Master's thesis project and was further adapted based on feedback from the consortium; the algorithm is publicly available under [251]. For further details regarding reference point definition and description of segment boundaries, the reader is refer to the manuscript.

Table 8.1: Segment descriptions and boundary definitions for biatrial regionalization. (*Left atrium)*

Number	Segment	Description	Boundaries definition	Ref. points
1a	Left venoatrial junction	Myocardial sleeves extending from the atrial antra on the left side	Shortest circumference path around the left PV antra connecting the uppermost point of the antral region (A) and the lowermost (B) in the longitudinal axis on the left side	A,B
1b	Left lateral ridge	Infolding between the left pulmonary veins and the left atrial appendage included in the left venoatrial junction segment	Shortest geodesic path connecting uppermost point of the antral region (A) and the intersecting point with the LAA (G)	A,G
2	Right venoatrial junction	Myocardial sleeves extending from the atrial antra on the right side	Shortest circumference path around the right PV antra connecting the uppermost point of the antral region defined by point C and the lowermost by point D in the longitudinal axis on the right side	C,D
3	Left posterior wall	Venous component of the LA	The superior border consists of the geodesic path connecting point A and C, also known as roof line, and the inferior border connecting point B and D	A,B,C,D
4	Left anterior wall	Region harbouring the principal interatrial connection of the Bachmmann Bundle	The superior border consists of the geodesic path connecting point A and C, also known as roof line, to the superior aspects of the MV ring defined by points E and F	A,B,E,F
5	Left atrial appendage	Protrusion from the LA	Junction of the LAA to the LA body passing through point G marking this intersection	G
6	Left lateral wall	Lateral aspect of the LA including the mitral isthmus	The inferior border consists of the geodesic path connecting point F and point H in the MV ring, the lateral part connects point H and B	F,H,B
7	Left inferior wall	MV vestibulum	The superior border consists of the geodesic path connecting point B and D, and inferiorly to the border connecting point I and H	B,D,H,I
8	Left septal wall	Interatrial septum adjacent to the right venoatrial junction	The superior border consists of the geodesic path connecting point C and D,and the inferior border connecting point E and I	C,D,E,I

LAA: left atrial appendage, LA: left atrium, MV: mitral valve

Table 8.2: Segment descriptions and boundary definitions for biatrial regionalization. (*Right atrium*)

Number	Segment	Description	Boundaries definition	Ref. points
9	Right septal wall	Interatrial septum in the RA	The inferior border consists of the geodesic path connecting the most inferior aspect of the coronary sinus in point J and the most septal part of the IVC point K, and the superior boundary defined by the most septal aspect of the SVC in point L and point M in the tricuspid valve ring	J,K,L,M
10	Right posterior venous wall	Area between the SVC and IVC	The superior border consists of the geodesic path connecting point L and O, at the SVC, and the inferior border connecting point K and N at the IVC	L,O,K,N
11	Right atrial appendage	Triangular protrusion in the RA	Staring with the point of maximum curvature between the RA body and the RAA denoted as point P, to the most lateral aspect in point Q, to the inferior aspect of the lateral vestibule in point R, and point S which is the most superior aspect of the SVC	P,Q,R,S
12	Right lateral vestibule	Region encircling the tricuspid valve	The inferior border consists of the geodesic path connecting the infero-lateral aspect of the tricuspid ring in point T and point N in the IVC, the superior border consists of the geodesic connecting the supero-lateral point U in the tricuspid valve ring and point Q	T,N,U,Q
13	Right atrial anterior wall	Region harbouring the principal interatrial connection of the Bachmmann Bundle	The superior border consists of the geodesic path connecting point S and L, the inferior border connecting point U and M, and the lateral border connecting S, P and Q	L,S,P,Q,U
14	Cavotricuspid isthmus	Region in the proximity of the IVC and the TV	The inferior border consists of the geodesic path connecting point K and point N in the IVC and the point V and T in the TV	N,K,J,V,T
15	Koch's triangle	Region in the proximity of the CS and the TV	The apical border consists of the geodesic path connecting point M and point V in the TV ring, the inferior border connects point V and J at the CS ostium and the basal border is defined by the geodesic between point M in the TV ring and point J	J,M,V

AF: atrial fibrillation, RA: right atrium, RAA: right atrial appendage, TV: tricuspid valve

Chapter 9

Ablation Planning Tool

This chapter provides a detailed description of the virtual reality ablation planning tool, Deliverable D2.4, within the scope of the PersonalizeAF project. The tool is an interactive software designed for planning and guiding ablation procedures based on simulations performed with the electrophysiology simulator openCARP [220, 221]. The chapter presents the software features and lists all the necessary software and hardware requirements for installing the ablation planning tool. The software design and prototype were developed collaboratively with Pascal Maierhofer, who primarily contributed to the code development. The tool is publicly available in [290].

9.1 Introduction

The architecture of the ablation planning tool is illustrated in Figure 9.1.

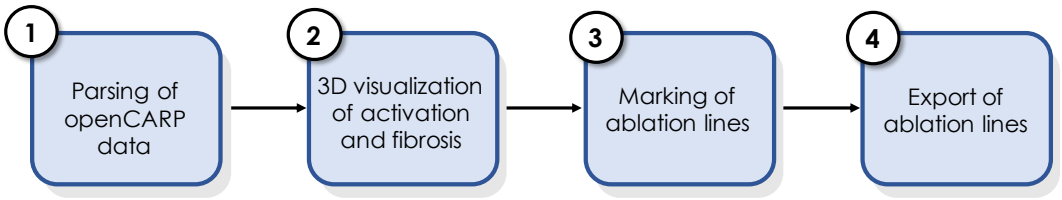

Figure 9.1: Architecture of the ablation planning tool. The four main steps covered by the software are shown.

1. **Parsing of data**: the software reads in files that describe the geometrical heart model, simulated data, and additional clinical features such as fibrotic tissue or ablation lines.
2. **Visualization of activation and fibrosis:** converts simulated transmembrane voltages and fibrotic tissue notation into a color spectrum that can be displayed dynamically on the heart model and interpreted by the user. This heart model visualization can be

rendered in a 3D virtual reality environment (3D headset required) or displayed in 2D on a standard monitor.

3. **Marking ablation lines:** ablation lines can be loaded from a file or manually drawn on the heart model by the user.
4. **Exporting ablation lines:** marked ablation lines can be exported to conduct further assessments and simulations.

9.2 Software Scope

The ablation planning tool is an interactive virtual reality (VR) software designed to visualize patient-specific heart models and clinical data from electro-anatomical mapping system (EAMS) and/or magnetic resonance imaging (MRI), along with the results from electrical activation simulations on the patient-specific models using the cardiac electrophysiology simulator openCARP [220, 221]. The software can display atrial fibrosis patterns informed by EAMS low voltage areas (LVA) or late gadolinium enhancement (LGE) MRI. If provided by the user, ablation lesions can also be imported and rendered. Additionally, the tool offers the possibility to manually draw potential ablation targets on the patient-specific anatomical model. The main goal of the ablation planning tool is to help visualize electrical wave propagation together with patterns of fibrotic substrate and to better understand the nature of the simulated reentries. We developed a planning tool with the capability for an immersive VR experience, allowing the user to better interact with the heart model. The interaction is user-friendly and reduces the need for multiple software tools to visualize clinical data and simulation data in parallel.

9.3 Motivation

Catheter ablation (CA) is a procedure that aims to make arrhythmogenic cardiac tissue harmless by delivering radiofrequency energy, cryoablation, or electroporation. The rationale behind CA is to eliminate tissue suspected to contribute to arrhythmia initiation and maintenance. Pulmonary vein isolation (PVI) is the standard minimally invasive CA treatment for patients suffering from atrial fibrillation (AF) [1]. However, in terms of recurrence, PVI alone has achieved less than a 50% success rate after 12 months, especially for patients with persistent AF. Additional substrate modification strategies such as lines of block, ablation of areas with complex fractionated atrial electrograms (CFAE), posterior wall ablation, and vein of Marshall ablation have not yet proven significantly beneficial in reducing AF recurrence [291, 292]. Clinicians still face the question of how to treat patients, especially when AF recurs after PVI. Therefore, the value of this planning tool is to provide a visualization platform to facilitate the analysis of personalized simulations and clinical data, improving

the understanding of the patient-specific arrhythmogenic substrate and aiding in the ablation planning process.

9.4 Intended Users

The tool is meant to be used by researchers in the field of cardiac computational electrophysiology, including engineers, computer scientists, and medical doctors.

9.5 Intended Use

This tool is intended for research use and demonstration purposes only. It is not intended for medical diagnosis or professional medical advice. This tool was designed and built with a focus on the visualization of openCARP simulation data. openCARP is an electrophysiology simulator freely available for academic use with public source code [220, 221]. Therefore, the file formats of openCARP are used, which are interoperable with established standards like the Visualization Toolkit (VTK). For details about the data format, please refer to the openCARP manual [293]. In preparation for using this tool, the following data should be available and stored inside a folder:

- Mesh of the heart model, consisting of a *.pts* file (points) and *.elem* file (connecting elements) defining the patient-specific geometry. A description of the creation of patient-specific geometries suited for electrophysiology simulations can be found here [49]. The code for mesh generation is found here [294].
- Time series of the transmembrane voltage at all nodes to view the propagating wave in the *.igb* format (output of openCARP simulation).
- Element IDs of fibrotic tissue in the *.regele* format consist of non-conductive and slow-conductive files. The *.regele* format comprises a list of IDs with the number of elements of the list at the top. The distribution of fibrotic tissue is extracted from clinical imaging and/or mapping data.

9.6 Code Availability

The code and documentation of the D2.4 tool have been published in compliance with the FAIR principles [295] for research software and is publicly available [290].

9.7 Code Features

In Figure 9.2, we show a diagram of the main software features and the interaction between them. All these features lead to a user-friendly tool for visualizing computer simulations, allowing the study of the role of reentrant patterns.

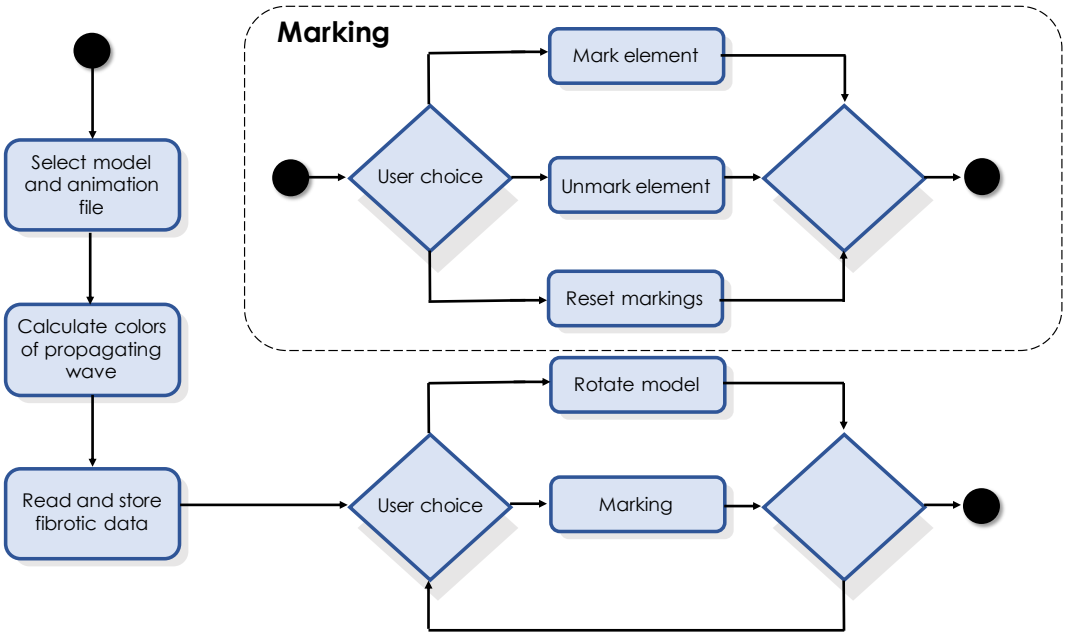

Figure 9.2: Sequence of the main software features starting at the top left in the arrow direction. The marking sequence is detailed at the top.

The ablation planning tool has the following features:

- **/F000/** File selection panel to choose the files for model rendering. Including *.pts* and *.elem* for the mesh, *.igb* for transmembrane voltages (wave excitation dynamics), and *.regele* for fibrotic tissue.
- **/F001/** Read in of mesh data in the form of *.pts* and *.elem* files.
- **/F010/** Support of *.igb* files to load time series of pointwise data (mainly transmembrane voltages).
- **/F015/** Display of this time series of transmembrane voltages in the tool to visualize, for example, reentry tachycardias.
- **/F017/** Display of a custom coloring method for the different transmembrane voltages including a color bar, which shows the minimal, middle, and maximal potential.
- **/F020/** Support of *.regele* files to load severe and mildly fibrotic tissue and display it on the patient-specific anatomical model.
- **/F025/** Display of fibrotic patterns and transmembrane voltage animation on the model.

- **/F030/** Marking tool to point at regions with the help of a VR controller. This marking tool can also be used to annotate possible ablation targets or draw ablation lines.
- **/F040/** Correction of markings with the help of an erase and reset tool.
- **/F051/** Head movement and rotation tracking to view the model from 360 degrees.
- **/F052/** Intuitive rotation of the whole model around two axes with the VR controllers.
- **/F055/** Movement in the scene with the VR controllers for confined spaces.
- **/F056/** Movement in the scene through walking around the model with the VR headset if enough space is available.

9.8 Graphical User Interface

The following Figure 9.3 shows the graphical user interface of the planning ablation tool:

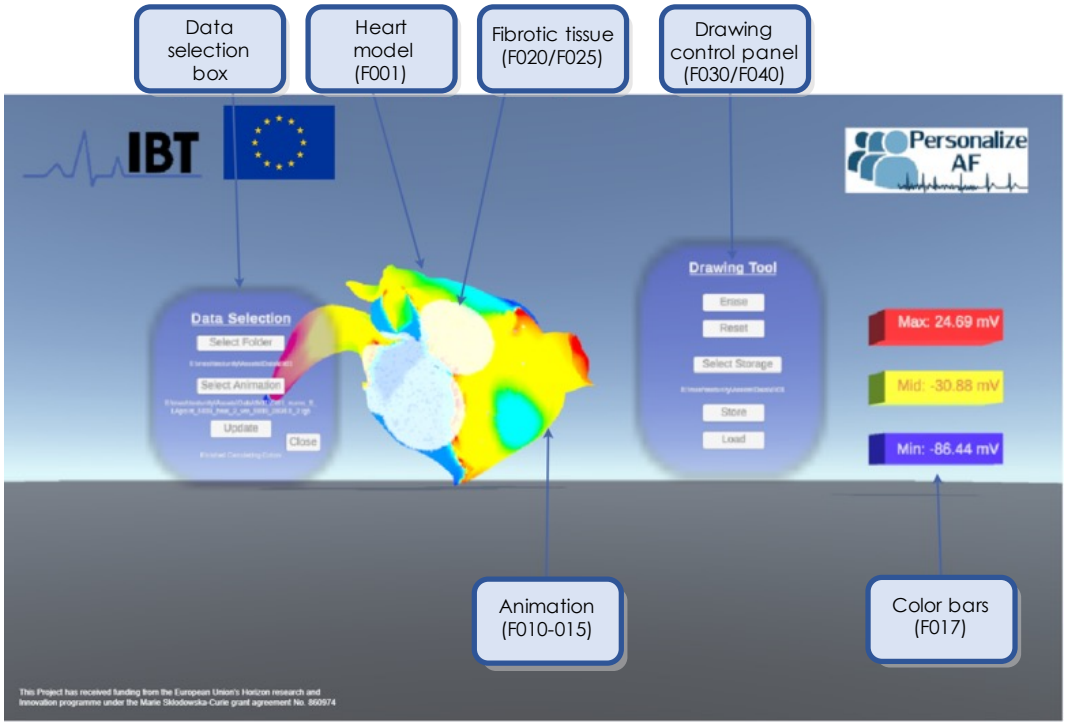

Figure 9.3: Graphical user interface. Main software features are shown in the boxes in blue. Numbers in parenthesis correspond to feature numbers.

9.9 Hardware Requirements

The following requirements are essential to use the planning tool:

- **HTC VIVE (Valve, HTC)**
  - Headset
  - 2 Controllers
  - 2 Tracking boxes
  - Connector

- **Suitable PC for the HTC Vive, according to SteamVR minimal requirements:**
  - Intel Core i5-4590/AMD FX 8350 equivalent or better
  - 4 GB of RAM
  - NVIDIA GeForce GTX 1060, AMD Radeon RX 480 equivalent or better
  - 1x USB 2.0 or newer, HDMI 1.4, DisplayPort 1.2 or newer

9.10 Software Requirements

The minimum software requirements needed to run the ablation tool:

- Operating system version: Windows 7 (SP1+), Windows 10 or Windows 11, 64-bit versions only
- CPU: X64 architecture with SSE2 instruction set support
- Graphics API: DX10, DX11, and DX12-capable GPUs
- Additional requirements: Head-mounted display of the HTC Vive family

PART IV

FINAL REMARKS

Chapter 10

Conclusions

In summary, this thesis aimed to evaluate the impact of selected input data on the arrhythmia vulnerability of patient-specific atrial models, as stated in the main research question. Three main projects guided the direction of this thesis: 1) anatomical personalization: a comparison of monoatrial versus biatrial models (**Chapter 4**), 2) functional personalization: a comparison of models with personalized refractory period versus non-personalized models (**Chapter 5**), 3) functional and substrate personalization: a comparison of pre-procedural versus procedural data (**Chapter 6**). In addition, vulnerability to arrhythmia in larger cohorts was evaluated and predicted using a machine learning classifier with the use of clinical and imaging features (**Chapter 7**). Finally, two clinical tools were developed: a division software to perform regionalizations of the atria (**Chapter 8**), and a virtual reality tool to visualize electrophysiology simulations (**Chapter 9**). In the following part, the key research questions that addressed the main research question are presented.

1. **Which role does the right atrium play in the development of arrhythmia *in silico*?**

   In the simulations, the right atrium (RA) was found to have two distinct roles: initiator and facilitator of arrhythmias. Firstly, the RA acted as an initiator, due to increased electrophysiological heterogeneity arising from structures such as the pectinate muscles, crista terminalis, and tricuspid valve. Despite modeling a lower amount of fibrosis compared to the left atrium (LA), the RA exhibited the highest vulnerability in the severe state (S). Secondly, the RA facilitated the induction of arrhythmia from points within the LA. The inclusion of the RA uncovered 5.5 ± 3.0 inducing points in the LA biatrial scenarios that did not induce in the monoatrial configuration. The results of this study indicate that the RA increases the likelihood of new reentrant circuits influenced not only by the presence of inter-atrial connections and larger size, but also by changes in the wavelength due to regional differences in conduction velocity and effective refractory period. Thus, the RA contributes to the development of arrhythmia *in silico*, not only through inducing points present in the RA, but also by facilitating inducibility in the LA.

2. What is the impact of the right atrium in the development of arrhythmia under different substrate remodeling states?

The impact of the RA in different remodeling states was assessed first by comparing arrhythmia vulnerability of the LA in monoatrial and biatrial configurations, and secondly by evaluating the tachycardia cycle length (TCL) of induced reentries. Only one reentry was induced in the healthy state (H) in the biatrial configuration, suggesting that in general, no reentries can be induced in the H state. Without the RA, the vulnerability of the LA was markedly higher in the S than in the mild state (M). Incorporating the RA notably diminished this difference in LA vulnerability. Incorporating the right atrium increased the mean vulnerability of the left atrium by 115.8% in the M state and by 29.0% in the S state. There were no significant differences in the TCL of RA-induced reentries between M and S states. However, for LA-induced reentries, adding the RA resulted in 5.5% significantly slower reentries in the M state and 7.2% significantly faster in the S state. Incorporating the RA had a state-dependent effect on arrhythmia dynamics.

3. To what extent does incorporating personalized effective refractory period measurements influence arrhythmia vulnerability of the patient-specific model?

To assess the influence of incorporating measurements of the effective refractory period (ERP) on arrhythmia vulnerability, four different scenarios were generated and compared for each of the seven patient-specific atrial models in the cohort. In general, non-personalized scenarios had a shorter ERP and reduced dispersion (158.9 ± 5.3 ms) compared to personalized scenarios (254.0 ± 32.7 ms). Among all scenarios, the homogeneous non-personalized scenario A had the lowest vulnerability ($3.4 \pm 3.9\%$), while the regional personalized scenario C had the highest vulnerability ($9.0 \pm 5.1\%$). Heterogeneities in the form of regions in scenario C promote unidirectional blocks, thereby increasing vulnerability, while the homogeneous scenario A makes it less likely to induce reentry even with a shorter ERP. Incorporating the ERP as a continuous distribution, as in scenario D, slightly decreased the vulnerability of the models compared to the state-of-the-art heterogeneous non-personalized scenario B ($7.6\pm3.4\%$ vs. $7.0\pm3.6\%$, p=0.81). Additionally, modeling the ERP as a gradient in scenario D significantly increased vulnerability by 51.43% compared to homogeneous scenario A ($3.4\pm3.9\%$ vs. $7.0\pm3.6\%$, p=0.04). This finding suggests that the incorporation of personalized ERP in the form of gradients had a greater impact on vulnerability than had the mean value of the ERP. There were no significant differences in the TCL of scenarios A and B (167.1 ± 12.6 ms vs. 158.4 ± 27.5 ms, p=0.43), both of which are not personalized, nor there were significant differences between scenarios C and D, both of which are personalized (265.2 ± 39.9 ms vs. 285.9 ± 77.3 ms, p=0.31). However, personalized scenarios had significantly slower TCL compared to non-personalized scenarios (p<0.001). Increased ERP dispersion had a greater effect on reentry dynamics than on the absolute value of vulnerability.

4. **How does arrhythmia vulnerability change when both the effective refractory period and substrate are personalized?**

   To evaluate the interaction between ERP and substrate, scenarios A and D, representing non-personalized homogeneous and personalized continuous configurations respectively, were compared to their counterparts with fibrosis and ablation scar (A2 and D2), as well as to scenarios with only fibrosis (A3 and D3). There was a higher increase in vulnerability when only fibrosis was present, e.g. scar modeled as healthy, compared to scenarios with both fibrosis and scar. The reduced atrial size in A2 and D2 due to scar from pulmonary vein isolation contributed to the decreased vulnerability. When comparing the differences between A2 vs A3 and to D2 vs D3, the difference was more pronounced between scenarios D2 and D3, suggesting that the gradient in scenarios D aided in increasing vulnerability. These observations indicate that changes in vulnerability attributed to personalized ERP persist even in the presence of fibrosis, suggesting that the effect of the ERP personalization cannot be neglected.

5. **What is the effect of the interplay between the personalization of activation and substrate on arrhythmia vulnerability?**

   In the presented patient cohort, total activation times and patterns were markedly different between modalities with a mean difference of 54.2 ms, electrocardiographic imaging being faster than electro-anatomical map on average. Therefore it was not possible to fully address this question. Also differences in the extent of substrate identified by low voltage area compared to image intensity ratio (18.2±23.5% vs. 4.0±8.0%) made the comparison overall challenging. In general, arrhythmia vulnerability was related to the extent of fibrosis which was lower in the non-invasive data.

6. **Can machine learning models be used to predict arrhythmia vulnerability *in silico*?**

   Indeed, but only to a certain degree with current methodology. The results reveal a moderate prediction accuracy of 0.75 ± 0.03, as exemplified by the AUC-ROC. The machine learning (ML) classifier had a good performance in detecting true non-inducible points. Fibrosis density measured at 10 mm from the stimulation points and global conduction velocity were the features showing the highest impact on point inducibility prediction. Due to the complex nature of AF, it is likely that point inducibility depends on the interplay of multiple factors, which may extend beyond the 20 mm proximity. The presented classifier may be a fast alternative for assessing arrhythmia vulnerability *in silico* without expensive computations of virtual pacing protocols, thus aiding the transition to clinical applications.

Chapter 11

Outlook

In this chapter, future directions for evaluating the effect of different personalization and modeling strategies of atrial digital twins are described, based on the observations and experience gained during this doctoral thesis. A question guiding future research is identifying which clinical data are necessary to create patient-specific digital twins to inform AF (AF) treatment and quantifying the impact on model behavior.

Modeling of Interatrial Connections

One of the biggest challenges in developing biatrial models for guiding AF treatment is modeling interatrial connections (IAC). Some studies have highlighted the importance of IAC for the maintenance of reentrant circuits in patient-specific computer models [233, 275]. Therefore, assessing different modeling approaches for IAC and their impact on arrhythmia maintenance is crucial for advancing biatrial modeling toward clinical implementation. As mentioned in Chapter 1, the limited spatial resolution of current imaging modalities restricts the accurate representation of cardiac structures, including IAC. This limitation has led to the development of various strategies for representing IAC in patient-specific computer models, such as modeling a single connection in the interatrial septum [15], defining multiple connections through rule-based definitions [71, 74], developing tubular structures [49, 296], defining flattened bundles in the endocardium and epicardium [297], or creating linear elements joining both atrial chambers [46]. For instance, future studies could assess the effect of modeling IAC on arrhythmia vulnerability by evaluating different configurations, including variations in the number of bridges, their locations, and their forms.

Personalization Considering Sex-specific Differences

The creation of patient-specific digital twins will still require the use of population-based data in the near future. As much research has predominantly conducted on male populations, incorporating data from female populations can help mitigate current biases [298]. Sex has been overlooked for many years, despite significant differences in cardiac electrophysiology between men and women. For instance, patient-specific models could assess the impact of sex differences in AF vulnerability due to variations in calcium handling [299]. Another area where digital twins could prove valuable is in elucidating the impact of sex-related differences in fibrosis. Studies have revealed differences in fibrosis characteristics between females and males undergoing cardiac surgery, with females exhibiting a higher burden of endomysial fibrosis than males [195]. In the future, the incorporation of sex-specific data could enhance the creation of digital twins, leading to improved personalized therapy delivery and a reduction in current biases in biomedical research.

Dynamic Personalization

Digital twins are evolving systems that capture changes between the physical and the virtual twin [300]. A main limitation of current patient-specific models is their reliance on static clinical data for model development. Future digital twins could dynamically adapt to mirror the current state of the physical patient through continuous monitoring devices, such as electrocardiogram (ECG) or blood biomarkers monitoring [13]. For example, the predictive capability of disease trajectories or therapeutic response of digital twins could be assessed by analyzing the impact of incorporating ECG data from implantable cardioverter defibrillators or pacemakers [301].

Personalization of Atrial Substrate

Current imaging modalities do not accurately represent the spatial distribution of atrial substrate. Recently, interest has been placed on the role of adipose tissue deposition in AF development [302]. Future computational studies could assess the impact of incorporating adipose tissue information from CT imaging. In addition, personalization could also explore the role of incorporating the autonomic nervous system [303] into the model and its potential role as a therapeutic target [304].

Robust Twinning Algorithms, Faster Simulations and Data Sharing

One of the main challenges of digital twin technologies is that current twinning processes, which consider anatomical and functional features, are not compatible with clinical time frames. Additionally, simulation times to evaluate arrhythmia vulnerability exceed procedural times, even with the use of high-performance computing. This underscores the need for the development of robust twinning algorithms and faster simulation approaches [262]. Mesh segmentation is usually time-consuming and requires experienced users, although machine learning (ML) algorithms offer promise to overcome this limitation [89]. Tools for preprocessing clinical data are already publicly available [90, 91], and also tools to perform anatomical personalization to develop simulation-ready meshes [46, 49]. However, there is currently no tool available to perform patient-specific model calibration based on clinical parameters. Efforts should be placed on developing methodologies that enhance the rapid creation of digital twins, from structural to functional personalization. Finally, in the near future, the implementation of collaborative federated learning for ML applications will help to overcome some of the main limitations regarding data sharing [305].

List of Figures

List of Tables

References

[1] G. Hindricks, T. Potpara, N. Dagres, et al., "2020 ESC guidelines for the diagnosis and management of atrial fibrillation developed in collaboration with the european association for cardio-thoracic surgery (eacts)," *Eur Heart J*, vol. 42, pp. 373–498, 2021. doi:10.1093/eurheartj/ehaa612

[2] H. Nothnagel, *Über arythmische herzthätigkeit*. Deutsches Archiv für Klinische Medizin, 1876.

[3] T. Lewis, "Report CXIX. Auricular Fibrillation: A common clinical condition," *BMJ*, vol. 2, pp. 1528–1528, 1909. doi:10.1136/bmj.2.2552.1528

[4] R. Ramirez, S. Bergman, and M. Jamal, "Experimental and computational models of atrial fibrillation," in *From Supraventricular Tachycardias to Cardiac Resynchronization Therapy*. Intechopen, 2024.

[5] J. K. Aronson, "One hundred years of atrial fibrillation," *British Journal of Clinical Pharmacology*, vol. 60, pp. 345–346, 2005. doi:10.1111/j.1365-2125.2005.02501.x

[6] G. Coorey, G. A. Figtree, D. F. Fletcher, et al., "The health digital twin to tackle cardiovascular disease—a review of an emerging interdisciplinary field," *npj Digital Medicine*, vol. 5, 2022. doi:10.1038/s41746-022-00640-7

[7] J. A. Joglar, M. K. Chung, A. L. Armbruster, et al., "2023 ACC/AHA/ACCP/HRS guideline for the diagnosis and management of atrial fibrillation: A report of the american college of cardiology/american heart association joint committee on clinical practice guidelines," *Circulation*, 2023. doi:10.1161/cir.0000000000001193

[8] B. P. Krijthe, A. Kunst, E. J. Benjamin, et al., "Projections on the number of individuals with atrial fibrillation in the european union, from 2000 to 2060," *Eur Heart J*, vol. 34, pp. 2746–2751, 2013. doi:10.1093/eurheartj/eht280

[9] D. Ko, F. Rahman, R. B. Schnabel, X. Yin, E. J. Benjamin, and I. E. Christophersen, "Atrial fibrillation in women: epidemiology, pathophysiology, presentation, and prognosis," *Nature Reviews Cardiology*, vol. 13, pp. 321–332, 2016. doi:10.1038/nrcardio.2016.45

[10] C. A. Emdin, C. X. Wong, A. J. Hsiao, et al., "Atrial fibrillation as risk factor for cardiovascular disease and death in women compared with men: systematic review and meta-analysis of cohort studies," *BMJ*, p. h7013, 2016. doi:10.1136/bmj.h7013

[11] P. E. Dilaveris and H. L. Kennedy, "Silent atrial fibrillation: epidemiology, diagnosis, and clinical impact," *Clinical Cardiology*, vol. 40, pp. 413–418, 2017. doi:10.1002/clc.22667

[12] J. Heijman, H. Sutanto, H. J. G. M. Crijns, S. Nattel, and N. A. Trayanova, "Computational models of atrial fibrillation: achievements, challenges, and perspectives for improving clinical care," *Cardiovascular Research*, vol. 117, pp. 1682–1699, 2021. doi:10.1093/cvr/cvab138

[13] M. J. M. Cluitmans, G. Plank, and J. Heijman, "Digital twins for cardiac electrophysiology: state of the art and future challenges," *Herzschrittmachertherapie + Elektrophysiologie*, 2024. doi:10.1007/s00399-024-01014-0

[14] N. A. Trayanova and A. Prakosa, "Up digital and personal: How heart digital twins can transform heart patient care," *Heart Rhythm*, 2023. doi:10.1016/j.hrthm.2023.10.019

[15] P. M. Boyle, T. Zghaib, S. Zahid, et al., "Computationally guided personalized targeted ablation of persistent atrial fibrillation," *Nat Biomed Eng*, vol. 3, pp. 870–879, 2019. doi: 10.1038/s41551-019-0437-9

[16] B. Lim, J. Kim, M. Hwang, et al., "In situ procedure for high-efficiency computational modeling of atrial fibrillation reflecting personal anatomy, fiber orientation, fibrosis, and electrophysiology," *Scientific Reports*, vol. 10, 2020. doi:10.1038/s41598-020-59372-x

[17] L. Azzolin, M. Eichenlaub, C. Nagel, et al., "Personalized ablation vs. conventional ablation strategies to terminate atrial fibrillation and prevent recurrence," *Europace*, vol. 25, pp. 211–222, 2023. doi:10.1093/europace/euac116

[18] C. H. Roney, I. Sim, J. Yu, et al., "Predicting atrial fibrillation recurrence by combining population data and virtual cohorts of patient-specific left atrial models." *Circ Arrhythm Electrophysiol*, vol. 15, pp. e010 253–e010 253, 2022. doi:10.1161/circep.121.010253

[19] J. K. Shade, R. L. Ali, D. Basile, et al., "Pre-procedure application of machine learning and mechanistic simulations predicts likelihood of paroxysmal atrial fibrillation recurrence following pulmonary vein isolation," *Circulation: Arrhythmia and Electrophysiology*, 2020. doi:10.1161/circep.119.008213

[20] Y.-S. Baek, O.-S. Kwon, B. Lim, et al., "Clinical outcomes of computational virtual mapping-guided catheter ablation in patients with persistent atrial fibrillation: A multicenter prospective randomized clinical trial," *Frontiers in Cardiovascular Medicine*, vol. 8, 2021. doi:10.3389/fcvm.2021.772665

[21] S. Zahid, H. Cochet, P. M. Boyle, et al., "Patient-derived models link re-entrant driver localization in atrial fibrillation to fibrosis spatial pattern." *Cardiovasc Res*, vol. 110, pp. 443–54, 2016. doi:10.1093/cvr/cvw073

[22] P. Pathmanathan, *Assessing the Credibility of Computational Modeling and Simulation in Medical Device Submissions - Guidance for Industry and Food and Drug Administration Staff*, FDA Std., 2024.

[23] J. Corral-Acero, F. Margara, M. Marciniak, et al., "The 'digital twin' to enable the vision of precision cardiology," *Eur Heart J*, vol. 41, pp. 4556–4564, 2020. doi:10.1093/eurheartj/ehaa159

[24] S. A. Niederer, J. Lumens, and N. A. Trayanova, "Computational models in cardiology," *Nat Rev Cardiol*, vol. 16, pp. 100–111, 2018. doi:10.1038/s41569-018-0104-y

[25] R. A. Gray and P. Pathmanathan, "Patient-specific cardiovascular computational modeling: Diversity of personalization and challenges," *Journal of Cardiovascular Translational Research*, vol. 11, pp. 80–88, 2018. doi:10.1007/s12265-018-9792-2

[26] M. Salvador, M. Strocchi, F. Regazzoni, et al., "Whole-heart electromechanical simulations using latent neural ordinary differential equations," *NPJ Digital Medicine*, vol. 7, 2024. doi:10.1038/s41746-024-01084-x

[27] C. Corrado, S. Williams, R. Karim, G. Plank, M. O'Neill, and S. Niederer, "A work flow to build and validate patient specific left atrium electrophysiology models from catheter measurements." *Med Image Anal*, vol. 47, pp. 153–163, 2018. doi:10.1016/j.media.2018.04.005

[28] D. Nairn, M. Eichenlaub, B. Müller-Edenborn, et al., "Differences in atrial substrate localization using late gadolinium enhancement-magnetic resonance imaging, electrogram voltage, and conduction velocity: a cohort study using a consistent anatomical reference frame in patients with persistent atrial fibrillation," *Europace*, vol. 25, 2023. doi:10.1093/europace/euad278

[29] D. G. Whittaker, M. Clerx, C. L. Lei, D. J. Christini, and G. R. Mirams, "Calibration of ionic and cellular cardiac electrophysiology models," *WIREs Systems Biology and Medicine*, vol. 12, 2020. doi:10.1002/wsbm.1482

[30] M. Strocchi, S. Longobardi, C. M. Augustin, et al., "Cell to whole organ global sensitivity analysis on a four-chamber heart electromechanics model using gaussian processes emulators," *PLOS Computational Biology*, vol. 19, p. e1011257, 2023. doi:10.1371/journal.pcbi.1011257

[31] S. Coveney, C. H. Roney, C. Corrado, et al., "Calibrating cardiac electrophysiology models using latent gaussian processes on atrial manifolds," *Scientific Reports*, vol. 12, 2022. doi:10.1038/s41598-022-20745-z

[32] L. Azzolin, S. Schuler, O. Dössel, and A. Loewe, "A reproducible protocol to assess arrhythmia vulnerability : Pacing at the end of the effective refractory period." *Front Physiol*, vol. 12, p. 656411, 2021. doi:10.3389/fphys.2021.656411

[33] M. W. Krueger, G. Seemann, K. Rhode, et al., "Personalization of atrial anatomy and electrophysiology as a basis for clinical modeling of radio-frequency ablation of atrial fibrillation," *IEEE Trans Med Imaging*, vol. 32, pp. 73–84, 2013. doi:10.1109/TMI.2012.2201948

[34] K. Gillette, M. A. Gsell, A. J. Prassl, et al., "A framework for the generation of digital twins of cardiac electrophysiology from clinical 12-leads ecgs," *Medical Image Analysis*, vol. 71, p. 102080, 2021. doi:10.1016/j.media.2021.102080

[35] C. H. Roney, J. Whitaker, I. Sim, et al., "A technique for measuring anisotropy in atrial conduction to estimate conduction velocity and atrial fibre direction," *Comput Biol Med*, vol. 104, pp. 278–290, 2019. doi:10.1016/j.compbiomed.2018.10.019

[36] B. M. Johnston and P. R. Johnston, "Approaches for determining cardiac bidomain conductivity values: progress and challenges," *Medical Biological Engineering Computing*, vol. 58, pp. 2919–2935, 2020. doi:10.1007/s11517-020-02272-z

[37] C. Mendonca Costa, E. Hoetzl, B. Martins Rocha, A. J. Prassl, and G. Plank, "Automatic parameterization strategy for cardiac electrophysiology simulations," in *Computing in Cardiology Conference (CinC), 2013*, Ieee, Ed., 2013, pp. 373–376.

[38] D. Deng, M. J. Murphy, J. B. Hakim, W. H. Franceschi, et al., "Sensitivity of reentrant driver localization to electrophysiological parameter variability," *Chaos*, vol. 27, p. 093932, 2017. doi:10.1063/1.5003340

[39] C. H. Roney, J. D. Bayer, S. Zahid, et al., "Modelling methodology of atrial fibrosis affects rotor dynamics and electrograms." *Europace*, vol. 18, pp. iv146–iv155, 2016. doi:10.1093/europace/euw365

[40] M. J. M. Cluitmans, L. R. Bear, U. C. Nguyên, et al., "Noninvasive detection of spatiotemporal activation-repolarization interactions that prime idiopathic ventricular fibrillation," *Science Translational Medicine*, vol. 13, 2021. doi:10.1126/scitranslmed.abi9317

[41] M. Cluitmans, D. H. Brooks, R. MacLeod, et al., "Validation and opportunities of electrocardiographic imaging: From technical achievements to clinical applications," *Front Physiol*, vol. 9:1305, 2018. doi:10.3389/fphys.2018.01305

[42] J. Whitaker, R. Rajani, H. Chubb, et al., "The role of myocardial wall thickness in atrial arrhythmogenesis," *Europace*, p. euw014, 2016. doi:10.1093/europace/euw014

[43] L. H. G. A. Hopman, P. Bhagirath, M. J. Mulder, et al., "Quantification of left atrial fibrosis by 3d late gadolinium-enhanced cardiac magnetic resonance imaging in patients with atrial fibrillation: impact of different analysis methods," *European Heart Journal - Cardiovascular Imaging*, vol. 23, pp. 1182–1190, 2022. doi:10.1093/ehjci/jeab245

[44] J. M. Hoermann, M. R. Pfaller, L. Avena, C. Bertoglio, and W. A. Wall, "Automatic mapping of atrial fiber orientations for patient-specific modeling of cardiac electromechanics using image registration." *Int J Numer Method Biomed Eng*, vol. 35, p. e3190, 2019. doi:10.1002/cnm.3190

[45] F. Pashakhanloo, D. A. Herzka, S. Mori, et al., "Submillimeter diffusion tensor imaging and late gadolinium enhancement cardiovascular magnetic resonance of chronic myocardial infarction," *Journal of Cardiovascular Magnetic Resonance*, vol. 19, 2017. doi:10.1186/s12968-016-0317-3

[46] C. H. Roney, J. A. Solis Lemus, C. Lopez Barrera, et al., "Constructing bilayer and volumetric atrial models at scale," *Interface Focus*, vol. 13, 2023. doi:10.1098/rsfs.2023.0038

[47] C. H. Roney, A. Pashaei, M. Meo, et al., "Universal atrial coordinates applied to visualisation, registration and construction of patient specific meshes." *Med Image Anal*, vol. 55, pp. 65–75, 2019. doi:10.1016/j.media.2019.04.004

[48] S. Schuler, N. Pilia, D. Potyagaylo, and A. Loewe, "Cobiveco: Consistent biventricular coordinates for precise and intuitive description of position in the heart – with matlab implementation," *Medical Image Analysis*, vol. 74, p. 102247, 2021. doi:10.1016/j.media.2021.102247

[49] L. Azzolin, M. Eichenlaub, C. Nagel, et al., "Augmenta: Patient-specific augmented atrial model generation tool." *Comput Med Imaging Graph*, vol. 108, pp. 102 265–102 265, 2023. doi:10.1016/j.compmedimag.2023.102265

[50] H. Ando, T. Yoshinaga, W. Yamamoto, et al., "A new paradigm for drug-induced torsadogenic risk assessment using human ips cell-derived cardiomyocytes," *Journal of Pharmacological and Toxicological Methods*, vol. 84, pp. 111–127, 2017. https://doi.org/10.1016%2Fj.vascn.2016.12.003

[51] M. Courtemanche, R. J. Ramirez, and S. Nattel, "Ionic mechanisms underlying human atrial action potential properties: insights from a mathematical model," *American Journal of Physiology-Heart and Circulatory Physiology*, vol. 275, pp. H301–H321, 1998. doi:10.1152/ajpheart.1998.275.1.H301

[52] D. Spragg and C. Hugh, "Comparing pulmonary vein isolation to pulmonary vein isolation + optima ablation in patients undergoing ablation for atrial fibrillation," 2019. https://clinicaltrials.gov/study/NCT04101539

[53] A. Nygren, C. Fiset, L. Firek, et al., "Mathematical model of an adult human atrial cell," *Circulation Research*, vol. 82, pp. 63–81, 1998. doi:10.1161/01.RES.82.1.63

[54] M. Wilhelms, H. Hettmann, M. M. C. Maleckar, J. T. Koivumäki, O. Dössel, and G. Seemann, "Benchmarking electrophysiological models of human atrial myocytes," *Front Physiol*, vol. 3, pp. 1–16, 2013. doi:10.3389/fphys.2012.00487/abstract

[55] D. E. Krummen, J. D. Bayer, J. Ho, et al., "Mechanisms of human atrial fibrillation initiation: clinical and computational studies of repolarization restitution and activation latency." *Circ Arrhythm Electrophysiol*, vol. 5, pp. 1149–59, 2012. doi:10.1161/circep.111.969022

[56] J. T. Koivumäki, T. Korhonen, and P. Tavi, "Impact of sarcoplasmic reticulum calcium release on calcium dynamics and action potential morphology in human atrial myocytes: A computational study," *PLoS Comput. Biol*, vol. 7, 2011. doi:10.1371/journal.pcbi.1001067

[57] A. Loewe, M. Wilhelms, F. Fischer, E. P. Scholz, O. Dössel, and G. Seemann, "Impact of herg mutations on simulated human atrial action potentials," in *Biomedizinische Technik/Biomedical Engineering*, vol. 58, no. s1, 2013. doi:10.1515/bmt-2013-4331

[58] M. Vagos, I. G. M. van Herck, J. Sundnes, H. J. Arevalo, A. G. Edwards, and J. T. Koivumäki, "Computational modeling of electrophysiology and pharmacotherapy of atrial fibrillation: Recent advances and future challenges," *Frontiers in Physiology*, vol. 9, 2018. doi:10.3389/fphys.2018.01221

[59] J. Sánchez, K. A. Ruales, M. Macarulla-Rodríguez, C. Barrios Espinosa, A. Loewe, and M. S. Guillem, "Inflammation-induced remodeling and atrial arrhythmias in systemic lupus erythematosus: In silico insights," in *2023 Computing in Cardiology (CinC)*, no. 10363691. IEEE, 2023, pp. 1–4. doi:10.22489/CinC.2023.292

[60] D. M. Harrild and C. S. Henriquez, "A computer model of normal conduction in the human atria," *Circ. Res.*, vol. 87, pp. e25–e36, 2000.

[61] E. J. Vigmond, R. Ruckdeschel, and N. Trayanova, "Reentry in a morphologically realistic atrial model," *J Cardiovasc Electrophysiol*, vol. 12, pp. 1046–1054, 2001.

[62] L. Dang, N. Virag, Z. Ihara, et al., "Evaluation of ablation patterns using a biophysical model of atrial fibrillation," *Ann Biomed Eng*, vol. 33, pp. 465–474, 2005.

[63] G. Seemann, C. Höper, F. B. Sachse, O. Dössel, A. V. Holden, and H. Zhang, "Heterogeneous three-dimensional anatomical and electrophysiological model of human atria," *Philos Trans A Math Phys Eng Sci.*, vol. 364, pp. 1465–1481, 2006.

[64] Y. Gong, F. Xie, K. M. Stein, et al., "Mechanism underlying initiation of paroxysmal atrial flutter/atrial fibrillation by ectopic foci: a simulation study," *Circulation*, vol. 115, pp. 2094–2102, 2007. doi:10.1161/circulationaha.106.656504

[65] A. Gharaviri, S. Verheule, J. Eckstein, M. Potse, N. H. L. Kuijpers, and U. Schotten, "A computer model of endo-epicardial electrical dissociation and transmural conduction during atrial fibrillation," *Europace*, vol. 14 Suppl 5, pp. v10–v16, 2012. doi:10.1093/europace/eus270

[66] M. Hwang, B. Lim, J.-S. Song, et al., "Ganglionated plexi stimulation induces pulmonary vein triggers and promotes atrial arrhythmogenecity: In silico modeling study," *PLOS ONE*, vol. 12, p. e0172931, 2017. doi:10.1371/journal.pone.0172931

[67] K. S. McDowell, F. Vadakkumpadan, R. Blake, et al., "Methodology for patient-specific modeling of atrial fibrosis as a substrate for atrial fibrillation," *J Electrocardiol*, vol. 45, pp. 640—-645, 2012. doi:10.1016/j.jelectrocard.2012.08.005

[68] I.-S. Kim, B. Lim, J. Shim, et al., "Clinical usefulness of computational modeling-guided persistent atrial fibrillation ablation: Updated outcome of multicenter randomized study," *Frontiers in Physiology*, vol. 10, 2019. doi:10.3389/fphys.2019.01512

[69] M. W. Krueger, "Personalized multi-scale modeling of the atria: Heterogeneities, fiber architecture, hemodialysis and ablation therapy," PhD thesis, KIT Scientific Publishing, Karlsruhe, 2012.

[70] A. Loewe, "Modeling human atrial patho-electrophysiology from ion channels to ecg: substrates, pharmacology, vulnerability, and p-waves," PhD thesis, KIT Scientific Publishing, Karlsruhe, 2016. doi:10.5445/KSP/1000054615

[71] S. Labarthe, J. Bayer, Y. Coudiere, et al., "A bilayer model of human atria: mathematical background, construction, and assessment," *Europace*, vol. 16 Suppl 4, pp. iv21–iv29, 2014. doi:10.1093/europace/euu256

[72] C. Corrado, J. Whitaker, H. Chubb, et al., "Personalized models of human atrial electrophysiology derived from endocardial electrograms," *IEEE Trans Biomed Eng*, 2016. doi:10.1109/tbme.2016.2574619

[73] M. W. Krueger, V. Schmidt, C. Tobón, et al., "Modeling atrial fiber orientation in patient-specific geometries: a semi-automatic rule-based approach," in *Functional Imaging and Modeling of the Heart 2011, Lecture Notes in Computer Science*, L. Axel and D. Metaxas, Eds., vol. 6666, 2011, pp. 223–232. doi:10.1007/978-3-642-21028-0_28

[74] A. Wachter, A. Loewe, M. W. Krueger, et al., "Mesh structure-independent modeling of patient-specific atrial fiber orientation," *CDBME*, vol. 1, pp. 409–412, 2015. doi:10.1515/cdbme-2015-0099

[75] J. D. Bayer, R. C. Blake, G. Plank, and N. A. Trayanova, "A novel rule-based algorithm for assigning myocardial fiber orientation to computational heart models," *Annals of Biomedical Engineering*, vol. 40, pp. 2243–2254, 2012. doi:10.1007/s10439-012-0593-5

[76] T. Colatsky, B. Fermini, G. Gintant, et al., "The comprehensive in vitro proarrhythmia assay (CiPA) initiative — update on progress," *Journal of Pharmacological and Toxicological Methods*, vol. 81, pp. 15–20, 2016. doi:10.1016/j.vascn.2016.06.002

[77] M. Viceconti, A. Henney, and E. Morley-Fletcher, "In silico clinical trials: how computer simulation will transform the biomedical industry," *International Journal of Clinical Trials*, vol. 3, p. 37, 2016. doi:10.18203/2349-3259.ijct20161408

[78] A. Ferrer-Albero, E. J. Godoy, M. Lozano, et al., "Non-invasive localization of atrial ectopic beats by using simulated body surface p-wave integral maps," *PLOS ONE*, vol. 12, p. e0181263, 2017. doi:10.1371/journal.pone.0181263

[79] K. Moulaei, M. Shanbehzadeh, Z. Mohammadi-Taghiabad, and H. Kazemi-Arpanahi, "Comparing machine learning algorithms for predicting COVID-19 mortality," *BMC Medical Informatics and Decision Making*, vol. 22, 2022. doi:10.1186/s12911-021-01742-0

[80] C. H. Roney, M. L. Beach, A. M. Mehta, et al., "In silico comparison of left atrial ablation techniques that target the anatomical, structural, and electrical substrates of atrial fibrillation," *Frontiers in Physiology*, vol. 11, 2020. doi:10.3389/fphys.2020.572874

[81] S. F. Bifulco, F. Macheret, G. D. Scott, N. Akoum, and P. M. Boyle, "Explainable machine learning to predict anchored reentry substrate created by persistent atrial fibrillation ablation in computational models," *Journal of the American Heart Association*, vol. 12, 2023. doi:10.1161/jaha.123.030500

[82] G. Luongo, G. Vacanti, V. Nitzke, et al., "Hybrid machine learning to localize atrial flutter substrates using the surface 12-lead electrocardiogram," *EP Europace*, vol. 24, pp. 1186–1194, 2022. doi:10.1093/europace/euab322

[83] C. Ruiz Herrera, T. Grandits, G. Plank, P. Perdikaris, F. Sahli Costabal, and S. Pezzuto, "Physics-informed neural networks to learn cardiac fiber orientation from multiple electroanatomical maps," *Engineering with Computers*, 2022. doi:10.1007/s00366-022-01709-3

[84] F. Sahli Costabal, Y. Yang, P. Perdikaris, D. E. Hurtado, and E. Kuhl, "Physics-informed neural networks for cardiac activation mapping," *Frontiers in Physics*, vol. 8, 2020. doi:10.3389/fphy.2020.00042

[85] C. Nagel, M. Schaufelberger, O. Dössel, and A. Loewe, "A bi-atrial statistical shape model as a basis to classify left atrial enlargement from simulated and clinical 12-lead ecgs," *Statistical Atlases and Computational Models of the Heart. Multi-Disease, Multi-View, and Multi-Center Right Ventricular Segmentation in Cardiac MRI Challenge*, vol. 13131, pp. 38–47, 2022. doi:10.1007/978-3-030-93722-5_5

[86] C. Rodero, M. Strocchi, M. Marciniak, et al., "Linking statistical shape models and simulated function in the healthy adult human heart," *PLOS Computational Biology*, vol. 17, p. e1008851, 2021. doi:10.1371/journal.pcbi.1008851

[87] C. H. Roney, R. Bendikas, F. Pashakhanloo, et al., "Constructing a human atrial fibre atlas." *Ann Biomed Eng*, 2020. doi:10.1007/s10439-020-02525-w

[88] W. Bai, W. Shi, A. de Marvao, et al., "A bi-ventricular cardiac atlas built from 1000+ high resolution mr images of healthy subjects and an analysis of shape and motion," *Med Image Anal*, vol. 26, pp. 133—-145, 2015. doi:10.1016/j.media.2015.08.009

[89] J. A. Solís-Lemus, T. Baptiste, R. Barrows, et al., "Evaluation of an open-source pipeline to create patient-specific left atrial models: A reproducibility study," *Computers in Biology and Medicine*, p. 107009, 2023. doi:10.1016/j.compbiomed.2023.107009

[90] P. C. Africa, R. Piersanti, M. Fedele, L. Dede', and A. Quarteroni, "lifex-fiber: an open tool for myofibers generation in cardiac computational models." *BMC Bioinformatics*, vol. 24, pp. 143–143, 2023. doi:10.1186/s12859-023-05260-w

[91] S. E. Williams, C. H. Roney, A. Connolly, et al., "OpenEP: A cross-platform electroanatomic mapping data format and analysis platform for electrophysiology research," *Frontiers in Physiology*, vol. 12, 2021. doi:10.3389/fphys.2021.646023

[92] R. Arnold, A. J. Prassl, A. Neic, et al., "pyceps: A cross-platform electroanatomic mapping data to computational model conversion platform for the calibration of digital twin models of cardiac electrophysiology," *eprint*, 2024. arXiv:2403.10394v1

[93] K. Gillette, M. A. F. Gsell, C. Nagel, et al., "Medalcare-xl: 16,900 healthy and pathological synthetic 12 lead ecgs from electrophysiological simulations." *Sci Data*, vol. 10, pp. 531–531, 2023. doi:10.1038/s41597-023-02416-4

[94] K. Gillette, M. A. Gsell, C. Nagel, et al., "MedalCare-XL: 16, 900 healthy and pathological synthetic 12 lead ecgs obtained through electrophysiological simulations," 2023. doi:10.5281/zenodo.7293654

[95] C. Roney, I. Sim, J. Yu, et al., "Predicting atrial fibrillation recurrence by combining population data and virtual cohorts of patient-specific left atrial models," 2022. doi:10.5281/zenodo.5801336

[96] C. Nagel, J. Sanchez, L. Azzolin, et al., "A bi-atrial statistical shape model and 100 volumetric anatomical models of the atria," 2021. doi:10.5281/zenodo.4309957

[97] L. Azzolin, M. Eichenlaub, C. Nagel, et al., "29 atrial models created with a patient-specific augmented atrial model generation tool (AugmentA)," 2021. doi:10.5281/zenodo.5589288

[98] S. Williams and R. Jo-Anne, "Realistic computational electrophysiology simulations for the targeted treatment of atrial fibrillation (recett-af)," 2021. https://clinicaltrials.gov/study/NCT05057507

[99] K. W. Johnson, K. Shameer, B. S. Glicksberg, et al., "Enabling precision cardiology through multiscale biology and systems medicine," *JACC: Basic to Translational Science*, vol. 2, pp. 311–327, 2017. doi:10.1016/j.jacbts.2016.11.010

[100] E. Grandi, D. Dobrev, and J. Heijman, "Computational modeling: What does it tell us about atrial fibrillation therapy?" *International Journal of Cardiology*, 2019. doi:10.1016/j.ijcard.2019.01.077

[101] K. Gilbert, C. Mauger, A. A. Young, and A. Suinesiaputra, "Artificial intelligence in cardiac imaging with statistical atlases of cardiac anatomy," *Frontiers in Cardiovascular Medicine*, vol. 7, 2020. doi:10.3389/fcvm.2020.00102

[102] T. D. Nguyen, O. E. Kadri, and R. S. Voronov, "An introductory overview of image-based computational modeling in personalized cardiovascular medicine," *Frontiers in Bioengineering and Biotechnology*, vol. 8, 2020. doi:10.3389/fbioe.2020.529365

[103] O. S. Kwon, I. Hwang, and H.-N. Pak, "Computational modeling of atrial fibrillation," *International Journal of Arrhythmia*, vol. 22, 2021. doi:10.1186/s42444-021-00051-x

[104] S. Pagani, L. Dede', A. Manzoni, and A. Quarteroni, "Data integration for the numerical simulation of cardiac electrophysiology." *Pacing Clin Electrophysiol*, 2021. doi:10.1111/pace.14198

[105] N. A. Trayanova, D. M. Popescu, and J. K. Shade, "Machine learning in arrhythmia and electrophysiology," *Circulation Research*, vol. 128, pp. 544–566, 2021. doi:10.1161/circresaha.120.317872

[106] Z. Wu, Y. Liu, L. Tong, D. Dong, D. Deng, and L. Xia, "Current progress of computational modeling for guiding clinical atrial fibrillation ablation," *Journal of Zhejiang University-SCIENCE B*, vol. 22, pp. 805–817, 2021. doi:10.1631/jzus.b2000727

[107] A. Loewe, P. Martínez Díaz, C. Nagel, and J. Sánchez, "Cardiac digital twin modeling," in *Innovative Treatment Strategies for Clinical Electrophysiology*. Singapore: Springer Nature Singapore, 2022, pp. 111–134. doi:10.1007/978-981-19-6649-1_7

[108] J. Bai, Y. Lu, H. Wang, and J. Zhao, "How synergy between mechanistic and statistical models is impacting research in atrial fibrillation," *Frontiers in Physiology*, vol. 13, 2022. doi:10.3389/fphys.2022.957604

[109] C. Rodero, T. M. Baptiste, R. K. Barrows, et al., "A systematic review of cardiac in-silico clinical trials," *Progress in Biomedical Engineering*, 2023. doi:10.1088/2516-1091/acdc71

[110] N. A. Trayanova, A. Lyon, J. Shade, and J. Heijman, "Computational modeling of cardiac electrophysiology and arrhythmogenesis," *Physiological Reviews*, 2023. doi:10.1152/physrev.00017.2023

[111] R. Laubenbacher, B. Mehrad, I. Shmulevich, and N. Trayanova, "Digital twins in medicine," *Nature Computational Science*, vol. 4, pp. 184–191, 2024. doi:10.1038/s43588-024-00607-6

[112] O. A. Jaffery, L. Melki, G. Slabaugh, W. W. Good, and C. H. Roney, "A review of personalised cardiac computational modelling using electroanatomical mapping data," *Arrhythmia Electrophysiology Review*, vol. 13, 2024. doi:10.15420/aer.2023.25

[113] T. Liu, F. Xiong, X.-Y. Qi, et al., "Altered calcium handling produces reentry-promoting action potential alternans in atrial fibrillation–remodeled hearts," *JCI Insight*, vol. 5, 2020. doi:10.1172/jci.insight.133754

[114] S. M. Narayan, M. R. Franz, P. Clopton, E. J. Pruvot, and D. E. Krummen, "Repolarization alternans reveals vulnerability to human atrial fibrillation," *Circulation*, vol. 123, pp. 2922–2930, 2011. doi:10.1161/circulationaha.110.977827

[115] E. Deroubaix, T. Folliguet, C. Rücker-Martin, et al., "Moderate and chronic hemodynamic overload of sheep atria induces reversible cellular electrophysiologic abnormalities and atrial vulnerability," *Journal of the American College of Cardiology*, vol. 44, pp. 1918–1926, 2004. doi:10.1016/j.jacc.2004.07.055

[116] B. Li, F. Luo, X. Luo, et al., "Effects of atrial fibrosis induced by mitral regurgitation on atrial electrophysiology and susceptibility to atrial fibrillation in pigs," *Cardiovascular Pathology*, vol. 40, pp. 32–40, 2019. doi:10.1016/j.carpath.2019.01.006

[117] Cambridge, "Definition of vulnerability," 2024, [Accessed 10-05-2024]. https://dictionary.cambridge.org/dictionary/english/vulnerability

[118] S. Tzeis, E. P. Gerstenfeld, J. Kalman, et al., "2024 european heart rhythm association/heart rhythm society/asia pacific heart rhythm society/latin american heart rhythm society expert consensus statement on catheter and surgical ablation of atrial fibrillation," *Europace*, vol. 26, 2024. doi:10.1093/europace/euae043

[119] F. Ravelli and M. Allessie, "Effects of atrial dilatation on refractory period and vulnerability to atrial fibrillation in the isolated langendorff-perfused rabbit heart," *Circulation*, vol. 96, pp. 1686–1695, 1997. doi:10.1161/01.cir.96.5.1686

[120] C. H. Roney, J. D. Bayer, H. Cochet, et al., "Variability in pulmonary vein electrophysiology and fibrosis determines arrhythmia susceptibility and dynamics," *PLOS Computational Biology*, vol. 14, p. e1006166, 2018. doi:10.1371/journal.pcbi.1006166

[121] S. Khurshid, U. Kartoun, J. M. Ashburner, et al., "Performance of atrial fibrillation risk prediction models in over 4 million individuals," *Circulation: Arrhythmia and Electrophysiology*, vol. 14, 2021. doi:10.1161/circep.120.008997

[122] M. Oliveira, M. N. da Silva, A. T. Timoteo, et al., "Inducibility of atrial fibrillation during electrophysiologic evaluation is associated with increased dispersion of atrial refractoriness," *International Journal of Cardiology*, vol. 136, pp. 130–135, 2009. doi:10.1016/j.ijcard.2008.04.097

[123] Kitware, "Paraview Simple Clean Documentation," 2014, [Accessed 12-05-2024]. https://kitware.github.io/paraview-docs/latest/python/paraview.simple.Clean.html

[124] D. Mann and V. Mehta, "Cardiovascular embryology," *International Anesthesiology Clinics*, vol. 42, 2004.

[125] J. Speller, "Development of the cardiovascular system," 2022. https://teachmeanatomy.info/the-basics/embryology/cardiovascular-system/

[126] R. D. Rosen and B. Bordoni, *Embryology, aortic arch*. StatPearls Publishing, Treasure Island (FL), 2023. http://europepmc.org/books/NBK553173

[127] T. W. Sadler, *Langman's medical embryology*. Philadelphia: Wolters Kluwer, 2010.

[128] I. Kucybała, K. Ciuk, and W. Klimek-Piotrowska, "Clinical anatomy of human heart atria and interatrial septum — anatomical basis for interventional cardiologists and electrocardiologists. part 1: right atrium and interatrial septum," *Kardiologia Polska*, vol. 76, pp. 499–509, 2018. doi:10.5603/kp.a2017.0248

[129] R. M. Lang, M. Cameli, L. E. Sade, et al., "Imaging assessment of the right atrium: anatomy and function," *European Heart Journal - Cardiovascular Imaging*, vol. 23, pp. 867–884, 2022. doi:10.1093/ehjci/jeac011

[130] R. H. Anderson, R. Razavi, and A. M. Taylor, "Cardiac anatomy revisited," *Journal of Anatomy*, vol. 205, pp. 159–177, 2004. doi:https://doi.org/10.1111/j.0021-8782.2004.00330.x

[131] S. Mori, J. T. Tretter, D. E. Spicer, D. L. Bolender, and R. H. Anderson, "What is the real cardiac anatomy?" *Clinical Anatomy*, vol. 32, p. 288–309, 2019. doi:10.1002/ca.23340

[132] M. Strocchi, C. M. Augustin, M. A. F. Gsell, et al., "A publicly available virtual cohort of four-chamber heart meshes for cardiac electro-mechanics simulations," 2020. https://doi.org/10.5281/zenodo.3890034

[133] N. Soto, T. Datino, D. Gonzalez-Casal, et al., "Anatomical knowledge for the ablation of left and right atrial flutter," *Herzschrittmachertherapie + Elektrophysiologie*, vol. 33, pp. 124–132, 2022. doi:10.1007/s00399-022-00865-9

[134] S. Ciuk, P. Janas, and W. Klimek-Piotrowska, "Clinical anatomy of human heart atria and interatrial septum — anatomical basis for interventional cardiologists and electrocardiologists.

part 2: left atrium," *Kardiologia Polska*, vol. 76, pp. 510–519, 2018. doi:10.5603/kp.a2018.0001

[135] A. Kandathil and M. Chamarthy, "Pulmonary vascular anatomy anatomical variants," *Cardiovascular Diagnosis and Therapy*, vol. 8, 2018. https://cdt.amegroups.org/article/view/19060

[136] M. Haïssaguerre, P. Jaïs, D. C. Shah, et al., "Spontaneous initiation of atrial fibrillation by ectopic beats originating in the pulmonary veins," *New England Journal of Medicine*, vol. 339, pp. 659–666, 1998. doi:10.1056/nejm199809033391003

[137] Y. Wang, L. Di Biase, R. P. Horton, T. Nguyen, P. Morhanty, and A. Natale, "Left atrial appendage studied by computed tomography to help planning for appendage closure device placement," *Journal of Cardiovascular Electrophysiology*, vol. 21, pp. 973–982, 2010. doi:10.1111/j.1540-8167.2010.01814.x

[138] C. V. DeSimone, B. G. Prakriti, J. Tri, F. Syed, A. N. Sm, and S. J. Asirvatham, "A review of the relevant embryology, pathohistology, and anatomy of the left atrial appendage for the invasive cardiac electrophysiologist," *J. Atr. Fibrillation*, vol. 8, p. 1129, 2015.

[139] N. C. Wunderlich, R. Beigel, M. J. Swaans, S. Y. Ho, and R. J. Siegel, "Percutaneous interventions for left atrial appendage exclusion: Options, assessment, and imaging using 2d and 3d echocardiography," *JACC: Cardiovascular Imaging*, vol. 8, pp. 472–488, 2015. doi:https://doi.org/10.1016/j.jcmg.2015.02.002

[140] L. Di Biase, P. Santangeli, M. Anselmino, et al., "Does the left atrial appendage morphology correlate with the risk of stroke in patients with atrial fibrillation?: Results from a multicenter study," *Journal of the American College of Cardiology*, vol. 60, pp. 531–538, 2012. doi:https://doi.org/10.1016/j.jacc.2012.04.032

[141] K. Piątek-Koziej, J. Hołda, K. Tyrak, et al., "Anatomy of the left atrial ridge (coumadin ridge) and possible clinical implications for cardiovascular imaging and invasive procedures," *Journal of Cardiovascular Electrophysiology*, vol. 31, pp. 220–226, 2020. doi:10.1111/jce.14307

[142] D. Dudkiewicz, K. Słodowska, K. A. Jasińska, H. Dobrzynski, and M. K. Hołda, "The clinical anatomy of the left atrial structures used as landmarks in ablation of arrhythmogenic substrates and cardiac invasive procedures," *Translational Research in Anatomy*, vol. 23, p. 100102, 2021. doi:10.1016/j.tria.2020.100102

[143] D. Sánchez-Quintana, J. R. López-Mínguez, Y. Macías, J. A. Cabrera, and F. Saremi, "Left atrial anatomy relevant to catheter ablation," *Cardiology Research and Practice*, vol. 2014, p. 1–17, 2014. doi:10.1155/2014/289720

[144] M. K. Hołda, M. Koziej, J. Hołda, et al., "Anatomic characteristics of the mitral isthmus region: The left atrial appendage isthmus as a possible ablation target," *Annals of Anatomy - Anatomischer Anzeiger*, vol. 210, pp. 103–111, 2017. doi:https://doi.org/10.1016/j.aanat.2016.11.011

[145] A. Arshad and A. J. Atkinson, "A 21st century view of the anatomy of the cardiac conduction system," *Translational Research in Anatomy*, vol. 28, p. 100204, 2022. doi:10.1016/j.tria.2022.100204

[146] R. Lemery, G. Guiraudon, and J. P. Veinot, "Anatomic description of bachmann's bundle and its relation to the atrial septum," *The American Journal of Cardiology*, vol. 91, pp. 1482–1485, 2003. doi:10.1016/s0002-9149(03)00405-3

[147] S. Nattel, "Atrial electrophysiology and mechanisms of atrial fibrillation," *Journal of Cardiovascular Pharmacology and Therapeutics*, vol. 8, pp. S5–S11, 2003. doi:10.1177/107424840300800102

[148] C. Cantwell, C. Roney, F. Ng, J. Siggers, S. Sherwin, and N. Peters, "Techniques for automated local activation time annotation and conduction velocity estimation in cardiac mapping," *Computers in Biology and Medicine*, vol. 65, pp. 229–242, 2015. doi:10.1016/j.compbiomed.2015.04.027

[149] D. Darbar and D. M. Roden, "Genetic mechanisms of atrial fibrillation: impact on response to treatment," *Nature Reviews Cardiology*, vol. 10, pp. 317–329, 2013. doi:10.1038/nrcardio.2013.53

[150] A. Goette, J. M. Kalman, L. Aguinaga, et al., "EHRA/HRS/APHRS/SOLAECE expert consensus on atrial cardiomyopathies: definition, characterization, and clinical implication," *Europace*, vol. 18, pp. 1455–1490, 2016. doi:10.1093/europace/euw161

[151] H. Dridi, A. Kushnir, R. Zalk, Q. Yuan, Z. Melville, and A. R. Marks, "Intracellular calcium leak in heart failure and atrial fibrillation: a unifying mechanism and therapeutic target," *Nat. Rev. Cardiol.*, vol. 17, pp. 732–747, 2020.

[152] S. V. Pandit, "31 - ionic mechanisms of atrial action potentials," in *Cardiac Electrophysiology: From Cell to Bedside (Seventh Edition)*, 7th ed., D. P. Zipes, J. Jalife, and W. G. Stevenson, Eds. Elsevier, 2018, pp. 293–303. doi:https://doi.org/10.1016/B978-0-323-44733-1.00031-6

[153] L. Skibsbye, T. Jespersen, T. Christ, et al., "Refractoriness in human atria: Time and voltage dependence of sodium channel availability," *Journal of Molecular and Cellular Cardiology*, vol. 101, p. 26–34, 2016. doi:10.1016/j.yjmcc.2016.10.009

[154] J. Andrade, P. Khairy, D. Dobrev, and S. Nattel, "The clinical profile and pathophysiology of atrial fibrillation: relationships among clinical features, epidemiology, and mechanisms," *Circ Res*, vol. 114, pp. 1453–1468, 2014. doi:10.1161/circresaha.114.303211

[155] S. Nattel, B. Burstein, and D. Dobrev, "Atrial remodeling and atrial fibrillation," *Circulation: Arrhythmia and Electrophysiology*, vol. 1, pp. 62–73, 2008. doi:10.1161/circep.107.754564

[156] R. S. Wijesurendra and B. Casadei, "Mechanisms of atrial fibrillation," *Heart*, vol. 105, pp. 1860–1867, 2019. doi:10.1136/heartjnl-2018-314267

[157] D. Dobrev and S. Nattel, "New antiarrhythmic drugs for treatment of atrial fibrillation," *The Lancet*, vol. 375, pp. 1212–1223, 2010. doi:10.1016/s0140-6736(10)60096-7

[158] S. Nattel and D. Dobrev, "Controversies about atrial fibrillation mechanisms," *Circulation Research*, vol. 120, pp. 1396–1398, 2017. doi:10.1161/circresaha.116.310489

[159] G. R. Mines, "On dynamic equilibrium in the heart," *The Journal of Physiology*, vol. 46, pp. 349–383, 1913. doi:10.1113/jphysiol.1913.sp001596

[160] T. Lewis, "Oliver-sharpey lectures on the nature of flutter and fibrillation of the auricle," *BMJ*, vol. 1, pp. 590–593, 1921. doi:10.1136/bmj.1.3147.590

[161] D. Scherf, F. Romano, and R. Terranova, "Experimental studies on auricular flutter and auricular fibrillation," *American Heart Journal*, vol. 36, pp. 241–251, 1948. doi:10.1016/0002-8703(48)90403-7

[162] G. Moe and J. Abildskov, "Atrial fibrillation as a self-sustaining arrhythmia independent of focal discharge," *American Heart Journal*, vol. 58, pp. 59–70, 1959. doi:10.1016/0002-8703(59)90274-1

[163] G. K. Moe, W. C. Rheinboldt, and J. A. Abildskov, "A computer model of atrial fibrillation," *American Heart Journal*, vol. 67, pp. 200–220, 1964.

[164] M. Allessie, W. Lammers, F. Bonke, and S. Hollen, "Experimental evaluation of moe's multiple wavelet hypothesis of atrial fibrillation," in *Cardiac Electrophysiology and Arrhythmias*, D. Zipes and J. Jalife, Eds. Orlando, FL: Grune & Stratton, 1985, pp. 265–275.

[165] M. A. Allessie, F. I. M. Bonke, and F. J. G. Schopman, "Circus movement in rabbit atrial muscle as a mechanism of tachycardia," *Circulation Research*, vol. 33, pp. 54–62, 1973. doi:10.1161/01.res.33.1.54

[166] M. A. Allessie, F. I. Bonke, and F. J. Schopman, "Circus movement in rabbit atrial muscle as a mechanism of tachycardia. iii. the "leading circle" concept: a new model of circus movement in cardiac tissue without the involvement of an anatomical obstacle." *Circulation Research*, vol. 41, pp. 9–18, 1977. doi:10.1161/01.res.41.1.9

[167] S. V. Pandit and J. Jalife, "Rotors and the dynamics of cardiac fibrillation," *Circ Res*, vol. 112, pp. 849–862, 2013. doi:10.1161/circresaha.111.300158

[168] R. B. Schuessler, T. Kawamoto, D. E. Hand, et al., "Simultaneous epicardial and endocardial activation sequence mapping in the isolated canine right atrium." *Circulation*, vol. 88, pp. 250–263, 1993. doi:10.1161/01.cir.88.1.250

[169] C. H. Roney, A. L. Wit, and N. S. Peters, "Challenges associated with interpreting mechanisms of af," *Arrhythmia & Electrophysiology Review*, vol. 8, pp. 273–284, 2020. doi:10.15420/aer.2019.08

[170] M. S. Guillem, A. M. Climent, M. Rodrigo, F. Fernandez-Aviles, F. Atienza, and O. Berenfeld, "Presence and stability of rotors in atrial fibrillation: evidence and therapeutic implications," *Cardiovasc Res*, vol. 109, pp. 480–492, 2016. doi:10.1093/cvr/cvw011

[171] S. M. Narayan and J. Jalife, "Crosstalk proposal: Rotors have been demonstrated to drive human atrial fibrillation," *The Journal of Physiology*, vol. 592, pp. 3163–3166, 2014. doi:10.1113/jphysiol.2014.271031

[172] N. M. de Groot, R. P. Houben, J. L. Smeets, et al., "Electropathological substrate of longstanding persistent atrial fibrillation in patients with structural heart disease," *Circulation*, vol. 122, pp. 1674–1682, 2010. doi:10.1161/circulationaha.109.910901

[173] R. H. Clayton, E. A. Zhuchkova, and A. V. Panfilov, "Phase singularities and filaments: simplifying complexity in computational models of ventricular fibrillation," *Progress in Biophysics and Molecular Biology*, vol. 90, pp. 378–398, 2006.

[174] J. Jalife, "Mother rotors and fibrillatory conduction: a mechanism of atrial fibrillation," *Cardiovascular Research*, vol. 54, pp. 204–216, 2002. doi:10.1016/s0008-6363(02)00223-7

[175] J. L. Cox, R. B. Schuessler, H. J. D'Agostino, et al., "The surgical treatment of atrial fibrillation," *The Journal of Thoracic and Cardiovascular Surgery*, vol. 101, pp. 569–583, 1991. doi:10.1016/s0022-5223(19)36684-x

[176] Y. Gao, H. Luo, R. Yang, et al., "Safety and efficacy of cox-maze procedure for atrial fibrillation during mitral valve surgery: a meta-analysis of randomized controlled trials," *Journal of Cardiothoracic Surgery*, vol. 19, 2024. doi:10.1186/s13019-024-02622-0

[177] S. M. Narayan, D. E. Krummen, K. Shivkumar, P. Clopton, W.-J. Rappel, and J. M. Miller, "Treatment of atrial fibrillation by the ablation of localized sources," *Journal of the American College of Cardiology*, vol. 60, pp. 628–636, 2012. doi:10.1016/j.jacc.2012.05.022

[178] A. J. Camm, G. V. Naccarelli, S. Mittal, et al., "The increasing role of rhythm control in patients with atrial fibrillation," *Journal of the American College of Cardiology*, vol. 79, pp. 1932–1948, 2022. doi:10.1016/j.jacc.2022.03.337

[179] C. A. Morillo, A. Verma, S. J. Connolly, et al., "Radiofrequency ablation vs antiarrhythmic drugs as first-line treatment of paroxysmal atrial fibrillation (raaft-2)," *JAMA*, vol. 311, p. 692, 2014. doi:10.1001/jama.2014.467

[180] N. F. Marrouche, J. Brachmann, D. Andresen, et al., "Catheter ablation for atrial fibrillation with heart failure," *New England Journal of Medicine*, vol. 378, pp. 417–427, 2018. doi: 10.1056/nejmoa1707855

[181] O. O. Olanisa, P. Jain, Q. S. Khan, et al., "Which Is Better? Rate Versus Rhythm Control in Atrial Fibrillation: A Systematic Review," *Cureus*, vol. 15, p. e49869, 2023.

[182] H. Calkins, G. Hindricks, R. Cappato, et al., "2017 HRS/EHRA/ECAS/APHRS/SOLAECE expert consensus statement on catheter and surgical ablation of atrial fibrillation." *Heart Rhythm*, vol. 14, pp. e275–e444, 2017. doi:10.1016/j.hrthm.2017.05.012

[183] Y. Huo, T. Gaspar, R. Schönbauer, et al., "Low-voltage myocardium-guided ablation trial of persistent atrial fibrillation," *NEJM Evidence*, vol. 1, 2022. doi:10.1056/evidoa2200141

[184] C. Sohns and N. F. Marrouche, "Atrial fibrillation and cardiac fibrosis," *Eur Heart J*, vol. 41, pp. 1123–1131, 2020. doi:10.1093/eurheartj/ehz786

[185] E. M. Benito, A. Carlosena-Remirez, E. Guasch, et al., "Left atrial fibrosis quantification by late gadolinium-enhanced magnetic resonance: a new method to standardize the thresholds for reproducibility," *Europace*, vol. 19, pp. 1272–1279, 2017. doi:10.1093/europace/euw219

[186] E. M. Benito, N. Cabanelas, M. Nuñez-Garcia, et al., "Preferential regional distribution of atrial fibrosis in posterior wall around left inferior pulmonary vein as identified by late gadolinium enhancement cardiac magnetic resonance in patients with atrial fibrillation." *Europace*, vol. 20, pp. 1959–1965, 2018. doi:10.1093/europace/euy095

[187] D. Nairn, "Multi-modality correspondence to enhance arrhythmogenic atrial substrate identification: Guiding persistent atrial fibrillation ablation therapy," PhD thesis, Karlsruher Institut für Technologie (KIT), 2022. doi:10.5445/ir/1000144762

[188] N. F. Marrouche, O. Wazni, C. McGann, et al., "Effect of mri-guided fibrosis ablation vs conventional catheter ablation on atrial arrhythmia recurrence in patients with persistent atrial fibrillation: The decaaf ii randomized clinical trial." *JAMA*, vol. 327, pp. 2296–2296, 2022. doi:10.1001/jama.2022.8831

[189] K. Higuchi, J. Cates, G. Gardner, et al., "The spatial distribution of late gadolinium enhancement of left atrial magnetic resonance imaging in patients with atrial fibrillation," *JACC: Clinical Electrophysiology*, vol. 4, pp. 49–58, 2018. doi:10.1016/j.jacep.2017.07.016

[190] L. H. G. A. Hopman, J. E. Visch, P. Bhagirath, et al., "Right atrial function and fibrosis in relation to successful atrial fibrillation ablation," *European Heart Journal - Cardiovascular Imaging*, vol. 24, pp. 336–345, 2023. doi:10.1093/ehjci/jeac152

[191] L. O'Neill, I. Sim, D. O'Hare, et al., "Cardiac magnetic resonance assessment of bi-atrial fibrosis in secundum atrial septal defects patients: Camera-asd study," *European Heart Journal - Cardiovascular Imaging*, vol. 23, pp. 1231–1239, 2022. doi:10.1093/ehjci/jeab188

[192] N. Akoum, C. McGann, G. Vergara, et al., "Atrial fibrosis quantified using late gadolinium enhancement mri is associated with sinus node dysfunction requiring pacemaker implant," *J Cardiovasc Electrophysiol*, vol. 23, pp. 44–50, 2012. doi:10.1111/j.1540-8167.2011.02140.x

[193] C. Gunturiz-Beltrán, M. Nuñez-Garcia, T. Althoff, et al., "Progressive and simultaneous right and left atrial remodeling uncovered by a comprehensive magnetic resonance assessment in atrial fibrillation," *J Am Heart Assoc*, vol. 11, p. e026028, 2022.

[194] P. G. Platonov, L. B. Mitrofanova, V. Orshanskaya, and S. Y. Ho, "Structural abnormalities in atrial walls are associated with presence and persistency of atrial fibrillation but not with age," *Journal of the American College of Cardiology*, vol. 58, pp. 2225–2232, 2011. doi: 10.1016/j.jacc.2011.05.061

[195] J. Winters, A. Isaacs, S. Zeemering, et al., "Heart failure, female sex, and atrial fibrillation are the main drivers of human atrial cardiomyopathy: Results from the catch me consortium," *Journal of the American Heart Association*, vol. 12, 2023. doi:10.1161/jaha.123.031220

[196] A. L. Hodgkin and A. F. Huxley, "A quantitative description of membrane current and its application to conduction and excitation in nerve," *J. Physiol.*, vol. 117, pp. 500–544, 1952.

[197] C. H. Luo and Y. Rudy, "A dynamic model of the cardiac ventricular action potential. i. simulations of ionic currents and concentration changes." *Circulation Research*, vol. 74, p. 1071–1096, 1994. doi:10.1161/01.res.74.6.1071

[198] R. Clayton, O. Bernus, E. Cherry, et al., "Models of cardiac tissue electrophysiology: Progress, challenges and open questions," *Progress in Biophysics and Molecular Biology*, vol. 104, pp. 22–48, 2011. doi:10.1016/j.pbiomolbio.2010.05.008

[199] K. H. Jæger, K. G. Hustad, X. Cai, and A. Tveito, "Efficient numerical solution of the emi model representing the extracellular space (e), cell membrane (m) and intracellular space (i) of a collection of cardiac cells," *Frontiers in Physics*, vol. 8, 2021. doi:10.3389/fphy.2020.579461

[200] D. B. Geselowitz and T. W. Miller, "A bidomain model for anisotropic cardiac muscle," *Annals of Biomedical Engineering*, vol. 11, pp. 191–206, 1983.

[201] J. G. Stinstra, B. Hopenfeld, and R. S. MacLeod, "On the passive cardiac conductivity," *Annals of Biomedical Engineering*, vol. 33, pp. 1743–1751, 2005. doi:10.1007/s10439-005-7257-7

[202] D. Bers, *Excitation-contraction coupling and cardiac contractile force*, vol. 237. Springer Science & Business Media, 2001.

[203] P. C. Franzone, L. Pavarino, and B. Taccardi, "Simulating patterns of excitation, repolarization and action potential duration with cardiac bidomain and monodomain models," *Mathematical biosciences*, vol. 197, pp. 35–66, 2005.

[204] M. Potse, B. Dube, J. Richer, A. Vinet, and R. Gulrajani, "A comparison of monodomain and bidomain reaction-diffusion models for action potential propagation in the human heart," *IEEE Transactions on Biomedical Engineering*, vol. 53, p. 2425–2435, 2006. doi:10.1109/tbme.2006.880875

[205] C. Nagel, C. Barrios Espinosa, K. Gillette, et al., "Comparison of propagation models and forward calculation methods on cellular, tissue and organ scale atrial electrophysiology," *IEEE Transactions on Biomedical Engineering*, vol. 70, pp. 511–522, 2023. doi:10.1109/tbme.2022.3196144

[206] N. Trayanova and G. Plank, *Bidomain model of defibrillation*. Springer US, 2009, p. 85–109. doi:10.1007/978-0-387-79403-7_5

[207] J. Sundnes, G. T. Lines, X. Cai, B. F. Nielsen, K.-A. Mardal, and A. Tveito, *enComputing the electrical activity in the heart*, 2006th ed., Monographs in Computational Science and Engineering. Berlin, Germany: Springer, 2006.

[208] S. M. Lundberg and S.-I. Lee, "A unified approach to interpreting model predictions," in *Advances in Neural Information Processing Systems 30*, I. Guyon, U. V. Luxburg, S. Bengio, et al., Eds. Curran Associates, Inc., 2017, pp. 4765–4774. http://papers.nips.cc/paper/7062-a-unified-approach-to-interpreting-model-predictions.pdf

[209] S. Lundberg, "Welcome to the shap documentation," 2018. https://shap.readthedocs.io/en/latest/index.html

[210] P. Martínez Díaz, J. Sánchez, N. Fitzen, U. Ravens, O. Dössel, and A. Loewe, "The right atrium affects in silico arrhythmia vulnerability in both atria," *Heart Rhythm*, 2024. doi:10.1016/j.hrthm.2024.01.047

[211] Y. C. Chen, A. Voskoboinik, A. L. Gerche, et al., "Prevention of pathological atrial remodeling and atrial fibrillation," *J Am Coll Cardiol*, vol. 77, pp. 2846–2864, 2021. doi:10.1016/j.jacc.2021.04.012

[212] A. Goette, J. M. Kalman, L. Aguinaga, et al., "EHRA/HRS/APHRS/SOLAECE expert consensus on atrial cardiomyopathies: definition, characterization, and clinical implication," *Europace*, vol. 18, pp. 1455–1490, 2016. doi:10.1093/europace/euw161

[213] J. Whitaker, R. Rajani, H. Chubb, et al., "The role of myocardial wall thickness in atrial arrhythmogenesis," *Europace*, vol. 18, pp. 1758–1772, 2016. doi:10.1093/europace/euw014

[214] M. Haissaguerre, M. Hocini, P. Sanders, et al., "Localized sources maintaining atrial fibrillation organized by prior ablation," *Circulation*, vol. 113, pp. 616–625, 2006. doi:10.1161/circulationaha.105.546648

[215] P. M. Boyle, T. Zghaib, S. Zahid, et al., "Computationally guided personalized targeted ablation of persistent atrial fibrillation," *Nat Biomed Eng*, vol. 3, pp. 870–879, 2019. doi:10.1038/s41551-019-0437-9

[216] L. Azzolin, M. Eichenlaub, C. Nagel, et al., "Personalized ablation vs. conventional ablation strategies to terminate atrial fibrillation and prevent recurrence," *Europace*, vol. 25, pp. 211–222, 2023. doi:10.1093/europace/euac116

[217] B. Lim, J. Kim, M. Hwang, et al., "In situ procedure for high-efficiency computational modeling of atrial fibrillation reflecting personal anatomy, fiber orientation, fibrosis, and electrophysiology," *Scientific Reports*, vol. 10, 2020. doi:10.1038/s41598-020-59372-x

[218] C. H. Roney, I. Sim, J. Yu, et al., "Predicting atrial fibrillation recurrence by combining population data and virtual cohorts of patient-specific left atrial models." *Circ Arrhythm Electrophysiol*, vol. 15, pp. e010 253–e010 253, 2022. doi:10.1161/circep.121.010253

[219] M. Courtemanche, R. J. Ramirez, and S. Nattel, "Ionic mechanisms underlying human atrial action potential properties: insights from a mathematical model," *Am J Physiol Heart Circ Physiol*, vol. 275, pp. H301–H321, 1998. doi:10.1152/ajpheart.1998.275.1.H301

[220] openCARP consortium, C. Augustin, P. M. Boyle, V. Loechner, et al., "openCARP (v13.0)," 2023. doi:10.35097/1027

[221] G. Plank, A. Loewe, A. Neic, et al., "The openCARP simulation environment for cardiac electrophysiology." *Comput Methods Programs Biomed*, vol. 208, p. 106223, 2021. doi:10.1016/j.cmpb.2021.106223

[222] P. Martínez Díaz and A. Loewe, "The right atrium affects in silico arrhythmia vulnerability in both atria," 2023. doi:10.35097/1830

[223] A. Loewe, M. Wilhelms, O. Dössel, et al., "Influence of chronic atrial fibrillation induced remodeling in a computational electrophysiological model," in *Biomedical Engineering*, vol. 59. Berlin, Boston: Walter de Gruyter, 2014, pp. S929–S932. doi:10.1515/bmt-2014-5012

[224] S. Prabhu, A. Voskoboinik, A. McLellan, et al., "A comparison of the electrophysiologic and electroanatomic characteristics between the right and left atrium in persistent atrial fibrillation: Is the right atrium a window into the left?" *J Cardiovasc Electrophysiol*, vol. 28, pp. 1109–1116, 2017. doi:10.1111/jce.13297

[225] A. Loewe, M. W. Krueger, P. G. Platonov, et al., "Left and right atrial contribution to the p-wave in realistic computational models," in *Lecture Notes in Computer Science*, FIMH, vol. 9126, 2015, p. 439–447. doi:10.1007/978-3-319-20309-6

[226] C. Nagel, G. Luongo, L. Azzolin, et al., "Non-invasive and quantitative estimation of left atrial fibrosis based on P waves of the 12-lead ECG—a large-scale computational study covering anatomical variability," *J Clin Med*, vol. 10, p. 1797, 2021. doi:10.3390/jcm10081797

[227] E. Vigmond, A. Pashaei, S. Amraoui, et al., "Percolation as a mechanism to explain atrial fractionated electrograms and reentry in a fibrosis model based on imaging data," *Heart Rhythm*, vol. 13, pp. 1536–1543, 2016. doi:10.1016/j.hrthm.2016.03.019

[228] C. H. Roney, J. D. Bayer, S. Zahid, et al., "Modelling methodology of atrial fibrosis affects rotor dynamics and electrograms." *Europace*, vol. 18, pp. iv146–iv155, 2016. doi:10.1093/europace/euw365

[229] L. Azzolin, S. Schuler, O. Dössel, et al., "A reproducible protocol to assess arrhythmia vulnerability : Pacing at the end of the effective refractory period." *Front Physiol*, vol. 12, p. 656411, 2021. doi:10.3389/fphys.2021.656411

[230] T. Nitta, H. Imura, R. Bessho, et al., "Wavelength and conduction inhomogeneity in each atrium in patients with isolated mitral valve disease and atrial fibrillation," *J Cardiovasc Electrophysiol*, vol. 10, pp. 521–528, 1999. doi:10.1111/j.1540-8167.1999.tb00708.x

[231] G. Hindricks, T. Potpara, N. Dagres, et al., "2020 ESC guidelines for the diagnosis and management of atrial fibrillation developed in collaboration with the European Association for Cardio-Thoracic Surgery (EACTS)," *Eur Heart J*, vol. 42, pp. 373–498, 2021. doi:10.1093/eurheartj/ehaa612

[232] J. A. Joglar, M. K. Chung, A. L. Armbruster, et al., "2023 ACC/AHA/ACCP/HRS guideline for the diagnosis and management of atrial fibrillation: A report of the american college of cardiology/american heart association joint committee on clinical practice guidelines," *Circulation*, 2023. doi:10.1161/cir.0000000000001193

[233] C. H. Roney, S. E. Williams, H. Cochet, et al., "Patient-specific simulations predict efficacy of ablation of interatrial connections for treatment of persistent atrial fibrillation." *Europace*, vol. 20, pp. iii55–iii68, 2018. doi:10.1093/europace/euy232

[234] S. Zahid, H. Cochet, P. M. Boyle, et al., "Patient-derived models link re-entrant driver localization in atrial fibrillation to fibrosis spatial pattern." *Cardiovasc Res*, vol. 110, pp. 443–54, 2016. doi:10.1093/cvr/cvw073

[235] A. Roy, M. Varela, H. Chubb, et al., "Identifying locations of re-entrant drivers from patient-specific distribution of fibrosis in the left atrium," *PLOS Comput Biol*, vol. 16, p. e1008086, 2020. doi:10.1371/journal.pcbi.1008086

[236] R. K. Kharbanda, P. Knops, van der Does, et al., "Simultaneous endo-epicardial mapping of the human right atrium: Unraveling atrial excitation," *J Am Heart Assoc*, vol. 9, 2020. doi:10.1161/jaha.120.017069

[237] P. Martínez Díaz, A. Dasí, C. Goetz, et al., "Impact of effective refractory period personalization on arrhythmia vulnerability in patient-specific atrial computer models," *Europace*, 2024. doi:10.1093/europace/euae215

[238] F. L. Burton and S. M. Cobbe, "Dispersion of ventricular repolarization and refractory period," *Cardiovascular Research*, vol. 50, pp. 10–23, 2001.

[239] Z. F. Issa, J. M. Miller, and D. P. Zipes, "Clinical arrhythmology and electrophysiology: A companion to braunwald's heart disease," *Clinical Arrhythmology and Electrophysiology: A Companion to Braunwald's Heart Disease*, pp. 1–752, 2018. doi:10.1016/C2014-0-03293-5

[240] P. M. I. Sutton, P. Taggart, T. Opthof, et al., "Repolarisation and refractoriness during early ischaemia in humans," *Heart*, vol. 84, pp. 365–369, 2000. doi:10.1136/heart.84.4.365

[241] L. N. van Staveren and N. M. de Groot, "Exploring refractoriness as an adjunctive electrical biomarker for staging of atrial fibrillation," *Journal of the American Heart Association*, vol. 9, 2020. doi:10.1161/jaha.120.018427

[242] S. Fareh, C. Villemaire, and S. Nattel, "Importance of refractoriness heterogeneity in the enhanced vulnerability to atrial fibrillation induction caused by tachycardia-induced atrial electrical remodeling," *Circulation*, vol. 98, pp. 2202–2209, 1998. doi:10.1161/01.cir.98.20.2202

[243] H. F. Tse, C. P. Lau, and G. M. Ayers, "Heterogeneous changes in electrophysiologic properties in the paroxysmal and chronically fibrillating human atrium," *Journal of Cardiovascular Electrophysiology*, vol. 10, pp. 125–135, 1999. doi:10.1111/j.1540-8167.1999.tb00653.x

[244] E. G. Daoud, F. Bogun, R. Goyal, et al., "Effect of atrial fibrillation on atrial refractoriness in humans," *Circulation*, vol. 94, pp. 1600–1606, 1996. doi:10.1161/01.cir.94.7.1600

[245] M. C. Wijffels, C. J. Kirchhof, R. Dorland, and M. A. Allessie, "Atrial fibrillation begets atrial fibrillation," *Circulation*, vol. 92, pp. 1954–1968, 1995. doi:10.1161/01.CIR.92.7.1954

[246] R. S. Wijesurendra and B. Casadei, "Mechanisms of atrial fibrillation," pp. 1860–1867, 2019. doi:10.1136/heartjnl-2018-314267

[247] P. Santangeli and F. E. Marchlinski, "Techniques for the provocation, localization, and ablation of non-pulmonary vein triggers for atrial fibrillation," *Heart Rhythm*, vol. 14, pp. 1087–1096, 2017. doi:10.1016/j.hrthm.2017.02.030

[248] M. W. Krueger, W. H. Schulze, K. S. Rhode, R. Razavi, G. Seemann, and O. Dössel, "Towards personalized clinical in-silico modeling of atrial anatomy and electrophysiology," *Medical and Biological Engineering and Computing*, vol. 51, pp. 1251–1260, 2013. doi:10.1007/s11517-012-0970-0

[249] C. Corrado, J. Whitaker, H. Chubb, et al., "Personalized models of human atrial electrophysiology derived from endocardial electrograms," *IEEE Transactions on Biomedical Engineering*, vol. 64, pp. 735–742, 2017. doi:10.1109/tbme.2016.2574619

[250] D. M. Lombardo, F. H. Fenton, S. M. Narayan, and W. J. Rappel, "Comparison of detailed and simplified models of human atrial myocytes to recapitulate patient specific properties," *PLoS Computational Biology*, vol. 12, 2016. doi:10.1371/journal.pcbi.1005060

[251] C. Goetz, A. Loewe, and P. Martínez Díaz, "DIVAID (v1.0)," 2023. doi:10.35097/1846

[252] A. Loewe, M. W. Krueger, P. G. Platonov, F. Holmqvist, O. Dössel, and G. Seemann, "Left and right atrial contribution to the p-wave in realistic computational models," *Lecture Notes in Computer Science (including subseries Lecture Notes in Artificial Intelligence and Lecture Notes in Bioinformatics)*, vol. 9126, pp. 439–447, 2015. doi:10.1007/978-3-319-20309-6_50/figures/4

[253] T. F. Oostendorp, A. V. Oosterom, and G. Huiskamp, "Interpolation on a triangulated 3d surface," *Journal of Computational Physics*, vol. 80, pp. 331–343, 1989.

[254] P. Boyle, "Smooth gradient heterogeneities (ionic adjustment), openCARP," 2019. https://opencarp.org/documentation/examples/02_ep_tissue/05c_cellular_dynamics_heterogeneity.

[255] E. Vigmond, A. Pashaei, S. Amraoui, H. Cochet, and M. Hassaguerre, "Percolation as a mechanism to explain atrial fractionated electrograms and reentry in a fibrosis model based on imaging data," *Heart Rhythm*, vol. 13, pp. 1536–1543, 2016. doi:10.1016/j.hrthm.2016.03.019

[256] P. Martínez Díaz, C. Goetz, A. Dasi, et al., "Atrial Models with Personalized Effective Refractory Period," 2024. doi:10.5281/zenodo.10726677

[257] M. J. Bishop, A. Connolly, and G. Plank, "Structural heterogeneity modulates effective refractory period: A mechanism of focal arrhythmia initiation," *PLoS ONE*, vol. 9, 2014. doi:10.1371/journal.pone.0109754

[258] S. E. Williams, L. O'Neill, C. H. Roney, et al., "Left atrial effective conducting size predicts atrial fibrillation vulnerability in persistent but not paroxysmal atrial fibrillation," *Journal of Cardiovascular Electrophysiology*, vol. 30, pp. 1416–1427, 2019. doi:10.1111/jce.13990

[259] K. J. Sampson and C. S. Henriquez, "Electrotonic influences on action potential duration dispersion in small hearts: a simulation study," *American Journal of Physiology-Heart and Circulatory Physiology*, vol. 289, pp. H350–H360, 2005. doi:10.1152/ajpheart.00507.2004

[260] J. B. Hakim, M. J. Murphy, N. A. Trayanova, and P. M. Boyle, "Arrhythmia dynamics in computational models of the atria following virtual ablation of re-entrant drivers." *Europace*, vol. 20, pp. iii45–iii54, 2018. doi:10.1093/europace/euy234

[261] C. H. Roney, S. E. Williams, H. Cochet, et al., "Patient-specific simulations predict efficacy of ablation of interatrial connections for treatment of persistent atrial fibrillation." *EP Europace*, vol. 20, pp. iii55–iii68, 2018. doi:10.1093/europace/euy232

[262] C. Barrios Espinosa, J. Sánchez, S. Appel, et al., "A cyclical fast iterative method for simulating reentries in cardiac electrophysiology using an eikonal-based model," *eprint*, 2024. arXiv: 2406.18619v1

[263] N. Akoum, D. Wilber, G. Hindricks, et al., "MRI assessment of ablation-induced scarring in atrial fibrillation: Analysis from the decaaf study," *Journal of Cardiovascular Electrophysiology*, vol. 26, pp. 473–480, 2015. doi:10.1111/jce.12650

[264] M. J. Gonzales, K. P. Vincent, W. J. Rappel, S. M. Narayan, and A. D. McCulloch, "Structural contributions to fibrillatory rotors in a patient-derived computational model of the atria," *Europace*, vol. 16, pp. iv3–iv10, 2014. doi:10.1093/europace/euu251

[265] P. Martínez Díaz, J. Sánchez, C. Nagel, et al., "Personalized modeling of atrial activation and p-waves: a comparison between invasive and non-invasive cardiac mapping," in *2022 Computing in Cardiology Conference*, vol. 49. Computing in Cardiology, 2022. doi:10.22489/cinc.2022.334

[266] D. Nairn, M. Eichenlaub, B. Müller Edenborn, et al., "LGE-MRI for diagnosis of left atrial cardiomyopathy as identified in high-definition endocardial voltage and conduction velocity mapping," *medRxiv*, p. doi:10.1101/2022.02.02.22269817, 2022.

[267] J. Salinet, R. Molero, F. S. Schlindwein, J. Karel, et al., "Electrocardiographic imaging for atrial fibrillation: a perspective from computer models and animal experiments to clinical value," *Front Physiol*, vol. 12, 2021. doi:10.3389/fphys.2021.653013

[268] B. Verma, T. Oesterlein, A. Loewe, et al., "Regional conduction velocity calculation from clinical multichannel electrograms in human atria," *Comp Biol Med*, vol. 92, pp. 188–196, 2018. doi:10.1016/j.compbiomed.2017.11.017

[269] A. J. Graham, M. Orini, E. Zacur, G. Dhillon, et al., "Simultaneous comparison of electrocardiographic imaging and epicardial contact mapping in structural heart disease." *Circ Arrhythm Electrophysiol*, vol. 12, p. e007120, 2019. doi:10.1161/circep.118.007120

[270] M. Lüthi, T. Gerig, C. Jud, and T. Vetter, "Gaussian process morphable models." *IEEE Trans Pattern Anal Mach Intell*, vol. 40, pp. 1860–1873, 2018. doi:10.1109/tpami.2017.2739743

[271] C. Nagel, C. B. Espinosa, K. Gillette, M. A. Gsell, et al., "Comparison of propagation models and forward calculation methods on cellular, tissue and organ scale atrial electrophysiology," *IEEE Trans Biomed Eng*, pp. 1–12, 2022. doi:10.1109/TBME.2022.3196144

[272] A. M. Janssen, D. Potyagaylo, O. Dössel, and T. F. Oostendorp, "Assessment of the equivalent dipole layer source model in the reconstruction of cardiac activation times on the basis of BSPMs produced by an anisotropic model of the heart." *Med Biol Eng Comput*, vol. 56, pp. 1013–1025, 2018. doi:10.1007/s11517-017-1715-x

[273] P. Martínez Díaz, P. Maierhofer, E. Invers-Rubio, et al., "Insights from explainable machine learning on biatrial arrhythmia vulnerability assessment," in *2024 Computing in Cardiology Conference*, vol. 52. Computing in Cardiology, 2024. doi:10.22489/cinc.2024.308

[274] S. F. Bifulco, F. Macheret, G. D. Scott, et al., "Explainable machine learning to predict anchored reentry substrate created by persistent atrial fibrillation ablation in computational models," *J Am Heart Assoc*, vol. 12, 2023. doi:10.1161/jaha.123.030500

[275] P. Martínez Díaz, J. Sánchez, N. Fitzen, et al., "The right atrium affects in silico arrhythmia vulnerability in both atria," *Heart Rhythm*, 2024. doi:10.1016/j.hrthm.2024.01.047

[276] Y.-L. Chen, J.-E. Ban, Y.-M. Park, J.-I. Choi, S.-W. Park, and Y.-H. Kim, "The spatial distribution of atrial fibrillation termination sites in the right atrium during complex fractionated atrial electrograms-guided ablation in patients with persistent atrial fibrillation," *Journal of Cardiovascular Electrophysiology*, vol. 24, pp. 949–957, 2013. doi:10.1111/jce.12187

[277] M. Nunez-Garcia, G. Bernardino, F. Alarcon, et al., "Fast quasi-conformal regional flattening of the left atrium," *IEEE Transactions on Visualization and Computer Graphics*, vol. 26, pp. 2591–2602, 2020. doi:10.1109/tvcg.2020.2966702

[278] R. Starreveld, L. J. M. E. van der Does, and N. M. S. de Groot, "Anatomical hotspots of fractionated electrograms in the left and right atrium: do they exist?" *EP Europace*, vol. 21, pp. 60–72, 2019. doi:10.1093/europace/euy059

[279] S.-L. Chang, C.-T. Tai, Y.-J. Lin, et al., "Biatrial substrate properties in patients with atrial fibrillation," *Journal of Cardiovascular Electrophysiology*, vol. 18, pp. 1134–1139, 2007. doi:10.1111/j.1540-8167.2007.00941.x

[280] R. Kogawa, Y. Okumura, I. Watanabe, et al., "Left atrial remodeling: Regional differences between paroxysmal and persistent atrial fibrillation," *Journal of Arrhythmia*, vol. 33, pp. 483–487, 2017. doi:10.1016/j.joa.2017.06.001

[281] Y. Nakatani, T. Sakamoto, Y. Yamaguchi, Y. Tsujino, N. Kataoka, and K. Kinugawa, "Left atrial wall thickness is associated with the low-voltage area in patients with paroxysmal atrial fibrillation," *Journal of Interventional Cardiac Electrophysiology*, vol. 58, pp. 315–321, 2020. doi:10.1007/s10840-019-00611-1

[282] K. Kumagai, K. Minami, D. Kutsuzawa, and S. Oshima, "Evaluation of the characteristics of rotational activation at high-dominant frequency and complex fractionated atrial electrogram sites during atrial fibrillation," *Journal of Arrhythmia*, vol. 33, pp. 49–55, 2017. doi:10.1016/j.joa.2016.05.008

[283] P. Álvarez Guirado, "Classification of atrial ectopic beats into spatial segments based on the 12-lead ecg," Master's thesis, Institute of Biomedical Engineering, Karlsruhe Institute of Technology (KIT), 2018.

[284] A. Yagishita, S. DE Oliveira, I. Cakulev, et al., "Correlation of left atrial voltage distribution between sinus rhythm and atrial fibrillation: Identifying structural remodeling by 3-d electroanatomic mapping irrespective of the rhythm," *J Cardiovasc Electrophysiol*, 2016. doi:10.1111/jce.13002

[285] A. W. Teh, P. M. Kistler, G. Lee, et al., "Electroanatomic remodeling of the left atrium in paroxysmal and persistent atrial fibrillation patients without structural heart disease," *J Cardiovasc Electrophysiol*, vol. 23, pp. 232–238, 2012. doi:10.1111/j.1540-8167.2011.02178.x

[286] Y. Lin, B. Yang, F. C. Garcia, et al., "Comparison of left atrial electrophysiologic abnormalities during sinus rhythm in patients with different type of atrial fibrillation," *J Interv Card Electrophysiol*, vol. 39, pp. 57–67, 2014. doi:10.1007/s10840-013-9838-y

[287] R. J. Hunter, Y. Liu, Y. Lu, W. Wang, and R. J. Schilling, "Left atrial wall stress distribution and its relationship to electrophysiologic remodeling in persistent atrial fibrillation," *Circ Arrhythm Electrophysiol*, vol. 5, pp. 351–360, 2012. doi:10.1161/circep.111.965541

[288] R. J. Hunter, I. Diab, M. Tayebjee, et al., "Characterization of fractionated atrial electrograms critical for maintenance of atrial fibrillation: a randomized, controlled trial of ablation strategies (the CFAE AF Trial)," *Circ Arrhythm Electrophysiol*, vol. 4, pp. 622–629, 2011. doi:10.1161/circep.111.962928

[289] M. D. Cerqueira, N. J. Weissman, V. Dilsizian, et al., "Standardized myocardial segmentation and nomenclature for tomographic imaging of the heart," *Circulation*, vol. 105, pp. 539–542, 2002. doi:10.1161/hc0402.102975

[290] P. Maierhofer, P. Martínez Díaz, M. Houillon, O. Dössel, and A. Loewe, "HeartVR - Interactive Software to Plan and Guide Ablation Procedures," 2024. doi:10.5281/zenodo.10222759

[291] A. Verma, C.-y. Jiang, T. R. Betts, et al., "Approaches to catheter ablation for persistent atrial fibrillation," *New England Journal of Medicine*, vol. 372, pp. 1812–1822, 2015. doi:10.1056/nejmoa1408288

[292] J. G. Quintanilla, S. Shpun, J. Jalife, and D. Filgueiras-Rama, "Novel approaches to mechanism-based atrial fibrillation ablation." *Cardiovasc Res*, 2021. doi:10.1093/cvr/cvab108

[293] A. Prassl, A. Neic, L. Axel, et al., "openCARP user's manual," 2024. https://opencarp.org/documentation/user-manual

[294] A. Luca, E. Martin, N. Claudia, et al., "GitHub - KIT-IBT/AugmentA: AugmentA: Patient-specific Augmented Atrial model Generation Tool — github.com," 2021. https://github.com/KIT-IBT/AugmentA.git

[295] N. P. Chue Hong, D. S. Katz, M. Barker, et al., "FAIR Principles for Research Software (FAIR4RS Principles)," 2022. doi:10.15497/RDA00068

[296] T. Zheng, L. Azzolin, J. Sánchez, O. Dössel, and A. Loewe, "An automate pipeline for generating fiber orientation and region annotation in patient specific atrial models," *Current Directions in Biomedical Engineering*, vol. 7, pp. 136–139, 2021. doi:10.1515/cdbme-2021-2035

[297] A. Gharaviri, E. Bidar, M. Potse, et al., "Epicardial fibrosis explains increased endo-epicardial dissociation and epicardial breakthroughs in human atrial fibrillation." *Front Physiol*, vol. 11, p. 68, 2020. doi:10.3389/fphys.2020.00068

[298] A. Ramadan, E. Chleilat, H. Martinez-Navarro, et al., "Gordon research conference on cardiac arrhythmia mechanisms 2023: early career investigators' views on emerging concepts and technologies." *J Physiol*, 2023. doi:10.1113/JP284666

[299] N. T. Herrera, "In silico investigation of sex-specific atrial electrophysiologic mechanisms and arrhythmia vulnerability," *Biophysical Journal*, vol. 123, 2024. doi:https://doi.org/10.1016/j.bpj.2023.11.1233

[300] D. Wagg, C. Burr, J. Shepherd, Z. Xuereb Conti, M. Enzer, and S. Niederer, "The philosophical foundations of digital twinning," *Engrxiv*, 2024. doi:10.31224/3500

[301] M. Z. Kolk, S. Ruipérez-Campillo, L. Alvarez-Florez, et al., "Dynamic prediction of malignant ventricular arrhythmias using neural networks in patients with an implantable cardioverter-defibrillator," *eBioMedicine*, vol. 99, p. 104937, 2024. doi:10.1016/j.ebiom.2023.104937

[302] N. Bodagh, M. C. Williams, K. Vickneson, A. Gharaviri, S. Niederer, and S. E. Williams, "State of the art paper: Cardiac computed tomography of the left atrium in atrial fibrillation," *Journal of Cardiovascular Computed Tomography*, vol. 17, pp. 166–176, 2023. doi:10.1016/j.jcct.2023.03.002

[303] P.-S. Chen, L. S. Chen, M. C. Fishbein, S.-F. Lin, and S. Nattel, "Role of the autonomic nervous system in atrial fibrillation: pathophysiology and therapy," *Circ. Res.*, vol. 114, pp. 1500–1515, 2014.

[304] P. Hanna, E. Buch, S. Stavrakis, et al., "Neuroscientific therapies for atrial fibrillation," *Cardiovasc. Res.*, vol. 117, pp. 1732–1745, 2021.

[305] N. Rieke, J. Hancox, W. Li, et al., "The future of digital health with federated learning," *npj Digital Medicine*, vol. 3, 2020. doi:10.1038/s41746-020-00323-1

List of Publications and Supervised Theses

Journal Articles

- **Patricia Martínez Díaz** , Jorge Sánchez, Nikola Fitzen, Ursula Ravens, Olaf Dössel, and Axel Loewe *"The Right Atrium Affects in silico Arrhythmia Vulnerability in Both Atria"*, Heart Rhythm 2024;21:799–805, DOI: 10.1016/j.hrthm.2024.01.047
- **Patricia Martínez Díaz** , Albert Dasí, Christian Goetz, Laura Unger, Annika Haas, Armin Luik, Blanca Rodríguez, Olaf Dössel, and Axel Loewe *"Impact of Effective Refractory Period Personalization on Arrhythmia Vulnerability in Patient-Specific Atrial Computer Models"*, Europace 2024, DOI: 10.1093/europace/euae215

Journal Articles Under Review

- Christian Goetz, **Patricia Martínez Díaz**, Eric Invers-Rubio, Sachal Hussain, Lluis Mont, Constanze Schmidt, Samuel Mañá, Martin Steghöfer, Cristina Corsi, Olaf Dössel, Andreu M. Climent, Blanca Rodríguez, Ulrich Schotten, José Ángel Cabrera, Axel Loewe, María S. Guillem, and Till Althoff *"Standardized Regionalization of the Atria for 3D Cardiac Imaging, Electroanatomical Mapping and Computational Modeling – A Multidisciplinary Consensus of the PersonalizeAF Consortium"*, manuscript under review in Europace 2024
- Cristian Barrios Espinosa, Jorge Sánchez, Stephanie Appel, Silvia Becker, Jonathan Krauß, **Patricia Martínez Díaz**, Laura Unger, Marie Houillon, Axel Loewe *"A Cyclical Fast Iterative Method for Simulating Reentries in Cardiac Electrophysiology Using an Eikonal-Based Model"*, Arxiv 2024, DOI: 10.48550/arXiv.2406.18619, manuscript under review in Engineering with Computers 2024

Book Chapters

- Axel Loewe, **Patricia Martínez Díaz**, Claudia Nagel, and Jorge Sánchez *"Cardiac Digital Twin Modeling. In: Innovative treatment strategies for clinical electrophysiology"* 2022. Springer. DOI: 10.1007/978-981-19-6649-17

Refereed Conference Articles

- **Patricia Martínez Díaz**, Jorge Sánchez, Claudia Nagel, Marta Martínez Pérez, Ismael Hernández Romero, María S. Guillem, Olaf Dössel, and Axel Loewe *"Personalized Modeling of Atrial Activation and P-waves: A Comparison Between Invasive and Non-Invasive Cardiac Mapping"*, Computing in Cardiology Conference (CinC). Vol. 49. 2022. DOI: 10.22489/CinC.2022.334
- **Patricia Martínez Díaz**, Pascal Maierhofer, Eric Invers-Rubio, Michael Beigl, Lluís Mont, Amir Jadidi, Olaf Dössel, and Axel Loewe *"Insights from Explainable Machine Learning on Biatrial Arrhythmia Vulnerability Assessment"*, manuscript accepted in Computing in Cardiology Conference (CinC) 2024
- Nikola Fitzen, **Patricia Martínez Díaz**, Olaf Dössel, and Axel Loewe *"Impact of the Right Atrium on Arrhythmia Vulnerability*, Biomedizinische Technik / Biomedical Engineering. Vol. 9. BMT 2023 - 57th Annual Conference of the German Society for Biomedical Engineering (VDE | DGBMT) 2023. Pp 142–145. DOI: 10.1515/cdbme-2023-1036
- Christian Goetz, **Patricia Martínez Díaz**, Jorge Sánchez, Amir Jadidi, Martin Eichenlaub, Olaf Dössel, and Axel Loewe *"Discrepancy Between LGE-MRI and Electro-Anatomical Mapping for Regional Detection of Pathological Atrial Substrate"* Biomedizinische Technik / Biomedical Engineering. Vol. 9. BMT 2023 - 57th Annual Conference of the German Society for Biomedical Engineering (VDE | DGBMT) 2023. Pp. 483–486. DOI: 10.1515/cdbme-2023-1121
- Christian Goetz, **Patricia Martínez Díaz**, Till Althoff, Constanze Schmidt, Axel Loewe *"DIVAID: Automatic Division of Bi-Atrial Geometries Into Clinically Important Regions"*, manuscript accepted to Computing in Cardiology Conference (CinC) 2024
- Joshua Steyer, **Patricia Martínez Díaz**, Laura Unger, and Axel Loewe *"Simulated Excitation Patterns in the Atria and Their Corresponding Electrograms"*, Functional Imaging and Modeling of the Heart (FIMH) 2023. Pp. 204–212. DOI: 10.1007/978-3-031-35302-4_21
- Ahmed Ramadan, Enaam Chleilat, Hector Martinez-Navarro, Jaclyn Brennan-McLean, Jaël Copier, Jessica Caldwell, Joachim Greiner, **Patricia Martínez Díaz**, Vladímir Sobota *"Gordon Research Conference on Cardiac Arrhythmia Mechanisms 2023: Early Career Investigators Views on Emerging Concepts and Technologies"* The Journal of Physiology 2023. Pp. 1-3. DOI: 10.1113/JP284666

Refereed Conference Abstracts

- **Patricia Martínez Díaz**, Jorge Sánchez, Nikola Fitzen, Ursula Ravens, Olaf Dössel, and Axel Loewe *"Integrating the Right Atrium in Patient-Specific Computer Models Increases Arrhythmia Vulnerability of the Left Atrium"*, Clinical Research in Cardiology. 90th Annual Meeting of the German Cardiac Society (DGK) 2024. DOI: 10.1007/s00392-024-02406-5
- **Patricia Martínez Díaz**, Jorge Sánchez, Nikola Fitzen, Ursula Ravens, Olaf Dössel, and Axel Loewe *"Integrating the Right Atrium in Patient-Specific Computer Models Increases Arrhythmia Vulnerability of the Left Atrium"*, Europace. Vol. 26. EHRA 2024 - Annual Congress of the European Heart Rhythm Association 2024. DOI: 10.1093/europace/euae102.586
- **Patricia Martínez Díaz**, Jorge Sánchez, Albert Dasí, Christian Götz, Nikola Fitzen, Laura Unger, Annika Haas, Ursula Ravens, Armin Luik, Olaf Dössel, and Axel Loewe *"Personalization of Atrial Computer Models for the Assessment of Atrial Fibrillation Vulnerability"* Isaac Newton Institute Fickle Heart: The intersection of Uncertainty Quantification, Artificial Intelligence and Digital Twins 2024
- **Patricia Martínez Díaz**, Jorge Sánchez, Albert Dasí, Christian Götz, Nikola Fitzen, Laura Unger, Annika Haas, Ursula Ravens, Armin Luik, Olaf Dössel, and Axel Loewe *"Digital-Twin Based Assessment of Atrial Arrhythmias: Influence of Personalization Strategies"* Virtual Physiome Human (VPH) Conference 2024
- **Patricia Martínez Díaz**, Christian Goetz, Albert Dasí, Laura Unger, Annika Haas, Olaf Dössel, Armin Luik, and Axel Loewe *"Impact of Effective Refractory Period Personalization on Prediction of Atrial Fibrillation Vulnerability"* Europace. Vol. 25. EHRA 2023 - Annual Congress of the European Heart Rhythm Association 2023. DOI: 10.1093/europace/euad122.542
- **Patricia Martínez Díaz**, Christian Goetz, Albert Dasí, Laura Unger, Annika Haas, Olaf Dössel, Armin Luik, and Axel Loewe *"Impact of Effective Refractory Period Personalization on Prediction of Atrial Fibrillation Vulnerability"* Clinical Research in Cardiology. 89th Annual Meeting of the German Cardiac Society (DGK) 2023. DOI: 10.1007/s00392-023-02180-w
- **Patricia Martínez Díaz**, Christian Goetz, Albert Dasí, Laura Unger, Annika Haas, Olaf Dössel, Armin Luik, and Axel Loewe *"Impact of Effective Refractory Period Personalization on Prediction of Atrial Fibrillation Vulnerability"* BMT 2023 - 57th Annual Conference of the German Society for Biomedical Engineering (VDE | DGBMT) 2023. DOI: 10.1515/bmte-2023-2001
- **Patricia Martínez Díaz**, Christian Goetz, Albert Dasí, Laura Unger, Annika Haas, Olaf Dössel, Armin Luik, and Axel Loewe *"Impact of Effective Refractory Period Personalization on Prediction of Atrial Fibrillation Vulnerability"* Gordon Research Conference on Arrhythmia Mechanisms 2023

- **Patricia Martínez Díaz**, Jule Bender, Eric Invers-Rubio, Jana Reventós-Presmanes, Marta Martínez Pérez, Maria Guillem, Lluís Mont, Olaf Dössel, and Axel Loewe *"Personalization of Atrial In Silico Models Using Non-Invasive Data Predicts Lower Arrhythmia Vulnerability Compared to Minimally Invasive Data"* Electrocardiographic Imaging (ECGI) Summit 2023
- **Patricia Martínez Díaz**, Luca Azzolin, Jorge Sánchez, Claudia Nagel, Olaf Dössel, and Axel Loewe *"Influence of the Right Atrium for Arrhythmia Vulnerability: Geometry Inference Using a Statistical Shape Model"* 4th Atrial Signals Proceedings 2021. DOI: 10.5445/IR/1000138456
- Christian Goetz, **Patricia Martínez Díaz**, Eric Invers-Rubio, Sachal Hussain, Lluis Mont, Constanze Schmidt, Samuel Mañá, Martin Steghöfer, Cristina Corsi, Olaf Dössel, Andreu M. Climent, Blanca Rodríguez, Ulrich Schotten, José Ángel Cabrera, Axel Loewe, María S. Guillem, and Till Althoff *"Standardized Regionalization of the Atria for 3D Cardiac Imaging, Electroanatomical Mapping and Computational Modeling – A Multidisciplinary Consensus of the PersonalizeAF Consortium"*, Heart Rhythm. Vol. 21. Annual Meeting of the Heart Rhythm Society (HRS) 2024. DOI: 10.1016/j.hrthm.2024.03.810
- Christian Goetz, **Patricia Martínez Díaz**, Eric Invers-Rubio, Sachal Hussain, Lluis Mont, Constanze Schmidt, Samuel Mañá, Martin Steghöfer, Cristina Corsi, Olaf Dössel, Andreu M. Climent, Blanca Rodríguez, Ulrich Schotten, José Ángel Cabrera, Axel Loewe, María S. Guillem, and Till Althoff *"Standardized Regionalization of the Atria for 3D Cardiac Imaging, Electroanatomical Mapping and Computational Modeling – A Multidisciplinary Consensus of the PersonalizeAF Consortium"*, Clinical Research in Cardiology. 90th Annual Meeting of the German Cardiac Society (DGK) 2024. DOI: 10.1007/s00392-024-02406-5
- Pablo Blochberger, Felix Wiedmann, Jorge Sánchez, **Patricia Martínez Diaz**, A. Paasche, B. Yesilgöz, M. Kraft, Axel Loewe, S. Kallenberger, N. Frey, and Constanze Schmidt *"Eine Neue Interventionelle Behandlungsstrategie Atrialer Arrhythmien Mittels Vorhoftätowierung"* Clinical Research in Cardiology. 89th Annual Meeting of the German Cardiac Society (DGK) 2023. DOI: 10.1007/s00392-023-02180-w
- Constanze Schmidt, Felix Wiedmann, P. L. Blochberger, Jorge Sánchez, **Patricia Martínez Díaz**, A. Paasche, B. Yesilgöz, M. Kraft, Axel Loewe, S. Kallenberger, and N. Frey *"Atrial Tattoo Lines: A New Method to Terminate Atrial Fibrillation by Creating Pathways of Increased Tissue Conductivity"* Clinical Research in Cardiology. 88th Annual Meeting of the German Cardiac Society (DGK) 2022. DOI: 10.1007/s00392-022-02002-5

Conference Presentations

- **Patricia Martínez Díaz**, Jorge Sánchez, Nikola Fitzen, Ursula Ravens, Olaf Dössel, and Axel Loewe *"Der Rechte Vorhof Beeinflusst die in silico Anfälligkeit für Arrhythmien in Beiden Vorhöfen"*, Clinical Science Box 2. Freie Vorträge: KI meets EP. 90th Annual Meeting of the German Cardiac Society (DGK) , Mannheim 2024. DOI: 10.1007/s00392-024-02406-5
- **Patricia Martínez Díaz**, Pascal Maierhofer, Eric Invers-Rubio, Michael Beigl, Lluís Mont, Amir Jadidi, Olaf Dössel, and Axel Loewe *"Insights from Explainable Machine Learning on Biatrial Arrhythmia Vulnerability Assessment"*, Rossana Degani Young Investigator Award Session. Computing in Cardiology Conference (CinC) Karlsruhe, Germany 2024
- **Patricia Martínez Díaz**, Jorge Sánchez, Nikola Fitzen, Ursula Ravens, Olaf Dössel, and Axel Loewe *"Integrating the Right Atrium in Patient-Specific Computer Models Increases Arrhythmia Vulnerability in Both Atria"*, Young Investigator Award Session. Basic and Translational Science. EHRA 2024 - Annual Congress of the European Heart Rhythm Association, Berlin, Germany 2024. DOI: 10.1093/europace/euae102.586
- **Patricia Martínez Díaz**, Christian Goetz, Albert Dasí, Laura Unger, Annika Haas, Olaf Dössel, Armin Luik, and Axel Loewe *"Impact of Effective Refractory Period Personalization on Prediction of Atrial Fibrillation Vulnerability"* Young Investigator Award Session. Basic and Translational Science. EHRA 2023 - Annual Congress of the European Heart Rhythm Association, Barcelona, Spain 2023. DOI: 10.1093/europace/euad122.542
- **Patricia Martínez Díaz**, Christian Goetz, Albert Dasí, Laura Unger, Annika Haas, Olaf Dössel, Armin Luik, and Axel Loewe *"Impact of Effective Refractory Period Personalization on Prediction of Atrial Fibrillation Vulnerability"* BMT 2023 - 57th Annual Conference of the German Society for Biomedical Engineering (VDE|DGBMT) Duisburg, 2023. DOI: 10.1515/bmte-2023-2001
- **Patricia Martínez Díaz**, Jorge Sánchez, Albert Dasí, Christian Götz, Nikola Fitzen, Laura Unger, Annika Haas, Ursula Ravens, Armin Luik, Olaf Dössel, and Axel Loewe *"Digital-Twin Based Assessment of Atrial Arrhythmias: Influence of Personalization Strategies"* Virtual Physiome Human (VPH) Conference, Stuttgart, Germany 2024
- **Patricia Martínez Díaz**, Jule Bender, Eric Invers-Rubio, Jana Reventós-Presmanes, Marta Martínez Pérez, Maria Guillem, Lluís Mont, Olaf Dössel, and Axel Loewe *"Personalization of Atrial In Silico Models Using Non-Invasive Data Predicts Lower Arrhythmia Vulnerability Compared to Minimally Invasive Data"* Digital Twins in ECGI. Electrocardiographic Imaging (ECGI) Summit Valencia, Spain 2023
- **Patricia Martínez Díaz**, Christian Goetz, Albert Dasí, Laura Unger, Annika Haas, Olaf Dössel, Armin Luik, and Axel Loewe *"Impact of Effective Refractory Period Personalization on Prediction of Atrial Fibrillation Vulnerability"* Gordon Research Conference (GRC) on Arrhythmia Mechanisms, Houston, Texas, USA 2023

Supervised Student Theses

- Pascal Maierhofer *"Explainable Machine Learning for the Assessment of Atrial Fibrillation Vulnerability"* Master Thesis, Institute of Biomedical Engineering, Karlsruhe Institute of Technology (KIT), 2024
- Annika Ladner, *"Influence of Atrial Electrophysiological, Anatomical and Substrate Characteristics on Atrial Fibrillation Vulnerability Assessment"*, Master Thesis, Institute of Biomedical Engineering, Karlsruhe Institute of Technology (KIT), 2024
- Nikola André Fitzen, *"Impact of the Right Atrium on Arrhythmia Vulnerability Assessment and Fitting of a Statistical Shape Model for Augmentation of Missing Right Atria"*, Bachelor Thesis, Institute of Biomedical Engineering, Karlsruhe Institute of Technology (KIT), 2023
- Christian Goetz *"Atrial Segment Division Method for Regional and Quantitative Analysis"* Master Thesis, Institute of Biomedical Engineering, Karlsruhe Institute of Technology (KIT), 2022

Supervised Assistant Students (HiWi)

- Jule Bender *"Personalized Modeling of Atrial Activation and P-waves"*, Institute of Biomedical Engineering, Karlsruhe Institute of Technology (KIT), 2023
- Pascal Maierhofer *"Interactive Software to Plan and Guide Ablation Procedures"*, Institute of Biomedical Engineering, Karlsruhe Institute of Technology (KIT), 2023

Data and Software

- **Patricia Martínez Díaz**, Jorge Sánchez, Nikola Fitzen, Ursula Ravens, Olaf Dössel, and Axel Loewe *"The Right Atrium Affects in silico Arrhythmia Vulnerability in Both Atria"*, DOI: 10.35097/1830, DOI: 10.5281/zenodo.10724337
- **Patricia Martínez Díaz**, Albert Dasí, Christian Goetz, Laura Unger, Annika Haas, Armin Luik, Blanca Rodríguez, Olaf Dössel, and Axel Loewe *"Atrial Models with Personalized Effective Refractory Period"*, DOI: 10.5281/zenodo.10726677
- Pascal Maierhofer, **Patricia Martínez Díaz**, Marie Houillon, Olaf Dössel, Axel Loewe, *"HeartVR - Interactive Software to Plan and Guide Ablation Procedures (v3.1)"* DOI: 10.5281/zenodo.10222758
- Christian Goetz, **Patricia Martínez Díaz**, and Axel Loewe *"DIVAID (Version 1.0)"* Repository: https://gitlab.kit.edu/kit/ibt-public/divaid DOI: 10.35097/184

Awards & Grants

- Finalist in the Young Investigator Award, Computing in Cardiology (CinC) Conference 2024. Karlsruhe, Germany, **Patricia Martínez Díaz**, Pascal Maierhofer, Eric Invers-Rubio, Michael Beigl, Lluís Mont, Amir Jadidi, Olaf Dössel, and Axel Loewe *"Insights from Explainable Machine Learning on Biatrial Arrhythmia Vulnerability Assessment"*
- 1st Finalist in the Young Investigator Award (Basic and Translational Science), EHRA 2024 - Annual Congress of the European Heart Rhythm Association 2024. Berlin, Germany, **Patricia Martínez Díaz**, Jorge Sánchez, Nikola Fitzen, Ursula Ravens, Olaf Dössel, and Axel Loewe *"Integrating the Right Atrium in Patient-Specific Computer Models Increases Arrhythmia Vulnerability in Both Atria"*
- 2nd Place in the Young Investigator Award (Basic and Translational Science), EHRA 2023 - Annual Congress of the European Heart Rhythm Association 2023. Barcelona, Spain, **Patricia Martínez Díaz**, Christian Goetz, Albert Dasí, Laura Unger, Annika Haas, Olaf Dössel, Armin Luik, and Axel Loewe *"Impact of Effective Refractory Period Personalization on Prediction of Atrial Fibrillation Vulnerability"*
- 1st Place for Best Poster, Gordon Research Seminar (GRS) on Cardiac Arrhythmia Mechanisms, Galveston, Texas, USA, **Patricia Martínez Díaz**, Christian Goetz, Albert Dasí, Laura Unger, Annika Haas, Olaf Dössel, Armin Luik, and Axel Loewe *"Impact of Effective Refractory Period Personalization on Prediction of Atrial Fibrillation Vulnerability"*
- Honorable Mention, Gordon Research Conference (GRC) on Cardiac Arrhythmia Mechanisms, Galveston, Texas, USA, **Patricia Martínez Díaz**, Christian Goetz, Albert Dasí, Laura Unger, Annika Haas, Olaf Dössel, Armin Luik, and Axel Loewe *"Impact of Effective Refractory Period Personalization on Prediction of Atrial Fibrillation Vulnerability"*
- 1st Place in Student Competition, 57th Annual Conference of the German Society for Biomedical Engineering (VDE | DGBMT) Christian Goetz, **Patricia Martínez Díaz**, Jorge Sánchez, Amir Jadidi, Martin Eichenlaub, Olaf Dössel, and Axel Loewe *"Discrepancy Between LGE-MRI and Electro-Anatomical Mapping for Regional Detection of Pathological Atrial Substrate"*
- Finalist in Student Competition, 57th Annual Conference of the German Society for Biomedical Engineering (VDE | DGBMT), Nikola Fitzen, **Patricia Martínez Díaz**, Olaf Dössel, and Axel Loewe *"Impact of the Right Atrium on Arrhythmia Vulnerability"*
- Travel grant from the German Heart Foundation for participation in the Gordon Research Conference on Cardiac Arrhythmia Mechanisms 2023 in Houston, Texas